Low-frequency modes of variability of the Indian Ocean and their connection with the Indian Ocean Dipole

by

Irina V. Sakova*

M.Eng.Sc., B.Sc (Hons.)

Submitted in fulfillment of the requirements for the Degree of

Doctor of Philosophy in Quantitative Marine Science

(A joint CSIRO and UTAS PhD program in quantitative marine science)

School of Geography and Environmental Studies
University of Tasmania
July, 2010

*present address Mohn-Sverdrup Center/Nansen Environmental and Remote Sensing Center, Bergen, Norway

Declaration of Originality

This thesis contains no material which has been accepted for a degree or diploma by the University or any other institution, except by way of background information and duly acknowledged in the thesis, and to the best of my knowledge and belief no material previously published or written by another person except where due acknowledgement is made in the text of the thesis, nor does the thesis contain any material that infringes copyright.

Irina V. Sakova
25 June 2010

Authority of Access

This thesis may be made available for loan and limited copying in accordance with the Copyright Act 1968.

Irina V. Sakova

25 June 2010

Statement of Co-authorship

Chapter 2 contains material that was published in Sakova et al. (2006), Geophys. Res. Lett., 33, L20603. Chapter 5 contains material that has been submitted for publication Sakova and Coleman (2009), Advances in Geosciences.

In all cases, the design and implementation of the research, data analysis, interpretation of the results and manuscript preparation was the responsibility of the candidate. Gary Meyers (CSIRO Marine and Atmospheric Research) and Richard Coleman (University of Tasmania) assisted with guidance and supervision in all aspects of the PhD and with help producing publishable quality manuscripts.

Professor Richard Coleman

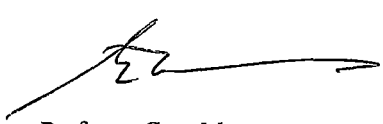

Professor Gary Meyers

Abstract

The thesis investigates the low-frequency variability of the Indian Ocean, based on a number of independent observational and reanalysis data sets. These data sets include altimetry sea level anomaly (SLA) gridded field, subsurface temperature from selected Expendable Bathythermograph (XBT) lines, NOAA Optimum Interpolation Sea Surface Temperature (SST) and Extended SST V2 (Kaplan) data sets, tide gaugé and reconstructed sea level data, surface winds from National Center for Environmental Prediction (NCEP) and Dipole Mode Indexes from HadISST, as well as coral core records used as a long term proxy climate signal. The analysis is primarily based on identifying the major temporal scales by means of spectral analysis.

It is found that in most regions of the Indian Ocean, the low-frequency variability (corresponding to periods of six months and longer) is concentrated in five spectral bands: semi-annual, annual, 18-20 months, 3 years, and 4 years and longer; at least during the last two decades. For each of the identified low-frequency variability modes, their spatial distributions as well as the temporal behaviour are investigated; the corresponding results are presented by means of spatial maps of power spectral density and movies. Despite the extensive literature on the variability of the Indian Ocean, to the best of our knowledge no systematic analysis of this kind has been conducted so far.

While the existence of semi-annual and annual signals is well known, the presence of such a pronounced and well defined 18-month signal has not been previously identified. Its discovery is one of the main results of this study.

Both the 18-month and 3-year signals are found to be directly related to the Indian Ocean Dipole (IOD) mode. The IOD events in the last two decades seem to predominantly occur as a result of their constructive interference. The connection established between these two quasi-periodic signals with the IOD allows us to suggest that the IOD phenomenon has oscillatory character. This suggestion opens up possibilities to improve the prediction of IOD, which is of a major importance for the seasonal weather prediction in Australia. In particular, it is shown that the status of the IOD in the last three years could be predicted two seasons ahead based on the estimate of the state of the 18-month signal.

Acknowledgements

I am ever grateful to my much loved supervisors Richard Coleman and Gary Meyers for their guidance, encouragement, support and patience throughout these 5 years. In particular, I thank Richard for his constant support of scientific merits of this study, and Gary for his extensive knowledge of the field and for giving me freedom to pursue multiple diversions from the original plan.

I thank University of Tasmania and CSIRO Marine and Atmospheric Research for providing me a financial support for the first 3.5 years of my research through a joint PhD program in Quantitative Marine Science (QMS); CSIRO's Wealth from Oceans Flagship for the top-up scholarship. I acknowledge the financial support over the last 1½ years for the PhD fellowship funded by a donation from Trond Mohn c/o Frank Mohn at the Mohn-Sverdrup Center/Nansen Environmental and Remote Sensing Center in Bergen, Norway where I am now employed. Particularly, I would like to thank my Norwegian hosts Bente and Ola Johannessen for their hospitality, friendliness and patience.

I thank Anne Muller, Jay McCreary, Ola Johannessen, and Fabian Durand for their interest in this research, which provided me with the motivation and encouragement at the time when I needed it.

I appreciate the input from the two Examiners. It substantially improved the quality and integrity of the thesis and provided interesting ideas for future work.

I would like to say many thanks to Neil White for his help with all aspects of altimetry SLA observations, Ann Gronell for help with the XBT data; John Church for help with reconstructed sea level data; Nerilie J. Abram and Michael K. Gagan for providing the coral core data; Alexey Kaplan and Sergey Lebedev for interesting and encouraging discussions.

I also thank all institutions around the world that maintain and allow public access to observational, reconstructed, or other data sets used in this thesis. I thank C. Torrence and G. Compo for their public software for wavelet analysis.

I thank Australia, which became my second motherland, its people and Government for giving me that wonderful opportunity to enter the PhD program after raising two kids, which would be almost impossible elsewhere in the world.

My thanks to my lovely sons Nikolai and Yaroslav, my extended family for continuing support and tolerance, to my husband Pavel whose help during all these years cannot be overestimated, and to all people who supported me with this thesis.

List of supporting Publications

Sakova I. V. and R. Coleman (2009): Interannual oscillatory modes in the Indian Ocean and predictability of the Indian Ocean Dipole. *Advances in Geosciences. Ocean Science,* (invited paper - submitted).

Sakova, I. V., G. Meyers, and R. Coleman (2006): Interannual variability in the Indian Ocean using altimeter and IX1-expendable bathy-thermograph (XBT) data: Does the 18-month signal exist?, *Geophys. Res. Lett.*, **33**, L20603, doi:10.1029/2006GL027117, (selected by AGU journal Editors as a highlight publication).

Sakova, I., G. Meyers, and R. Coleman (2006): On the low frequency variability in the Indian Ocean, *(In) Dynamic Planet - Monitoring and Understanding a Dynamic Planet with Geodetic and Oceanographic Tools, IAG Symposia Series*, **130**, Springer-Verlag, P. Tregoning and C. Rizos (Eds), pp. 47-50.

Table of Contents

Chapter 1
Description of the Indian Ocean region and its variability

The climate of the countries surrounding the Indian Ocean is known to be strongly influenced by the ocean variability on various spatial and temporal scales (Schott and McCreary, 2001). It is therefore important for the climate prediction in the Indian Ocean region to be able to identify and understand its variability. This chapter provides general information essential in the context of this study. It starts with a description of the oceanography of the Indian Ocean region, followed by a brief discussion of known features and mechanisms of the low-frequency variability, and by a description of Indian Ocean Dipole (IOD) mode.

1.1 Description of the Indian Ocean region

1.1.1 Regional background

The Indian Ocean is the smallest of all oceans. It has an east-west dimension about 7800 km (between Australia and southern Africa) and a north-south dimension about 9600 km (from Antarctica to the Bay of Bengal). Although the average depth of the Indian Ocean is 3800 m, most of the basin has depth well below 5000 m. Two ridge systems, the Central Indian Ridge and Ninety East Ridge, divide the Indian Ocean into three parts of about equal size (Fig. 1.1.1). The existence of numerous ridges and plateaus influences ocean currents (e.g., Tomczak and Godfrey, 2002) and propagation of long planetary waves (e.g., Wang *et al.*, 2001; Killworth and Blundell, 2003a, 2003b, 2003c; Tailleux, 2003).

The significant difference of the Indian Ocean from other oceans is that it is the only semi-enclosed ocean: it is closed in the North. "The absence of a temperate and polar region north of the equator" (Tomczak and Godfrey, 2002), and not significant northward heat export (Schott *et al.*, 2009) influences ocean circulation and climate.

Another feature of the Indian Ocean is its low-latitude connection with the Pacific Ocean through the Indonesian Throughflow. The low salinity warm water from the Pacific enters the Indian Ocean and creates a zonal jet across the Indian tropical region, following the South Equatorial Current (Wijffels and Meyers, 2004).

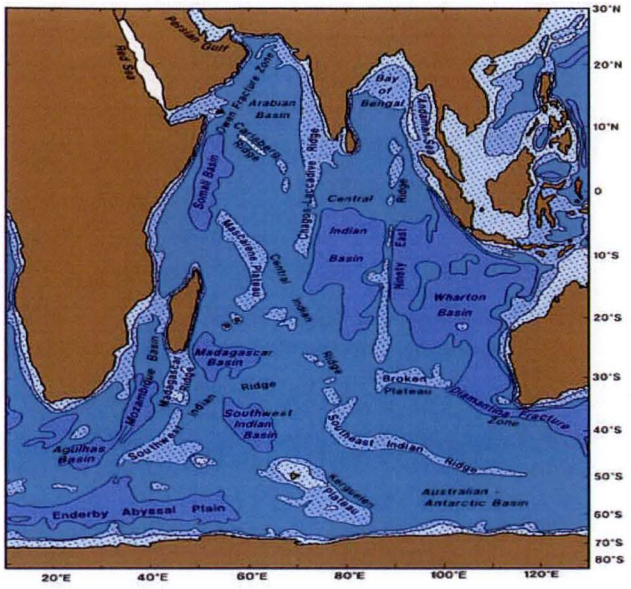

Figure 1.1.1. Topography of the Indian Ocean. The 1000, 3000, and 5000 m isobars are shown, and regions shallower than 3000 m are shaded (after Tomczak and Godfrey, 2002).

1.1.2 Winds and Indian Ocean monsoon

Winds over the Indian Ocean have a number of unique regional features. One of them is the seasonally reversing monsoon wind, particularly prominent in the northern part of the ocean. This monsoon wind determines the climate of the northern Indian Ocean rim countries: during the northern summer – by the Southwest, or Summer Monsoon (July-September) and during northern hemisphere winter – by the Northeast, or Winter Monsoon (December – March). The monsoon winds derived from the National Center for Environmental Modeling (NCEP) /National Center for Atmospheric Research (NCAR) reanalysis data is shown in Figure 1.1.2. The Winter Monsoon is characterized by high pressure over the Asian land mass; the winds are north-easterly, away from the Asian continent, causing north-easterly wind stresses over the Arabian Sea and Bay of Bengal. During the Summer Monsoon, the wind stresses are south-westerly over both these basins.

Another feature of the Indian Ocean is the absence of sustained easterly winds along the equator, which are present in other oceans. Instead, there is a tendency for westerly wind-bursts two times a year during monsoon transition periods and as a result a weak westerly annual mean (e.g., Schott *et al.*, 2009).

The situation in the southern hemisphere is dominated by the pressure gradient between the tropical low and the subtropical high pressure belts. The axis of low pressure in the tropics is near 10°S. The Asian-Australian monsoons bring a hot and wet season to north-west of Australia during December-April (northwest monsoon), a cooler and drier season during June-October (southeast monsoon)

(Tomczak and Godfrey, 1994). The Southeast Trades persist in the Indian Ocean throughout the year south of 10°S, with some shift northward (southward) of their northern edge during northern summer and fall (winter and spring) (Schott *et al.*, 2009).

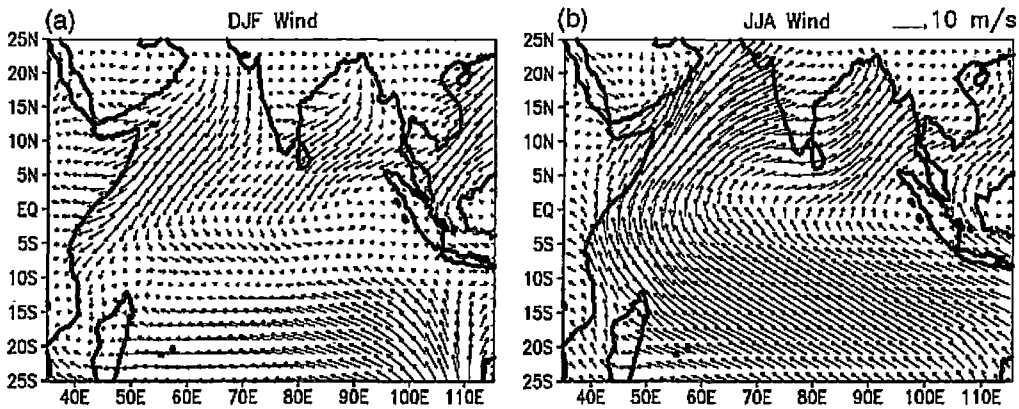

Figure 1.1.2. Surface winds derived from the NCEP–NCAR reanalysis data for the periods December–February and June–August (after Behera *et. al*, 2000).

A unique wind stress pattern produces forcing on the Indian Ocean that results in currents with unique variability scales and patterns, the main features of which are described in the following section.

1.1.3 Indian Ocean currents and upwelling

The strong monsoon winds generate large seasonal variation in ocean currents. As a result, many of Indian Ocean currents are locked to the seasons and display annual reversal patterns. Figure 1.1.3 shows schematic diagrams of the near-surface flow field in the Indian Ocean during northern hemisphere summer (a) and winter (b) monsoons.

Upwelling can be generated by wind in the open ocean or along coastlines as well as by remotely forced Kelvin or Rossby waves. There are several regions in the Indian Ocean with strong seasonal upwelling. In the Northern Hemisphere upwelling occurs off Northeast Africa, Arabian Peninsula and around India. In the Southern Hemisphere it exists along the northern edge of the southeast trades (Schott *et al.*, 2009). Due to the absence of steady easterly equatorial winds, there is no climatological equatorial upwelling in the eastern part of the ocean. Equatorial downwelling occurs during the transition months (May and November) when the wind turns eastward at the equator, producing convergence due to Ekman transport. Although the Sumatra-Java coast is considered as a region with weak upwelling, unusually strong upwelling occurs here from time to time that is

associated with a climate anomaly known as the IOD (Schott *et al.*, 2009). The IOD will be discussed in detail in Section 1.3.

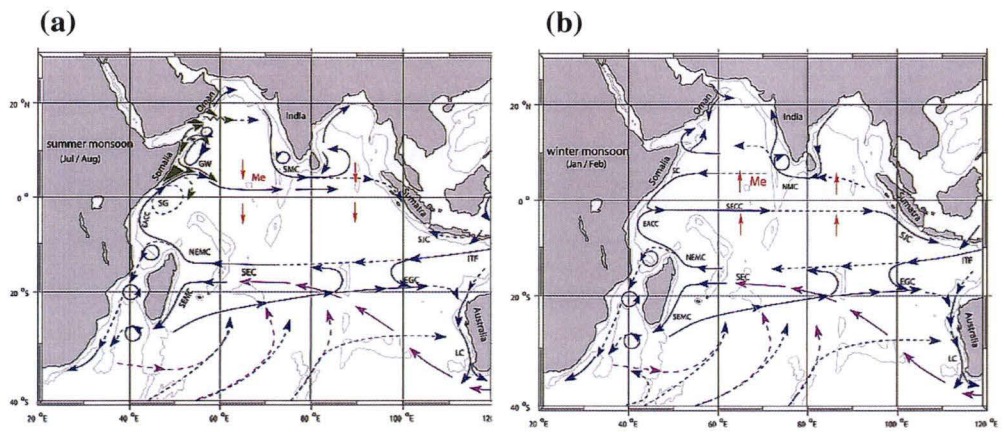

Figure 1.1.3. Schematic representation of identified current branches during the summer (a) and winter (b) monsoons. Current branches indicated are the South Equatorial Current (SEC), South Equatorial Countercurrent (SECC), Northeast and Southeast Madagascar Current (NEMC and SEMC), East African Coastal Current (EACC), Somali Current (SC), Southern Gyre (SG) and Great Whirl (GW) and associated upwelling wedges (green shades), Southwest and Northeast Monsoon Currents (SMC and NMC), South Java Current (SJC), East Gyral Current (EGC), and Leeuwin Current (LC). The subsurface return flow of the supergyre is shown in magenta. Depth contours shown are for 1000 m and 3000 m (grey). Red vectors (Me) show directions of meridional Ekman transports. ITF indicates Indonesian Throughflow (after Schott *et. al*, 2009).

1.2 Low-frequency variability of the Indian and Pacific Oceans

This study focuses on an investigation of the low-frequency variability of the Indian Ocean, by which we mean processes with characteristic time scales from semi-annual to several years. Below we provide a summary of the current knowledge of such processes in the Indian Ocean, while a more detailed analysis will be given in Chapter 3.

1.2.1 Variability of the Indian Ocean

Annual variability

The annual cycle is the most dominant component of the low-frequency variability over the Indian Ocean. The arising pattern is a result of a complicated interaction between the ocean and the atmosphere (Masumoto and Meyers, 1998; Birol and Morrow, 2001; White, 2001; Brandt *et al.*,

2002). The existence of annual and semi-annual processes in the Indian Ocean is well known; they have been the subject of numerous studies (Clarke and Liu, 1993; Yamagata *et al.*, 1996; Masumoto and Meyers, 1998; Schott and McCreary, 2001; Wang *et al.*, 2001; Yuan, 2005).

Monsoon winds over the northern part of the Indian Ocean create a strong annual signal in the Arabian Sea and Bay of Bengal. Strong seasonal fluctuations exist along 6°N and 10°N in the middle of the Arabian Sea. These fluctuations are associated with westward propagation of annual Rossby waves radiated from the west coast of India and continuously forced by the wind over the central Arabian Sea (Brandt *et al.*, 2002). These Rossby waves are mostly remotely forced from the Bay of Bengal rather than by local winds (Shankar *et al.*, 2004). The strong southeasterly monsoon winds blowing along the Somali and Oman coasts during summer create strong summer upwelling along these coasts and downwelling in the interior of the Arabian Sea.

In the southern tropical Indian Ocean (10°S to 20°S), the annual cycle of the trade winds generates Rossby waves in the open ocean that have westward phase propagation (Perigaud and Delecluse, 1992; Masumoto and Meyers, 1998). The high intensity annual band exists between 20°S and 35°S that is forced by local wind as well as remote forced from the tropical Indian Ocean and Pacific via the Indonesian Throughflow (Morrow and Birol, 1998; Birol and Morrow, 2001). The speed of propagation of annual Rossby waves changes in the middle of the Indian Ocean due to the bottom topography (Matano 1995; Wang *et al.*, 2001). The spatial distribution of the annual signal over the Indian Ocean is clearly represented by two regions with high variability – in the south-eastern Indian Ocean and near 6N across the Arabian Sea (Sakova *et al.* 2006a,b).

The annual signal in the Indian Ocean that is due to the forcing from the Pacific via the Indonesian Throughflow propagates poleward around Australia and can be detected as far as the southern tip of Tasmania (Wijffels and Meyers, 2004).

Semi-annual variability

The semi-annual variability is a strong feature of the Indian Ocean. Zonal winds at the equator are generally light, with the meridional wind component being dominated by the annual monsoon cycle (Tomczak and Godfrey, 2002). The strong zonal wind component occurs during transition periods between the two monsoons: during transition from Northeast to Southwest Monsoon in April-June and during transition from Southwest to Northeast Monsoon in November-December. The transition is characterized by intense Indian Equatorial Jet (or Wyrtki Jet) (Han *et al.*, 1999; Schott and McCreary, 2001) first described by Wyrtki (1973). The formation of the jet is accompanied by thermocline uplifting at the western origin of the jet and by sinking at its eastern Indian Ocean edge. In this way, the semi-annual zonal equatorial winds in the interior of the Indian Ocean basin do remotely generate the semi-annual sea level fluctuation in the eastern Indian Ocean (Clarke and Liu, 1993).

The spatial distribution of the semi-annual signal has been independently obtained from the altimetry sea level anomaly (SLA) data by Sakova *et al.* (2006a,b) and Fu (2007). These studies employed different data processing methods. Fu used complex-valued empirical orthogonal function (EOF) analysis of the high-passed data, while Sakova *et al.* used spectral analysis methods. Yet, the spatial patterns of the semi-annual signal obtained in both studies are very similar (Fig. 1.2.1).

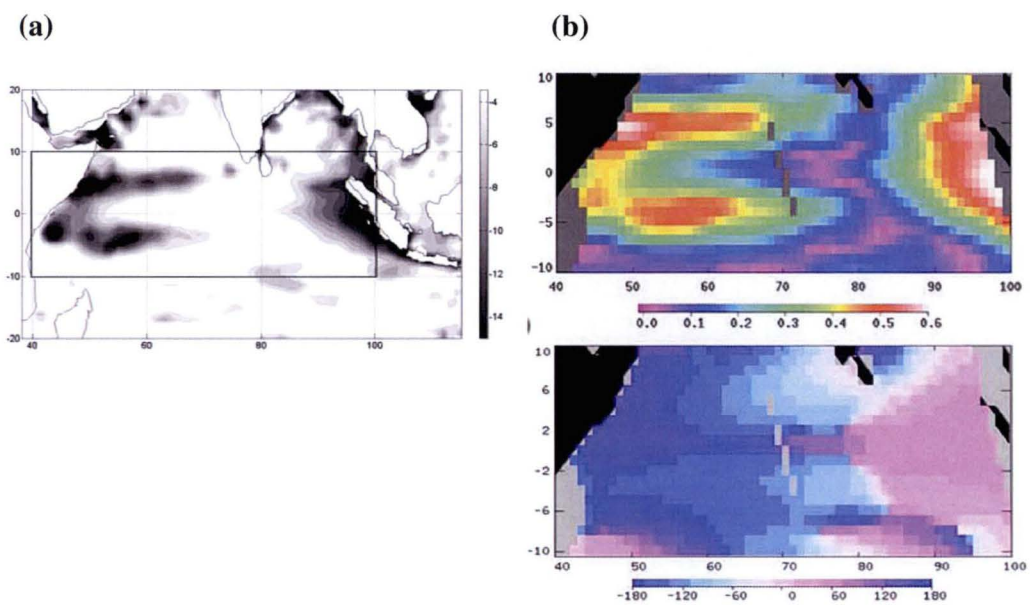

Figure 1.2.1. Spatial distribution of the semi-annual altimetry sea surface heights: (a) by Sakova *et al.* (2006b), in units of (power spectral density)·Δf (cm²), with the black rectangle corresponding to the region analysed in Fu (2007); and (b) by Fu (2007), where the upper panel - amplitude (in arbitrary units) and low panel - phase (in degrees) of the leading complex-valued EOF of the band-passed signal.

The transition period of the monsoon is characterized not only by the formation of the Wyrtki Jet, but also by formation of upwelling Rossby waves manifested in the distribution of the semi-annual signal over the Indian Ocean. This distribution is characterized by a C-shaped pattern in the western part of the ocean (Sakova *et al.*, 2006b; Fu, 2007). "This C-shaped pattern indicates the effects of the western boundary in reflecting Rossby waves. The phase of the mode reveals westward propagation in the regions off the equator and eastward propagation along the equator. These features suggest the roles of Kelvin waves on the equator and Rossby waves off the equator...." (Fu, 2007). When the upwelling Kelvin waves arrive at the central basin, the semi-annual winds reverse their direction. Because of the different phase, the directly forced and reflected waves cancel each other significantly at the central basin (Fu, 2007; Yuan and Han, 2006). For this reason, no semi-annual signal exists in the middle of the Indian Ocean basin.

Interannual variability

In the past decades, studies of the interannual variability of tropical oceans have mainly been limited to the tropical Pacific region. El Niño-Southern Oscillation phenomenon (ENSO) and related variability of the Pacific Ocean have been extensively investigated using both observational data and model simulations (see J. Geophysical Research, special issue on the TOGA decade, vol. 103, No C7, 1998). The variability of the tropical Indian Ocean has generate limited interest, partly owing to the belief that the Indian Ocean climate simply responds to changes in the tropical Pacific climate (Latif and Barnett 1995; Tourre and White 1997; Venzke *et al.* 2000). There is little doubt that ENSO is the dominant mode of the interannual variability in the Indian Ocean, and the close relation of the interannual variability in the Indian Ocean to ENSO has been confirmed by a number of statistical studies (e.g. Shinoda *et al.*, 2004a,b), while the degree of its independence from ENSO is a subject of scientific debate (Latif and Barnett, 1995; Tourre and White, 1995; Nicholson, 1997; Chambers *et al.*, 1999; Reason *et al.*, 2000; Allan *et al.*, 2001; Shinoda *et al.*, 2004a,b).

In the last 10 -15 years, there has been a growing interest to the interannual variability in the tropical Indian Ocean (Perigaud and Delecluse, 1993; Masumoto and Meyers, 1998), particularly after occurrence of a pronounced basin-wide anomalous pattern of sea surface temperature (SST) in the equatorial Indian Ocean called in 1999 the IOD (Behera *et al.*, 1999; Saji *et al.*, 1999; Webster *et al.*, 1999); althought this pattern of the interannual variability has been described long before (Hastenrath *et al.*, 1993).

The interannual variability of the Indian Ocean exhibits a wide spectrum of features and scales, both in time and space domains. Today, the recognized temporal scales of the interannual variability of the Indian Ocean are: ENSO, biennial signal or oscillation (Meehl, 1993; Reason *et al.*, 2000; Meehl and Arblaster, 2002; Meehl *et al.*, 2003; Allan *et al.*, 2003; Feng. and Meyers, 2003), and decadal variability (Ashok *et al.*, 2004; Annamalai *et al.*, 2005). The latter two signals are also often referred to in the literature as quasi-biennial signal (or QB) and quasi-decadal oscillation (Allan *et al.*, 2003; Tourre and White, 2003; White and Tourre, 2007). There is also evidence of the existence of bi-decadal oscillations (Tourre and White, 2003).

The ENSO mode has a characteristic period of order ~ 3-7-year, the quasi-biennial signal has a period of ~ 2-3 years, and is related to the tropospheric biennial oscillations (TBO) (Feng and Meyers, 2003; Loschnigg *et al.*, 2003). We note that by interannual variability, most authors consider signals with periods of 2 years and longer. The time scale between one and two years is mostly avoided or ignored. The variability with periods between one and two years will be discussed in more detail in Chapter 3.

1.2.2 Variability of the Pacific Ocean

Variability of the Indian Ocean is very dependent on variability of the Pacific Ocean. Due to the close geographical position of the two oceans, their connection through the Indonesian Throughflow, as well as an atmospheric teleconnection over the Indo Pacific basin, the two oceans are very closely related and share many properties. For this reason, as well because of the continuing debate about the relationship between IOD and ENSO in the literature, we provide below a brief description of Pacific-Ocean variability.

The low-frequency variability of the Pacific has a broad range of scales, from semi-annual to decadal, where the most important scale is that of the ENSO related signal with a period of about 3-8 years.

Apart from ENSO, there also exists a strong near-annual coupled ocean-atmosphere mode in the Tropical Pacific (Wang *et al.*, 2000). Annual wind variability in the eastern-to-central equatorial Pacific is mostly responsible for westward propagation of annual oscillations associated with the annual Rossby waves (Yuan, 2005). The semi-annual signal in the Pacific is primarily associated with oscillations of sea level.

At interannual timescales, there are several well known oscillations in the tropical Pacific Ocean the most important of which is El Niño - Southern Oscillation. Another important oscillation in the Pacific region with a longer time scale is the so-called Pacific Decadal Oscillation with a period of about 11 year (Latif *et al.*, 1996; Tourre *et al.*, 2001; Yeh and Kirtman, 2005; Matei *et al.*, 2008). The existence of quasi-biennial signals with periods about 2.2-2.8-years as for the Indian Ocean usually connected with the TBO (Meehl, 1993; White and Allan, 2001; Meehl and Arblaster, 2002; Wu and Kirtman, 2005).

In 2003, Jin and co-authors (Jin *et al.*, 2003) presented observational evidence for the existence of a near-annual mode in the Tropical Pacific, with a period of about 8 to 18 months that co-exists with ENSO. In their research, the authors used the NCEP ocean reanalysis data sets, high-pass filtered at 22 months. They called this mode the "fast mode", and suggested that it may be viewed as an independent coupled variability mode in the Pacific. The evidence of a near-annual or fast mode in the Pacific has also been found in other data sets and model output (Jin *et al.*, 2003; Kang *et al.*, 2004; Wu and Kirtman, 2005; Keenlyside *et al.*, 2007). Keenlyside (2007) referred to this mode as "sub-ENSO mode".

1.3 Indian Ocean Dipole Mode

1.3.1 Historical overview

The IOD is a coupled ocean-atmosphere phenomenon in the Indian Ocean characterized by an anomalous cold SST in the south-eastern equatorial Indian Ocean and anomalous warming of the western equatorial Indian Ocean. This anomalous pattern was first described as a "dipole" or "zonal" mode independently in two studies in 1999, by groups from the USA (Webster *et al.*, 1999) and Japan (Saji *et al.*, 1999). Both studies suggested that IOD is a native mode of the Indian Ocean that exists independently from the Pacific. The term IOD itself was introduced by Saji *et al.* (1999). It reflects a zonal structure of the phenomena with two maxima of different "polarity". This anomaly can be found not only in SST but also in other oceanic and atmosphere fields over the Indian Ocean, such as sea surface heights (SSH), wind, pressure, rainfall, and outgoing long wave radiation. Later, some authors referred to the anomalous pattern as proposed by Webster *et al.* (1999) – the Indian Ocean Zonal Mode (IOZM) (e.g., Black *et al.*, 2003; Clark *et al.*, 2003), or Indian Ocean Dipole Zonal Mode (Annamalai *et al.*, 2005; Song *et al.*, 2007) because "it matches the out-of-phase development of the SST extreme in the east and west Indian Ocean. The term dipole, on the other hand, suggests simultaneous variation in the east and west" so Clark *et al.* (2003), claim that the IOD does not represent a consistent oscillation phenomena (sea-saw) pattern, as for example, North Atlantic Oscillation, and therefore cannot be referred to as a dipole. Also it was found that anomalies along Sumatra-Java coast is a persistence property of IOD events, while the SST anomaly in the western part of the Indian Ocean varies significantly from event to event (Le Blanc and Boulanger, 2001; Huang and Kinter, 2002). This property agrees, and partly overlaps with the previous study of Reverdin *et al.* (1986) which described the anomalous interannual condition of wind and rainfall over the eastern and central equatorial Indian Ocean in October and November of certain years. Nevertheless, IOD is now the common name for this phenomenon in the scientific literature.

Prior to the above mentioned studies by Webster *et al.* (1999) and Saji *et al.* (1999), investigations of the interannual variability of the Indian Ocean were mainly focused on understanding its response to the ENSO variability (Latif and Barnett, 1995; Tourre and White, 1995). Although anomalous dipole-like patterns of SST variability between the Indonesian region and central Indian Ocean were noticed and suggested to be independent from ENSO before 1999 (Nicholls, 1989; Hastenrath *et al.*, 1993), these studies did not attract wide attention. Only the huge climate anomalies in 1994 and 1997 have been finally connected with the SST anomaly in the southeast Indian Ocean, stimulating interest in Indian Ocean research. Saji *et al.* (1999) and Webster *et al.* (1999) were the first to provide a comprehensive ocean-atmosphere description and identify a plausible mechanism for independent behaviour of the Indian Ocean. These publications provoked debate about the interannual variability of the Indian Ocean. The main questions to answer were whether IOD is an

independent or dependent mode of the Indian Ocean (from ENSO), and what is the triggering/driving mechanism of IOD (Yamagata *et al.*, 2004; Fischer *et al.*, 2005).

1.3.2 Quantitative description

For a quantitative analysis of IOD, a Dipole Mode Index (DMI) was introduced by Saji in 1999 (Saji *et al.*, 1999). It is calculated as the anomaly in SST gradient between two particular regions of rectangular shape in the western (50°E-70°E and 10°S-10°N) and south-eastern (90°E-110°E and 10°S-0°N) tropical Indian Ocean (Fig. 1.3.1). These regions are denoted as WTIO and SETIO in Figure 1.3.1, and the corresponding indices will be referred as IOD west (IODW) and IOD east (IODE) in the thesis.

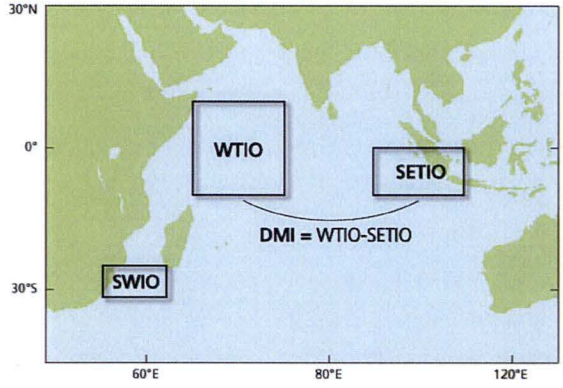

Figure 1.3.1. DMI calculated as the SST difference between two regions in the western tropical Indian Ocean (WTIO or IODW), at 50°E-70°E, 10°S-10°N, and south-eastern tropical Indian Ocean (SETIO or IODI), at 90°E-110°E, 10°S-0°N: DMI = SST(WTIO) – SST(SETIO) (http://ioc3.unesco.org/oopc/state_of_the_ocean/sur/ind/).

1.3.3 Positive/negative phases of IOD

IOD as any tropical phenomena is strongly locked to the annual cycle, reaching a peak during boreal autumn in September-October. The pattern has positive and negative phases. The positive IOD is characterised by the anomalously cold SST in the east and warm in the west; the equatorial wind is anomalous easterlies, coupled with anomalous SST and blowing from east to west towards warmer waters (Fig. 1.3.2, left panel), causing excessive rain at the eastern African coast and drought in Australia. The negative IOD has an opposite pattern (Fig. 1.3.2, right panel). During the negative phase of the IOD, "there are warmer than average SST's near Indonesia and cooler than average SST's in the western Indian Ocean, resulting in more westerly winds across the Indian Ocean, greater convection near Australia, and enhanced rainfall in the Australian region" (Australian Bureau of Meteorology, http://www.bom.gov.au/watl/about-weather-and-climate/australian-climate-influences.html?bookmark=iod).

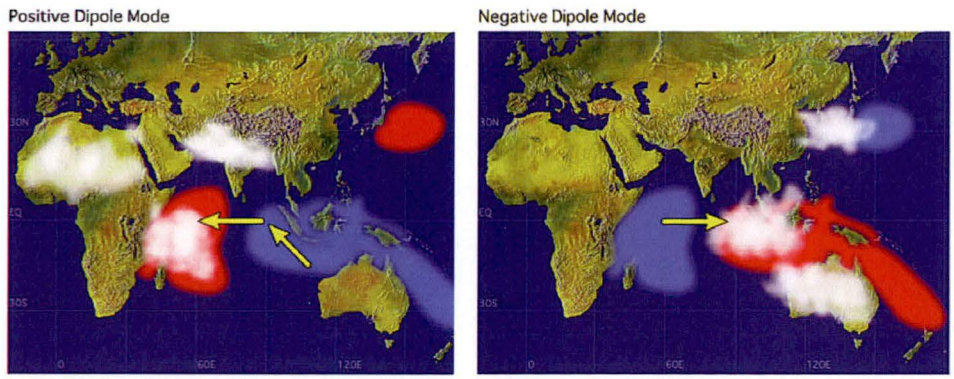

Figure 1.3.2. Schematic of a positive IOD (left panel) and a negative IOD event (right panel). SST anomalies are shaded (red for warm anomalies and blue for cold anomalies). White patches indicate increased convective activities, and arrows indicate anomalous wind directions (http://www.jamstec.go.jp/frcgc/research/d1/iod/).

1.3.4 Lists of IOD events

Lists of the years when El Niño or La Niña occurred and when positive or negative IOD occurred are available in the literature and on the internet. The lists of years do not agree in all details. This uncertainty in classification of IOD as well as in classification of ENSO can be one of the reasons for the debate about the dependence/independence of IOD on/from the ENSO phenomenon (Meyers *et al.*, 2007). We note here that there are at least four classifications of IOD years that are slightly different: Rao *et al.*, 2002 (Fig. 1.3.3); Yamagata *et al.*, 2004 (Fig. 1.3.4); Meyers *et al.*, 2007 (Fig.1.3.5); and Ummenhofer *et al.*, 2009 (Fig. 1.3.6).

Strong positive IOD events	Strong negative IOD events
1877	*1874*
1902	*1879–80*
1923	1889
1926	1890
1935	*1892–93*
1944	1899
1946	1901
1953	1906
1961	*1909–10*
1963	1917
1972	1920
1982	*1954–55*
1994	1958–60
1997	1964
	1975
	1984
	1989
	1992
	1996

Figure 1.3.3. Years of strong IOD events. Italic values identify years when positive (negative) IOD events co-occurred with strong El Niño (La Niña) in the Pacific. The value in bold indicates the negative IOD event that occurred along with El Niño (after Rao *et al.*, 2002).

	Years of Positive IOD	Years of Negative IOD	Years of El Niño	Years of La Niña
1	**1961***	**1958***	1963	1964
2	1963	**1960***	**1965***	**1967***
3	**1967***	1964	**1969***	1970
4	1972	1970	1972	**1971***
5	**1977***	**1989***	**1976***	**1973***
6	1982	**1992***	1982	**1975***
7	**1994***	**1996***	**1986***	**1988***
8	1997	-	**1991***	-
9	-	-	1997	-

Figure 1.3.4. Years of IOD and ENSO events. The asterisk denotes pure events, i.e. no El Niño (La Niña) during a positive (negative) IOD event (after Yamagata *et al.*, 2004)

	Negative IOD	No event	Positive IOD
El Niño	**1930**	**1877, 1888, 1899, 1911, 1914,** 1918, 1925, **1940,** 1941, **1965, 1986, 1987**	**1896, 1902, 1905, 1923,** 1957, **1963, 1972, 1982, 1991, 1997**
No event	**1880, 1958, 1968, 1974, 1980, 1985, 1989, 1992**	1881, **1882, 1883, 1884, 1895, 1898,** 1901, **1904, 1907, 1908, 1912,** 1915, 1920, **1921, 1927, 1929,** 1931, **1932, 1934, 1936, 1937, 1939, 1943, 1947, 1948,** 1951, 1952, **1953,** 1956, 1959, 1960, **1962, 1966, 1969, 1976, 1979, 1990,** 1993, **1995**	**1885, 1887, 1891, 1894,** 1900, 1913, **1919, 1926, 1935, 1944, 1945, 1946, 1961,** 1967, 1977, **1983,** 1994
La Niña	**1906, 1909, 1910,** 1916, **1917, 1928, 1933, 1942, 1950, 1975,** 1981	**1878,** 1879, 1886, 1889, **1890, 1892, 1893, 1897, 1903,** 1922, 1924, **1938, 1949,** 1954, 1955, **1964,** 1970, 1971, **1973,** 1978, 1984, **1988,** 1996, 1998	

Figure 1.3.5. Classification of years of positive/negative IOD along with El Niño or La Niña events. Boldface (lightface) indicates a higher (lower) level of certainty in the classification. A year is given a lower certainty if either the ENSO phenomenon or the IOD phenomenon is not clear (after Meyers *et al.*, 2007).

An important starting point for the analysis of the IOD is the identification of IOD events in the past. Without a common agreement on that, it is hardly possible to conduct a meaningful analysis of features of the atmoshere-ocean system identified with the IOD. Because there exist a number of different classifications of years of positive and negative IOD, we provide below the tables of existing classifications that will be referred to thoughout this thesis.

	Negative IOD	Neutral	Positive IOD
El-Nino	1930	"1877, 1888, 1899, 1905, 1911, 1914, 1918, 1925, 1940, 1941, 1965, 1972, 1986, 1987"	"1896, 1902, 1957, 1963, 1982, 1991, 1997"
Neutral	"1915, 1958, 1968, 1974, 1980, 1985, 1989, 1992"	"1880, 1881, 1882, 1883, 1884, 1895, 1898, 1900, 1901, 1904, 1907, 1908, 1912, 1920, 1921, 1927, 1929, 1931, 1932, 1934, 1936, 1937, 1939, 1943, 1947, 1948, 1951, 1952, 1953, 1959, 1960, 1962, 1966, 1967, 1969, 1971, 1976, 1977, 1979, 1983, 1990, 1993, 1995, 2001, 2002, 2003, 2005, 2006"	"1885, 1887, 1891, 1894, 1913, 1919, 1923, 1926, 1935, 1944, 1945, 1946, 1961, 1994, 2004"
La-Nina	"1906, 1909, 1916, 1917, 1933, 1942, 1975"	"1878, 1879, 1886, 1889, 1890, 1892, 1893, 1897, 1903, 1910, 1922, 1924, 1928, 1938, 1949, 1950, 1954, 1955, 1956, 1964, 1970, 1973, 1978, 1981, 1984, 1988, 1996, 1998, 2000"	1999

Figure 1.3.6. Classification of years of positive/negative IOD along with El Niño and La Niña events (after Ummenhofer *et al.*, 2009). This is an extended version of classification provided by Meyers *et al.* (2007).

1.3.5 Stages of development of IOD

The development of a positive IOD starts with anomalous SST cooling along the Sumatra–Java coast at the beginning of the normal upwelling season in May–June. The westerly winds that are usually present in the equatorial Indian Ocean during June–August reverse direction or weaken. The easterly wind anomaly and associated Ekman pumping shoal the thermocline and lift cold water to the surface along the Sumatra-Java coast due to upwelling. Cold SST further intensifies the easterly wind anomalies, creating a positive feedback. The upwelling strengthens, and cold SST extends westwards to the west of Sumatra as far as 80°E along the equator possibly due to horizontal advection of cold water (Shinoda *et al.*, 2004a; Du *et al.*, 2008). The upwelling and anomalous wind generates off-equatorial Rossby waves travelling westward, which deepen the thermocline in the west and enhance warm SST anomalies to the western tropical Indian Ocean several months later (Webster *et al.*, 1999). Positive IOD is characterised by the difference in SST in these two regions with anomalies of different signs, with peaks in September-November and rapid termination in early winter (Feng and Meyers, 2003; Luo *et al.*, 2008).

1.3.6 Decay of positive IOD events and onset of negative events

A positive IOD is followed by a negative IOD. Decay of a positive IOD and onset of a negative IOD is characterized by a slow eastward propagation of the warm SST anomaly along the equator (Webster *et al.*, 1999; Feng and Meyers, 2003). When the warm anomaly arrives at the eastern boundary, the resulting deeper thermocline reduces upwelling. This causes growth of a positive SST anomaly in the eastern Indian Ocean in the following year, or a positive IOD event. At the same time, the western Indian Ocean becomes anomalously cold, that leads to a stronger than usual monsoon. Webster *et al.* (1999) suggested that a stronger monsoon increases mixing and Ekman transports, forcing coastal upwelling along the western boundary of the Indian Ocean and greater evaporation, all of which would contribute to rapid cooling.

1.3.7 Importance of subsurface dynamics

There is no doubt today that the subsurface dynamics plays an important role in the development, support and decay of IOD events. Kelvin and Rossby waves can change the depth of the thermocline in the regions where thermocline water is ordinarily entrained into the surface layer anomously cooling SST – namely in the Sumatra-Java upwelling zone (Rao et al., 2002; Feng and Meyers, 2003) and in the Seychelles-Chagos thermocline ridge (Xie *et al.*, 2002; Vialard *et al.*, 2008). A shallower (or deeper) thermocline decreases (or increases) the temperature of entrained water. It was demonstrated that anomalous, equatorial, easterly wind during boreal summer prior to the onset of IOD excites equatorial Kelvin waves that travel eastward (Vinayachandran *et al.*, 1999). 'The wind anomaly and associated Ekman pumping generate off-equatorial Rossby waves that travel westward, deepen the thermocline, and warm SST in the western Indian Ocean' (Feng and Meyers, 2003). Downwelling Rossby waves generated in the central Indian Ocean later reflect off the Somali coast as downwelling equatorial Kelvin waves, which in turn terminate the positive IOD and excite a negative IOD by deepening the thermocline in the eastern Indian Ocean in the next year. This cycle leads to a quasi-biennial behaviour of IOD, when a positive IOD is followed by a negative IOD (Rao *et al.*, 2002; Feng and Meyers, 2003).

The above understanding of the basic mechanism of IOD underlies the important role of Kelvin and Rossby waves and associated subsurface dynamics. Rao *et al.* (2002) found that the subsurface ocean temperature consistently has a dipole structure that does not always appear in SST. Using EOF for analysis of SLA altimeter data for the period 1993-1999, as well as the ocean model output, they found two dominant modes of the interannual subsurface variability of the tropical Indian Ocean. "The dominant (first EOF) mode of interannual variability at the surface is characterized by a monopole (i.e. a basin-wide pattern) and related to ENSO, whereas the dominant subsurface mode (first EOF) is a dipole and related to the IOD" (Rao *et al.*, 2002).

The ENSO-induced basin-wide pattern is primarily controlled by surface heat fluxes indicating an atmospheric teleconnection from the Pacific to the India Ocean. However, the subsurface dipole is generated internally within the Indian Ocean region (Rao *et al.*, 2002; Feng and Meyers, 2003; Shinoda *et al.*, 2004a).

1.3.8 Relation between IOD and ENSO

There is an ongoing debate about whether the IOD is an inherent structure of the Indian Ocean or if it is driven remotely by ENSO in the tropical Pacific. Although a number of studies have argued that IOD is an independent mode (Saji *et al.*, 1999; Webster *et al.*, 1999; Iizuka *et al.*, 2000) other studies also provided evidence that interannual variability of the Indian Ocean depends on interannual variability in the Pacific. For example, Baquero-Bernal *et al.* (2002), Dommenget and Latif (2002), Shinoda *et al.* (2004b) considered IOD as driven by ENSO in the Pacific.

Regardless of the ultimate outcome of this discussion, there is clear evidence of the existence of IOD events in the absence of ENSO events. For example, Rao *et al.* (2002) showed that during the last 127 years only 5 of 14 strong positive events co-occurred with ENSO events, as well as 7 of 19 strong negative IOD events. In other words, 65% of strong IOD events occurred when there were no ENSO events in the Pacific. Therefore, IOD events have shown ability to evolve independently of ENSO and can be considered as an independent phenomenon.

One of the main questions in our understanding of the IOD concerns identification of the triggering mechanism of this interannual anomaly. Fisher *et al.* (2005) proposed a triggering mechanism of IOD that can explain its dependency as well as independency from ENSO. They found the existence of two triggers for a dipole mode — the first one independent of ENSO, and the second phase locking the IOD to El Niño. "The first is an anomalous Hadley circulation over the eastern tropical Indian Ocean and Maritime Continent, the second trigger is a consequence of a zonal shift in the center of convection associated with a developing El Niño, a Walker cell anomaly" (Fisher *et al.*, 2005). The existence of two triggers can give a clue to understanding of the development of IOD with/without ENSO and significant observed correlation between IOD and ENSO.

1.3.9 IOD: a triggered or oscillatory event?

The development of positive IOD is traditionally considered as an isolated event triggered by a particular ocean-atmosphere state (Fisher *et al.*, 2005), in contrast to ENSO that has an oscillatory character (e.g. Philander and Fedorov, 2003; Wang and Fiedler, 2006). However, there is an increasing evidence in favour of existence of a precondition for positive IOD events and/or successive IOD events (Horii *et al.*, 2008). Based on data from the recently deployed mooring buoys in the eastern Indian Ocean (1.5°S, 90°E) Horii *et al.* (2008) detected a negative temperature

anomaly at the thermocline depth in May 2006, that is about three months before the positive IOD 2006 signature developed at the surface.

Overall, there is little doubt today that positive IOD events are followed by negative IOD events, creating 'two-year time scales' (Rao *et al.*, 2002; Feng and Meyers, 2003; Behera and Yamagata, 2003). Some of authors have pointed out the possibility of an oscillatory nature of IOD. Based on ocean model output, Murtugudde *et al.* (2000) noted that "weaker Indian Ocean events occur quite regularly... that evolve similarly to the 1997 event" and suggested that "these events represent a natural mode of oscillation in the Indian Ocean".

1.3.10 Decadal variability of IOD

It was noted that IOD undergoes a decadal variability (Ashok *et al.*, 2004; Annamalai *et al.*, 2005; Tozuka *et al.*, 2007). On the basis of Simple Data Assimilation (SODA) reanalysis, Ashok *et al.* (2004) found that "the time series of decadal IOD and decadal ENSO indices are not well correlated" and that the decadal IOD is strongly correlated with the 20°C isothermal surface anomaly.

Later Annamalai *et al.* (2005) found that the decadal variability of IOD is correlated with the decadal variability in the Pacific, so that the "thermocline in the eastern equatorial Indian Ocean is raised or lowered depending on the phase of Pacific decadal variability".

1.3.11 Conclusions

The main purpose of this study is investigation of variability modes of the Indian Ocean, based primarily on temporal scales of these modes. The modes are isolated based mainly on results of spectral analysis of various physical fields, although other methods such as wavelet analysis and EOF analysis are also extensively used. Despite large literature on the variability of the Indian Ocean, to the best of our knowledge no systematic analysis of this kind has been conducted so far. One of the reasons for that is perhaps that the satellite era has just reached the age when the duration of the observed SST and altimetry fields make it possible to analyse the interannual variability (although not the decadal variability) with sufficient degree of confidence. The same mainly applies to the available data from Expendable Bathythermograph (XBT) lines, and indeed to reanalyses based on these observations.

Chapter 2.
Data sets and Methodology

2.1 Data sets used in this Thesis

This section describes the data sets used in the analysis of low-frequency variability in the Indian Ocean region. With the aid of spectral analysis and wavelet analysis, we try to identify low-frequency variability modes of the ocean and obtain their characteristics. To analyse ocean dynamic processes with periods of several years, one needs time-series of at least 10 years. Moreover, to be suitable for application of spectral and wavelet analyses, the analysed time series must not have any major data gaps, by which we mean gaps no longer than a small fraction of the characteristic period of the signal.

There are not many direct measurements of the ocean state that satisfy these conditions of duration and continuity. First of all, and most importantly, there are measurements of altimetry SLA, which are available from 1992 until present. This is the most important single data source for our analyses because of the good spatial coverage, temporal continuity, high quality, and the nature of the signal, which contains integral information about the dynamics and properties of the whole water column.

The next most important data set used in this study is the subsurface temperature measured along XBT lines. We use all data available along the Indian Ocean XBT lines from January 1989 to December 2002, because during this period it is regular enough for our analysis. There are also some tide gauge data and coral record data that provide an important opportunity for cross-validation and analysis of long-term tendencies, to complement the relatively short time span (~ 15 years) of the altimetry SLA data.

Along with the data from direct observations, there are a number of reanalysis products that represent reconstructed fields of ocean state variables, often for periods of several decades or even longer. These data sets include SST, SSH and wind. These data are used to support the conclusions we draw from direct observations.

Finally, this thesis also analyses the Indian Ocean Dipole Mode Index, which is a synthetic characteristic of an Indian Ocean coupled interannual variability mode.

2.1.1 Sea level

Sea level, or sea surface height, is the instantaneous height of the ocean surface, adjusted for atmospheric pressure and tides, above a reference surface. The reference level, typically adopted as mean sea level or mean sea surface height is mostly affected by the gravitation field. Since the Earth's gravitational field is relatively stable on decadal to centennial time-scales, the change in SSH on seasonal to interannual time-scales is mostly affected by the ocean circulation and water density variations. Its variations are caused by steric effects due to changes in the subsurface fields (including thermal expansion due to changes in subsurface temperature and changes in density caused by fresh water input), and dynamic processes, such as eddies, currents, and internal wave propagation.

The dominant contributors to SSH variability are density changes and internal, planetary wave propagation. "The ~5 cm surface height signatures of Rossby waves are mirrored as thermocline displacements of the opposite sign with amplitudes of ~50 m. These large variations of upper ocean thermal content have important implications about the role of the ocean in seasonal to interannual climate variations" (Chelton and Schlax, 1996).

Altimetry SLA

In this study we use the altimetry SLA data product processed by AVISO (http://www.aviso.oceanobs.com/). These data were collected by the ERS/Envisat/TOPEX/Jason-1 satellites and represent a highly processed data set containing deviation of the sea level from a chosen mean value (https://www.marine.csiro.au/~whi359/dmr/tp-ers-html/readme.htm). As stated above, it contains integrated information about subsurface ocean dynamics and thermodynamics. For analysis we use gridded, 1°-latitude/longitude, weekly-averaged SLA data. They cover a period from October 1992 to January 2008.

Tide gauge sea level

Traditionally, global sea level has been estimated from tide gauge measurements collected at coastal sites over the last century. Some tide gauge data are available for even longer periods. For example, the data collected in Amsterdam dates back to 1700 (Wikipedia: http://en.wikipedia.org/wiki/Tide_gauge). Tide gauges, usually placed on piers, measure the sea level relative to land, established at a nearby geodetic benchmark.

We use monthly sea-level data downloaded from the Permanent Service for Mean Sea Level (PSMSL), hosted at the Proudman Oceanographic Laboratory, UK (Woodworth and Player, 2003) and available at web (http://www.pol.ac.uk/psmsl/). The PSMSL data service was established in 1933 and represents a global data bank for long term sea level change information from tide gauges.

It contains over 55,000 station-years of monthly and annual mean values of sea level from almost 2,000 tide gauge stations around the world.

The Indian Ocean lacks long historical tide gauge records. We identify 18 stations with sufficiently long periods to be suitable for analysis at regions of interest for this study. Figure 2.1.1 shows the locations of these stations; their summary is provided in Figure 2.1.2. Sea level at small islands is likely to be representative of the depth of the thermocline while stations on continental coasts are influenced by other factors.

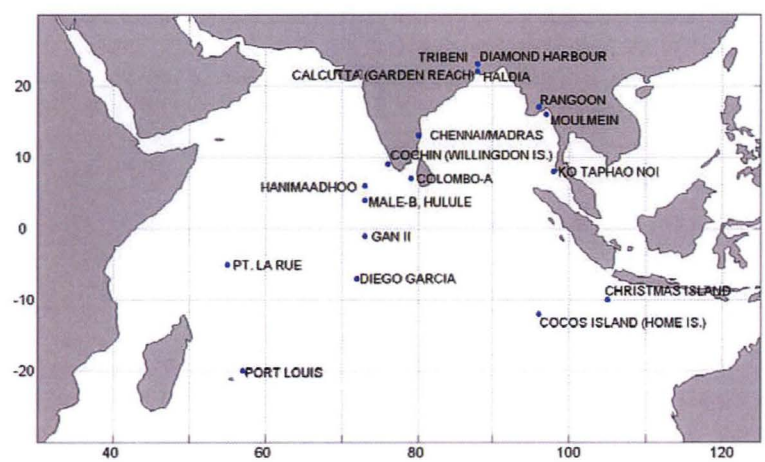

Figure 2.1.1. Positions and names of tide gauge stations in the Indian Ocean.

The records for each station were quality controlled: gaps of up to 3 months were filled by values linearly interpolated in time, while time series with longer gaps were considered as unsuitable for analysis.

Reconstructed sea level

We use reconstructed sea level data for the period 1950-2000 hosted by CSIRO Division of Marine and Atmospheric Research, Hobart (contributed by John Church and Neil White). This data set was created primarily to improve estimations of monthly distributions of large-scale sea level variability and change. The procedure of calculation of this dataset is described in Church *et al.* (2004) and Church and White (2006). The authors used TOPEX/Poseidon satellite altimeter data and tide gauge data to interpolate an optimal space-time coverage. This data set is nearly-global (65°S to 65°N) on a $1° \times 1°$ monthly grid and covers the period from January 1950 to December 2001, with seasonal (yearly) signals removed. It can be downloaded from CSIRO Marine and Atmospheric Research: http://www.cmar.csiro.au/sealevel/sl_data_cmar.html

Latitude	Longitude	Station Name	Recoded time	Analyzed time
04.40 S	55 32 E	PT. LA RUE	Feb.1993 - Sep.2004	Feb.1993 - Sep.2004
20.09 S	57.30 E	PORT LOUIS	Jan.1942 - Dec.1965	Jan 1942 - Dec.1947
07 14 S	72.27 E	DIEGO GARCIA	Jul.1959 - Mar.1964	not used
0 41 S	73.09 E	GAN II	Mar.1987 - Dec.2003	Aug.1991 - Dec.2003
04.11 N	73.32 E	MALE-B, HULULE	Dec.1990 - Dec.2003	Dec.1990 - Dec.2003
06.46 N	73.10 E	HANIMAADHOO	Aug.1991 - Jul.2002	Feb.1992 - Jul.2002
09.58 N	76.16 E	COCHIN	Jan.1939 - Dec.2004	Jan.1939 - Dec 1956
				Feb.1958 - Oct.1978
13 06 N	80.18 E	CHENNAI/MADRAS	Jan.1916 - Dec.2003	Sep.1952 - Feb.1967
22.02 N	88. 06 E	HALDIA	Jun.1970 - Dec 2004	Jun.1970 - Dec.1996
22 12 N	88. 10 E	DIAMOND HARBOUR	Jan 1948 - Dec.2004	Jan.1948 - Dec.1996
22.33 N	88 18 E	CALCUTTA	Jan.1932 - Jun.2000	Jan.1932 - Dec 1996
22.59 N	88 24 E	TRIBENI	Jan.1962 - Dec.2003	Jan.1962 - Dec.1997
06.56 N	79.51 E	COLOMBO-A	Jan.1953 - Dec.1965	Jan.1953 - Nov.1964
16.46 N	96.10 E	RANGOON	Jan 1916 - Dec.1962	Ja.1937 - Dec 191
16.29 N	97 37 E	MOULMEIN	Jan.1954 - Sep.1964	Jan. 1954 - Sep 1964
07.50 N	98.26 E	KO TAPHAO NOI	Jan.1940 - Dec.2005	Jan.1946 - Aug.1961
				Jan.1962 - Apr 1978
				Mar.1979 - Dec.2002
10 25 S	105.40 E	CHRISTMAS ISLAND	Jul.1962 - May 1966	not used
12.07 S	96.53 E	COCOS ISLAND	Nov.1961 - Dec.2004	Dec.1985 - Dec.2004

Figure 2.1.2. Tide gauge stations used for analysis.

2.1.2 Ocean subsurface temperature

In situ ocean temperature data available for the Indian Ocean are very sparse compared to the Atlantic and Pacific Oceans. The availability of subsurface temperature in the Indian Ocean at regular intervals started only after the launch in 1985 of the Tropical Ocean Global Atmosphere (TOGA) and World Ocean Circulation Experiment (WOCE) programs. Under these programs, the temperature in the upper ocean in the Indian and Pacific Oceans has been collected along XBT lines on a regular basis. In the Indian Ocean, data have been collected through an extensive Ship of Opportunity (SOOP) network established by CSIRO Division of Marine Research (now CMAR), as a national contribution to the international TOGA/WOCE programs. The broad scale and frequently repeated routes were covered by volunteer merchant ships, which measured temperatures down to depths between 450 m and 800 m, depending on the type of XBTs deployed from the ship. The positions of the XBT lines over the Indian Ocean are shown in Figure 2.1.3.

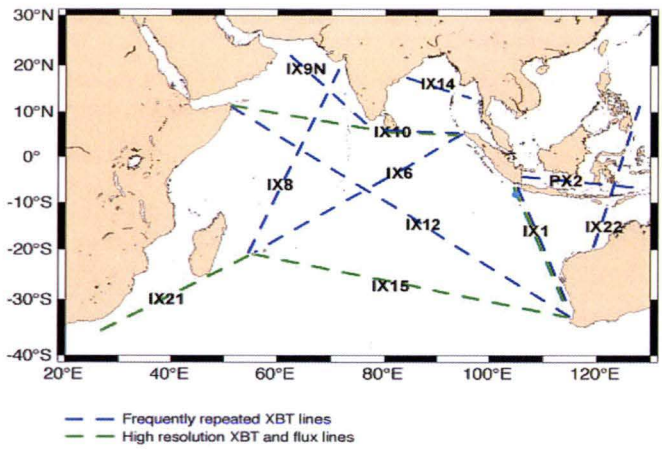

Figure 2.1.3. Positions of XBT lines over the Indian Ocean (http://www.clivar.org/organization/indian/IndOOS/XBT.php)

In this work we use carefully quality controlled subsurface temperature data from the Indian Ocean Thermal Archive (IOTA), hosted by CSIRO Marine and Atmospheric Research (Gronell and Wijffels, 2008). It is a compilation of historical upper ocean temperature data from various archives. In addition to the XBT data set, described in the CSIRO report (http://www.marine.csiro.au/~pigot/REPORT/overview.html) (Meyers and Pigot, 1999), it includes World Ocean Dataset (1998 and 2002), the NODC Indian Ocean archives, CSIRO's CTD database, Japanese fisheries and other data. Specifically, we use profiles along XBT line IX-1 from Fremantle, Western Australia to Sunda Strait, Indonesia. The positions of available temperature profiles along this line are shown in Figure 2.1.4.

The data in each profile were collected from surface to a depth of up to 1000 m, and have been interpolated to 201 vertical levels at intervals of 5 m. The spatial and temporal distribution of profiles is irregular; for analysis we used monthly averaged data collected at each level within rectangular boxes of size 1° of latitude by 2° of longitude (Fig. 2.1.4). The missing data were substituted by linear interpolation in time.

The availability of data for 6 boxes closest to Indonesia is depicted in Figure 2.1.5. Data in all boxes (see Fig. 2.1.4 for their numbered locations) are quite sparse prior to 1986 and not regular enough for time series spectral analysis. The data in Box 1 closest to the Indonesian coast is too sparse at all times. Therefore, we mostly use data in Box 2, with its location defined by opposite corners at (7.0°S, 104.0°E) and (8.0°S, 106.0°E). This box is located in the Java upwelling region and is the second closest to the Indonesian coast.

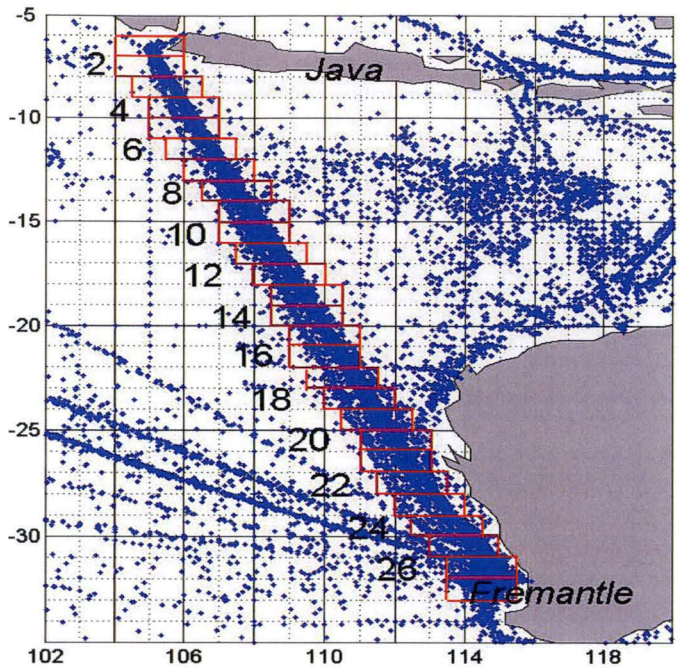

Figure 2.1.4. Locations of subsurface temperature profiles from IOTA along XBT line section IX-1. The data are spatially averaged inside each box shown in the figure.

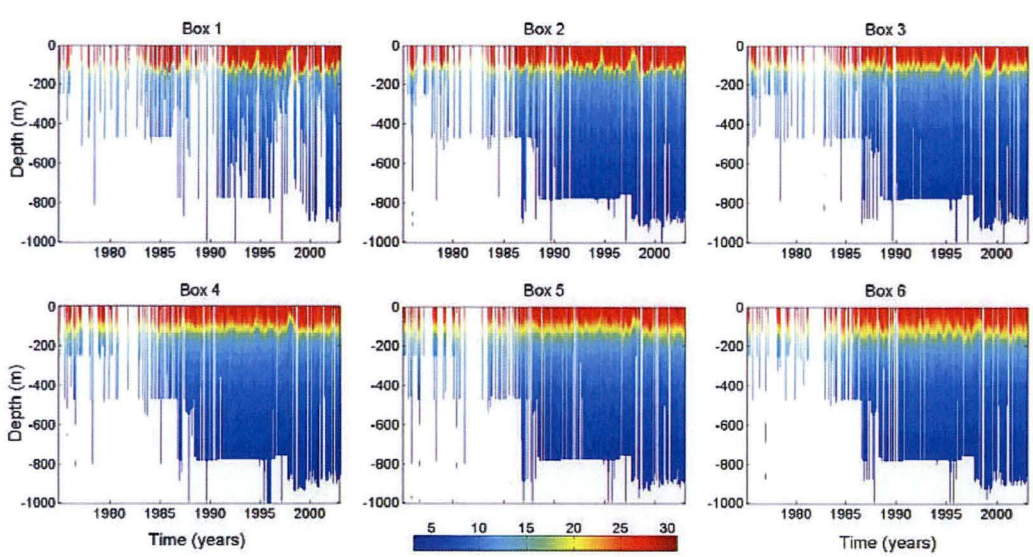

Figure 2.1.5. Subsurface temperature profiles for Boxes 1-6 from Figure 2.1.4.

For analysis of subsurface temperature we use data for the period from January 1989 to December 2002. The data before 1989 are considered not dense enough for our analysis.

2.1.3 Sea surface temperature

For SST analysis we mainly use two datasets: NOAA Optimum Interpolation SST or Reynolds (Reynolds *et al.,* 2002) data sets and Kaplan Extended SST V2 (Kaplan *et al.,* 1998).

Kaplan Extended SST V2 dataset uses optimal estimation in the subspace of 80 EOFs to fit ship observations from the U.K. Met Office database. The data after 1981 represents the projection of the NCEP Optimum Interpolation analysis (that combines ship observations with remote sensing data) by (Reynolds and Smith, 1994) on the same set of 80 EOFs used in (Kaplan *et al.,* 1998). These SST data represent the monthly SST anomalies from January 1856 until present time, and are available on a 5 degree global grid between 87.5°S and 87.5°N. Kaplan SST V2 dataset is provided by NOAA/OAR/ESRL PSD, Boulder, Colorado, USA from http://www.cdc.noaa.gov/ and also by IRI/LDEO Climate Data Library, http://iridl.ldeo.columbia.edu/.

The optimum interpolation SST analysis is produced weekly on a one-degree grid. This analysis uses in situ and satellite SSTs plus SSTs simulated by sea ice cover (Reynolds *et al.,* 2002). The dataset covers the period from December 1981 to June 2004 and is available from http://www.cdc.noaa.gov/

2.1.4 Wind

To analyse long term wind variability over the Indian Ocean we use data from the National Centers for Environmental Prediction - NCEP/DOE AMIP-II Reanalysis 2 monthly mean wind data. NCEP/DOE Reanalysis 2 provides an improved version of the original NCRP/NCAR Reanalysis 1 by fixing errors and by updating the parameterization of the physical processes (Kanamitsu *et al.,* 2002). The data have global coverage and are interpolated from model (sigma) surfaces to a Gaussian grid. It is available on 17 pressure levels from 1000 to 10 hPa. In our analysis, we use wind at 10 m above the ground/ocean surface for both u (zonal, west-east) and v (meridional, north-south) components. We use monthly mean data for the 29-year period from January 1979 to January 2008. NCEP Reanalysis 2 data are provided by the NOAA/OAR/ESRL PSD, Boulder, Colorado, USA from http://www.cdc.noaa.gov/ .

2.1.5 Coral proxy climate records

To understand the Indian Ocean multidecadal variability, and in particular its connection with the Indian Dipole Mode, we analyse long period time series from coral records extending back to ~1850 AD. Ocean corals can be used as proxy climate records along with others, such as ice cores, tree rings, and lake and ocean sediments for climate reconstruction. It was found that cooler temperatures and denser (salinity) water tend to cause coral to use heavier isotopes in its structure. Therefore, the measurements of oxygen isotope ratios (δ^{18} O) can be considered as a proxy for SST and changes

in rainfall/evaporation (Gagan *et al.,* 1998). The changes Sr/Ca in coral can be considered as a proxy for SST (Gagan *et al.,* 1998). In this study, we use Coral Oxygen Isotope monthly data from Bali (8.15°S, 115.30°E) from January 1782 to January 1989 (2497 months) and Mentawai Islands (2.5°S, 99 E) from April 1858 to December 1997 (1677 months). The detailed description of procedures of coral analysis to obtain these data sets can be found in (Charles *et al.,* 2003; Abram *et al.,* 2007). These data sets became available only recently and were kindly provided to us by Abram, N.J. (currently British Antarctic Survey, UK) and Gagan, M.K. (Research School of Earth Sciences, ANU, Australia). We have to note here, that we have got only one time series from each site, due to complication in obtaining corals and processing data. It is, possible, not enough to be convenient in results of spectral analysis, but coral data provided good and possible one kind of data of ocean variability in the past.

2.1.6 Dipole Mode Index

It is common to quantify the intensity of the IOD by anomalous SST gradients between the western Tropical Indian Ocean, averaged over the region 50° E-70°E and 10°S-10°N, and the south-eastern Tropical Indian Ocean, averaged over the region 90°E-110°E and 10°S-0°N. This gradient is referred to as the Dipole Mode Index. When the DMI is positive, then the phenomenon is characterized as positive IOD, when negative, as negative IOD.

There are a number of DMI products; they differ in the details of the calculation procedure and in datasets used. In this research we use several available indexes calculated on the basis of different data sources. We use DMIs calculated by JAMSTEC (Japan Agency for Marine-Earth Science and Technology) available from http://www.jamstec.go.jp/frcgc/research/d1/iod/. We used the following indexes:

- DMI as in Saji *et al.* (1999). The authors used GISST2.3b (Global Sea-Ice and SST Data Set) by British Atmospheric Data Centre, Meteorological Office. The data are selected for the time period from March 1958 to October 1999. At the preprocessing stage the authors high-pass filter the data with the cut-off period of 7 years and then smooth by applying a 5-month running mean;
- DMI derived from NOAA Optimum Interpolation SST Analysis or Reynolds data set (Reynolds *et al.,* 2002) (December 1981 - June 2004);
- DMI indexes derived from HadISST (Rayner *et. al.,* 2003) for DMI, and also calculated separately for the eastern (IODE) and western (IODW) poles of the dipole (see Fig. 1.3.1) (monthly average, 1870 - 2001).

Most of the above DMI time series can also be located at the UNESCO Observation Panel for Climate website http://ioc3.unesco.org/oopc/.

2.2 Data analysis methods and methodology

To analyse of the temporal dynamics of the oceanographic time series and data fields described above, this thesis makes extensive use of spectral analysis and wavelet analysis. It also uses EOF analysis, also known as principal component analysis. While wavelet analysis and EOF analysis became traditional methods of data analysis in contemporary physical oceanography, the use of spectral analysis is sometimes viewed by oceanographers as outdated and redundant when compared to the previous methods. We see all three methods as important tools in particular circumstances. "Fourier analysis is one of the most commonly used methods for identifying periodic components in near-stationary time series oceanographic data. If the time series are strongly nonstationary, more localized transforms such as the Hilbert and Wavelet transforms should be used" (Emery and Thomson, 2001).

In this chapter we give a brief description of each of these data analysis methods and discuss their relative advantages and disadvantages in the context of this work.

2.2.1 Application of spectral analysis

Spectral analysis is a traditional and widely used method of decomposition of temporal signals into orthogonal periodic components with different frequencies. For many oceanographic applications, the spectral representation of the signal (e.g. SSH, temperature, depth of thermocline, wind stress) makes it possible to identify and quantify the periodic or quasi-periodic components and separate them from random and aperiodic components. (A quasi-periodic component is represented by a superposition of a number of periodic components with close frequencies). Apart from providing the spectral composition of a signal, spectral analysis also makes it possible to filter the signal in a selected band (or bands) and analyse the filtered signal, as well as to estimate qualitatively the relative contribution of the variance of the signal in a particular band into the total variance of the signal. All these analysis possibilities are based on the specific properties of the spectral analysis, such as orthogonality of the basis functions and representation of the energy of the signal through the spectral components via the Parseval's theorem; they are not available, or not feasible with the other methods used in this thesis, namely wavelet analysis and EOF analysis.

Spectral analysis also has certain limitations. The magnitude of a given spectral component characterises the whole time period of the analysis. It does not contain information about the temporal variability of this component. Such information can be obtained by reconstruction of the signal in a frequency band of interest, which is by summing up the spectral components in this band. Alternatively, one can analyse a sequence of spectral decompositions of a signal in a moving time window. In this case, the calculated spectral components can be attributed with the middle time of

the corresponding time window, while the half width of the window can characterise the related uncertainty.

To illustrate the above, let us consider the spectral decomposition of the altimetry SSH anomaly in the Indian Ocean near Sumatra coast at (103°E, 5°8 S) shown in Figure 2.2.1(a). The time series has 798 weekly entries. Figure 2.2.1 (b) shows the power spectral density (PSD or psd) of the signal. The PSD is also often referred to as a periodogram (Emery and Thomson, 2001) of a signal and will be formally introduced later in this Chapter. The spectrum contains several maxima seen at 6, 12, 18, and 36 months. Let us consider the maximum with the period of about 18 months. The dashed line in Figure 2.2.1 (c) shows the temporal behaviour of one spectral harmonic, with the period of 18 months. As any single harmonic, it has constant amplitude throughout the whole time interval of the signal. The question "how did this harmonic change in time" is meaningless, and can only be applied to a signal in a band. Formally, this is related to the time-frequency uncertainty principle, which states that the product of characteristic widths of a signal in the frequency and time domains is greater than one: $\Delta f \Delta t \geq 1$ (e.g., Claerbout, 1976).

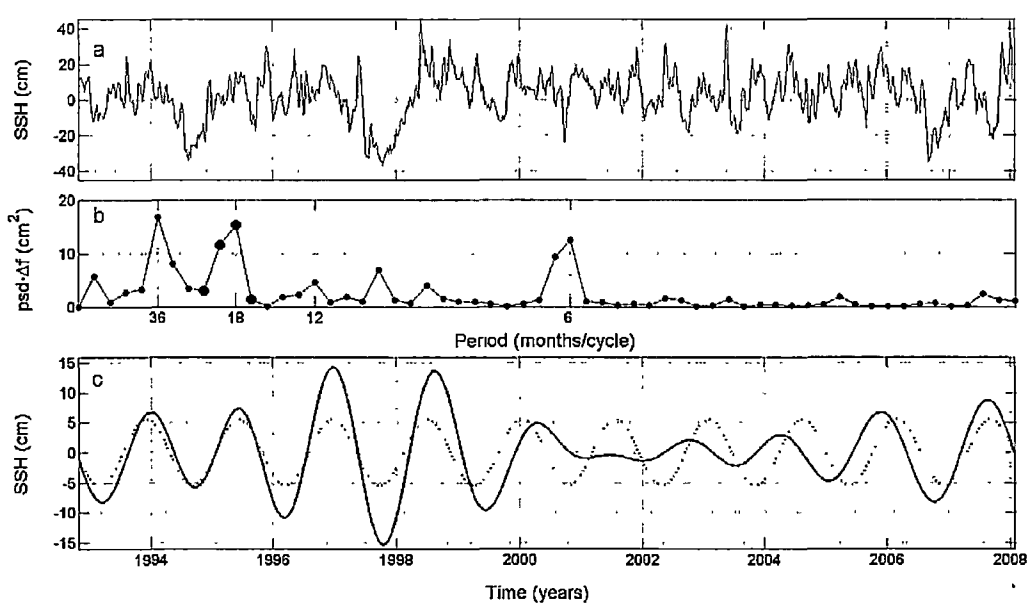

Figure 2.2.1 Example of spectral analysis of a SLA time series. (a) SLA variability in the Indian Ocean near Sumatra coast at (103 E, 5.8 S). (b) PSD of this signal. (c) Temporal behaviour of a single harmonic with the period of 18 month (dashed line) and of a sum of four harmonics with periods close to 18 months that are marked by diamond markers in panel (b) (solid line).

The solid line in Figure 2.2.1 (c) shows the band-passed filtered signal containing four components across the 18-month spectral maximum: 22.9, 20.4, 18.4, and 16.7 months that correspond to 9, 10, 11, and 12 points in the spectrum. Because of the interference of harmonics with different but close

frequencies, this filtered signal exhibits slow variations in time. These variations are related only to the process within the given spectral window, without interference of processes at other frequencies.

The filtering technique can be applied not only to a single time series, but also to the time series in every grid point of a series of two-dimensional fields, for example, SLA, SST, thermocline depth etc. After that, the succession of reconstructed fields makes it possible to analyse both the spatial and temporal variability of the field.

Applications of the spectral analysis methods in this thesis are mainly defined by the type of data involved. For a time series at a point, including historical tide gauge or coral record data, the one dimensional spectral decomposition and filtering are applied. For gridded two-dimensional oceanographic fields, these operations are applied at every node of the grid.

We use spectral analysis and band pass filtering to identify dominant low-frequency spectral modes of the Indian Ocean and analyse their spatio-temporal behaviour. Specially, we identify individual modes with well pronounced peaks in the frequency spectra, as well as differences in spatial distribution of spectral density of these modes and their temporal behaviour.

For example, the narrow maxima of the one-year and 6-month signals in the power spectrum of SLA over the Indian Ocean in Figure 3.3.3 (e) have an obvious temporal separation and a big gap between spectral peaks. This makes it possible to identify these signals as separate modes. A further investigation shows that the one-year signal has a strong presence in some locations of the Indian Ocean, while the strong 6-month signal can be found in other locations (see Fig. 3.3.8 a,b).

The decomposition of signals by frequency is different from the decomposition of a time series into orthogonal spatial modes as done by the EOF method. EOF considers the input as an unordered collection of states. An orthogonal mode calculated by the EOF method usually contains different spectral components and therefore signals from different processes. For example, a particular EOF mode can contain a leading one-year signal in one part of the ocean, a 6-month signal in another part, an ENSO signal or any combination of the above in a third region. In other words, such a mode may contain contributions of different, sometimes unrelated processes.

Applications of spectral analysis in practice are commonly done or based on the Fourier transform. The following is a brief description of the Fourier transform and some practical aspects of its application used in this thesis. The data analysis was conducted using Matlab ® based on the Fast Fourier transform (FFT) and the Inverse Fast Fourier transform (IFFT) functions.

Fourier Transform

Any finite length, infinitely repeated time series $y(t)$, defined over the principal interval $[0,T]$, can be represented by a linear combination of sines and cosines, or harmonics, of the form

$$y(t)=\sum_{k=0}^{\infty}[A_k \cos(\omega_k t)+B_k \sin(\omega_k t)], \quad (2.1)$$

where

$$A_k=\frac{2}{T}\int_0^T y(t)\cos(\omega_k t)\,dt, \qquad (2.2),$$

$$B_k=\frac{2}{T}\int_0^T y(t)\sin(\omega_k t)\,dt, \qquad (2.3)$$

$$\omega_k=\frac{2\pi k}{T}. \qquad (2.4)$$

Here A_k and B_k are referred to as Fourier coefficients, ω_k is the frequency of the k th harmonic, and T is the total length of the time series. The representation of the time series given in equation (2.1) can be rearranged to another form:

$$y(t)=\sum_{k=0}^{\infty}C_k \cos(\omega_k t-\varphi_k), \quad (2.5)$$

where

$$C_k=\sqrt{A_k^2+B_k^2} \qquad (2.6)$$

is referred to as the amplitude of the k th harmonic, while

$$\varphi_k=\tan^{-1}\frac{B_k}{A_k} \qquad (2.7)$$

is the phase of the k th harmonic. The amplitude of the zeroth harmonic (C_0) represents the time averaged value of the signal.

There are a number of important properties of the Fourier series. One of them is the Parseval Theorem, which states that the sum of squared Fourier amplitudes C_k^2 is equal to the sum of initial signal squared. This property can also be interpreted as the conservation of "energy" (or, more precisely, the variance of the signal) during Fourier transform. Because of this conservation of variance, the sum of squared Fourier amplitudes in a certain frequency interval ("band") can be interpreted as the variance (or "energy") of the signal in this band.

In equation (2.1), a continuous signal $y(t)$ is decomposed into an infinite series of Fourier harmonics. However, in practice one never deals with a continuous signal, but has a truncated digitized time series of $y(t)$. The initially continuous signal is represented by a series of N samples, usually sampled at equal time intervals dt one after another. In this case the Fourier transform can be modified to take advantage of the discrete form of the signal and is referred to as discrete Fourier transform.

Discrete Fourier Transform

Discrete Fourier transform (DFT) is a specific form of Fourier transform that takes advantage of the discrete signal to transform the signal from the discrete time domain to the discrete frequency domain. The basis of this transform is Parseval's theorem which states that the mean square (or average) energy of a time series *y(t)* can be separated into contributions from individual harmonic components to make up the time series. The resulting discrete decomposition takes the form (Emery and Thomson, 2001)

$$\begin{aligned} y_n &= \tfrac{1}{2}A_0 + \sum_{k=1}^{N/2}\left(A_k \cos\frac{2\pi kn}{N} + B_k \sin\frac{2\pi kn}{N}\right) \\ &= \tfrac{1}{2}C_0 + \sum_{k=1}^{N/2} C_k \cos(\frac{2\pi kn}{N} - \varphi_k), \end{aligned} \qquad (2.8)$$

where

$$A_k = \frac{2}{N}\sum_{n=1}^{N} y_n \cos\frac{2\pi kn}{N}, \qquad B_k = \frac{2}{N}\sum_{n=1}^{N} y_n \sin\frac{2\pi kn}{N}, \qquad (2.9)$$

$$C_k = \sqrt{A_k^2 + B_k^2}, \qquad \varphi_k = \tan^{-1}\frac{B_k}{A_k}. \qquad (2.10)$$

Here k is the harmonic index, while n is the time series index, so that, for example $k = 2$ corresponds to the second harmonic, and $n = 2$ corresponds to the second point in the time series. The arguments of sine and cosine in the k th term of the decompositions (2.8) can be represented as the product of the discrete time $t_n = nT / N = n\,\Delta t$ and circular frequency $\omega_k = 2\pi k / T$:

$$\frac{2\pi kn}{N} = \omega_k y_n.$$

Accordingly, the k th harmonic in the discrete Fourier series (2.8) is associated with the circular frequency

$$\omega_k = \frac{2\pi}{T}k. \qquad (2.11)$$

Equations (2.9) can be used to calculate Fourier coefficients A_k and B_k, or Fourier amplitudes C_k and phases φ_k, and are referred to as the DFT; while equation (2.8), reconstructs the initial signal, is referred to as the inverse DFT.

Some practical aspects of using DFT

A standard way of calculating the DFT involves use of an alternative representation to equation (2.8), with basis functions written in the exponential form:

$$y_n = \sum_{k=0}^{N-1} F_n e^{\frac{2\pi kn}{N}}, \qquad F_n = \frac{1}{N}\sum_{k=0}^{N-1} y_n e^{-\frac{2\pi kn}{N}}.$$

This, for example, applies to the Matlab function FFT, which will be used for conducting the DFT in this thesis. In this form, applying the DFT results in calculating N complex coefficients F_k, from which one can then calculate N real coefficients A_k, B_k, or C_k, φ_k used in equation (2.8). In particular, to calculate Fourier amplitudes C_k, one needs simply to use the absolute value of the complex Fourier coefficients F_k above:

$$C_k = |F_k|, \quad k = 0,\ldots,N-1.$$

It is easy to see that $C_k = C_{N-k}, \quad k = 1,\ldots,N-1$. In other words, the Fourier coefficients calculated by the above formula are symmetric about the index value $N/2-1$. This is closely related to the phenomenon of *aliasing*, which refers to the distortion that occurs when a continuous time signal has frequencies higher than half of the sampling rate. When this happens, the components of the signal at high frequencies calculated by DFT are mistaken for components at lower frequencies. This conclusion is known as the *Nyquist Sampling Theorem,* and the critical sampling rate equal to twice the highest frequency present in the signal is referred to as the *Nyquist sampling rate,* $f_N = 2f_{\max}$. To obtain meaningful results from a DFT, it is necessary to ensure that the sampling rate is greater than the Nyquist frequency, or, in other terms, that there are more than two data points in a period of the components with the highest frequency presented in the signal. "A sampling rate of 2.5 samples per cycle of the frequency of interest appears to be acceptable whereby $\Delta t = 1/(2.5f_N) = (2/5)(1/f_N)$" (Emery and Thomson, 2001, p.438).

In the context of this thesis, applying a DFT to a signal sampled at, for example, weekly (monthly) intervals assumes that the signal contains no substantial components with periods shorter than two weeks (months). Although the Indian Ocean has substantial oscillation at periods less than two months, such as MJOs (30-60 days) and biweekly variability, generally "it is well known that the oceanic frequency spectrum is "red" with the background spectral level ever increasing with decreasing frequency, except for peaks such as the annual cycle" (Fu, 2001).

Fast Fourier Transform

FFT (Danielson and Lanczos, 1942) refers to an algorithm of DFT that requires only $O(N \log N)$ operations versus $O(N^2)$ operations required to conduct DFT by direct use of equations (2.9). Most implementations of FFT require that the number of points in the time series is a power (p) of 2, that is $N = 2^p$; however, there also exist more general approaches. In practice, if the length of the time series is not a power of 2, it can be truncated or padded with zeros up to the nearest power of 2.

Energy spectral density

The Parseval's theorem for the DFT takes the following form (e.g., Emery and Thomson 2001, p. 414):

$$\Delta f \sum_{k=0}^{N-1} C_k^2 = \Delta t \sum_{k=1}^{N} y_k^2. \qquad (2.12)$$

One can interpret the right hand side of equation (2.12) as the energy of the signal (the second power of the signal integrated over time). Then C_k^2 can be interpreted as the energy spectral density of the signal in the frequency domain. Using the relation $\Delta f = 1/(N\Delta t)$, equation (2.12) can be rewritten as

$$\frac{1}{N}\sum_{k=1}^{N} y_k^2 = \langle y^2 \rangle = \frac{1}{N^2(\Delta t)^2}\sum_{k=0}^{N-1} C_k^2 = \frac{1}{T^2}\sum_{k=0}^{N-1} C_k^2 . \qquad (2.13)$$

Therefore, the right hand side in (2.13) gives the mean square value of the signal. In practice, once one has digitized a time series of the signal in certain units, e.g. cm, the interval of acquisition (Δt) does not affect the mean square of the signal. Consequently, one can calculate spectral amplitudes C_k from the signal time series assuming $\Delta t = 1$, then $\frac{1}{N^2}\sum_{k=0}^{N-1} C_k^2$ will be equal to the mean square of the signal:

$$\langle y^2 \rangle = \frac{1}{N^2}\sum_{k=0}^{N-1} C_k^2 . \qquad (2.14)$$

Therefore, equations (2.13-2.14) provide a useful way of normalizing the energy spectral density, because the amplitudes $C_k^{\,2}$ are then equal to the contribution of the *k*th harmonic to the total variability of the signal. Note that for a signal sampled at a constant rate, the right hand side in (2.13-2.14) remains equal to the mean square of the signal.

Because the left hand side in (2.12) represents the energy of the signal, divided by the duration of the time series T, it represents the power of the signal, so that the individual spectral amplitudes squared normalized by $\Delta f / T$ are commonly referred to as the PSD. The PSD is a commonly used variable

for characterizing the relative contribution of a given spectral component to the energy of the signal. However, in this thesis we will use the normalization (2.14), because it provides a more simple interpretation in the units of the signal, regardless of the sampling rate and length of the sampling interval. If, for example, the time series of sea surface elevation has units of cm, and the sum of squared Fourier amplitudes scaled by $1/N^2$ in some frequency band is equal to 4, then the mean squared signal in this band is equal to $4\,cm^2$, so that the RMS value of the signal in this band is $2\ cm$.

Two-dimensional fields of spectral density

For analysis of two-dimensional SLA fields in the ocean, we apply DFT to the time series of SLA at each grid point. The resulting gridded spectra are then either presented as PSD maps using normalization (2.14), or used to select a particular frequency band and conduct inverse DFT to investigate the temporal dynamics of the signal in the corresponding frequency band.

2.2.2 Application of wavelet analysis

Because Fourier amplitudes describe the signal as a whole (at all times), Fourier analysis is often considered as an appropriate method for the analysis of stationary data sets. To study the spatial-temporal behaviour of the spectral composition of the signal in time, one could apply DFT to the time limited subsets of the signal, for example, by computing running Fourier spectra of the signal for a smaller time window. An alternative technique for studying the temporal dynamics of a time series that has became very popular in the last few decades is *wavelet analysis* (e.g. Emery and Thomson, 2001, p. 500). This term refers to the application of the wavelet transform. In particular, the wavelet transform has advantages over the traditional Fourier transform for analysing signals that have discontinuities, sharp peaks, or exhibit non-stationary behaviour.

We note that while wavelet analysis is a useful tool for analysing temporal variability of the signal, it is not suitable for filtering the signal because the individual components of the decomposition of the signal are not, generally, orthogonal. For this purpose, spectral analysis is a natural instrument.

Wavelet analysis is conducted by applying a wavelet transform to the time series of the signal. We used software provided by *C. Torrence and G. Compo* (http://paos.colorado.edu/research/wavelets) and customized it for analysis of our data sets.

Wavelet transform

The wavelet transform is based on a particular family of wavelets, which is a class of orthogonal functions localized both in time and frequency domains. In contrast, the Fourier transform is based

on harmonic functions (sine, cosine or a complex exponent) that are localized only in the frequency domain but are infinite in time.

A family of wavelets can be constructed from a function $\psi(x)$, sometimes known as the "mother wavelet", which is confined in a finite interval. "Daughter wavelets" $\psi_{a,b}(x)$ are then formed by translation (described by index b) and contraction, or scale dilation (described by a) (e.g., Emery and Thomson, 2001, p. 501):

$$\psi_{a,b}(x) = \frac{1}{\sqrt{a}}\psi(\frac{x-b}{a}). \qquad (2.16)$$

The projection of the function $f(x)$ onto the subspace of the scale a then has the form

$$f_a(x) = \int_{-\infty}^{\infty} W_\psi\{f\}(a,b)\cdot\psi_{a,b}(x)dx, \quad (2.17)$$

with the *wavelet coefficients* $W_\psi\{f\}(a,b)$ given by

$$W_\psi\{f\}(a,b) = \frac{1}{\sqrt{a}}\int_{-\infty}^{\infty} f(x)\psi^*_{a,b}dx, \qquad (2.18)$$

where * denotes complex conjugation. The inverse transform is given by

$$f(x) = \int_{-\infty}^{\infty}\int_{-\infty}^{\infty} W_\psi\{f\}(a,b)\cdot\psi_{a,b}(x)\,da\,db\,. \qquad (2.19)$$

A common type of wavelet used for analysis is the Haar wavelet, which is simply composed of step functions (e.g., Jensen and Cour-Harbo, 2001):

$$f(x) = \begin{cases} 1, & 0 < x < 1/2, \\ -1, & 1/2 < x < /1, \\ 0 & otherwise. \end{cases}$$

Discrete wavelets

The discrete wavelet transform (DWT) was introduced by Daubechies (1992). It is based on the modified wavelet representation where equation (2.16) is replaced by

$$\psi_{j,k}(x) = \frac{1}{\sqrt{s_0^j}}\psi\left(\frac{x - k\tau_0 s_0^j}{s_0^j}\right). \qquad (2.20)$$

This function is called a discrete wavelet. j and k are integers and $s_0 > 1$ is a fixed dilation step. The translation factor τ_0 depends on the dilation step. The effect of discretizing the wavelet is that the time-space scale is now sampled at discrete intervals. It is usually chosen such that $s_0 = 2$ so that

the sampling of the frequency axis corresponds to *dyadic sampling*. For the translation factor, one usually uses $\tau_0 = 1$, which then results in dyadic sampling of the time axis.

Use of discrete values to transform a continuous signal results in a series of wavelet coefficients, and is referred to as the *wavelet series decomposition.* The discrete wavelets can be made orthonormal to their own dilations and translations by special choices of the mother wavelet. In this case

$$\int \psi_{j,k}(x)\, \psi^{*}_{m,n}(x)\, dx = \begin{cases} 1, & j = m, k = n \\ 0, & otherwise. \end{cases} \qquad (2.21)$$

An arbitrary signal can be reconstructed by summing the orthogonal wavelet basis functions, weighted by the wavelet transform coefficients (Sheng, 1996)

$$f(x) = \sum_{j,k} W\{f\}(j,k)\, \psi_{j,k}(x). \qquad (2.22)$$

There is an extensive literature on effective numerical implementation of the DWT, most commonly by using so-called filter banks (Mallat, 1989). What is most important from the practical point of view is that the coefficients of the DWT allow one to simultaneously characterize the signal at different spatial and temporal scales; and therefore make it possible to analyse the time dynamics of components of a certain frequency, including identifying the time intervals when these components are strongest or weakest.

2.2.3 Application of EOF analysis

EOF analysis, or principal component analysis, are the common terms in earth and other applied sciences for use of the singular vector decomposition (SVD) for transforming a number of possibly correlated states into a smaller number of uncorrelated states. Any (*n x m*) matrix A formed by *m* column vectors A_i, $i = 1,...,m$ of *n* elements each can be factorized as follows:

$$A = ULV^T, \qquad (2.23)$$

Where U is a (*n x n*) orthonormal matrix, *L* is a (*m x m*) diagonal matrix, and *V* is a (*m x m*) orthonormal matrix, and superscript "T" denotes a transposed matrix. The columns of *U* are the singular vectors and, also referred to as EOF modes; the diagonal entries of *L* are the singular values, equal to standard deviations, or square root of variances of these modes; and rows of V contain coefficients of expansion of the input vectors A_i in the basis of *U*. If the column vectors of the input matrix A represent time series of states, then columns of V contain weights of each singular vector, or EOF mode, in the corresponding states. In this context they are sometimes called the temporal function of EOF, while the singular vectors are called the spatial function of EOF. The factorization (2.23) can be also written as

$$A = \sum_{i=1}^{m} \sigma_i U_i (V_i)^T, \qquad (2.24)$$

Where U_i and V_i are the *i*-th columns of U and V, and σ_i is the *i*-th singular value.

The properties of the EOF analysis follow from the properties of SVD; some of them are listed hereafter:

1. The expansion (2.23) is unique in the sense that each unique singular value has unique vectors U_i and V_i in (2.24).
2. The sum of the entries squared is equal to the total variance of the signal.
3. If the singular values are ordered from larger to smaller values, then any truncated sum in (2.24) represents best possible approximation of A in the least squares sense.

Because of the third property, the EOFs are the most effective data representation method in the least squares sense. They are particularly useful if the field's variability can be described by a small number of EOFs, that is, if a small number of singular values carry most of the variance of the signal. In this case one can describe the variability of a field by describing a small number of EOFs (see for example Church *et al.*, 2004).

Another useful application of EOFs used in this thesis is the analysis of the temporal function. In particular, spectral analysis of the temporal function makes it possible to investigate the temporal variability of a given EOF mode, that is, to identify the frequencies of the processes contributing to this mode.

2.3 Software overview

The data analysis and visualization in this thesis has been done by using Matlab scripts written by the author. The only exception are the scripts used for wavelet analysis, which are based on the Matlab code provided by C. Torrence and G. Compo (1998), and is publicly available at http://paos.colorado.edu/research/wavelets. The code was adapted for the current thesis needs.

The code for FFT analysis is written based on the Matlab library functions FFT and IFFT. It includes preprocessing, Fourier transforms, calculation of PSD or filtering and inverse transform, and visualization. Similarly, the code for EOF analysis is based on the Matlab library function SVD.

Chapter 3
Low frequency variability of the Indian Ocean

3.1 Introduction

3.1.1 Motivation and goals

This chapter investigates the low-frequency variability of the Indian Ocean, by which we understand processes with characteristic time scales from 6 months to several years. As we mentioned in Chapter 1, it is commonly accepted today that the variability of the Indian Ocean in the low-frequency part of the spectrum can be divided into several bands corresponding to periodic or quasi-periodic signals that contain most of the total variance: semi-annual (with a period of 6-months), annual (one-year), quasi-biennial (~ 2-3-years), ENSO (~ 3-7 years), decadal, and bi-decadal. Although this classification has been the subject of previous studies or has been referred to in a lot of literature (e.g Allan, 2000; Li *et al.*, 2001; Meehl and Arblaster, 2002; Loschnigg *et al.*, 2003; Tourre and White, 2003), we argue below in favour of a different division of the part of the spectrum corresponding to signals with 1-3 year period. This will be done based on frequency spectra of various time series observed in different locations over the Indian Ocean and representing different properties of the ocean-atmosphere system.

The study of the temporal variability of the Indian Ocean was initially motivated by the discovery of a strong quasi-periodic signal with period of ~18-20 months during routine analysis of XBT data in the Java upwelling region. We demonstrate that this signal, overlooked or misunderstood in previous studies, plays a major role in the variability of the tropical Indian Ocean in general, and specifically in the life cycle of the IOD.

After identifying the main frequency bands that carry most of the variance, we study the spatial distribution of variance in each band over the Indian Ocean. This is done for the altimetry SLA data because, firstly, it is an integral signal depending on a number of factors, and secondly, because of the good coverage and availability of the corresponding data (see Chapter 2.1). Using the spatial distribution of altimetry, we also investigate the spatial/temporal propagation of the signals in each frequency band. Maps and movies showing the temporal behaviour of the signals complement the maps of the first two EOFs of SLA (e.g. Feng and Meyers, 2003) and help to identify the sources and processes behind the corresponding physical modes of the ocean.

In this Introduction an overview of existing concepts of the low-frequency variability of the Indian Ocean is given. Particular attention is paid to the signals with periods of 1-3 years and to possible reasons why the 18-20-month signal has been previously overlooked.

3.1.2 Classification of the Indian Ocean variability

As was noted in the overview of the low-frequency variability of the Indian Ocean in Chapter 1.2, the Indian Ocean exhibits variability at a wide range of frequencies at interannual times scales, as well as have very strong annual and semi-annual signals.

The annual and semi-annual processes in the Indian Ocean are generally well studied today, and continue to be subjects of scientific interest. In particular, understanding of propagation of annual and semi-annual waves in the Indian Ocean has been substantially improved after inventory of altimetry measurements. For example, propagation of semi-annual Rossby and Kelvin waves and their constructive/destructive interaction was recently studied by Fu (2007), propagation of local and remotely forced annual waves along the Indian coast by Brandt *et al.* (2002) and Shankar *et al.* (2004), and description of the break-up of annual waves in the middle of the Indian Ocean by Wang *et al.* (2001).

Along with the continuing interest in the annual and semi-annual processes, in the last decade there has been a growing interest to the interannual variability of the tropical Indian Ocean. (Perigaud and Delecluse, 1993; Masumoto and Meyers, 1998). Tourre and White (2003) argued that the interannual variability of SST (with periods from 2 to 20 years) over the Indian Ocean represents the global climate signal that includes the quasi-biennial oscillation (2.1-2.8-year period); the ENSO oscillation (3-7-year period); and the quasi-decadal oscillation.

Analyses of SST were followed by studies of the subsurface temperature interannual variability in the Indian Ocean (Rao *et al.*, 2002; Vinayachandran *et al.*, 2002; Feng and Meyers, 2003; Loschnigg *et al.*, 2003). Rao *et al.* (2002) found that subsurface temperature consistently has a dipole structure that does not always appear in SST. The authors suggested that the observed quasi-biennial signals (with periodicity of 2-3 years) in the southern tropical Indian Ocean are associated with Rossby wave propagation.

Feng and Meyers (2003) found a two-year time-scale of the upper-ocean evolution in the tropical Indian Ocean near the Java coast that is unique to the IOD (that is, not directly forced by an atmospheric teleconnection from the Pacific). Their conclusion was based on the timing of the temperature anomalies associated with the strength of upwelling offshore of Java, when "cold anomalies during 1994 and 1997 [was] followed by warm anomalies during 1995/96 and 1998 (see Feng and Meyers, 2003, p.2268)" which "may be related to biennial oscillation described by Meehl

and Arblaster (2002)". In another study Loschnigg *et al.* (2003) found that the ocean dynamics in the tropical Indian Ocean contributes to the SST anomalies and constitutes an integral part of the TBO and the monsoon system.

The above studies of interannual variability of the Indian Ocean identified signals with time scales of two years and longer. Below, we identify possible reasons why existence of a shorter, repetitive signal with periods of 18-20 months was overlooked.

3.1.3 Why was the 18-month signal overlooked?

The existing classification of the time scales of the low-frequency variability of the Indian Ocean distinguishes the following main time scales (periods): semi-annual, annual, biennial, decadal and bi-decadal. Below, we identify the possible reasons why the strong signal in the Indian Ocean with period around 18-20 months has not been noticed until recently (Sakova *et al.,* 2006a,b; Keenlyside *et al.,* 2007). Analysis of the literature makes it possible to identify the following four main reasons, discussed in details below.

1. **Analysis excluded signals with periods of less than two years**
   In the majority of studies of the interannual variability of the Indian Ocean only the signals with period of two years and longer were analysed. Usually, signals with shorter periods were filtered out or the data used for analysis had a sampling frequency of one year.

2. **The common classification was used**
   Many studies on interannual variability just referred to previously published papers and did not conduct their own analysis to identify the main spectral bands. These studies applied band-pass filtering according to the existing understanding. For example, to analyse the ENSO signal, a band-pass filter corresponding to periods of 3-7 years is typically used, while to analyse the quasi-biennial signal, a band-pass or a low-pass filter with a cut-off at 2-3 years was used.

3. **A qualitative estimation for the period of the signal was used**
   In some cases, the signal was not filtered out, but conclusions about its period were based on a qualitative estimation rather than quantitative methods like spectral analysis, and signals with periods shorter or longer than two years were considered to be quasi-biennial.

4. **The signal has appeared in the spectra, but did not attract attention**

Below we review the issues related to each of the case studies in more detail.

1. **Analysis excluded signals with periods of less than two years**

The most used method for the analysis of the interannual variability of the Indian Ocean is spectral analysis (e.g. Allan, 2000; Tourre *et al.,* 2001; Li *et al.,* 2001; Li and Zhang, 2002; Tourre and White, 2003). White and Cayan (2000) considered the interannual variability of SST and sea level

pressure in different frequency bands in the Indo-Pacific region. The analysis was conducted for SST from 1900 to 1997, and for sea level pressure anomalies from 1950 to 1997. They found that the frequency spectra contain the following signals: 3-7 years signal "that can be attributed to the global ENSO waves", "propagating signals at decadal and interdecadal periods near 10 and 24 years", and "at the quasi-biennial period of 2.3 years"; however, their analysis did not take into consideration variability with period shorter than two years.

Allan (2000) calculated the spectrum for joint SST and sea level pressure data (Fig. 3.1.1). Tourre *et al.* (2001) calculated the joint fraction variance spectrum for the Pacific Ocean (30°S-60°N) and White and Tourre (2003) did the same analysis for the global data (not shown), and Tourre and White (2003) - for the Indian Ocean at 30°S-20°N (Fig. 3.1.2). All spectra in the above studies are very similar. The variability is divided in several bands: "quasi-biennial (~2.2-year period), interannual (3- to 7-year period band), quasi-decadal (~11-year period), and interdecadal (~17-year period)". The abbreviations QB or QBO and BDO are commonly used for the quasi-biennial and bi-decadal signals. In all these analyses, signals with periods shorter than two years were excluded from consideration.

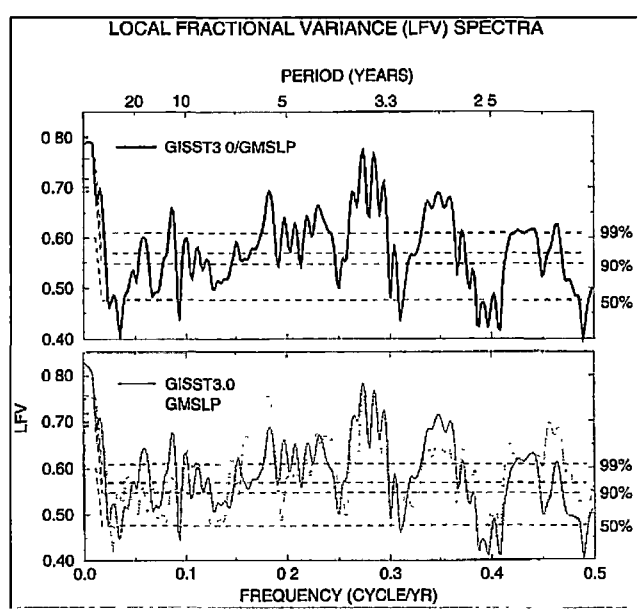

Figure 3.1.1. Multi-taper frequency-domain singular value decomposition (MTM-SVD) localized variance spectrum of (a) joint analysis of historical GISST, and (b) separate analysis of historical GISST and GMSLP (after Allan, 2000).

White and Allan (2001) studied quasi-biennial anomalies using "SST and sea level pressure anomalies along 10°N around the globe for 48 years from 1950 to 1997" and its decadal modulation. They found "significant peak spectral energy density for eastward propagating waves of 2.0 and 2.4

year periods ... associated with TBO (quasi-biennial oscillation in troposphere)". They found that these signals were "separated from the ENSO of 3 to 7 year periodicity by a spectral gap that indicated the relative independence of these two climate variability phenomena". To prepare data for analysis the authors used band pass filtering of data with the high-pass frequency set at (a period of) 18 months. This allowed them to retain the two-year signal, but cut off signals with shorter periods.

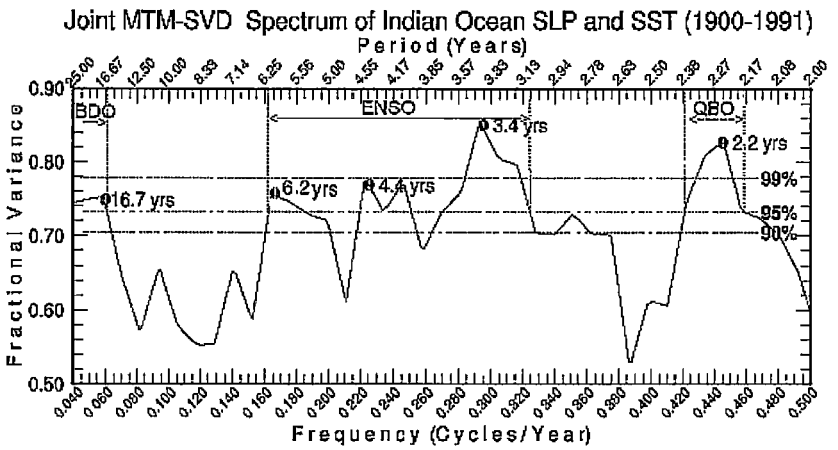

Figure 3.1.2. Local fraction variance spectrum (represents a fraction of variance in a particular frequency band) as a function of frequency (cycles per year) for SST and sea level pressure anomaly. Vertical dashed lines represent bi-decadal (BDO), ENSO and quasi-biennial (QBO) signals (after Tourre and White, 2003).

Li *et al.* (2001) and Li and Zhang (2002) studied the quasi-biennial and low-frequency variability of the South Asian Monsoon using SST and rain data. They found that the power spectrum of the time series of Indian rainfall (Fig. 3.1.3) reveals two distinctive peaks: quasi-biennial (period of 2-3 years) and low-frequency (3-7 years). The spectrum of the rainfall has a maximum at 4.5-8 years and two more maxima at 2.2 and 2.7 years. For the analysis, the authors use an All-India monsoon rainfall index with sampling frequency of one year. To obtain a meaningful result from a spectral analysis, however, it is necessary to have the sampling rate greater than the Nyquist frequency or "a sampling rate of 2.5 samples per cycle of the frequency of interest appears to be acceptable' (Emery and Thomson, 2001, p. 438). It is means that with a sampling rate of one year, then, no definitive conclusions can be made about signals shorter than 2.5 years, so any signals between 1 and ~2.5 years were missed from this analysis.

The paper that is most referred to in regard to biennial oscillation in the Asian-Australian Monsoon rainfall is Meehl and Arblaster (2002). It presents spectra of seasonal and area-averaged monthly anomaly in the Australian and Indian monsoon (Fig. 3.1.4). Once again, while the spectra have clear maxima for periods between 2 and 3 years, signals with periods shorter than two years were not presented in these plots and not discussed in the paper.

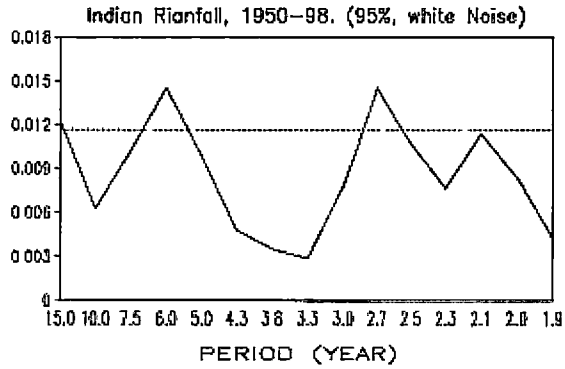

Figure 3.1.3. Power spectrum of the domain-averaged Indian rainfall time series for a period of 1949-1998. The dashed line shows the 95% significance level (after Li and Zhang, 2002).

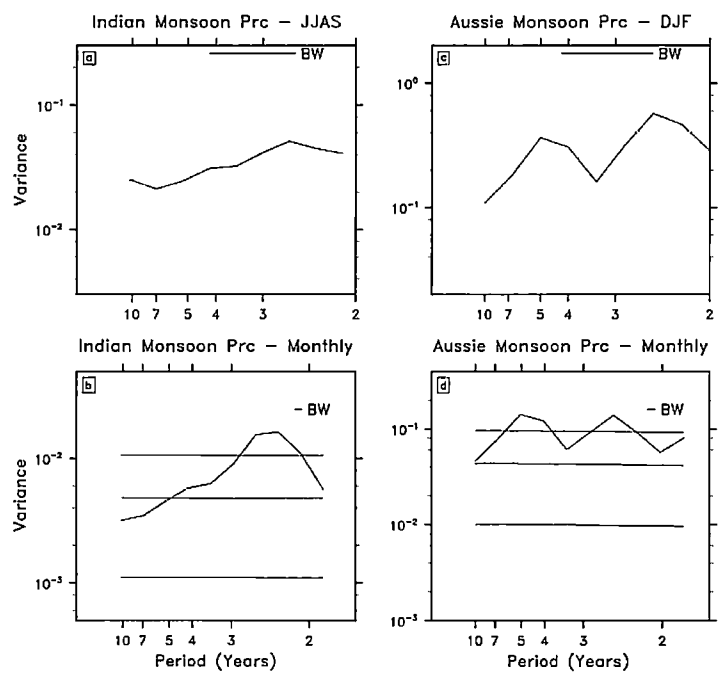

Figure 3.1.4. (a) Spectra of seasonal Indian monsoon rainfall; (b) spectra of area-averaged monthly anomaly Indian monsoon region rainfall (all months); (c) spectra of seasonal Australian monsoon rainfall; (d) spectra of area-averaged monthly anomaly Australian monsoon region rainfall (all months) (after Meehl and Arblaster, 2002).

In another study, Loschnigg *et al.* (2003) discussed the biennial nature of climate in the Indo-Pacific region using a 100 years long model run. The authors found that the IOD is "an inherent feature of the Asian summer monsoon and TBO" and made a claim that "IOZM is a part of the biennial nature of the Indian-Pacific region" and that this explains "the Indian Ocean biennial cycle". They

calculated spectra for Monsoon Rainfall and Westerly Shear index (Fig. 3.1.5 b, c), but both of them do not present signals shorter than two years.

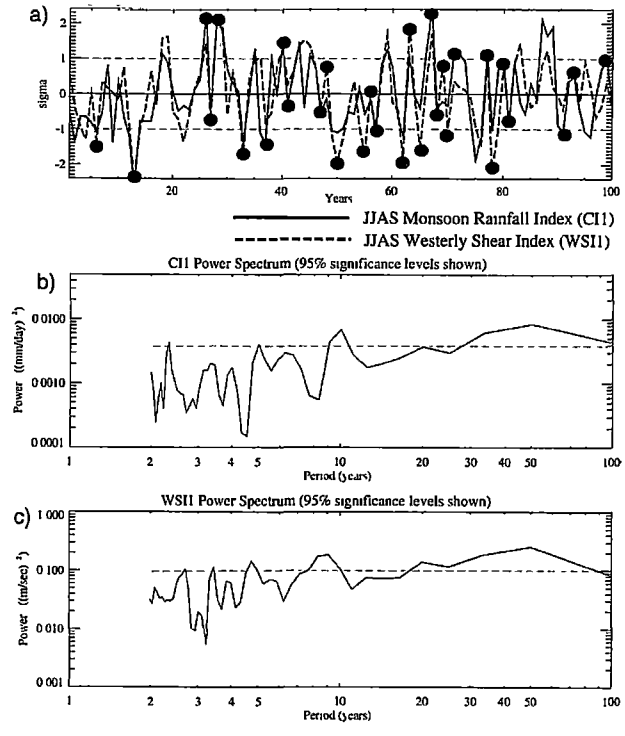

Figure 3.1.5. (a) Time series of normalized Monsoon rainfall index (CI1) and westerly shear index anomalies (WSI1). Black dots signify strong and weak TBO years, where both the CI1 and WSI1 are relatively greater or less than in preceding and following years. (b) Power spectrum of the monthly values of CI1, with the 95% significance level shown as the dotted line. (c) Power spectrum of the monthly values of WSI1 (after Loschnigg, 2003).

2. The common classification was used

It is common before analysing variability to prepare the data by band pass filtering in a particular frequency band. The majority of studies used a band pass filter to isolate the "known" variability mode.

To analyse propagation of biennial, interannual and decadal signal in Pacific, White *et al.* (2003) used band-pass filtering of SST, wind and isotherm depth data based on previously determined peaks: 2.2 years and 2.8 years for biennial signals, 3.5-7 years and 11 years for interannual and decadal signal. To isolate the biennial peak, the band from 1.5 to 3 years was used, which removed the 18-month signal from the analysis.

Reason *et al.* (2000) analysed the quasi-biennial signal across the Indian Ocean. Based on the spectral analysis conducted by Allan (2000) (Fig. 3.1.1), the authors set the cut-off in the band-pass

filter at 2-2.5 years. In a later paper, Allan *et al.* (2003) also used a filter set at 2-2.5 years to analyse quasi-biennial variability to study the impact of ENSO on the Indian Ocean.

3. A qualitative estimation for the period of the signal was used

Some authors qualitatively estimated the period of a signal. Feng and Meyers (2003) analysed the subsurface ocean dynamics of IOD using altimeter SLA and XBT temperature data and found a two-year time-scale of IOD. Their conclusion was based on the timing of the temperature anomalies associated with the strength of upwelling offshore of Java, when "cold anomaly during 1994 and 1997 [was] followed by warm anomaly during 1995/96 and 1998" and "may be related to biennial oscillation described by Meehl and Arblaster (2002)".

4. The signal has appeared in the spectra, but did not attract attention

There are only a few studies that contain indications of the existence of signals with periods between 1 and 2 years. McClean *et al.* (2005) analysed the repeat IX-1 XBT data and Parallel Ocean Program model output and calculated spectra of time series of dynamic height anomaly at the northern and southern ends of the XBT line, for both XBT data and model output. Although these spectra clearly show large peaks at 18-20 months for the northern end of the XBT line (Fig. 3.1.6) (McClean *et al.*, 2005, Fig. 5), the authors did not pay attention to this signal because their "focus was on long-period signals". They conclude that the long-period signal contains two distinct components and "refer to the 2.7 year signal as quasi-biennial and 5.5 year as quasi-pentadal".

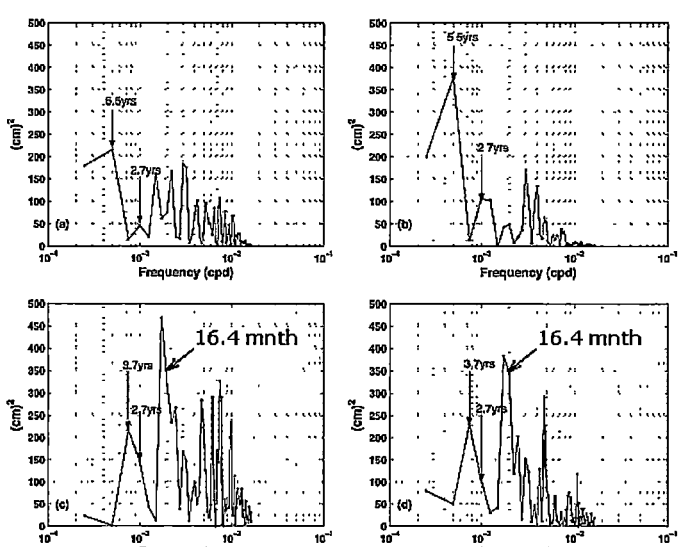

Figure 3.1.6. Variance preserving spectra (cm²) of dynamic height anomaly from (a,c) XBT data and (b,d) the POP model at the southern (a, b) and northern (c, d) ends of the IX 1 line (after McClean *et al.*, 2005; the mark at 16.4 months estimated and added by Sakova).

Three-year and 18-month peaks in the spectra were identified, but not discussed, in a study of intraseasonal variability of SSH of the equatorial Indian Ocean by Fu (2007). Figure 3.1.7 illustrates the dominant time scales of SSH and zonal wind stress averaged over 10°S–10°N, 40°E–100°E. Because the author was interested in signals with periods of six months and shorter, the picture labels only contain maxima corresponding to these time scales. However, the figure contains two more peaks in the low-frequency part of the spectra. Their frequencies can be estimated from the figure as 0.00092 cycles/day and 0.0019 cycles/day, which corresponds to periods of about 35.7 and 17.3 months. These values agree with the results obtained by Sakova *et al.* (2006a,b) for the low-frequency variability of the Indian Ocean (Chapter 3.3 in thesis), namely, the existence of two major components of the interannual variability in the Indian Ocean with periods of about 3 years and 18 months (Sakova *et al.*, 2006a,b).

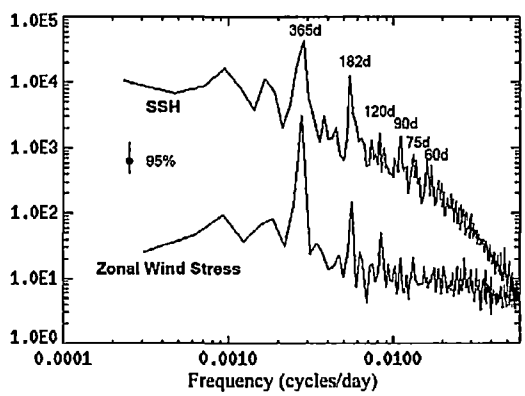

Figure 3.1.7. Spectra of SSH (upper curve; cm^2 $cycles^{-1}$ day^{-1}) and zonal wind stress [lower curve; 0.1 × (dyne cm^{-2})^2 $cycles^{-1}$ day^{-1}]. The spectra are averaged over 10°S–10°N, 40°–100°E. The periods for the major spectral peaks are indicated. The 95% error bar for the spectra is shown (after Fu, 2007).

Wijffels and Meyers (2004) analysed variability in the Indonesian Throughflow region. They write: "To reveal the spatial characteristics of temperature variability, total variance was binned into four broad spectral bands: for periods less than 0.4 yr (intraseasonal/mesoscale), periods between 0.4 and 1.1 yr (seasonal), periods between 1.1 and 3.2 yr [quasi-biennial (QB) band], and for periods greater than 3.2 yr (ENSO band)". Their spectrum of the anomaly from the mean seasonal cycle of equatorial wind stress in the Pacific and Indian Oceans is shown in Figure 3.1.8 b. Although the authors noted the existence of two "spectral peaks near periods of 3 yr and between 1 and 2 yr", they considered these two peaks as one signal with periods of from 1.1 to 3.2 years (quasi-biennial or QB).

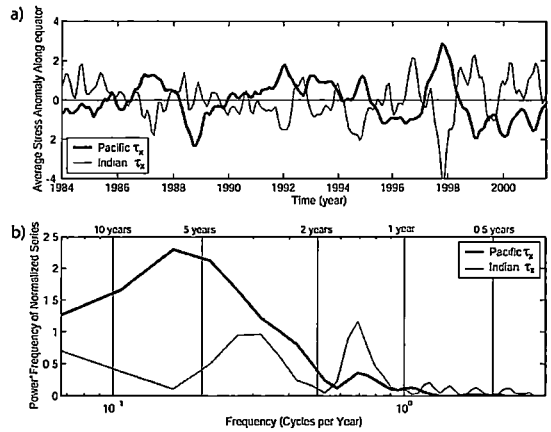

Figure 3.1.8. (a) Time series of interannual anomalies of along path wind averaged along the equatorial and coastal waveguides in the Indian and Pacific Oceans (see text). (b) Variance-preserving spectra of the wind series in (a). The line frequencies plotted are, from left to right, for 10, 5, 2, 1, and 0.5 yr (after Wijffels and Meyers, 2004)

3.2 Spectral analysis of XBT subsurface temperature data

3.2.1 Introduction

The interannual variability of subsurface temperature in the Indian Ocean is much less studied than that of the SST or atmospheric characteristics because these data are less available. Subsurface temperature variability of the Indian Ocean was described by Rao *et al.* (2002), Feng and Meyers (2003), and Wijffels and Meyers (2003) using XBT data. Their results are reviewed below to provide a geographic setting to our spectral analyses.

Using XBT subsurface temperature along with anomalies of altimetry SSH, Feng and Meyers (2003) identified two regions with high levels of variability of SLA in the Indian Ocean: near the coast of Sumatra-Java in the east and within the Seychelles-Chagos Thermocline Ridge (SCTR) in the west, with the peak standard deviations of 8-9cm (Fig. 3.2.1). These two areas almost coincide with the poles of the IOD, and therefore are of particular importance for understanding of the interannual variability of the entire Indian Ocean. Figure 3.2.1 shows two XBT lines that cross these high variability areas: section IX-1 from Fremantle, Australia, to Sunda Strait (between Sumatra and Java), Indonesia; and section IX-12 from Fremantle to the Red Sea. Because the SLA represents cumulative properties of the water column, including the thermocline depth, one can expect to find similarities in the spatial and temporal characteristics of the subsurface temperature and SLA.

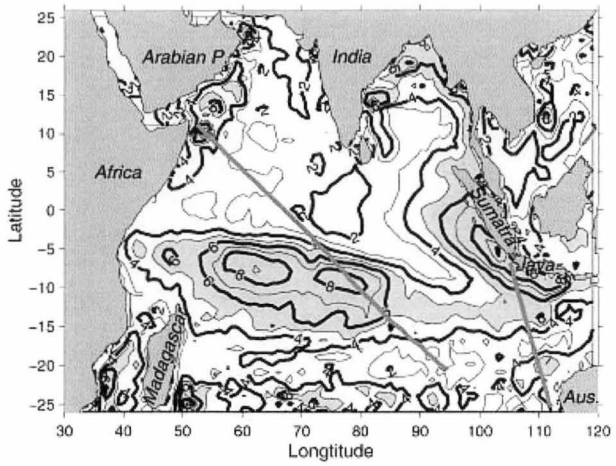

Figure 3.2.1. Standard deviation of the sea surface height anomaly in the tropical Indian Ocean (in cm). The shaded areas correspond to standard deviation larger than 5 cm. The straight lines show XBT sections IX-1 and IX-12 (after Feng and Meyers, 2003).

Feng and Meyers (2003) conducted a detailed study of the subsurface temperature along these two lines that are particularly close to the poles of the Indian Ocean Dipole. The upper panel of Figure 3.2.2 shows the time series of temperature near Sumatra-Java coast from IX-1 line at 6.78°S, 105.17°E. "The surface isothermal layer depth is about 50 m and the surface-layer temperature exhibits a regular annual cycle during most years... In the thermocline, there exists intensive semi-annual variability, which is remotely driven by the equatorial Indian Ocean semi-annual Wyrtki jet. Superimposed on the semi-annual cycle, there is an annual component driven by local monsoon wind, with upwelling favourable south-easterly wind for 6 months from April to September, and downwelling favourable wind during the other 6 months" (Feng and Meyers, 2003). The lower panel of Figure 3.2.2 shows the time series of temperature anomaly. The authors found that due to the strong upwelling during the 1994 and 1997 IOD events, the thermocline has lifted to a very shallow depth, so that a strong cold temperature anomaly appeared at the sea surface.

Figure 3.2.3 depicts the subsurface temperature structure and its standard deviation. Analysis of the standard deviation reveals that the high variability region seen along the IX-1 line is consistent with the region of high variability of SLA and that the strongest variability is near the Sumatra-Java coast (with the maximum of above 2°C). "The highest variability is close to the depth of 20°C isotherm where the vertical temperature gradient is larger" (Feng and Meyers, 2003).

Along with the semi-annual and annual signals, Feng and Meyers (2003) also studied the interannual variability of the Indian Ocean. Although the time series of XBT data used is quite short from a historical point of view (1986 – 1999), it covers two very strong IOD events. Based on an analysis of the behaviour of the IOD and subsurface ocean dynamics, the authors concluded that the IOD, and

thus the variability of the Indian Ocean itself, has a two-year time scale that may be related to the biennial oscillation described by Meehl (1993).

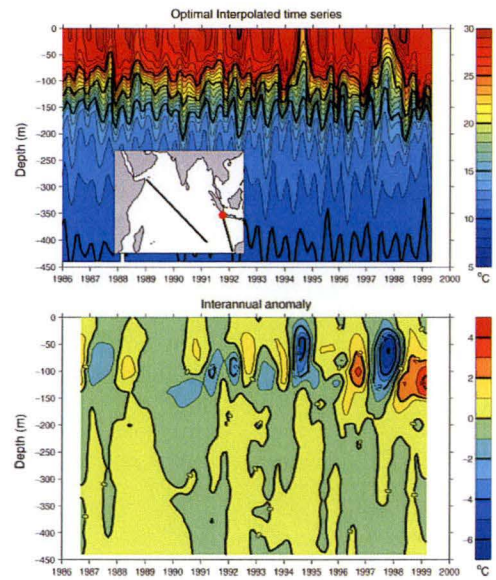

Figure 3.2.2. Time series of temperature profile (upper panel) and interannual temperature anomaly profile (lower panel) at the northern end of IX-1 section of XBT line, 6.78°S, 105.17°E. The station position is marked as a red dot in the inset of the upper panel (after Feng and Meyers, 2003).

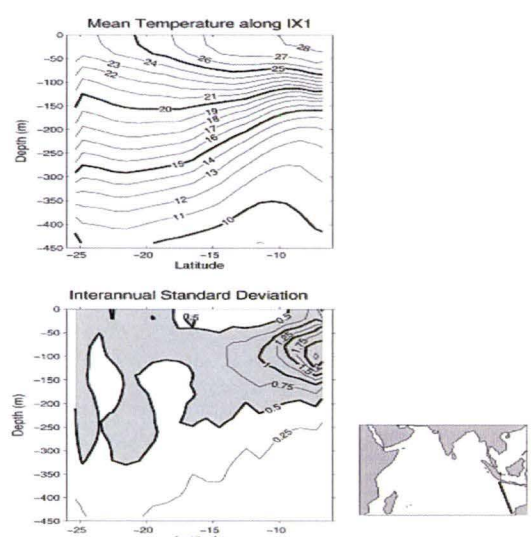

Figure 3.2.3. Annual mean temperature structure (upper panel) and interannual temperature standard deviation (lower panel) in the upper 440m along the XBT IX-1 section. The shaded areas in the lower panel denote standard deviation larger than 0.5°C. The inset shows the location of the XBT IX-1 section (after Feng and Meyers, 2003).

The temporal and spatial time scales of subsurface temperature fields are analysed below in greater details with spectral analysis methods, with an emphasis on the interannual variability signal using data from the IOTA (see Chapter 2 for a description of the data and data processing).

3.2.2 Spectral analysis of subsurface temperature near the Indonesian coast

We start with the analysis of temperature profiles close the Sumatra-Java coast in Box 2 (see Fig. 2.1.4), with the opposite corners at 7.0°S, 104.0°E and 8.0°S, 106.0°E. Figure 3.2.4(a) shows the time series of IOTA temperature data, where the yellow line represents the depth of the 20°C isothermal surface (D20). Both Figure 3.2.2 (Feng and Meyers, 2003) and Figure 3.2.4(a) show a number of strong upward displacements of the thermocline associated with upwelling. They result in appearance of the cold water at the sea surface, most noticeable during the 1994 and 1997 IOD events and, possibly, in 1991. There are also a number of more frequent minor displacements that can be seen from the shape of the D20. These observations can be further quantified by applying frequency analysis methods.

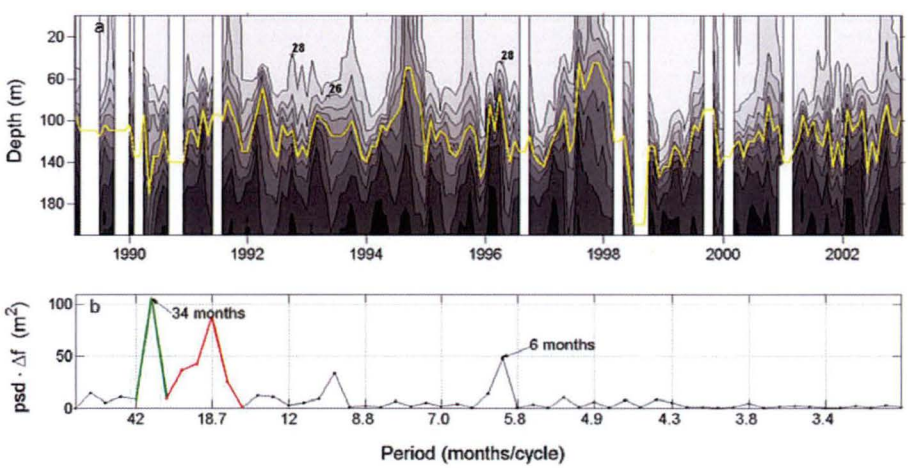

Figure 3.2.4. (a) IOTA temperature data in Box 2 (Fig. 2.1.4) with corners at 7.0°S, 104.0°E and 8.0°S, 106.0°E. The yellow line represents the depth of the 20°C isotherm. (b) PSD of the depth of the 20°C isotherm. Here psd is power spectral density, and Δf is frequency resolution in cycles per month; psd·Δf is equal to the time averaged variance, with units of m^2.

Figure 3.2.4(b) shows the PSD of the depth of the D20 surface. Interestingly, the spectrum clearly contains a number of well-separated maxima. Along with the expected semi-annual component there are also two surprisingly clear and strong low-frequency maxima corresponding to periods of approximately 18.7 months (red line) and 34 months (green line). These low-frequency maxima rise far above the "noise" level in the spectrum and carry more energy than the 6-month component. On average these signals are responsible for the upward/downward movement of the D20 surface by almost 10 meters each, while the 6-month signal is responsible for a displacement with an amplitude

of only about 7 meters. There is also some evidence of a signal with a period of about 10 months. Interestingly, there is no signal with a period of one year. Existence of two standalone low-frequency periodic signals of about 3 years and 19 months has not been described in the literature before 2006 (Sakova *et al.,* 2006a,b). Below we will present analysis of the temperature variation at different depths. The reason for analysing the subsurface temperature rather than the movement of isothermal surfaces is that the quality of frequency analysis of isothermal surfaces at temperatures of 23°C or higher suffers from the discontinuity at times when they reach the sea surface during strong upwelling events.

Figure 3.2.5 shows the temperature at the same location as Figure 3.2.4 at different depths (5m, 30m, 70m, 100m, 120m, and 140m), while Figure 3.2.6 shows the corresponding PSD. We see that the variability at depths of 5 and 30m is not significant due to the existence of the mixed layer. The dominant frequency in the mixed layer is 1 year (Fig. 3.2.6 a,b); this also can be seen from the time series by Feng and Meyers (2003) (Fig. 3.2.2, upper panel). This signal is largely due to variation of heat fluxes at the sea surface over the year. The three-year temperature signal is clearly visible in Figure 3.2.5. At depths of 70-120m, the dominant frequencies correspond to periods of approximately 3 years and 18-19 months (Fig. 3.2.6 c,d,e). These two frequencies are represented by standalone maxima in the spectra separated by significant gaps at all depth levels. In Figure 3.2.6 the amplitudes of spectral components at these frequencies rise significantly above those at other frequencies. The 18-month signal reaches maximum amplitudes on the depth of about 100 m, while the 3-year signal reaches maximum amplitude at depth of about 70m. These signals are superimposed on the higher frequency signals, and while there seemingly are some clear peaks in the time series of temperature in the mixed layer (Fig. 3.2.5 a,b), they are difficult to separate at the 100m depth (Fig. 3.2.5 d) without using spectral analysis. Therefore, at 100m and below there is a very strong high frequency signal that mostly represents the 6-month component (Fig. 3.2.6 e,f). The amplitude of this semi-annual signal grows with depth and at 140m it carries most of the temperature variability (Fig. 3.2.6 f).

Figure 3.2.7 shows the distribution of variance over depth in four main frequency bands for Box 2. The variance for each band is calculated by summing up three points in the frequency spectra (that of the main maximum and two adjacent points). The bands are: 28 months to 42 months for the 3-year signal; 16.8 to 21 months for the 18-month signal; 11.2 to 12.9 months for the 1 year signal; 5.8 to 6.2 months for the 6-month signal.

Figure 3.2.7 shows that amplitudes of the 1 year signal are very stable in the mixed layer, has a small peak in the vicinity of the top of the thermocline (100-120m, see Fig.3.2.3, upper panel), and rapidly decays at approximately 150m. The semi-annual signal has an opposite pattern: it is small in the mixed layer and reaches a maximum between 100m and 150m. It is known that there is a strong 6-

month variability in the surface current near the Indonesia coast that results from the equatorial Wyrtki jet (Wyrtki, 1973).

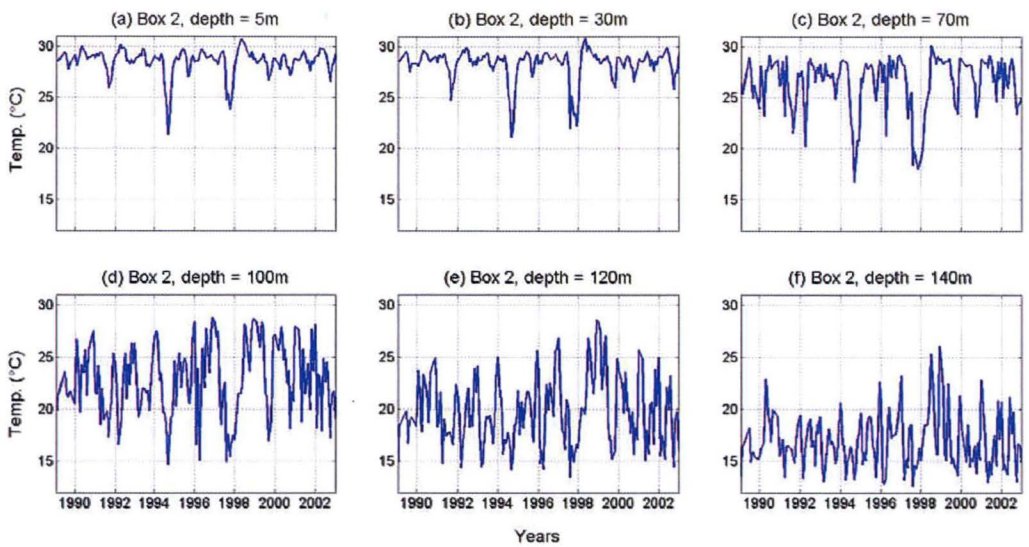

Figure 3.2.5. Subsurface temperature from IOTA data set averaged in Box 2 (Fig. 2.1.4) with corners at 7.0°S, 104.0°E and 8.0°S, 106.0°E at different depths: 5m, 30m, 70m, 100m, 120m, and 140m.

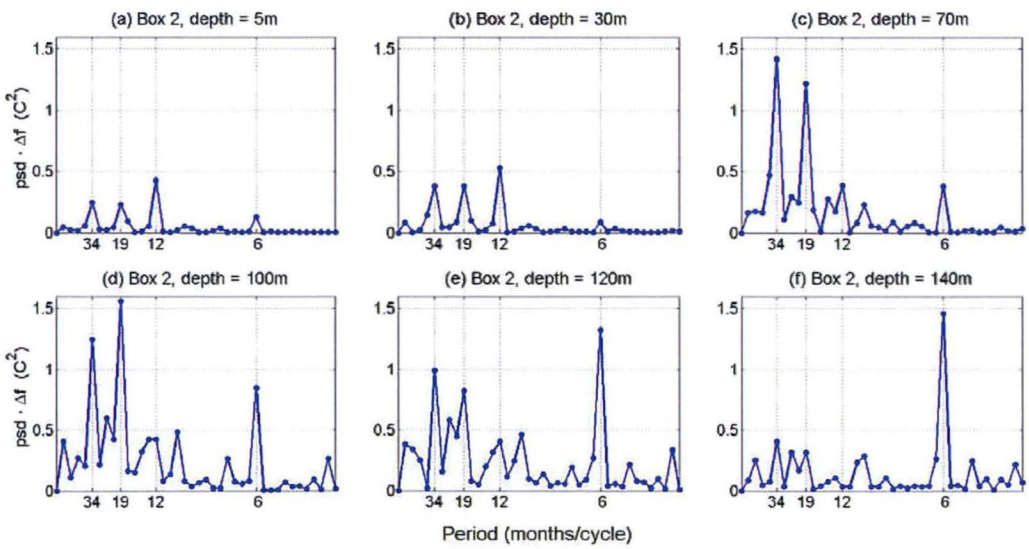

Figure 3.2.6. PSD of subsurface temperature from IOTA data set averaged in Box 2 (Fig. 2.1.3) with corners at 7.0°S, 104.0°E and 8.0°S, 106.0°E at the same depths as in Figure 3.2.5: 5m, 30m, 70m, 100m, 120m, and 140m.

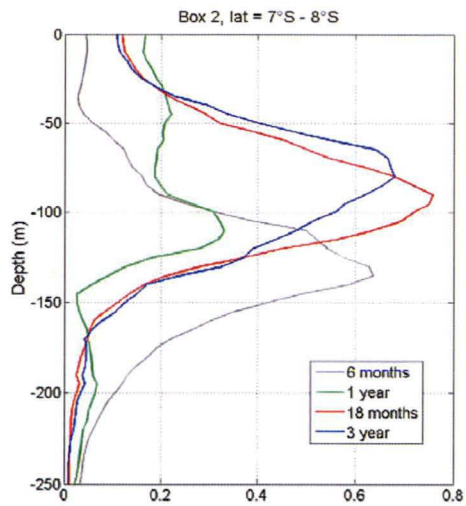

Figure 3.2.7. Distribution of variance over depth for four frequency bands: 6-month (gray), 1-year (green), 18-month (red), and 3-year (blue) near Sumatra-Java coast at 7°S-8°S.

The time series of the subsurface temperature at 5m and 30m depth in Figure 3.2.5 (a,b) show clear and sharp temperature minima in 1991, 1994, and 1997 caused by strong upwelling during the recognized IOD events. These minima are separated in time by about 3 years, and the variability of the signal between them is relatively small. The peaks can be seen clearer after removing the high-frequency signal. This is done in Figure 3.2.8, which represents the 6-month running average of the temperature time series from Figure 3.2.5 (a,b,c). From this figure we can suggest that the 3-year signal is dominant at 30m; however, at 70m the 3-year signal is still dominant, but there start to appear relative minima and maxima between the major ones (b - black arrows), and the signal at 120m looks as quasi-periodic. From December 1991 to December 1999 (8 years) it exhibits five full cycles with period about (8 · 12)m / 5 = 19 months. The vertical structure supports the results of FFT analysis and indicates that the 3-year and the 18-month signals are distinct processes in this location.

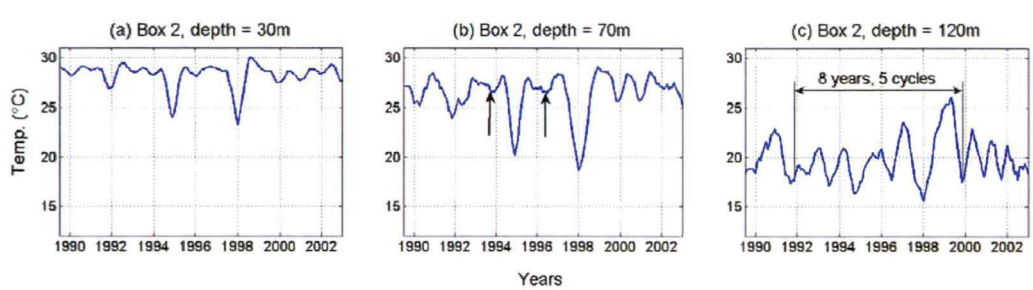

Figure 3.2.8. 6-month running average of the subsurface temperature from IOTA data set at 30m, 70m, and 120m in Box 2 (see Fig. 2.1.4 for Box description).

We will now analyse the D20 signal in Box 2 depicted in Figure 3.2.4 by means of wavelet analysis. This may reveal the variability of the signal at different frequencies within the time interval of the signal. The wavelet amplitudes are shown colour coded in Figure 3.2.9 (a). The signal has strong interannual variability with maxima at periods of approximately 18.7 (18-month signal) and 32 months (3-year signal). These two maxima can be also clearly identified from the global wavelet spectrum in Figure 3.2.9 (b). The global wavelet spectrum is a method to determine the power spectrum based on wavelet analysis method, (Torrence and Combo, 1998). Note that it cannot be used to determine the variance in the corresponding spectral bands (Wu and Liu, 2005). The 3-year signal starts developing in 1990, at the beginning of the time series, and remains strong until approximately 2001, while the 18-month signal is quite prominent from 1993 to 2000. The 18-month signal is particularly strong during 1996-1998, when its amplitude exceeds that of the 3-year signal. The 6-month signal also exists over the whole time period.

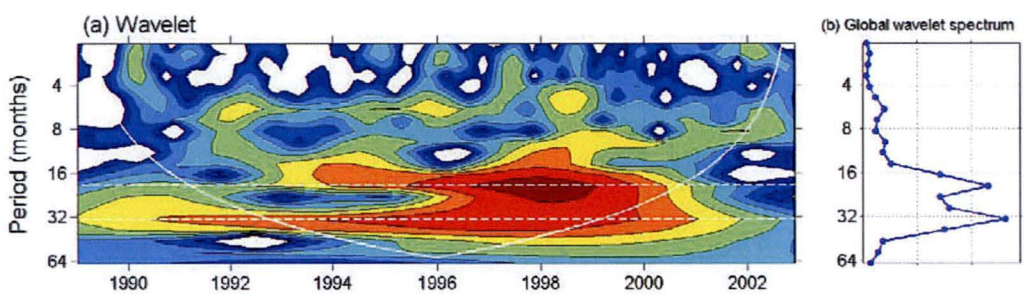

Figure 3.2.9. (a) Wavelet spectrum of 20° C isotherm in Box 2 (Fig. 2.1.3) with corners at 7.0°S, 104.0°E and 8.0°S, 106.0°E , where the white solid line represents the cone of influence; (b) Global wavelet spectrum of D20.

These observations are in agreement with the frequency spectrum of temperature at 100m and 120m in Figure 3.2.6 (d,e), while the mean depth of D20 is about 115m.

The existence of a very strong 18-month signal in subsurface XBT data near the Sumatra-Java coast is one of the main findings of this study. We will now investigate the spatial distribution of the signals in all major frequency bands, with particular attention to the 18-month signal. Also we will investigate the dependence of the subsurface temperature variability on the distance from the Java coast along XBT line section IX-1 (Fig. 2.1.3).

3.2.3 Spectral analysis of subsurface temperature along XBT IX-1 line

While the exact mechanism of the IOD is not yet fully understood, there is little doubt that the upwelling along the Indonesian coast plays an important role in the IOD and can be used as one of the early indicators of the development of IOD. It is shown in the previous section that both the 18-month and 3-year signals are prominently present in subsurface temperature signals, reaching a

maximum at about thermocline depth. In this section, the subsurface temperature at different locations along XBT line, section IX-1 corresponding to different distances from the Sumatra-Java coast, will be investigated.

The spectral analysis of subsurface temperature in different locations along IX-1 line reveals quite different variability. Figures 3.2.10 and 3.2.11 show the PSD of subsurface temperature data at the same depths as in Figures 3.2.5 and 3.2.6 (5m, 30m, 70m, 100m, 120m, and 140m), but calculated for Box 3 (8.0°S, 104.5°E and 9.0°S, 106.5°E) and Box 4 (9.0°S, 105.0°E and 10.0°S, 107.0°E).

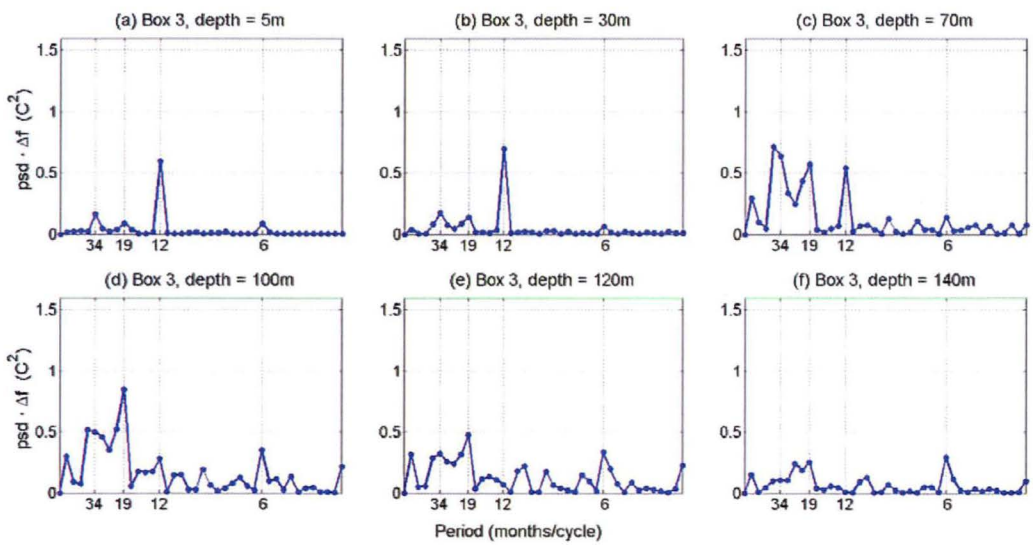

Figure 3.2.10. PSD of subsurface temperature from IOTA data set averaged in Box 3 (Fig. 2.1.3), with corners at 8.0°S, 104.5°E and 9.0°S, 106.5°E, at the same depths as in Figure 3.2.5: 5m, 30m, 70m, 100m, 120m, and 140m.

All signals except the one-year signal become weaker with the distance from the Sumatra-Java coast. The 6-month signal that is very strong near the Indonesia coast at 7.0°S-8.0°S (see Fig. 3.2.6 and Fig. 3.2.7), almost disappears just at an additional 1-2° south from the coast. The amplitude of the 18-month signal also drops significantly with distance from the coast. The 3-year signal is still quite strong below the mixed layer. The sharp decrease offshore in the strength of all signals except the annual can be explained by the existence of a coastal wave guide, coastal trapped currents or upwelling along the coast. The offshore drop in signal amplitude can also be seen in Figure 3.2.12.

Figures 3.2.12 and 3.2.13 present the temperature variability in different locations along XBT line. Figure 3.2.12 shows the variance of the signal in each of the main frequency bands (6-months, one year, 18-months, and 3-years) versus depth for the 12 boxes along the line, while Figure 3.2.13 shows the long term monthly mean temperature anomalies at each depth level in the same 12 locations.

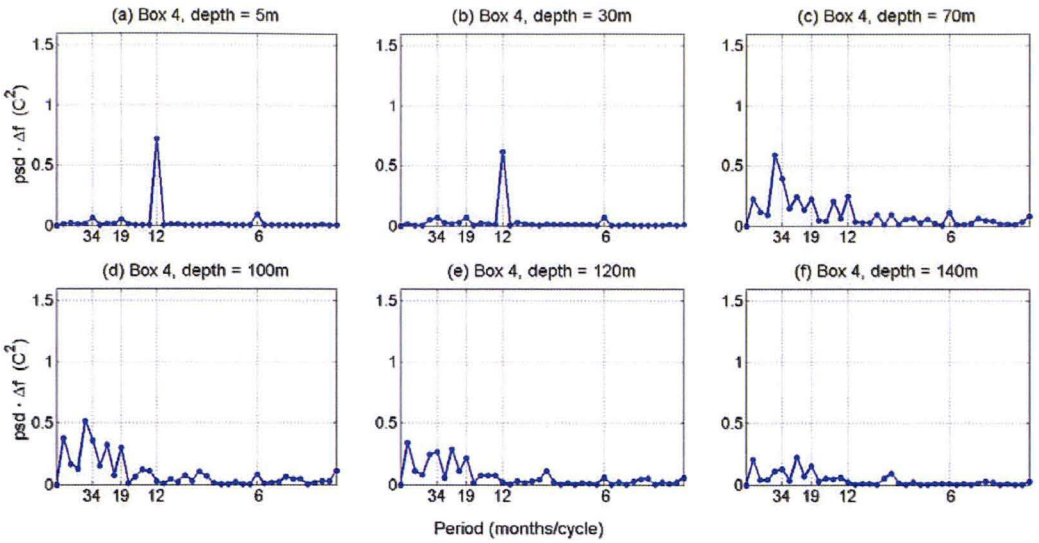

Figure 3.2.11. PSD of subsurface temperature from IOTA data set averaged in Box 4 (Fig. 2.1.3), with corners at 9.0°S, 105.0°E and 10.0°S, 107.0°E, at the same depths as in Figure 3.2.5: 5m, 30m, 70m, 100m, 120m, and 140m.

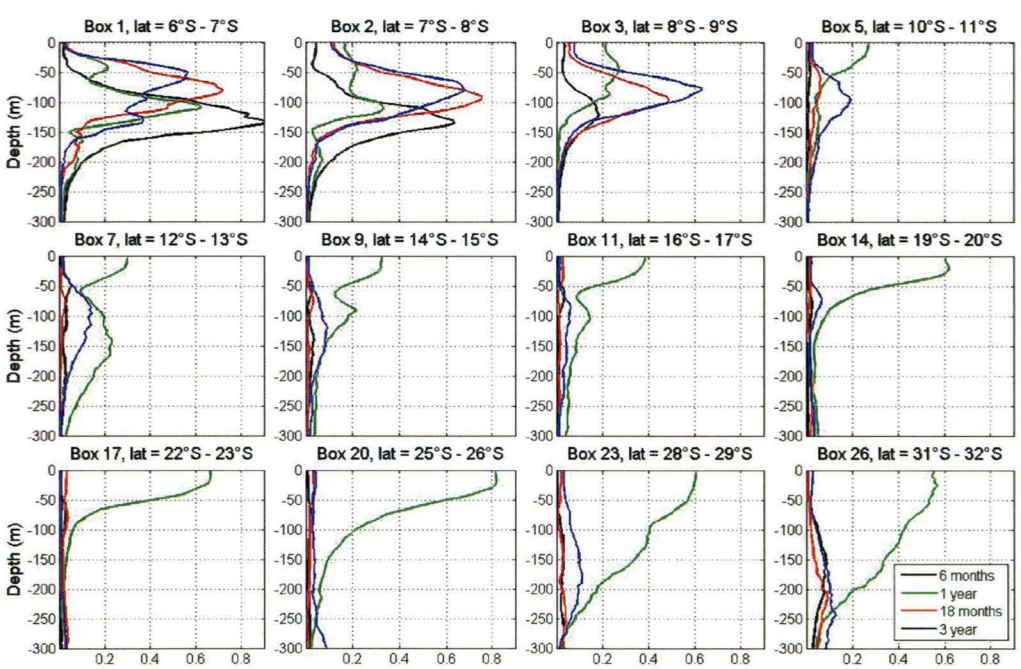

Figure 3.2.12. Distribution of variance over depth for four main frequency bands: 6-months (black), 1-year (green), 18-months (red), and 3-years (blue) in 12 boxes along XBT IX-1 line.

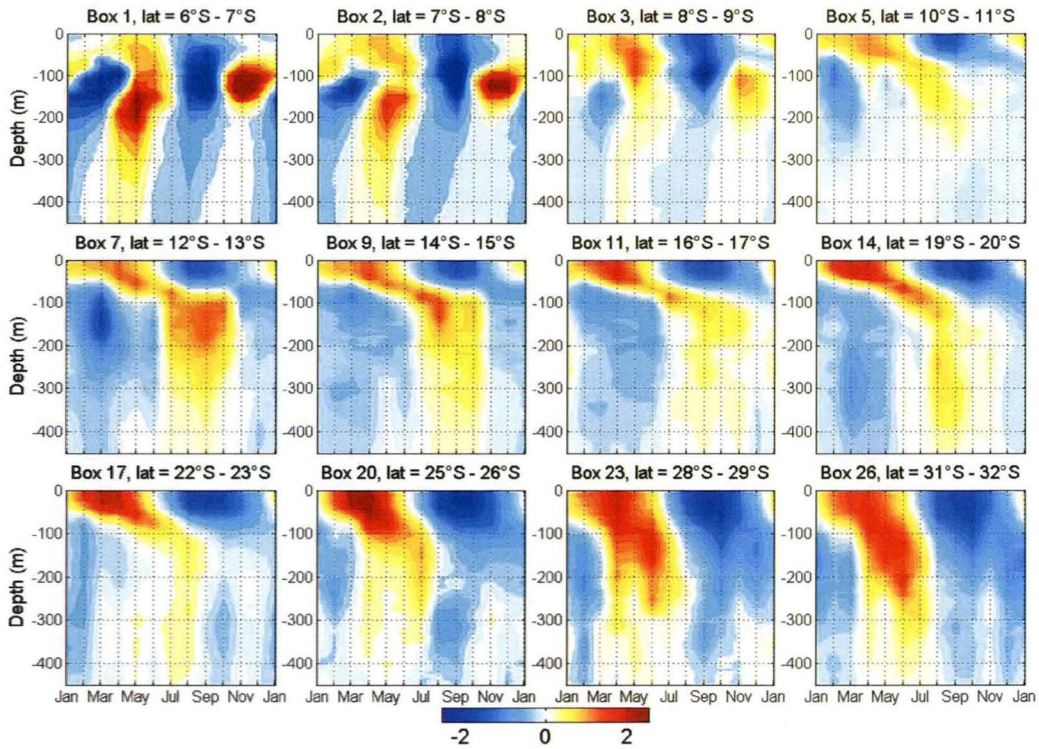

Figure 3.2.13. Deviation from long term monthly mean temperature in 12 boxes along XBT IX-1 line.

The climatology reveals the structure of a strong 12-month cycle along XBT IX-1 line. In the Java upwelling region there is a strong semi-annual signal that dominates at depths of 75-200 meters in Boxes 1-3, latitude from 6.0°S to 9.0°S (Fig. 3.2.12 and Fig. 3.2.13). At this depth the temperature has maxima two times a year during April-June and October-November - the time of development of the Wyrtki jet during monsoon transition periods between Southwest and Northeast monsoons. The semi-annual signal almost disappears just 3 degrees south from the Indonesia coast, at 9°S. The one-year signal is stronger than the semi-annual signal in Boxes 1-3 in the isothermal layer, to the depth of up to 75m.

Around the middle of the XBT line, between 10°S and 23°S, the annual signal is very strong in the upper 50 m. Two distinct processes likely cause this variability: surface temperature driven by surface heat fluxes and Ekman pumping, and Rossby-wave propagation, as described in Masumoto and Meyers (1998). These signals overlap over the depth with varying amplitude, which give the appearance of vertical propagation.

Closer to either Indonesia or the West Australia coast, the 1-year signal has significantly different pattern. Near Indonesia it is not as strong as in other locations (Fig. 3.2.12), with the 6-month signal dominating at depths 75-200 m, and the 1-year signal being stronger closer to the surface.

Near Australia the XBT IX-1 line between 25°S -31°S (Boxes 20-26) runs parallel to the shelf edge of western Australian coast, inside the Leeuwin Current. Figure 3.2.13 shows penetration of the annual signal to the depth of 250-300m. This agrees with the finding that the isotherm gradually deepens at this location after austral summer in March-July (Morrow and Birol, 1998), and probably results from the annual modulation of the coastal trapped Leeuwin Current (Feng *et al.*, 2003). Interestingly, that in the region between 12°S and 15°S, the annual cycle in the surface layer (0-100m) is 180 degrees out of phase with the cycle in the 100-200 m layer.

Complementary to the spectral analysis, the wavelet analysis can provide information about the temporal variability of the signal components of different time scales. Specifically, we post the question do both these signals exist during the whole data set period (from 1989 to 2002) or represent a temporal feature. To address this issue, we analyse the variability of the subsurface signal in Boxes 2, 3, and 4 at the depth of 75 m, close to the vertical maxima of 18-month and 3-year signals in Figure 3.2.12.

The wavelet and spectral analyses (Fig. 3.2.14) show that the 18-month signal is stronger than the 3-year signal at 75 m near the coast. The signal exists during 1992-2000. The 3-year signal has maximal amplitude in Box 2, and exists during 1990-2002. Both signals appear during IOD events of 1994 and 1997. A possible connection of these signals with IOD will be discussed in Chapter 4.

This Chapter has described the spectral structure of temperature variability along XBT line IX-1. The spectra change with depth and spatially along the line. The existence of a very strong 18-month signal in the Java upwelling region is a very interesting result that requires further investigation. The variation in depth (Fig. 3.2.7, Fig. 3.2.8, and Fig. 3.2.12) and along XBT line (Fig. 3.2.14) indicates that it is a different process than the 3-year signal. In the following sections we will confirm the existence of the 18-month and 3-year signals for different data types, including some data of longer duration then the XBT data. We will suggest a possible role for the 18-month signal in development of the Indian Ocean Dipole. The analysis of the spectral distribution of the subsurface temperature with depth and horizontal location is also interesting result of current study and possible requires further investigation, but out of topic of this thesis.

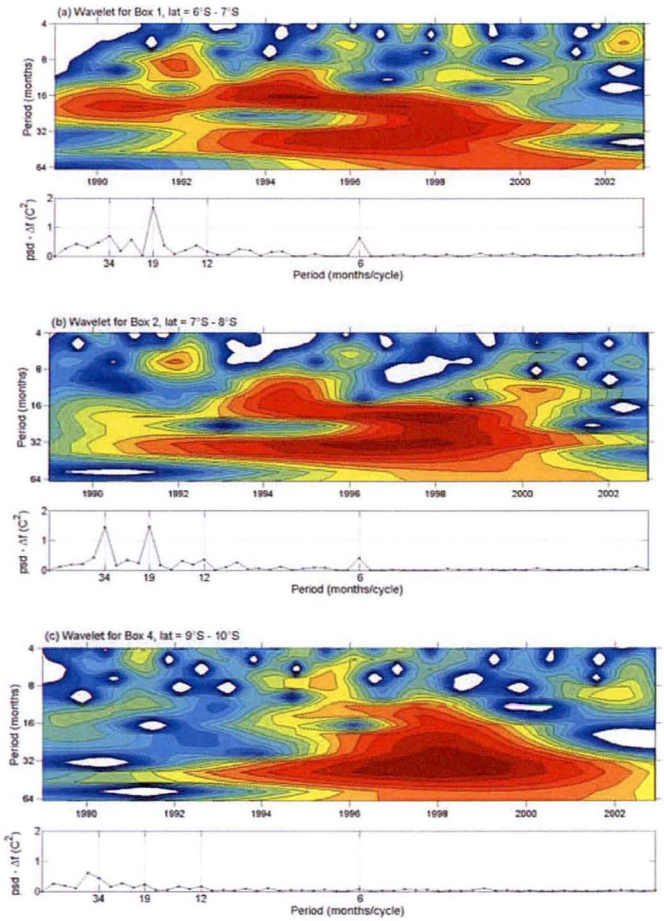

Figure 3.2.14. Wavelet spectrum of temperature at 75 m; in (a) Box 1 with latitude 6°S-7°S, (b) Box 2 with latitude 7°S-8°S, and (c) Box 4 with latitude 9°S-10°S.

3.3 Analysis of altimetry SLA

This section investigates the interannual variability of the Indian Ocean using gridded (1 degree) altimeter SLA data. We first build frequency spectra in each grid cell over the Indian Ocean and plot the variability maps for each frequency presented in the spectra. Based on these maps, we divide the whole SLA spectrum into a number of spectral bands. After that the temporal and spatial variability of each spectral band is investigated to improve the understanding of physical processes driving the variability in each band. Finally, we investigate the spectral composition of the several first EOF modes to obtain information about the dominant time scales associated with each mode.

3.3.1 Introduction

The spectral analysis of the subsurface temperature in the Java upwelling region conducted in Section 3.2 reveals the existence of a number of significant components of the signal in the low-frequency part of the spectrum. Depending on location and depth, apart from the usual annual and semi-annual components, there may exist significant 18-month, 3-4-year, and 7-year components. A strong and well pronounced 18-month signal that has been ignored in earlier studies was documented. Because of the long time scales of these signals, the corresponding ocean processes may be expected to manifest themselves not only near the Java coast but also at larger spatial scales. This motivates us to conduct a spectral analysis of the low-frequency variability in the whole Indian Ocean. Altimetry SLA data represent an ideal type of data for this purpose.

The altimetry SLA data set analysed in this study starts in 1992, and covers presently a period of 17 years, with high-quality measurements that are dense enough for our purposes, both in time and space. The duration of the data of 17 years is quite good for studying the interannual variability of the ocean, particularly if compared with the situation just 10 years ago.

As soon as altimetry SLA data became available in the 90s, they started to be used in a large number of studies. Most of the earlier studies focused on the Rossby/Kelvin wave propagation and western boundary current reflection in the Indian Ocean (Morrow and Birol, 1998; Birol and Morrow, 2001; Le Blanc and Boulanger, 2001; Challenor *et al.,* 2004). Eddy propagation became another common subject of the altimetry-based studies, as soon as the spatial density of the altimetry data started to allow investigators to resolve eddies (Morrow and Birol, 1998; Morrow *et al.,* 2004; Reddy *et al.,* 2004; Vaid *et al.,* 2008). SLA measurements contain information about both the ocean dynamics and integrated properties of the water column. Such data have been used to study the thermocline depth (Behera *et al.,* 1999; Feng and Meyers, 2003). Using altimetry SLA data, Feng and Meyers (2003) identified two regions in the tropical Indian Ocean with high level of variability of SLA (up to 8 cm). This work is described in Section 3.2 (also see Fig. 3.2.1).

A number of analyses conducted analysis of the interannual variability of the Indian Ocean using EOFs. Applying EOFs for analysis of the TOPEX/POSEIDON altimetry data, Chambers *et al.* (1999) found that the interannual warming in the Indian Ocean occurs with a frequency similar to El-Nino in the Pacific. Rao *et al.* (2002) and Feng and Meyers (2003) also applied EOF analysis to SLA data from 1992 to the end of 1999, which includes two strong positive IOD events of 1994 and 1997. These papers aimed at studying the interannual variability of the Indian Ocean; they removed annual and semi-annual signals before applying the singular value decomposition (SVD) and came to similar results for the first two EOF modes. Rao *et al.* (2002) found that the first EOF mode (EOF-1) explains about 46% of the interannual variance of the altimetry SLA, while according to Feng and Meyers (2003), it explains about 38% of the SLA variance. The left upper panel of Figure 3.3.1

shows EOF-1 as calculated by Rao *et al.* (2002), while the right panel shows EOF-1 as calculated by Feng and Meyers (2003). Figure 3.3.2 shows the second EOF mode.

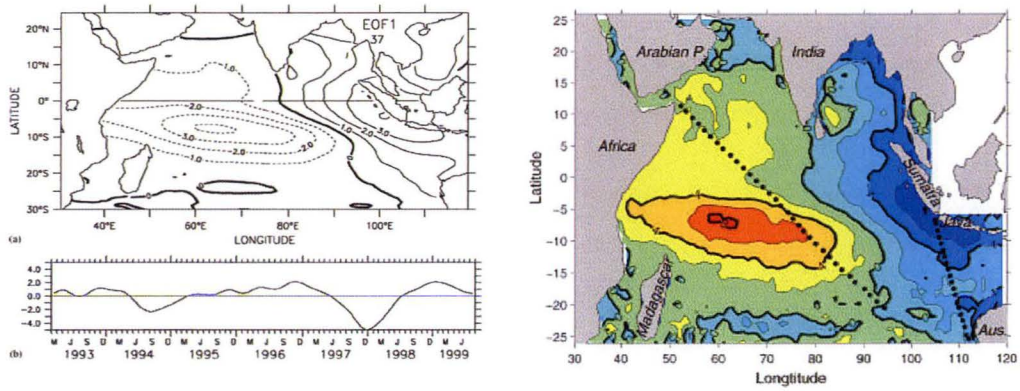

Figure 3.3.1. First leading EOF mode of altimetry SLA anomaly. Left panel - as calculated by Rao: (a) spatial function and (b) temporal function; dashed (solid) lines denote negative (positive) loadings (after Rao *at. al*, 2002). Right panel - as calculated by Feng and Meyers, the units are in cm, and the contour interval is 2cm (after Feng and Meyers, 2003).

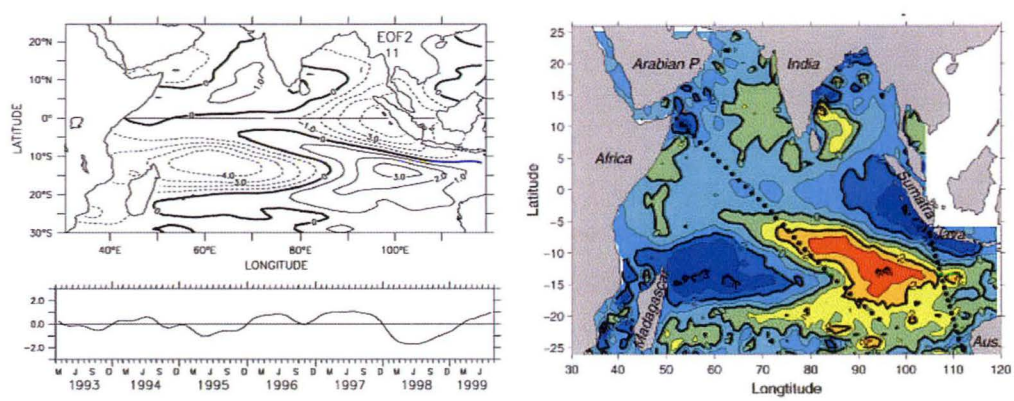

Figure 3.3.2. Same as Figure 3.3.1 but for EOF-2 mode.

The structure of EOF-1 of SLA anomaly is very similar in both papers. "The dipole pattern is clearly seen in the tropical Indian Ocean with positive loading in the east and negative loading in the west. This is in agreement with the seesaw oscillation observed between the eastern and western equatorial Indian Ocean thermocline depths identified previously by Masumoto and Meyers (1998) and Murtugudde and Busalacchi (1999).... The associated time series (Figure 3.3.1, left bottom panel) coincides with two major positive IOD events; one during 1994 and the second one during 1997" (Rao *et al.,* 2002). The authors considered "the relevance of EOF modes to the physical modes" and come to the conclusion that "the first EOF is associated with the Indian Ocean Dipole" (Rao *at al.,* 2002, p.1559) representing the subsurface aspect of the dipole.

The second EOF (EOF-2) mode explains 11% of the total sea level variance in the tropical Indian Ocean according to (Rao *et al.*, 2002) and 13% according to Feng and Meyers (2003). The spatial pattern of EOF-2 mode has a negative loading confined to the Sumatra-Java coast, and positive loading centred near 13°S, 95°E and extended in the northwest-southeast direction. There is also a negative loading northeast of Madagascar. Figure 3.3.2 shows the EOF-2 as calculated by Rao *et al.* (2002), left panel, and by Feng and Meyers (2003), right panel.

Both papers suggested that EOF-2 is associated with the quasi-biennial signal in the tropical Indian Ocean, based on a qualitative look of the temporal function. "The transformation of the subsurface dipole from a positive phase to a negative phase gives rise to the quasi-biennial signal observed in the off-equatorial regions through propagation of Rossby waves. Further, analysis of in situ subsurface temperature data at selected locations in the tropical Indian Ocean using the wavelet transform has revealed that significant quasi-biennial variance is observed only during and after the IOD events, thereby confirming the quasi-biennial variance associated with the turnabout of a positive dipole to a negative dipole in the subsurface Indian Ocean" (Rao *at al,* 2002). Feng and Meyers (2003) wrote that EOF-2 is unique to the Indian Ocean Dipole. Later in this Chapter we will conduct a spectral analysis of EOF modes to better understand their temporal variability.

3.3.2 Spectral composition of SLA in different locations of the Indian Ocean

Many of the results for the spectral analysis of SLA presented in this dissertation have already been published in Sakova *et al.* (2006a,b). Figure 3.3.3 shows the PSD of SLA in a number of different locations of the Indian Ocean, with the following coordinates: **a** – 7.7°S, 75°E; **b** – 13.6°S, 87°E; **c** – 24°S, 75°E; and **d** – 5.7°S, 104°E, while Figure 3.3.3(**e**) depicts the mean power spectrum over the larger domain of the Indian Ocean shown by the black dashed line, obtained by averaging of 2118 spectra in individual grid cells. These locations are chosen to demonstrate that variability of the Indian Ocean is significantly different in different parts of the ocean. The weekly-averaged SLA data used for the analysis covered the period from October 1992 to August 2004 and contained 618 weekly entries. (In this thesis we use longer altimetry data available for today).

All these spectra have one common feature: they contain a few, rather strong and well separated maxima. Apart from the semi-annual peak near the Sumatra coast (Fig. 3.3.3 **d**, point N 25 in the spectrum), with an amplitude of about 4.5 cm, and annual components (Fig. 3.3.3 **a,b**, point 13 of the spectra) in the central Indian Ocean with amplitude ~6.3 cm in location **b**, there are also three interannual variability modes. Two of them have been encountered above in the spectrum of D20 of XBT data in the Java upwelling region (Fig. 3.2.4): the maxima corresponding to periods of approximately 36 months (Fig. 3.3.3 **a,d**, point 5 of the spectra) and 18-20 months (Fig. 3.3.3 **a-d**). The maximum of the latter signal corresponds to a period of ~17.8 months (point 9 of the spectra) in location **a, c** and to a period of 20.3 months in location **b** (point 8). In location **d**, both frequencies

are present. There is also a signal with periods of 4-6 years (Fig. 3.3.3 **b-d**). Figure 3.3.3 (**e**) represents the mean power spectrum over the larger domain of the Indian Ocean and contains all of the described above spectral maxima. Interestingly, the signal with period of 2 years (corresponding to point 7 of the spectra, and a period of 23.7 months) has a clear minimum in all spectra.

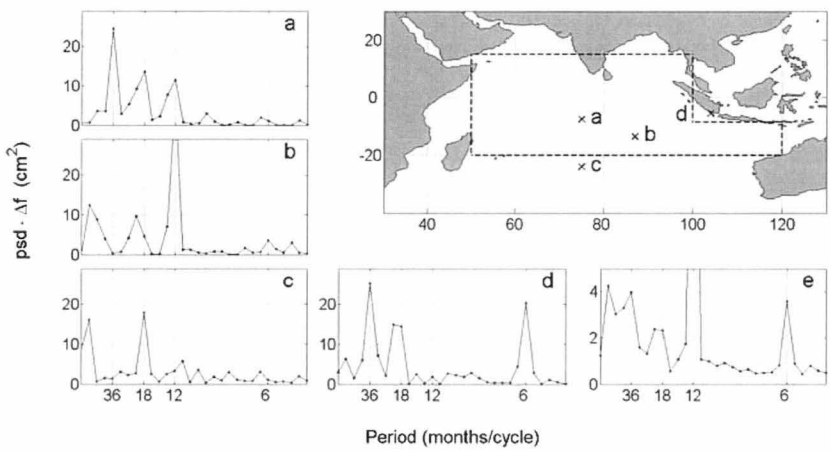

Figure 3.3.3. PSD of SLA in different locations of the Indian Ocean: **a** – 7.7°S, 75°E; **b** – 13.6°S, 87°E; **c** – 24°S, 75°E; and **d** – 5.7°S, 104°E, and over the region enclosed by the dashed line (**e**).

Overall, in some locations of the Indian Ocean the power spectra of SLA may lack one or other of the identified maxima, but in all cases any well-separated narrow maxima do belong to one of these five frequency bands: semi-annual, annual, 18-20-month, 3-year, and a signal with periods longer than 4 years.

To investigate the temporal variability of SLA signals in the main bands for the same locations as in Figure 3.3.3, the wavelet transform is used. The resulting wavelet spectra show that the signals in the particular bands have quite different temporal behaviour (Fig. 3.3.4). The six-month (Fig.3.3.4 d) and one-year signals (Fig. 3.3.4 b) are continuously present during the whole time period of the data set, while the 3-year (Fig. 3.3.4 a,d) and 18-month (Fig. 3.3.4 a-d) signals exist only at certain time intervals or locations. Specifically, both signals exist during 1993-2000 at points **a** and **d**. At point **b**, the signal with a period of 20 months (point N 8 in the spectrum) is present only from 1996 to 2002, while the 3-year signal at point **a** is strong throughout the whole time period. Such differences in temporal variability of signals in different spectral bands indicate that they may correspond to different physical modes of the Indian Ocean or the coupled atmosphere-ocean system.

We note here that the data used at the time of writing the thesis, for 1992-2008, represent only 17 years of the altimetry data collection. This does not allow us to make reliable conclusions about the variability of SLA in the Indian Ocean with time scales longer than about 7 years.

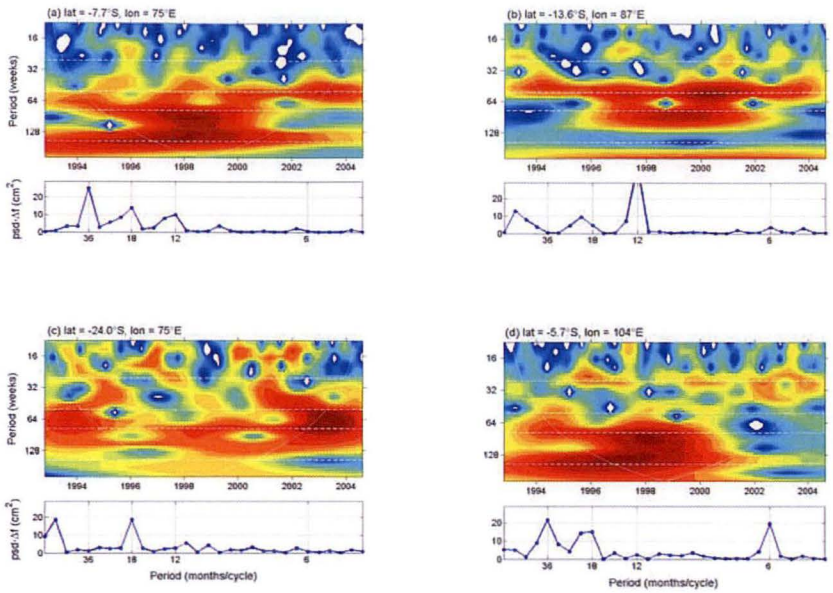

Figure 3.3.4. Wavelet spectra and Fourier spectra of SLA for the same locations as in Figure 3.3.3. White dashed lines in wavelet spectra denote the half-year, one-year, 18-month, and 3-years signals.

3.3.3 Spatial variability of SLA over the Indian Ocean. Five main spectral bands of the SLA signal

To analyse the spatial distribution of the variance of SLA in each particular frequency and each particular frequency band identified in the previous section over the whole Indian Ocean, we calculate maps of PSD for each frequency. This is done by calculating power spectra for each grid cell of the gridded SLA data over the Indian Ocean and plotting the resulting maps; or summing up within each spectrum the PSD values corresponding to each identified band; and plotting the resulting maps.

Figure 3.3.6 lists periods for each component in the spectra in Figure 3.3.5 obtained from SLA time series of 728 weekly values, corresponding to the period from October 1992 to September 2006 (14 years). The period corresponding to the i-th point (component) in the spectrum is equal to the full duration of the data set divided by (i – 1).

The calculated maps of PSD are presented in Figure 3.3.7. It contains maps for signals with periods from 7 years to 5.6 months, corresponding to points from 3 to 31, or spectral components from 2 to 30 (the first point corresponds to the 0^{th} spectral components, which is proportional to the mean value of the signal for the whole time period). The points 18-26 corresponding to the spectral components with periods from 6.7 to 9.8 months, are not shown because no significant signal is

found at these time scales. This agrees with the results by Fu (2007, Fig. 1), who also did not find any significant signals with periods between 182 and 365 days.

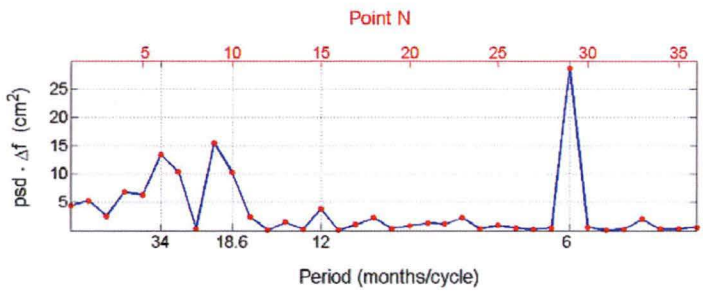

Figure 3.3.5. A frequency spectrum of altimetry SLA for 728 weeks for the period from October 1992 to September 2006, at 5.7°S, 104°E.

Point	**3**	**4**	**5**	**6**	**7**	**8**	**9**	**10**	**11**	**12**
Period (months)	83.8	55.8	41.9	33.5	27.9	23.9	20.9	18.6	16.8	15.2
Point	**13**	**14**	**15**	**16**	**17**	**27**	**28**	**29**	**30**	**31**
Period (months)	14	12.9	12	11.2	10.5	6.4	6.2	6	5.8	5.6

Figure 3.3.6. Conversion of frequencies in the spectrum in Figure 3.3.5 to period, for the points 3 to 31 in the frequency spectrum (spectral components 2 to 30).

There are very strong annual (point 15) and semi-annual (point 29) signals. Both signals have very sharp maxima in the spectra: they are both represented by only one spectral component in the spectra, as there is almost no signal in the adjacent points (corresponding to periods of 11.1 and 12.9 months for the one-year signal and 5.8 and 6.2 months for the six-month signal). The annual signal has particularly strong variability in the Arabian Sea, in the South-East part of the Indian Ocean, and in the Indonesian seas. The semi-annual signal is weaker than the one-year signal, and its distribution is similar to that obtained by Fu (2007). Overall, it follows from Figure 3.3.7 that the annual and semi-annual signals are represented by strong standalone spectral maxima, and that the annual signal has significantly larger total variance than the semi-annual signal.

In the low-frequency part of the spectra, there is no significant signal with periods between 18 months and one year. There are strong signals with periods of about 21 months (point 9) and 18.6 months (point 10). These two spectral components have similar spatial patterns, and we can consider them to be a single component of the SLA signal. They are characterized by strong variability along the Sumatra-Java coast and along a narrow strip between 55°E - 90°E and 4°S -15°S; at the same time, there is no 18-month signal in the Indonesian seas. In Figure 3.3.3 (d,e) this signal can be clearly identified with two-point maxima. We refer to it as 18-month or 18-20-month signal.

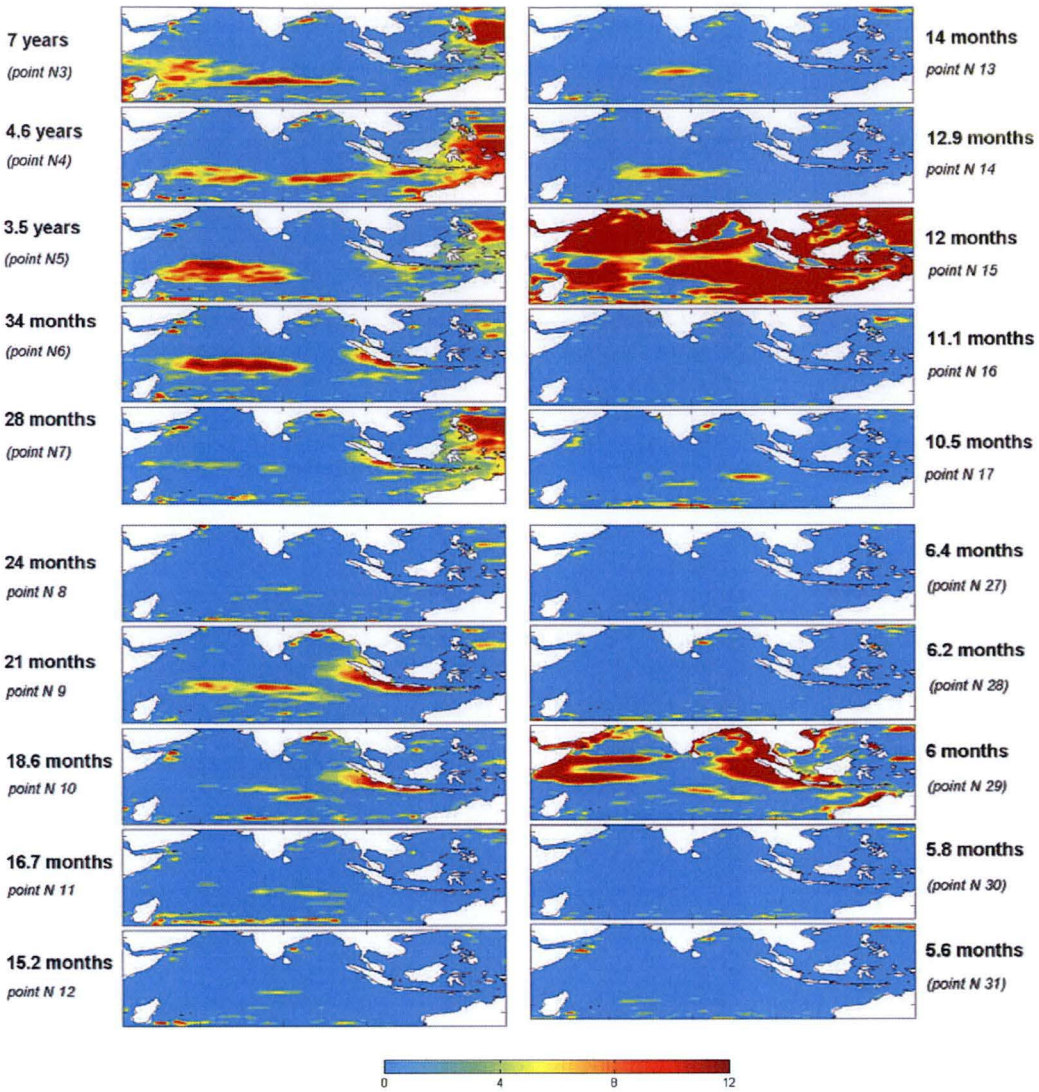

Figure 3.3.7. Maps of PSD of SLA for individual spectral components (cm^2).

Interestingly, despite claims in a number of studies about the existence of a quasi-biennial mode, no significant signal with the bi-annual (24-month, corresponding to point 8 in the spectra) period is found, at least for the analysed period, defined by the altimetry data collection (1992-2006). This spectral gap is present in all spectra in Figure 3.3.3; it separates the 18-month signal from the lower part of the spectrum.

The rest of the spectra can be divided in two dominant frequency bands: 7–4.6 years (points 3 and 4) and 3.5 years–34 months (points 5 and 6). Although there is no spectral gap between these two components (point 3 and 4 versus 5 and 6), the corresponding signals have different spatial distributions. The 3-year signal has a clear dipole pattern with two poles, one with a well defined boundary at around 5°S-18°S and 50°E-85°E, and the second is along the south-west coast of Sumatra-Java. The 4.6-7 year signal is mostly concentrated in a zonally elongated region in the

southern Indian Ocean between latitudes about 5°S-15°S; with the western part of this region being somewhat wider than the eastern part. It is possible that the resolution of the spectra obtained from analysis of 14-year data may be insufficient to resolve the spectral gap between the points 4 and 5 in the spectrum, if it is narrower than the frequency resolution of the analysis, of about 1/14 yr^{-1}. This agrees well with the spectra at different locations of the Indian Ocean presented in Figure 3.3.3(a-e), where signals at points 3, 4 and points 5, 6 have different magnitudes at different locations. As we had noticed above, the resolution in this low-frequency part of the spectrum may be not sufficient, but it will improve in the future with longer altimetry data becoming available for the analysis.

At this stage, we can identify five main frequency bands that carry most of the variance of the SLA in the Indian Ocean: 6-month, 12-month, 18-20-month, 3-year, and 4-7-year. Four of these bands have been previously described in the literature, and their period and spatial distribution agree well with our analysis. The fifth band with the periodicity of 18-20-month has not been described before, although this signal is quite strong, at least during the altimetry data collection period (1992-2006).

Figure 3.3.8 contains maps of the spatial distributions of PSD for each of the above identified spectral bands, calculated by summing up the PSDs of individual spectral components within each band. The signals in each band have different spatial distributions. Although all of these components, except the 18-20-months signal, have been recognized previously in the literature, to the best of our knowledge the spatial distributions of PSD of the SLA for each band were first calculated and plotted in Sakova *et al.* (2006a) and Sakova *et al.* (2006b).

The top panel (a) in Figure 3.3.8 shows the spatial distribution of PSD for the semi-annual signal. There is a strong signal in the Indonesian upwelling region; north-propagating coastally trapped Kelvin waves around the Bay of Bengal; and a C-shaped structure in the western tropical Indian Ocean with the maxima off the equator that is caused, according to Fu (2006), by propagating and reflecting Kelvin and Rossby waves.

The spatial distribution of the 1-year signal is shown in Figure 3.3.8(b). The signal in this band is generally much stronger than in others (by roughly a factor of 3), and is plotted in a different scale. It has maxima in the Red Sea, along the Arabian Sea between about 5°N-12°N, the western part of the Bay of Bengal, and in the south tropical Indian Ocean between 8°S-15°S from 75°E to the Indonesian Throughflow region up to 120°E. The maximum south of the equator is due to wind-forced, annual Rossby waves (Masumoto and Meyers, 1998).

Figure 3.3.8(c) shows the spatial distribution of PSD for the 18-20 month signal. It contains strong signals offshore of Indonesia and in the Bay of Bengal caused by northward-propagating coastal trapped waves. There are also two strong maxima in the central Indian Ocean, one at approximately 5°S -15°S and 60°E - 95°E and a zonally elongated, narrow maximum at 23°-24°S and between 65°E

and 98°E. There is no significant signal at these frequencies in the Indonesian Throughflow region and in the western Pacific. This signal and its temporal variability will be discussed in more detail later in this thesis.

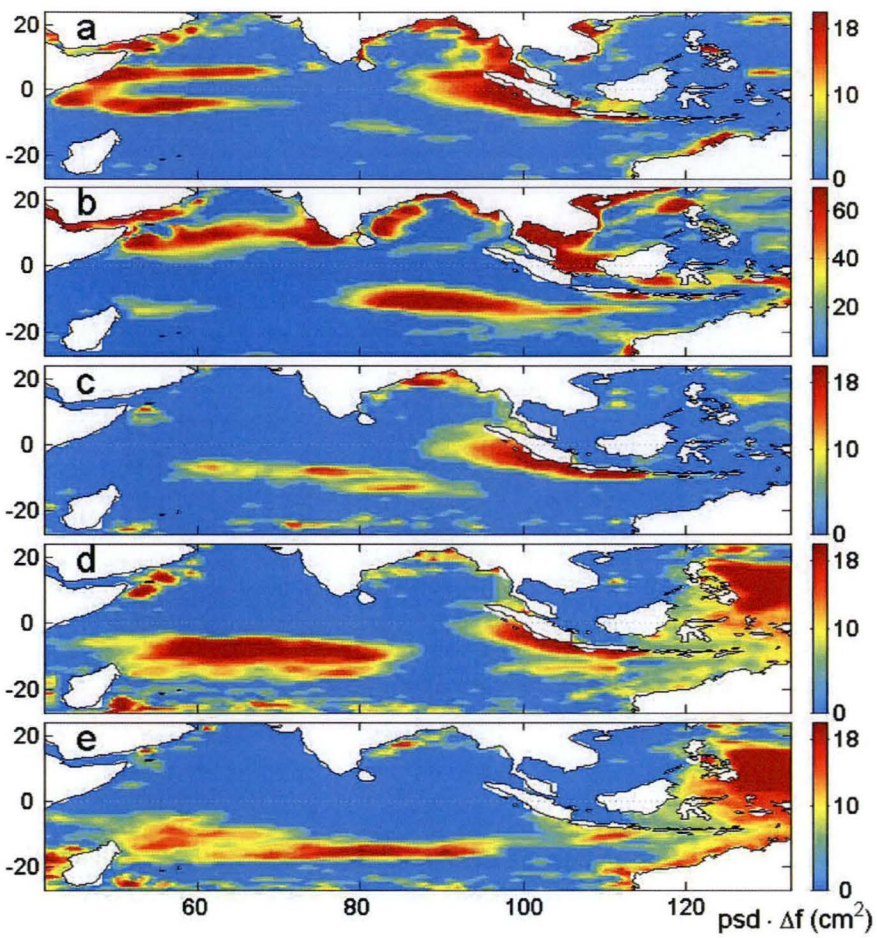

Figure 3.3.8. Spatial spectral density of SLA for signals: (a) 6-month; (b) 1-year; (c) 18-20-month; (d) 3-year; and (e) 4-7-year, where psd is the power spectral density and Δf is the frequency resolution.

The spatial distribution of the 3-year signal shown in Figure 3.3.8(d) contains two major maxima in the Indian Ocean: offshore of Indonesia, and in the central western Indian Ocean. The maximum offshore of Indonesia is weaker than that for the 18-20 month signal, while the signal in the central Indian Ocean is stronger, covers a larger area, and is centred further westwards. The strong signal is also present around the Indonesian Throughflow region and in the western part of Pacific Ocean. This signal and its temporal variability also will be discussed in more detail later in this thesis.

Figure 3.3.8(e) represents the PSD for the 4-7-year signal. It has strong maxima in the western Indian Ocean, Indonesian Throughflow, and western Pacific regions. There is no obvious signal in this band along the western Indonesian coast.

3.3.4 Temporal variability of the five main spectral components of the SLA signal over the Indian Ocean

While the spatial distributions of PSD provide information on the physical structure of the corresponding modes, they contain no phase information and therefore cannot be used for studying the temporal variability of the modes. Yet, it is possible to observe the temporal behaviour of the signal in different frequency bands by conducting a Fourier transform of the signal at every grid point; filtering the signal by setting the amplitudes of the Fourier components outside the specified band to zero; conducting an inverse Fourier transform of the filtered signals; and then plotting the obtained sequence of the reconstructed modal fields one after another. The filtering conducted by means of forward and inverse Fourier transforms is essentially equivalent to the common band pass filtering methods; but, importantly, it makes possible the filtering of particular spectral components without any leakage from the components outside the filtered band. The resulting movies contain important information about the phase dynamics of the corresponding spectral components and are provided in the auxiliary material to Sakova *et al.* (2006b, movies 1-5) and in Appendix A of the current thesis.

Below we plot selected sequences of images of the reconstructed signals using the above analysis. Although a detailed analysis of the temporal variability for the 6-month and 1-year bands is outside the scope of this study, and they agree with already published results, to the best of our knowledge, this kind of analysis has not been published before.

Figure 3.3.9 depicts the temporal variability of the 6-month signal. It contains 14 maps of the signal for every second week, from Week 1 (October) to Week 27 (April), which covers one full cycle of the signal period of 6 months. In particular, one can see the westward propagation of the Rossby waves north of equator to the Somalian coast, its reflection and propagation east as equatorial Kelvin waves. This agrees with the description of the semi-annual signal by Fu (2007). Based on the analysis of the phase of the signal, Fu concludes that "the phase of the mode reveals westward propagation in the regions off the equator and eastward propagation along the equator". This can be considered as a validation of the filtering method (by the forward and inverse Fourier transforms) used in this study to restore signals in other frequency bands.

Figure 3.3.10 depicts the temporal behaviour of the 1-year signal. It contains 14 maps for every fourth week, from week 1 (July) to week 53 (August), and represents one full cycle of the signal period of one year. It clearly shows the westward Rossby waves propagating from the western coast of India and its reflection from the Somalian coast as Kelvin waves; this agrees with the existing description of the one-year signal. It also clearly shows the westward propagation of Rossby waves in the southern Indian Ocean.

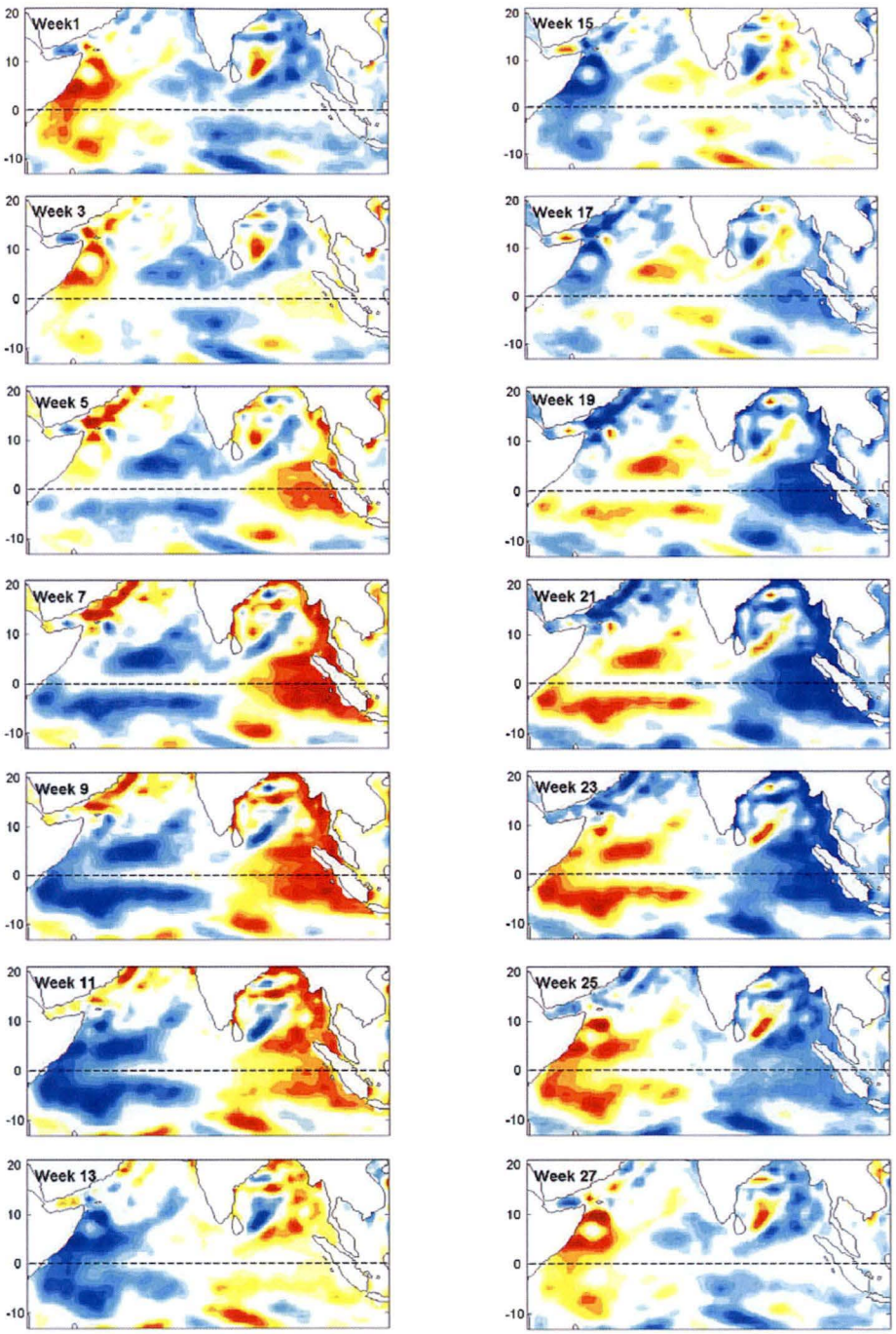

Figure 3.3.9. Sequence of maps for the filtered 6-month signal.

Note that because both the 6-month and 1-year signals contained only one filtered harmonic, their temporal behaviour can be also described by a map of the phase distribution, as has been done in Fu (2007). However, this is not the case for the signals in the other three main bands, which represent a superposition of a number of harmonics.

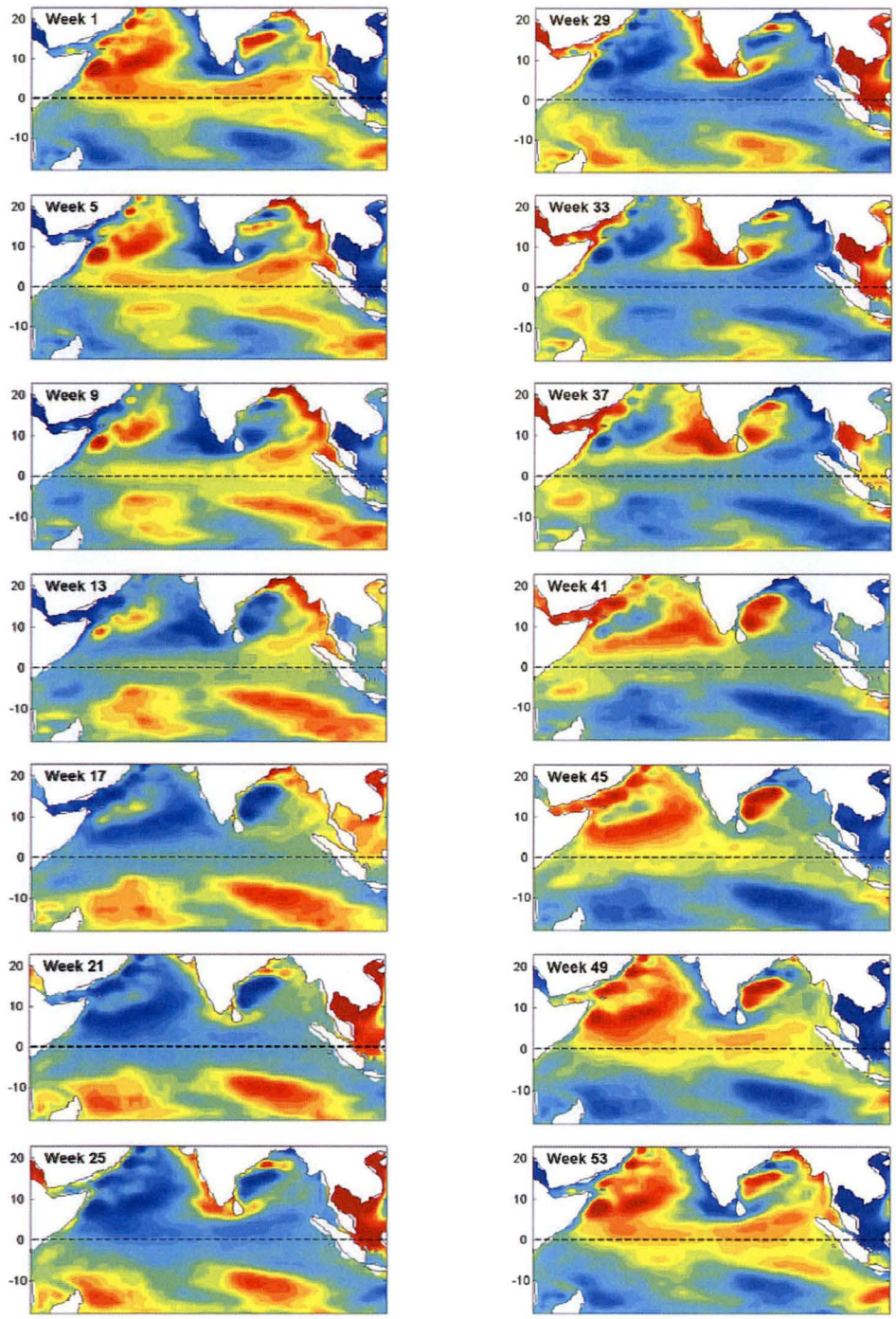

Figure 3.3.10. Sequence of maps for the filtered 1-year signal.

Figure 3.3.11 depicts temporal variability of the 4-7 year signal. It contains 12 maps separated by 6 months, from January 1997 to July 2002, and includes both the 1997 El Niño and 1998 La Niña. The signal first appears in the western Pacific. It propagates poleward in the eastern Indian Ocean along the northern and western coasts of Australia. It also starts to propagate slowly westward along about

15°S-20°S. When this signal reaches the central part of the Indian Ocean (65°E-100°E, 5°S-15°S), it is remotely amplified by atmospheric teleconnections from the Pacific. At that time the signal in the Pacific has already changed its sign (phase). The large warm pool around the north of Madagascar remains in place for two years (July 1997 to July 1999). There is also evidence of the existence of Kelvin wave propagation from west to east along the equator in the Indian Ocean that can be seen in the relevant movie (Sakova *et al.*, 2006b).

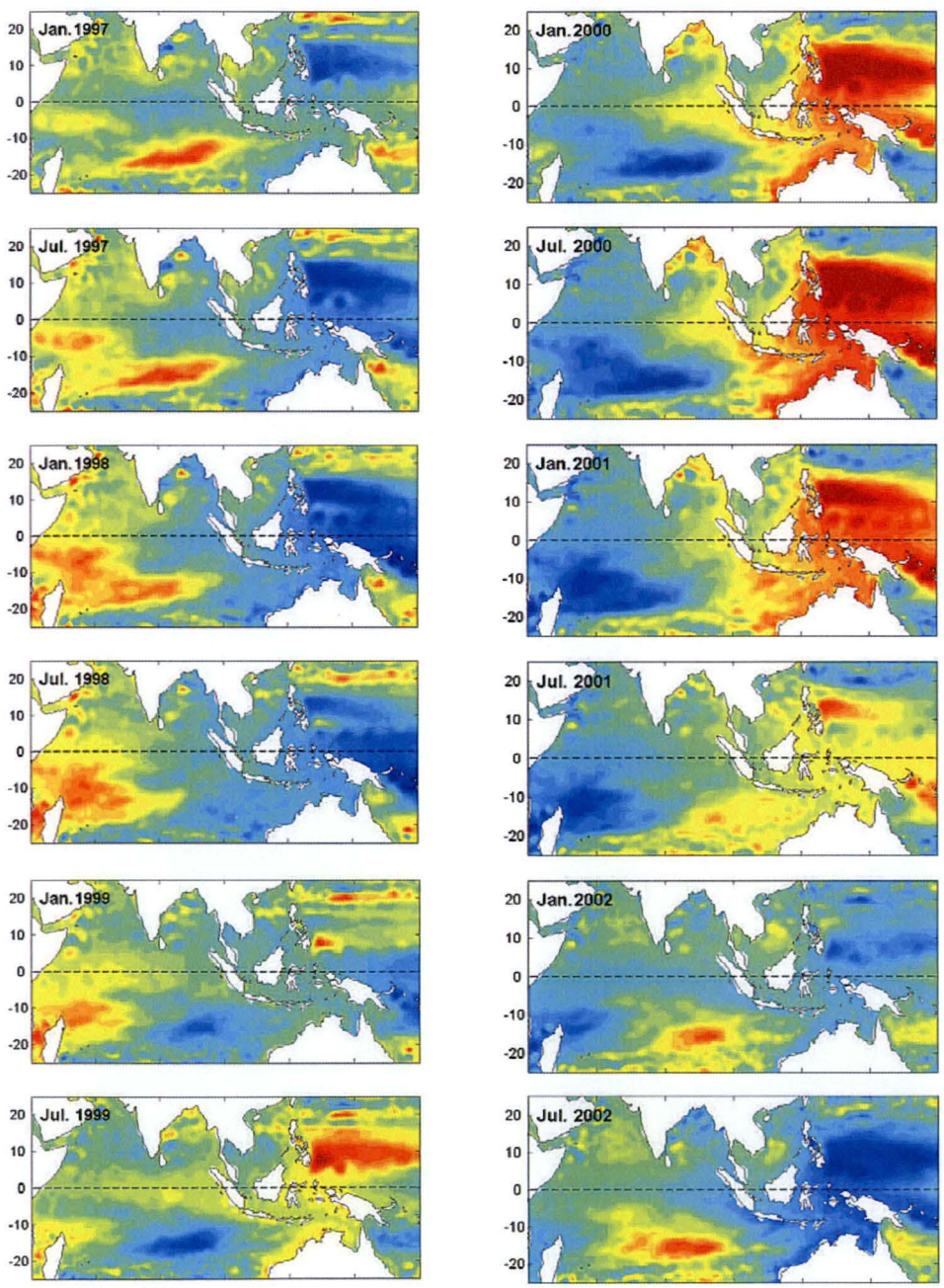

Figure 3.3.11. Sequence of maps for the filtered 4-7-year signal.

Figure 3.3.12 depicts a temporal sequence of maps for the 3-year signal. The maps are plotted every three months, from July 1994 to the end of 1997, 14 plots altogether. This time series includes positive IOD years 1994 and 1997 and negative IOD year 1995. Figure 3.3.13 depicts the sequence of maps for the 18-month signal.

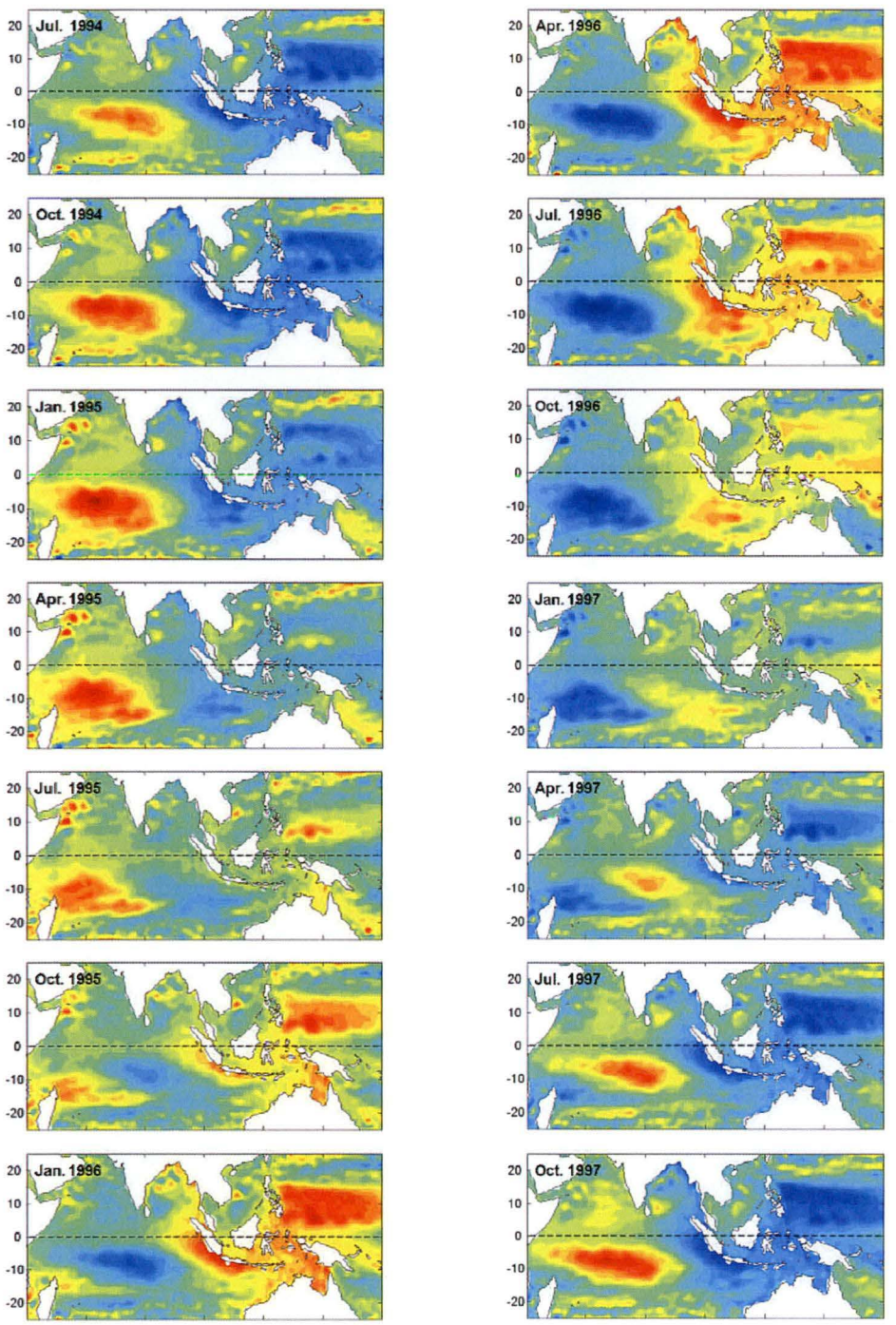

Figure 3.3.12. Sequence of maps for the filtered 3-year signal.

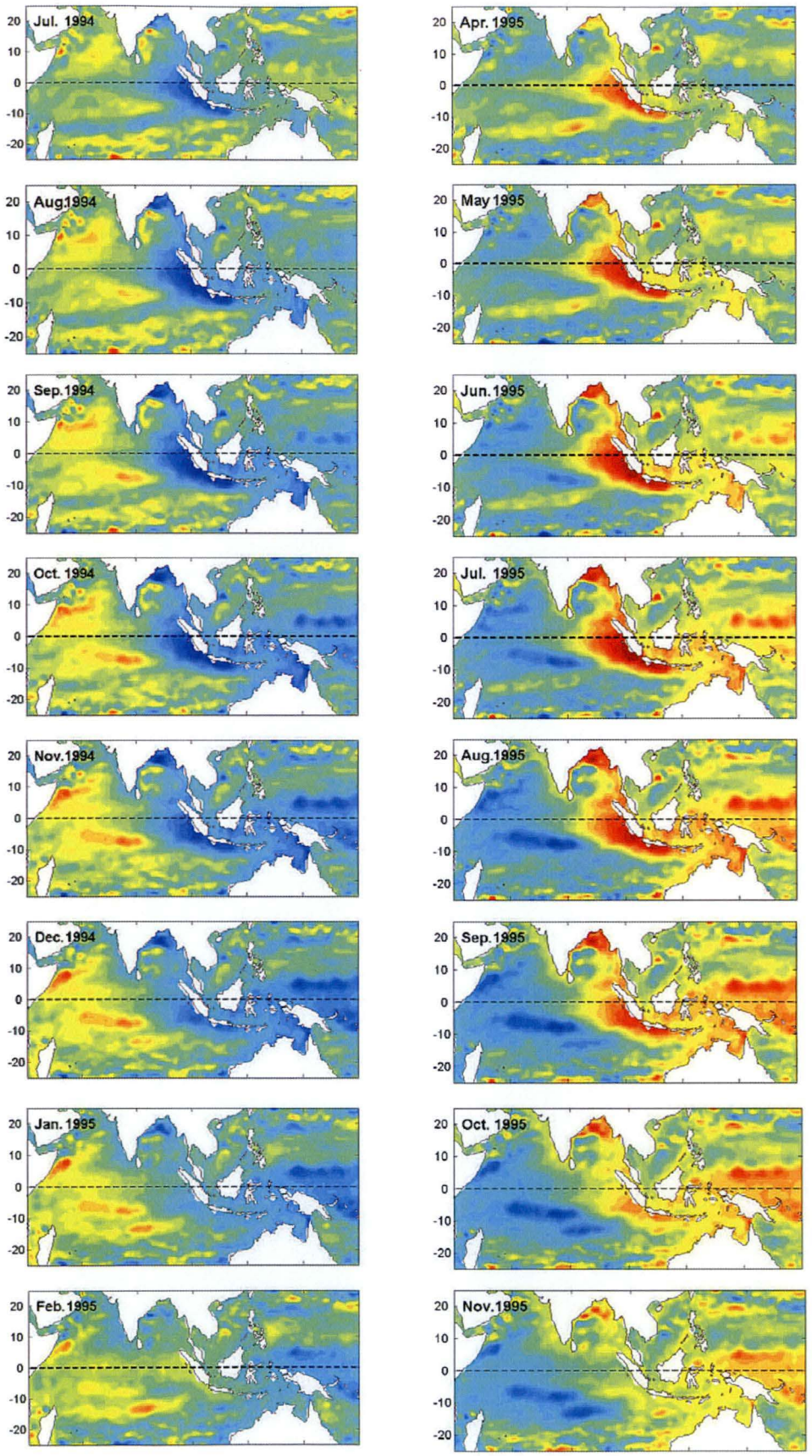
Jul. 1994
Aug.1994
Sep.1994
Oct. 1994
Nov.1994
Dec.1994
Jan. 1995
Feb.1995
Apr. 1995
May 1995
Jun.1995
Jul. 1995
Aug.1995
Sep.1995
Oct. 1995
Nov.1995
20
10
0
-10
-20

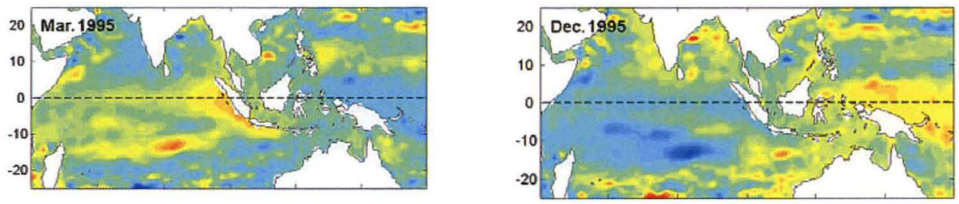

Figure 3.3.13. Sequence of maps for the filtered 18-month signal.

It is interesting to compare the spatial dynamics of the 3-year signal and 18-20-month signal (Fig. 3.3.12 and Fig. 3 3.13 respectively). The 18-20-month signal is particularly strong in the period 1993–2000. It first starts developing near the Sumatra coast and then propagates north into the Bay of Bengal and east towards the Indonesian Throughflow region; later a second maximum of an opposite sign develops over the region 96°E, 15°S to 55°E, 4°S and moves south-west as it amplifies, reaches a maximum, and then gradually subsides. The 3-year signal is also strong in the 1994–2000 period. The initial maximum, located offshore of Indonesia, develops simultaneously with a strong maximum of the same sign in the western Pacific and western part of the Bay of Bengal; later a second strong and broad maximum of opposite sign develops over the western part of the Indian Ocean.

3.3.5 EOF modes and their spectral decomposition

EOF analysis is now a common method for the analysis of the ocean variability. Here, we use EOF methods to analyse Indian Ocean SLA variability, and compare these results with those obtained with traditional signal analysis FFT/IFFT methods.

To understand interannual variability of the Indian Ocean, Rao *et al.* (2002) and Feng and Meyers (2003) conducted an EOF analysis of the altimetry SLA data. A description of their results was provided in the beginning of this chapter. Both authors come to conclusions that the first EOF mode represents an internal mode of the Indian Ocean and they suggested that the second EOF mode is associated with a quasi-biennial signal in the tropical Indian Ocean.

Here we are going to answer the question "do EOF modes represent any physical process or do they have a mix of different signals? ". Emery and Thomson (2001, p.336) wrote: 'In interpreting the meaning of EOFs, we need to keep in mind that, while EOFs offer the most efficient statistical compression of the data field, empirical modes do not necessary correspond to true dynamical modes or modes of physical behaviour. Often, a single physical process may be spread over more than one EOF. In other cases, more than one physical process may be contributing to the variance contained in a single EOF. The statistical construct derived from this procedure must be considered in light of the accepted physical mechanism rather than as physical modes themselves. It often is likely that

strong variability associated with the dominant modes is attributable to several identifiable physical mechanisms".

Below we conduct a spectral analysis of the temporal functions of both the data set used by Rao *et al.* (2002) and Feng and Meyers (2003) and for the longest altimetry data set available at the moment. To verify our methodology, we first start with the same data set as used by Rao *et al.* (2002) and Feng and Meyers (2003). Figure 3.3.14 represents results of the EOF analysis of 376 weekly entries of SLA over the Indian Ocean for the time period from October 1992 to the end of 1999; the spatial borders are set at 25°S–25°N, 30°E–120°E. Before decomposing the signal into orthogonal modes, it is low-pass filtered with the cut-off frequency at 1/14 months, so that the annual and semi-annual signals are removed.

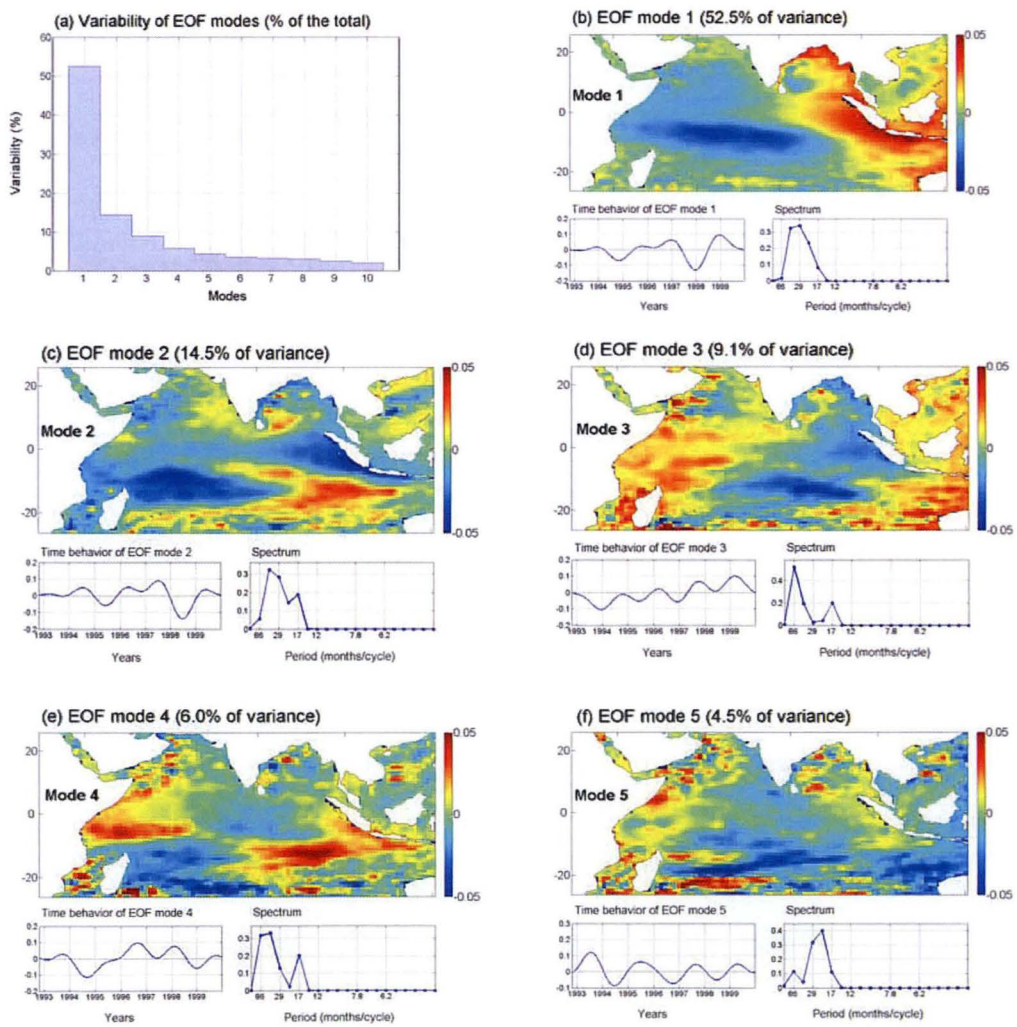

Figure 3.3.14. EOFs of low-pass filtered SLA for the period from Oct. 1992 to Dec. 1999. Panel (a) – normalized variance of EOF modes (%). Other panels: spatial patterns for the first five leading EOF modes; the corresponding temporal functions; and frequency spectra of the temporal function.

The first EOF mode, that explains about 52.5% of the variance, has a dipole pattern with positive loading in the eastern part of the Indian Ocean near the Sumatra-Java coast. The second EOF mode represents 14.5% variance and has a negative loading along the Indonesia coast. (Note that the sign of an EOF mode is not uniquely defined; it can be changed to the opposite sign by changing the sign of the temporal function for this mode). Spatial distribution as well as loading of the first two EOF modes agrees with the results of the above mentioned papers, which contain detailed analysis of these two modes; but they did not undertake the spectral analysis.

Figure 3.3.14 (b-f) represents the five first EOF modes and percentage variance for the first ten modes (Fig. 3.3.14 a). We also plot the temporal function and conduct its spectral analysis for each mode (Fig. 3.3.14 b-f). The first EOF mode has a spectrum with maxima at points 3 and 4 of the spectrum that correspond to periods of 43 and 29 months. Taking into consideration that we have quite low spectral resolution, particularly in the low-frequency part of the spectrum (with the total duration of data for only 376 weeks, or 86.5 months), we suggest that these maxima in the spectrum represent a 3-year (36 months) signal. There is also significant variability at point 5, corresponding to a period of 21 months. EOF-2 mode has the same maxima at points 3 and 4, but there is also a maximum at point 6 that corresponds to a signal with a period of 17.3 months.

The time behaviour of the two first EOF modes looks remarkably similar (Fig. 3.3.15 a), with a phase shift of about 31 weeks (Fig. 3.3.15 b). They may therefore be related to the same physical process, although the strength of these modes is very different – 52.5% and 14.5%. This is supported by the analysis of the temporal behaviour of the 3-year signal in Figure 3.3.12. For example, Figure 3.3.16 represents two snapshots of the temporal variability of the 3-year signal taken from Figure 3.3.12 for April 1996 and for April 1997. These two snapshots look very similar to the spatial distribution of EOF-1 and EOF-2 modes (Fig. 3.3.14 b,c, Fig. 3.3.1 and Fig. 3.3.2). This can be explained by the statement "often, a single physical process may be spread over more than one EOF" (Emery and Thomson, 2001, p.336). We suggest that the relationship of these two first EOF modes is worth investigating in the future.

Mode 3 (Fig. 3.3.14) represents 9% of variability. Its spectrum contains two maxima: one that corresponds to the 17-month signal, and a low-frequency maxima corresponding to the period equal to the duration of the data set, or about 7 years. From the temporal time series we can see the 18-month oscillation over the low-frequency trend. Mode 4 (EOF-4) represents 6% of variability and also has a clear 17-month signal in combination with a low-frequency signal. Mode 5 (EOF-5) represents 4.5% of variability. This mode has a clear frequency maximum around two years represented by two points in the spectrum – points 4&5 corresponding to periods of 29&22 months. This signal, possibly, can represent the 2-year cycle, as well as can also represent two different signals with periods of ~29 and ~22 months. This signal has maxima in 1993, 1995, 1997, 1999 and

minima in 1994, 1996, and 1998. It is quite weak in the region near Indonesia and central Indian Ocean, and therefore unlikely to have a strong connection with the IOD.

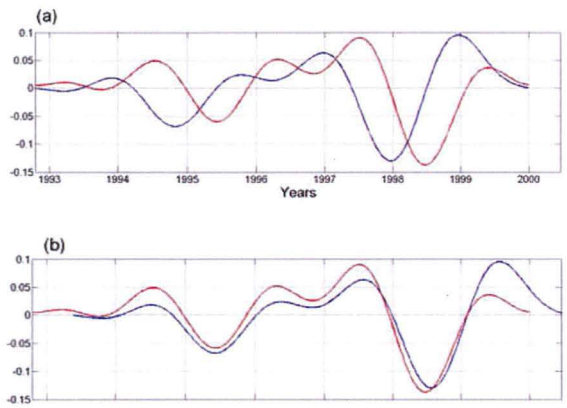

Figure 3.3.15. (a) Temporal behavior of EOF-1 (blue line) and EOF-2 (red line) from Fig. 3.3.14; (b) the same but with a time shift of 31 weeks.

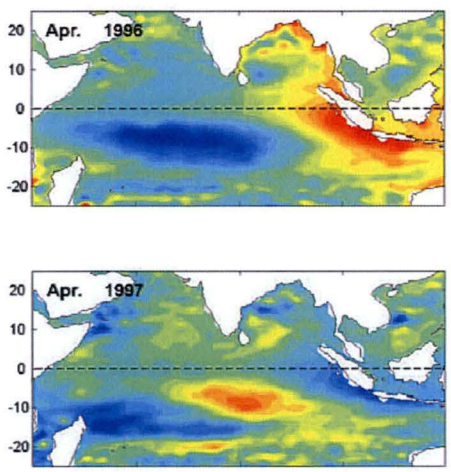

Figure 3.3.16. Two snapshots of the filtered 3-year SLA signal separated by 1 year.

Now let us extend the above EOF analysis and include the annual and semi-annual signals. In this new analysis, any SLA variability with periods of 5 months and shorter is removed. Figure 3.3.17 represents the first seven EOF modes and percentage variance for the first ten modes (Fig. 3.3.17 a). It also contains the time series and spectra for each mode.

It is clear that the EOF-1 and EOF-3 now represent the one-year signal. This can be interpreted as two different modes of the one-year signal, although these modes have quite different variances 26.2% and 15.9%. They also have different spatial patterns, but this can be expected for different modes of a physical process. For example, the signal in the Bay of Bengal comes in phase with a signal in the southern Indian Ocean for EOF-3, but in opposite phase for EOF-1. The spreading of

the one-year signal over two EOF modes supports the statement that "a single physical process may be spread over more than one EOF" (Emery and Thomson, 2001, p.336).

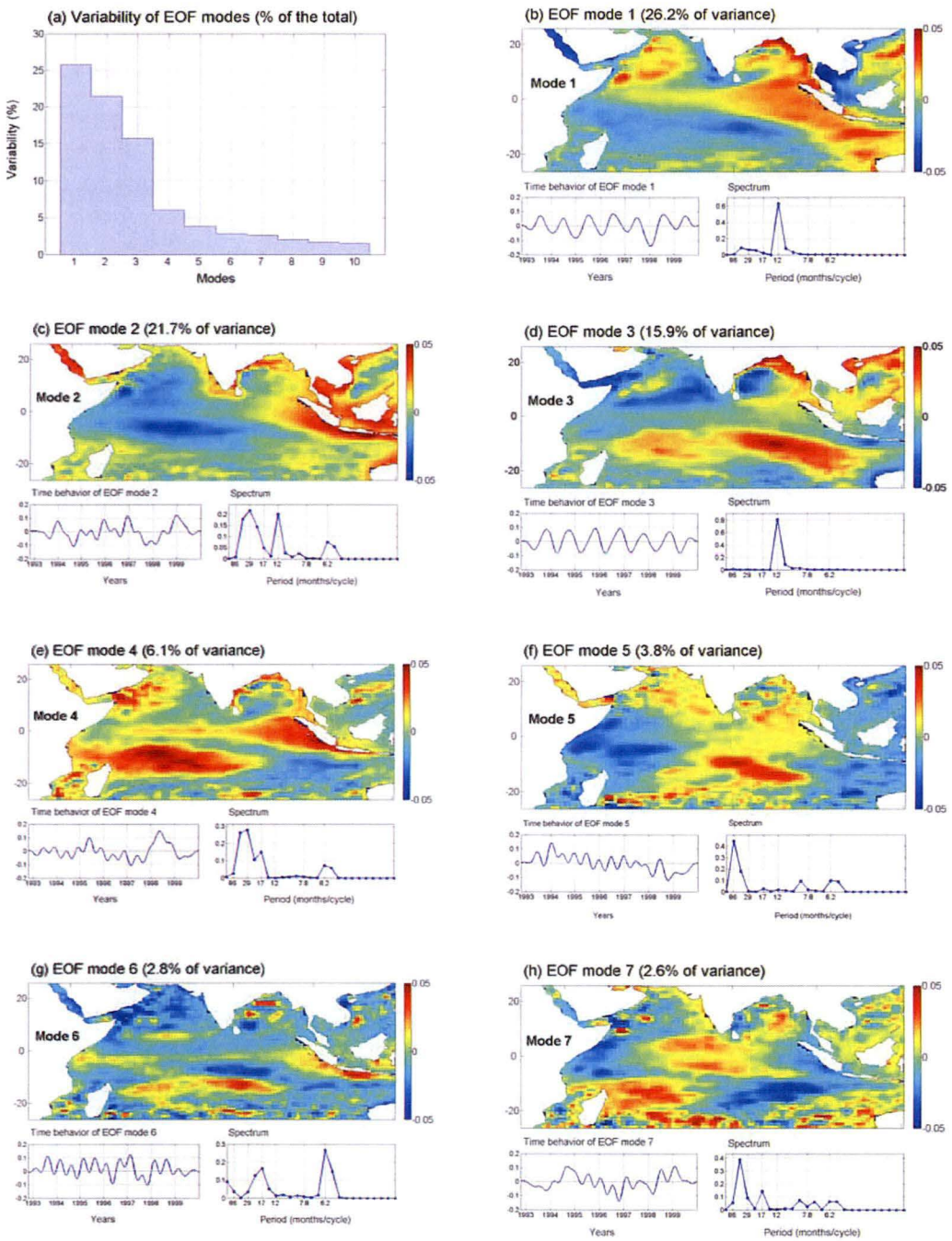

Figure 3.3.17. Same as Figure 3.3.14, but with the annual and semi-annual signals not filtered out

The two EOF modes that represent the one-year signal, along with EOF-2 (21.7%) accumulate most of the variance, while all other modes combined have about half of the variance of these three modes. This agrees with EOF analysis of the filtered data, where most of the variance is carried by a single EOF mode (Fig. 3.3.14).

The spatial distributions and spectra of EOF-2 and EOF-4 for the unfiltered signal are very close to EOF-1 and EOF-2 for the low-pass filtered signal. However, EOF-2 for the unfiltered signal, in addition to the 3-year signal, also has a very strong one-year component. This one-year signal is merged with the 3-year signal, and once again we can see that "more than one physical process may be contributing to the variance contained in a single EOF" as well as that "a single physical process may be spread over more than one EOF" mode (Emery and Thomson, 2001). EOF modes 4, 6 and 7 have a prominent 17-month signal in their frequency spectra. Interestingly, the EOF-6 has two merged signals, the 17- and 6-months. The signal has minima at the end of 1994, beginning 1996 and end of 1997 that are correlated with positive IOD events. Moreover, this mode has a zonal spatial pattern that can be interpreted as corresponding to the zonal wave .propagation. This insight possibly can help to understand the physics of the 18-month signal later in the thesis.

Because of our interest in the interannual variability of the Indian Ocean and its connection with IOD, we now exclude the regions belonging to the Southern Indian Ocean, Pacific and Red Sea (20.3°S – 20.8°N, 40°E – 110°E). We also expand the time period to April 2007. The first three of the corresponding EOF modes are shown in Figure 3.3.18. EOF-1 represents 42.2% of variability, EOF-2 – 17.9%, and EOF-3 – 14.1%. Interestingly, EOF-1 and EOF-3 have very similar spectra – several peaks in the low-frequency part of spectrum and a second peak with the period of about 17-21 months, separated with spectral gaps around 2 years. The EOF-2 represents a low-frequency trend that is more noticeable in the southern part of the Indian Ocean.

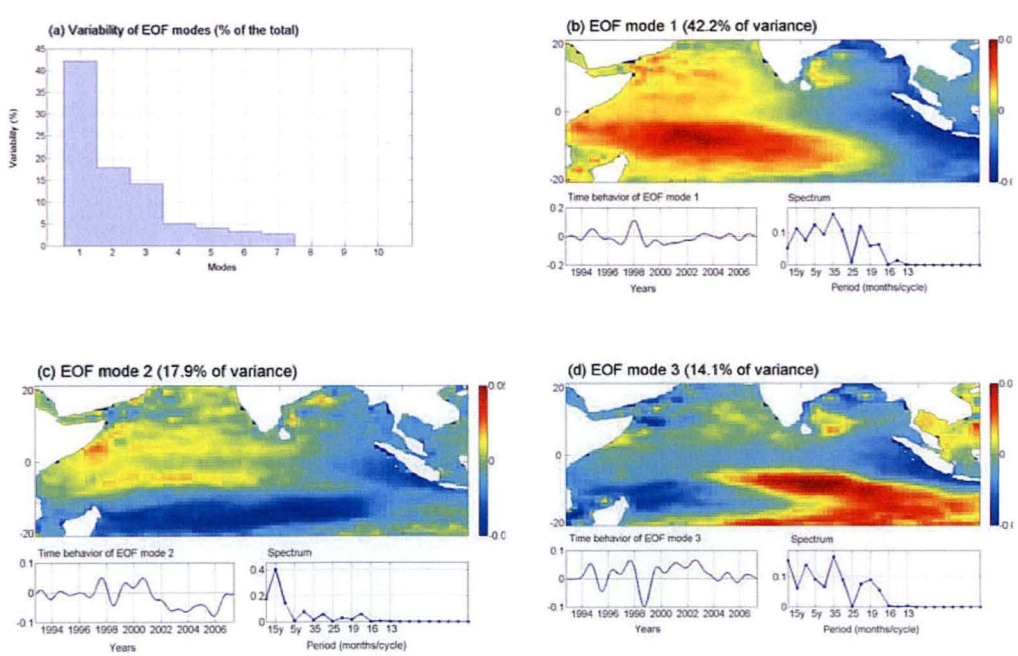

Figure 3.3.18. The same as Figure 3.3.14, but for a longer time period (October 1992 – April 2007), and for the tropical Indian Ocean only (20.3°S – 20.8°N, 40°E – 110°E).

3.3.6 Conclusions

In this section we have analysed the altimetry SLA data using spectral analysis and EOF analysis. Specifically, we conducted Fourier transforms of the altimetry SLA anomaly; computed distribution patterns of the SLA variability over the Indian Ocean at different frequencies; identified principal quasi-periodical components of the signal; conducted inverse Fourier transforms of the filtered signals in each of the principal frequency bands to investigate their temporal behaviour that have been visualized by means of movies (see Sakova *et al.*, 2006b) and maps; performed EOF analysis of the signal and applied frequency analysis to the temporal time series of the leading EOF modes to determine their spectral components.

We have identified five well separated spectral bands carrying most of the low-frequency SLA variability in the Indian Ocean: semi-annual, annual, 18-20-month, 3-year, and 4-7-years. This classification is based mostly on the altimetry data collected during October 1992 to September 2008. These years are characterised by very strong IOD events in 1994/1995 and 1997/1998. The analysis of other time periods can produce different periodicity, magnitude and/or spatial distribution of the dominant modes.

The discovery and confirmation of a strong 18-20-month signal is the key new result of this study. The signal clearly exists in the Indian Ocean. Interestingly, despite the previous research investigating the quasi bi-annual (QB) mode, no major signal with the 24-month period was found. This leaves two possibilities: either the QB mode described in the previous studies consists of two distinct 18-20-month and 3-year signals; or it in fact corresponds to the 3-year signal, while the 18-20 month signal represents a separate process. A detailed analysis of the 18-20-month signal will be carried out in Chapter 4. In that Chapter we will also analyse the 3-year signal and the possible relationship between these two low-frequency signals.

Our analysis of the 6-month and 1-year signals agrees with the independent analysis of others researchers; however, we have extended these analyses by calculating and presenting temporal variability of these signals over the Indian Ocean (Fig. 3.3.9 and Fig. 3.3.10, see also movies 1 and 2 in Sakova *et al.*, 2006b, and Movies movie_SLA_6m.avi and movie_SLA_1y.avi from Appendix). These new results clearly show the Rossby and Kelvin wave propagation around the Indian Ocean basin.

The 4-7-year signal possibly corresponds to the signal identified in the literature as the ENSO signal. The Pacific origin of this mode can be verified by investigation of its temporal dynamics (Fig. 3.3.11, see also Movie 5 in Sakova *et al.*, 2006b and Movie movie_SLA_5y.avi from Appendix). However, a note of caution with this 4-6-year signal is that, because of the limited time span of the data used in this study, the analysis of this extremely low-frequency signal is not as reliable as that

for the higher-frequency bands. To reach more definite conclusions on the spatial and temporal properties of this signal, one needs to extend the time span of the currently available SLA data or use ocean climate model output data.

In conclusion, the same type of analysis can be conducted on any distributed (gridded) data series over the Indian Ocean, such as SST, wind, atmospheric pressure, reconstructed sea level etc., but within the scope of this thesis, we conduct only some limited analysis of wind and SST data in the next part of this Chapter.

3.4 Analysis of wind data

3.4.1 Introduction

Coupled ocean-atmosphere dynamics is important not only for annual and semi-annual variability of the Indian Ocean, but also plays an important role in the interannual variability (Huang and Kinter, 2002). The wind-field over the Indian Ocean has a different pattern compared to other oceans. "An important difference from the other tropical oceans is the absence of sustained easterly winds along the equator. Instead, the near-equatorial winds have an easterly component only during the late winter/early spring, a semi-annual westerly component during both inter-monsoons, and weak westerly annual mean" (Schott *et al.*, 2009). As a result, the thermocline is flat, and there is little or no mean upwelling along the eastern boundary (Schott *et al.*, 2009). During IOD events, strong south-easterly wind arises. These wind anomalies along the Sumatra-Java coast provoke an intensive upwelling, decrease SST, and support Bjerknes feedback, a key process in dynamics of IOD (Schott *et al.*, 2009). Therefore, we can expect to find the interannual signals presented in the altimetry SLA data and in other data sets, such as SST and wind, at least in the Sumatra-Java upwelling region.

In the previous parts of Chapter 3, an analysis of low-frequency variability over the whole Indian Ocean has been conducted using altimetry SLA and XBT profile temperature data sets. Below we analyse monthly wind from the National Centers for Environmental Prediction - NCEP/DOE AMIP-II Reanalysis 2 for both u (zonal, west-east) and v (meridional, north-south) components. After that we analyse NOAA Optimum interpolation (Reynolds) SST and Kaplan SST anomalies data. Although there has been a considerable discussion of the air-sea interaction on the interannual time scale, especially associated with IOD events (Schott and McCreary, 2001, Schott *et al.*, 2009), we know of no published work containing systematic spectral analysis of the variability of these fields. To produce results comparable with our previous analysis of SLA, we will use data for the period from January 1990 to July 2002.

3.4.2 Power spectral density maps

Figure 3.4.1 presents the PSD maps for u- and v-components of the NCEP/DOE AMIP-II Reanalysis 2 wind fields. Along with very strong 6-month and 1-year signals, there also are strong signals with periods of 33.5 months (~ 3 years) and 18.6 months, in both meridional and zonal components of the wind. No significant signal with periods of 2 years is found, similar to the altimetry SLA and subsurface temperature fields. Below we will briefly discuss all major spectral components.

3.4.3 One year signal

Figure 3.4.1 documents the contribution of each spectral component into the variability of the u- and v-winds over the Indian Ocean. Because the amplitudes of one-year and 6-month signals are much higher than those of other spectral components, it is not easy to make meaningful conclusions for these two signals from this figure. We therefore plot the PSD maps for the one-year and 6-month signals separately in Figure 3.4.2 and Figure 3.4.3. As could be expected for the one-year signal, the monsoon circulation dominates the annual cycle in the Indian Ocean. The v-winds are strong along the Somalian coast and in the Bay of Bengal, while the u-component of the wind is stronger in the northern part of the Indian Ocean between 5°N to 20°N in the Arabian Sea and Bay of Bengal. In the southern Indian Ocean much weaker zonal components are located along 5°S-10°S in the trade winds and along 35°S-40°S in the westerlies.

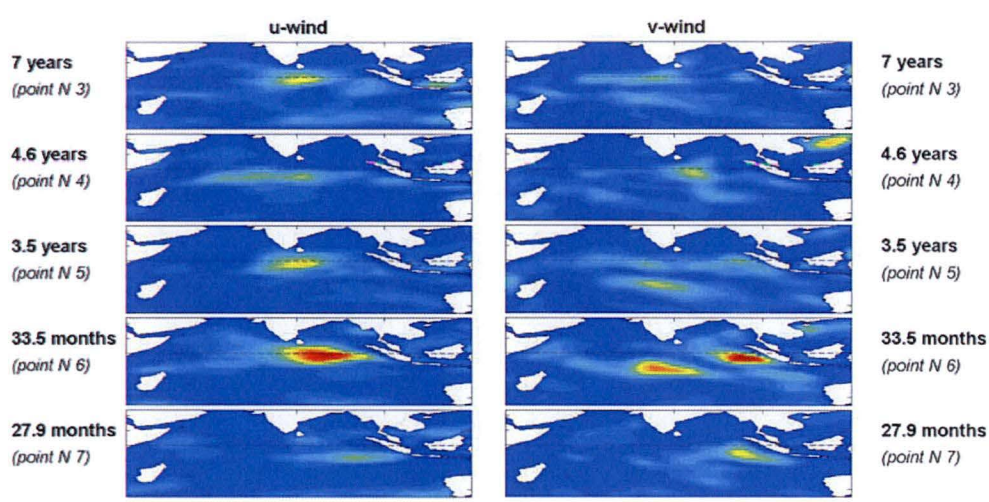

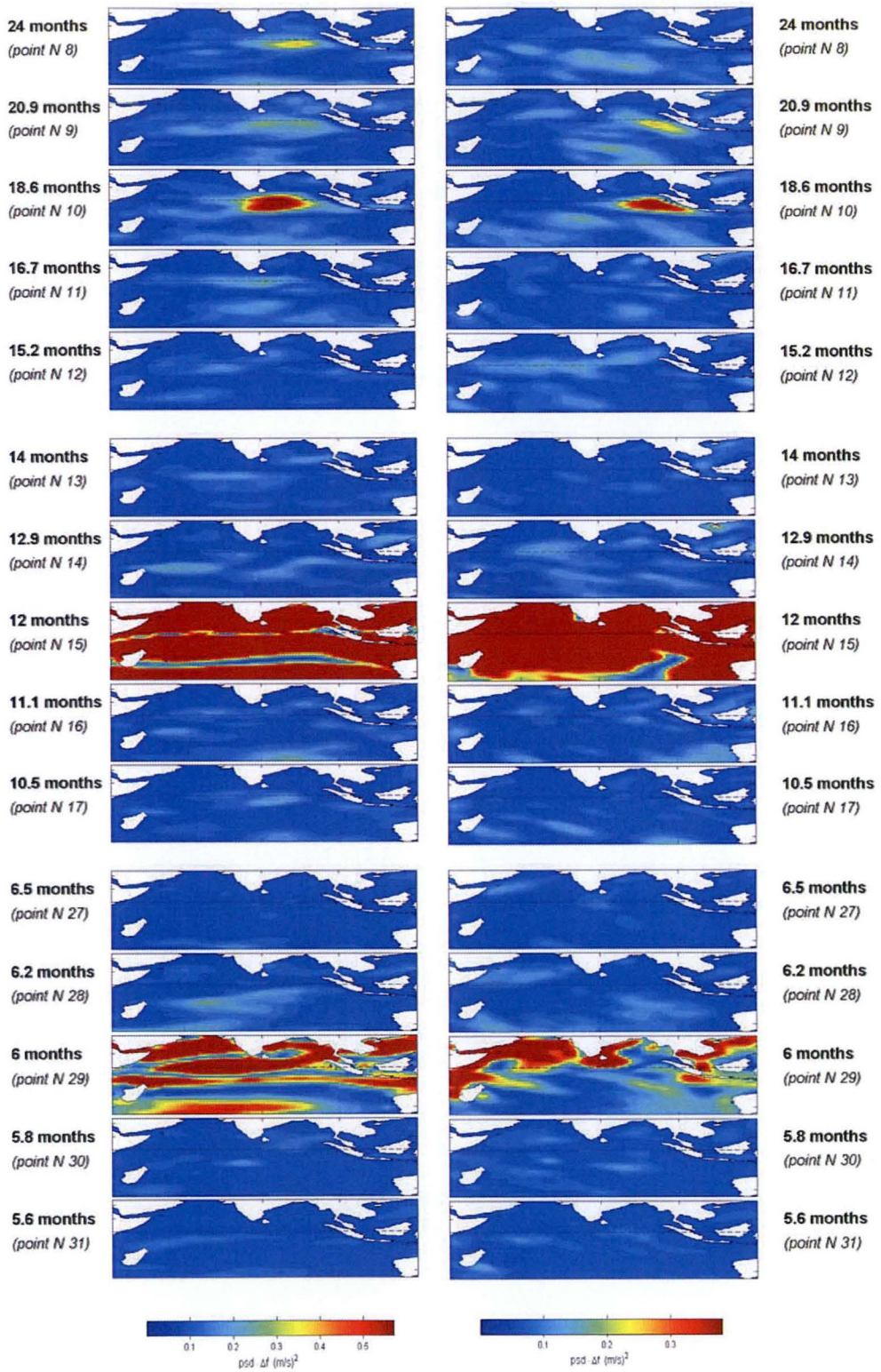

Figure 3.4.1. Maps of the PSD of u- and v-wind components at each frequency for the period from January 1990 to July 2002.

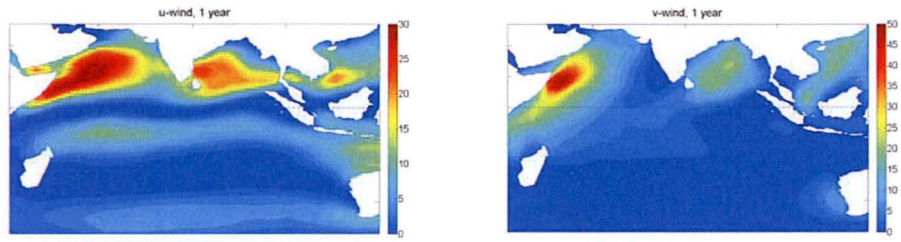

Figure 3.4.2. Maps of the PSD of u- and v-wind components for the one-year signal ((m/s)^2).

3.4.4 Six month signal

It is well known that the westerly winds in the equatorial Indian Ocean occur two times a year during the transition periods between the summer and winter monsoons. A very strong u-wind along equator between 55°E to 85°E is depicted in Figure 3.4.3. "A unique wind forcing pattern occurs over the Indian Ocean....It involves the occurrence of semi-annual eastwards winds over the equator, during April to June and October to November" (Schott and McCreary, 2001). This feature is extensively studied and described in the literature. In this region the wind with a 6-month period is easy to study because it is straightforward to separate from winds with other time scales; there is no other signal with comparable amplitude (see Fig. 3.4.1, Fig. 3.4.2). Interestingly, the 6-month wind is also very strong in the Arabian Sea (u-wind) and along the Somalian coast (v-wind). These features have not attracted attention in literature. This can possibly be explained by a relative weakness of the 6-month signal in these locations compared to the one-year signal (which has about 3-5 times bigger amplitude). As a result, the one-year signal masks the 6-month signal, and spectral analysis is required to separate and analyse the much weaker 6-month component.

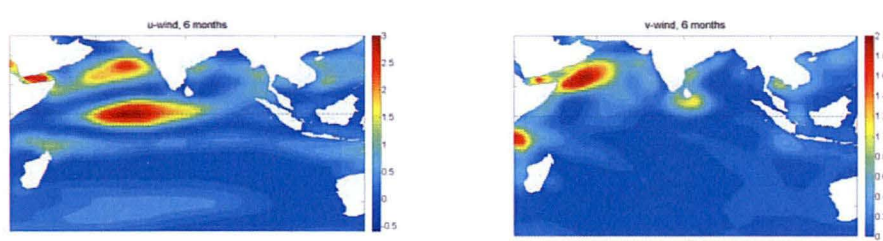

Figure 3.4.3. Maps of the PSD of u- and v-wind components for the 6-month signal ((m/s)^2).

3.4.5 3-year and 18-month signals

The spatial distribution of the u-wind component for the 3-year and 18-month signals is very similar, as can be seen from Figure 3.4.1. The 18-month signal seems to be stronger than the 3-year signal, at least during 1990-2002. The maxima of the u-wind component of these signals are located close to

the centre of the Indian Ocean, approximately between 75°E and 95°E, and are shifted a little south from the equator.

The spatial distributions of variability of the 18-month and 3-year signals for the v-wind are quite different. The 18-months signal is strong and concentrated along the coast of Sumatra Island, while the 3-year signal has lower intensity and is concentrated in two locations, one along Sumatra, similar to the for 18-month signal, and another at 3°S-15°S and 70°E-90°E. The different spatial distribution of the 18-month and 3-year signals for v-wind results from their different behaviour, which can be seen from the Movies movie_SLA_Wind_18m.avi and movie_SLA_Wind_3y.avi from Appendix. In Figure 3.4.4, we plot four snapshots from these movies, two for each of these bands, separated by a half period. We selected times that correspond to negative (July 1997 for the 3-year signal and August 1997 for the 18-month signal) and positive (February 1996 for the 3-year signal and December 1996 for the 18-month signal) SLA along the Sumatra-Java coast. It can be seen from that the 18-month wind vectors are directed along the equator from negative to positive SLA anomalies; but the 3-year wind vectors form a curly shape with its centre at about 10°S and 90°E. This curl produces two spots in the v-wind component in maps of spectral density (Fig. 3.4.1).

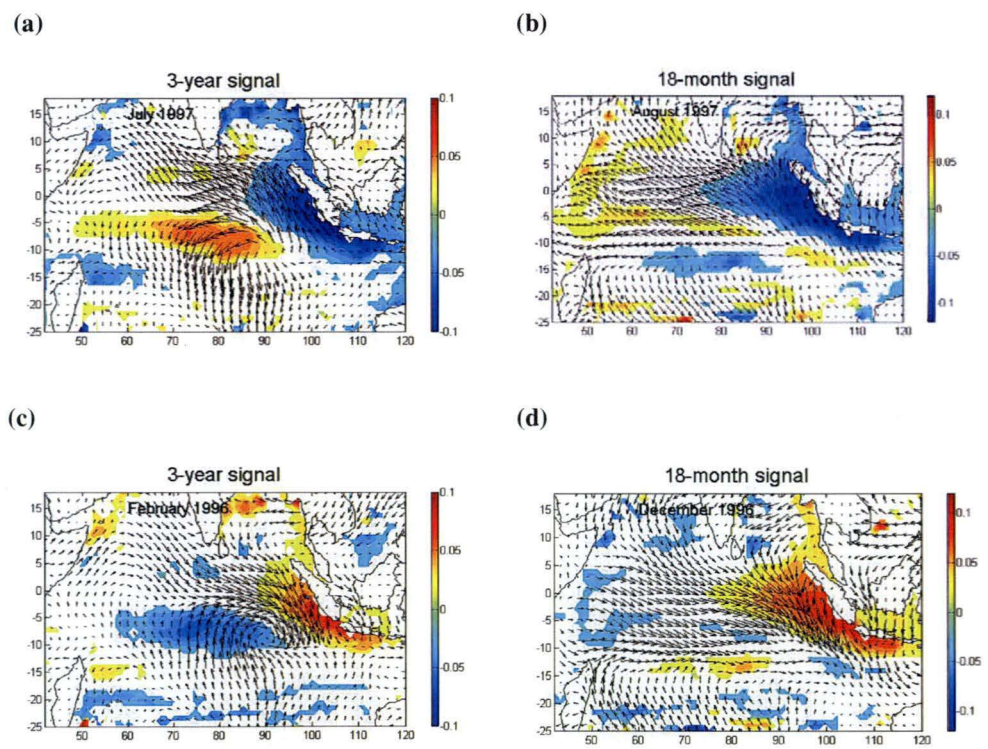

Figure 3.4.4. SLA map and wind vectors over the Indian Ocean for two spectral bands: 3-year (a, c) and 18-month (b, d). Snapshot from Movies: movie_SLA_Wind_18m and movie_SLA_Wind_3y.

Analysis of a longer time series shows that the wind periodicity changes over time. Figure 3.4.5 presents a wavelet analysis of u- and v-wind for the time interval from January 1979 to December

2006 (336 months) for locations close to the maxima of these signals – (–2.9°S, 86°E) for u-wind and (–4.7°S, 97.5°E) for v-wind. It can be seen that the 18-month and 3-year signals exist approximately from 1991 to 2000. Interestingly, these plots also indicate that before 1991 and after 2000 the signal with 3-year period has slightly longer period at about 4 years. It is impossible to make far reaching conclusions at this stage but this can indicate a shift of the regime of the Indian Ocean similar to that of the ENSO periodicity in the Pacific; or it can be just a natural fluctuation of the Indian Ocean wind variability.

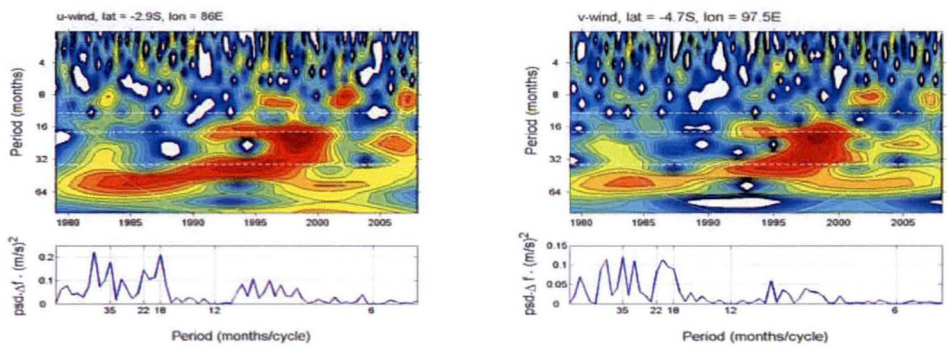

Figure 3.4.5. Wavelet analysis of u-wind (at 2.9°S 86°E) and v-wind (at 4.7°S 97.5°E) for the time interval from January 1979 to December 2006.

Figure 3.4.6 shows the maps of PSD of wind components for this longer 336 month time interval. As expected, along with the signals of about 3 years, there also exists quite clear signals with periods of about 48 months (4 years), that was presented in wavelet transform analysis (Fig. 3.4.5) during 1979-1989 and after 2000. The spatial distribution of the 4-year signal for the wind is very similar to that of the 3-year signal. The relationship of the 3-year and 18-month signals will be addressed in Chapter 4 but we can note here that if the18-month signal represents a second harmonic of the 3-year signal, no such "second harmonic" exists for the 4-year signal (Fig. 3.4.5).

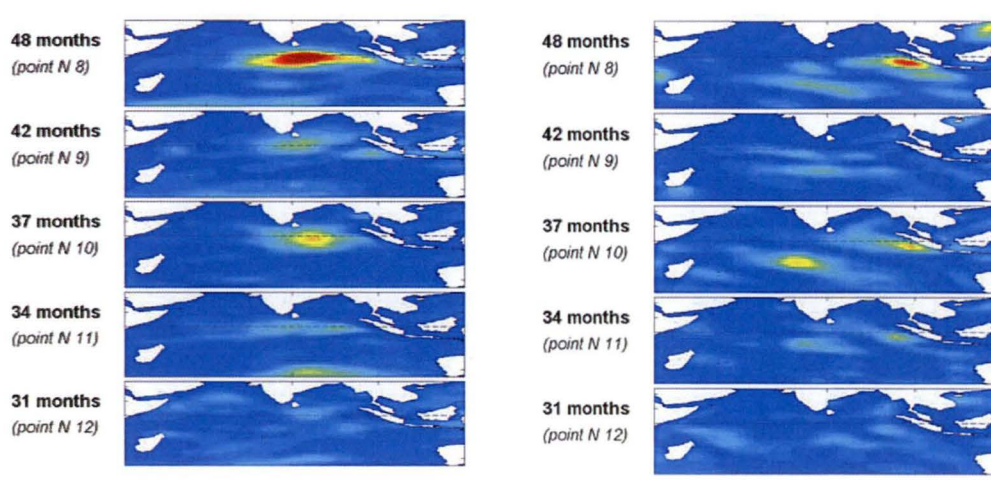

Figure 3.4.6. Maps of the PSD of u- and v-wind for the spectral components with periods from 31 to 48 months, for the time interval from 1979 to 2006.

3.5 Analysis of SST data

While SLA represents the accumulated variability of the subsurface state of the ocean, SST is the best indicator of ocean-atmosphere interaction in interannual climate variability, and in IOD events in particular. SST couples the wind field to the subsurface state of the ocean by controlling two-way feedback between ocean and atmosphere. In this section we will analyse the interannual variability of SST in the Indian Ocean.

During 1990 – 2000, the period that attracts the main attention in this thesis, two strong positive IOD events occurred in the Indian Ocean in 1994 and 1997, and a weaker event in 1991. The movement of the thermocline in the Java upwelling region (Fig. 3.2.4) clearly shows that the sea surface cooling has occurred near the Sumatra-Java coast because of the lift of the subsurface cold water up to the surface in the second part of 1991, 1994, and 1997.

These anomaly events happened 3 years apart, and therefore one can expect to find a strong interannual signal in SST with a period of about 3-years, particularly in the above mentioned regions. To analyze the low-frequency variability of SST in the Indian Ocean, we first conducted the spectral analysis and calculated the spectral density maps for each frequency in the spectra using reconstructed NOAA SST temperature data. Although this data set is available for a long interval of time (see Sec. 2.1 for details), in this section we use SST for the time interval from October 1992 to July 2003 (728 weekly data altogether), to match the time interval of the analysed altimetry SLA data and make results comparable. The analysis of the reconstructed SST for a longer period will be conducted in Chapter 6 "Periods of IOD activity and historical data analysis".

The plots below (Fig. 3.5.1) are obtained following the same procedure as for the altimetry SLA in Section 3.3 and wind in Section 3.4 -- by calculating the power spectrum for each grid cell of the gridded NOAA SST data over the Indian Ocean and plotting the resulting maps.

The plotted maps contain signals with periods from 7 years to 5.6 months, corresponding to the components from 3 to 31 in the frequency spectra. The maps for components 18-26 are not shown because no significant signal is found at these time scales.

From these plots one can see a very strong semi-annual signal (component 29, 6 months) in the Arabian Sea and Bay of Bengal, and a very strong annual signal (component 15, 12 months) in the southern part of the Indian Ocean.

As expected, there is also a very strong 3-year signal (component 6, 33.5 months) near the Sumatra-Java coast. We suggest that this signal represents the strong SST variability during 1991, 1994, and 1997 IOD events, each 3 years apart. There is also a strong variability in the Southern Indian Ocean

between -35°S to -15°S and 5°E to 100°E with period a little longer than 3 years (component 5, 3.5 years). A noticeable variability with a longer timescale of about 7 years (point 3) is also present in the middle of the Indian Ocean south of the equator. Concerning the 18-month signal, there exists a very strong signal with the period of 18.6 months near the Sumatra-Java coast (component 10, 18.6 months), and also a strong SST variability in the Southern Indian Ocean between -35°S to -15°S and 75°E to 100°E with a period of 20.9 months (component 9, 20.9 months).

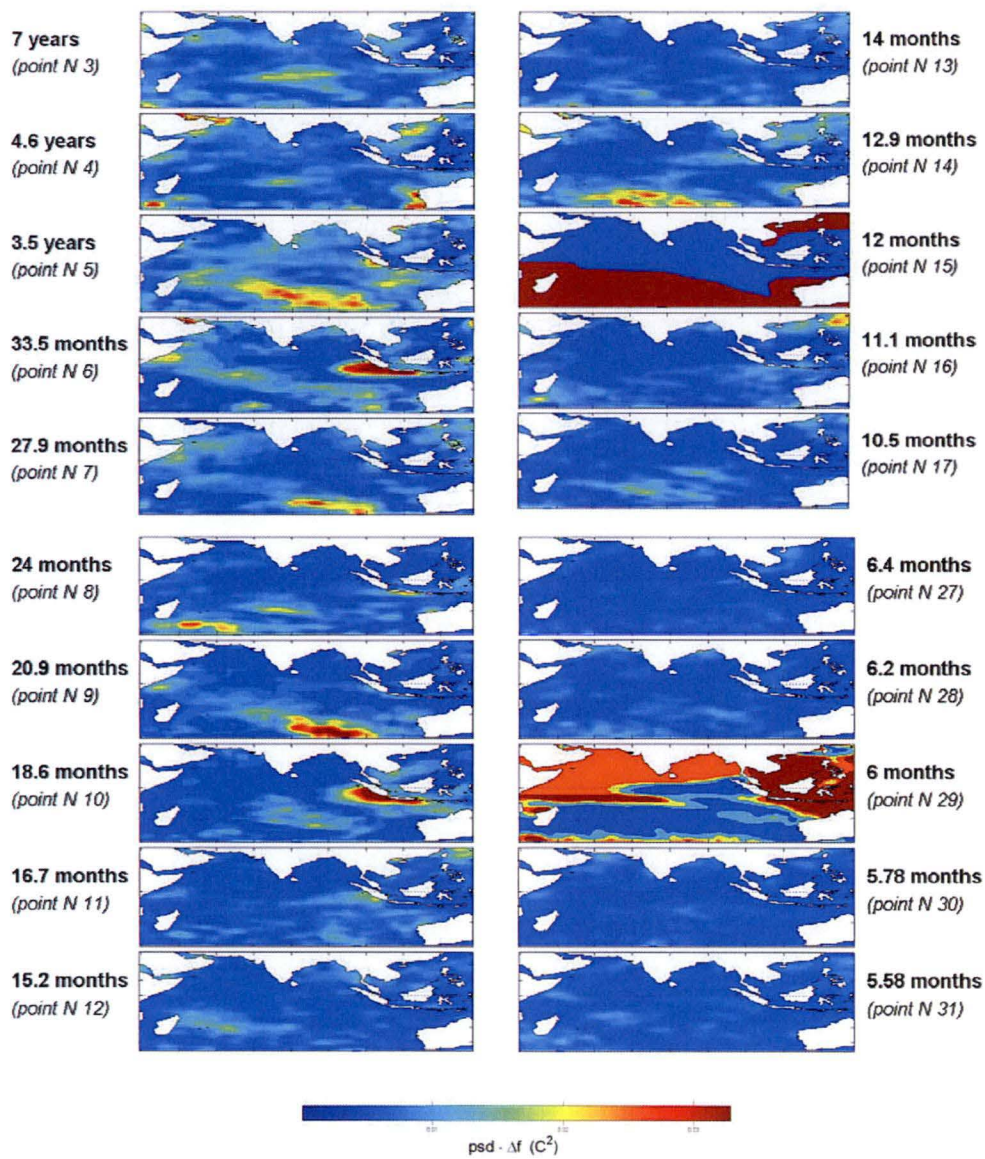

Figure 3.5.1. Maps of the PSD of SST for each frequency component.

There are a number of new features in the Figure 3.5.1 compared for the plots of the PSD for SLA presented in Figure 3.3.7. Firstly, the patterns for the 18.6-month (point 10) signal and 33.5-month

(point 6) signal have a more similar shape than for SLA. Secondly, the patterns for the neighbour components 9 with period of ~21 months and 5 with period 3.5 year are very different.

Note that because of the limited time interval of the data, the temporal resolution in the low-frequency part of the spectra is quite low. For example, the 5th and 6th components correspond to signals with periods of 33.5 months and 3.5 years have very different spatial patterns. Ideally, it is desirable to have several spectral components for each such signal, or to have at least one spectral component between them.

Figure 3.5.2 shows the PSD for 18.6-months and 33.5-months signals in the Java upwelling region, which is the region that contains most of the overall variance for these fields over the Indian Ocean.

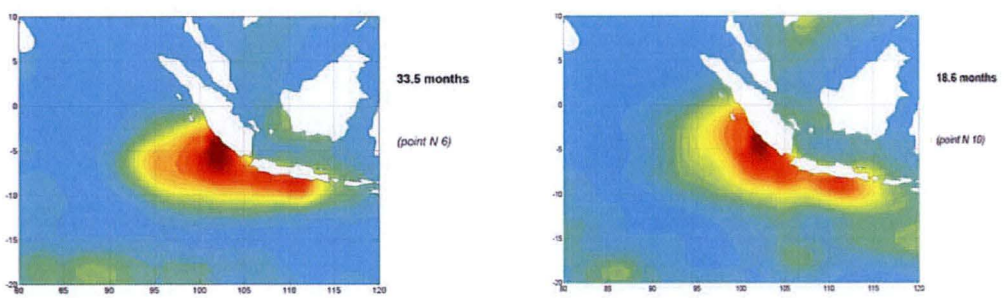

Figure 3.5.2. PSD of SST for 33.5-month (left panel) and 18.6-month (right panel) signals.

One can observe some difference between the patterns of PSD for these two signals. The distribution of the 18-month signal is shaped more along the Java coast, concentrating in the upwelling region and extends to the Indian Ocean equator, while that of the 33.5-months signal is more elongated in the direction off shore and does not extend to the equator. That is possible due to different wind forcing (see Fig.3.4.4).

We now analyse the time series of SST at one point in the Java upwelling region, at (-5.5°S, 102.5°E) to analyse the details of superposition of the 18-month and 3-year signals in the context of the IOD events.

Figure 3.5.3 shows the SST signal at (-5.5°S, 102.5°E). The upper panel contains the signal time series, where the blue line represents the unfiltered signal, and black line – the low-pass filtered signal with cut-off frequency at 14 months. The lower panel contains the power spectrum of this signal (unfiltered SST in Java region). One can easily identify from the unfiltered signal (blue line, upper panel) the drop of SST in falls of 1991, 1994, and 1997 that are associated with IOD events (indicated by the black arrows). But between these three events one can find a noticeable drop in SST (indicated by the red arrow). This signal has a period of 18 months and can be interpreted as the

second harmonic of the main 3-year signal that is necessary to represent a non-harmonic process with a 3-year period (Fig. 3.5.3, lower panel).

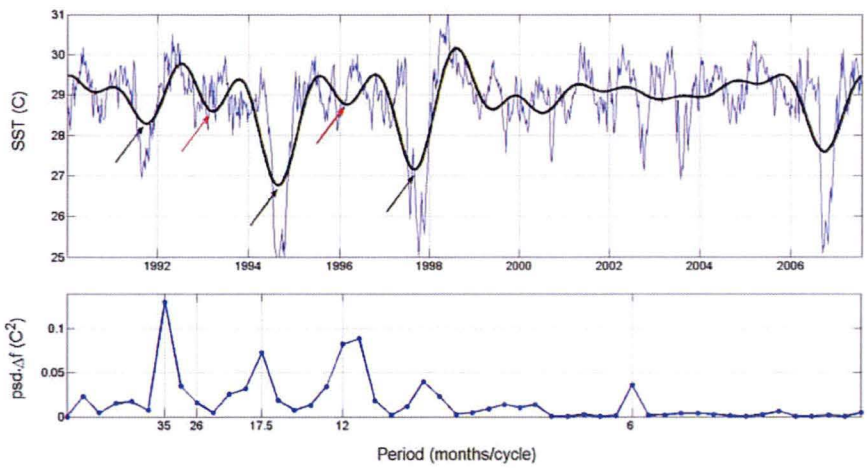

Figure 3.5.3. SST (reconstructed NOAA) in Java upwelling region (-5.5°S, 102.5°E). The upper panel – the unfiltered signal (blue line) and low-pass filtered signal (black line) with cut-off at 14 months. The lower panel – PSD of the unfiltered SST.

We will now compare these data with another available SST data set – SST anomaly by Kaplan (Kaplan *et al.,* 1998). Figure 3.5.4 shows the SST anomaly from this data set at (-7°S, 107°E). (This data set contains monthly mean data). Panel (a) represents the unfiltered signal. Panel (b) and (c) represent the low-pass filtered signal using two different methods: (b) low-passed signal (black) using FFT method with the cut-off set up at 14 months; (c) running average over 5 months (red). Both these panels show a drop of SST not only in 1991, 1994, and 1997 as in the reconstructed NOAA SST (Fig.3.5.3), but also between these years in 1992 and 1996. Panel (d) shows that the interval between maxima and minima of these "oscillations" during 1992-2000 are separated by time intervals of 16-21 months, which is reflected in spectral decomposition of this signal (panel e) and its wavelet decomposition (panel f).

The above analysis of SST data sets shows that apart from the low-frequency 3-year oscillation, there is also a visible modulation with the 18-month period; however, while the Kaplan SST anomaly data set clearly contains variability with period of 18 months during 1992-1999 years, the Reynolds reanalysis does not contain this signal as clearly.

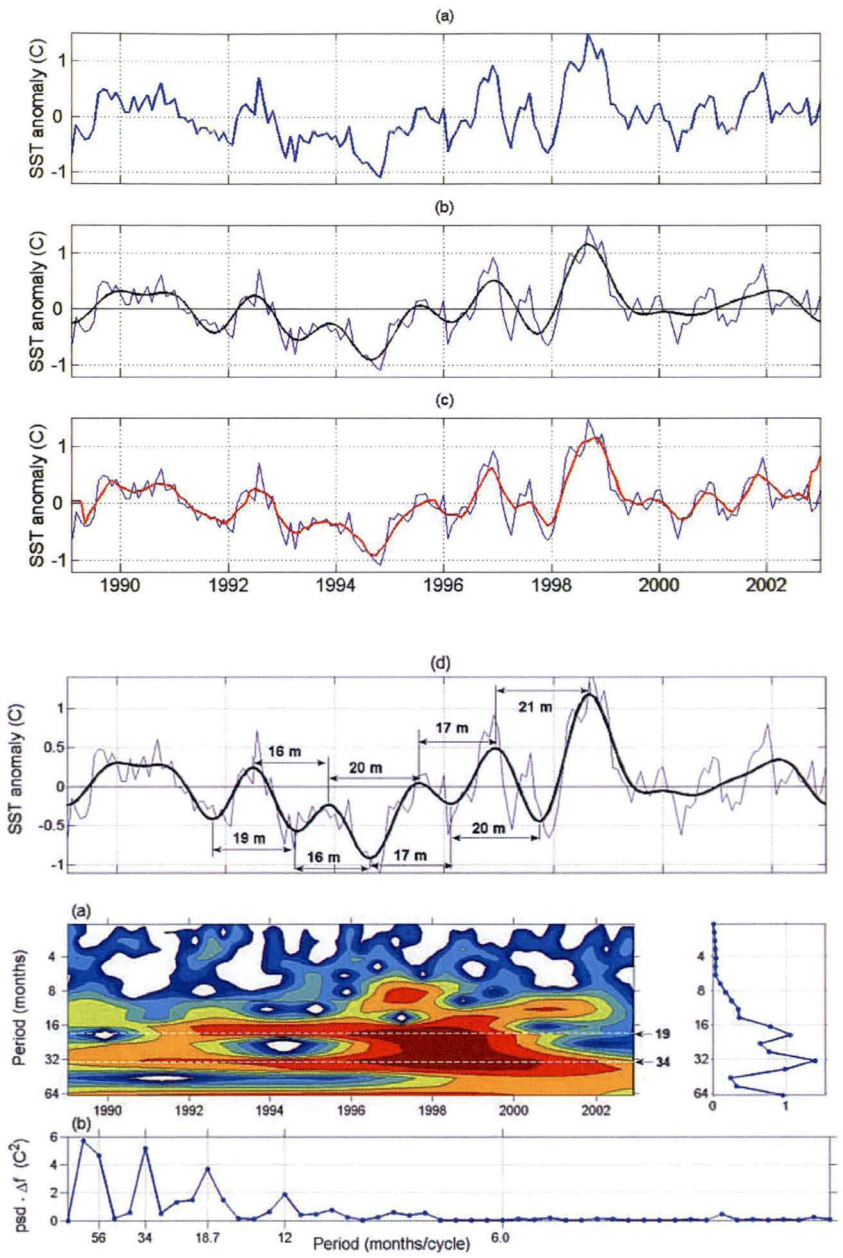

Figure 3.5.4. Analysis of Kaplan SST anomaly dataset at (-7.5°S, 105°E). (a) – the signal; (b) – the signal (blue) and low-passed signal (black) with the cut-off at 14 months; (c) –the signal (blue) and its running average over 5 months (red); (d) – as (b), with some time intervals (in months) between the signal maxima and minima shown; (e) – wavelet spectrum of the signal (left) and its global wavelet spectrum (right); (f) – PSD.

3.6 Visualization of the temporal variability of signals

To study the temporal variability of these signals (or propagation of phase of these signals) in different frequency bands, we plotted a series of snapshots of the reconstructed signal in the given frequency band. The resulting movies are provided in the Appendix A. These movies show either the evolution of SLA or evolution of SLA with wind vector overlaid for each of the following frequency bands: semi-annual, annual, 18-20 months, 3 years, and 5-7 years.

Following is the list of movies from Appendix A with the description of spectral harmonics used.

For SLA movies we use gridded (1 degree) SLA weekly-averaged data from October 1992 to December 2008, a total of 843 weekly entries.

- **movie_SLA_6m.avi** shows the SLA signal with period from 5.1 to 6.9 months, spectral harmonics 29-39;
- **movie_SLA_1y.avi** shows the SLA signal with period from 10.8 to 13.9 months, spectral harmonics 15-19;
- **movie_SLA_18m.avi** shows the SLA signal with period from 16.2 to 24.2 months, spectral harmonics 9-13;
- **movie_SLA_3y.avi** shows the SLA signal with period from 27.7 to 38.8 months, spectral harmonics 6-8;
- **movie_SLA_5y.avi** shows the SLA signal with period from 48.5 to 97.0 months, spectral harmonics 3-5.

The wind movies show the wind vector overlaid with the SLA data. For the spectral analysis we use NCEP reanalysis monthly-averaged wind data from January 1979 to January 2008, a total of 349 monthly entries and plot it only for the period that overlaps with the altimetry SLA data from January 1993 to December 2007.

- **movie_SLA_Wind_18m.avi** shows the SLA signal with period from 17 to 23 months., spectral harmonics 17-23 and for wind data 17-23, spectral harmonics with period from 15.8 to 21.8 months;
- **movie_SLA_Wind_3y.avi** shows the SLA signal with period from 26 to 37 months, spectral harmonics 10-14; and for wind data 10-14, spectral harmonics with period from 26.8 to 38.8 months;
- **movie_SLA_Wind_5y.avi** shows the SLA signal with period from 46 to 92 months, spectral harmonics 4-8 and for wind data 4-8, spectral harmonics with period from 50 to 116 months;

3.7 Comparison of temporal and spatial variability of the main spectral components

In this section we compare the results of analyses of low-frequency variability of the Indian Ocean for different data sets used in this thesis: altimetry SLA, NCEP reanalysis wind data and NOAA Optimum interpolation SST data. The primary purpose is to compare the spatial and temporal structure of the 18-month and 3-year signals. But before that we will compare the spatial distributions of each variable for the 6-month and 1-year signals, which difficult to do from spectral distribution maps plotted in Figures 3.3.7, 3.4.1, and 3.5.1 because their amplitudes are much higher than those in other bands. After that we will compare the 18-month and 3-year signals. We do not make any comparisons for signals with longer periods (5-8 years) because the temporal resolution of the data (due to the short time interval of the data availability) does not allow one to make any meaningful conclusions.

3.7.1 Six month signal

"The semiannual variability of the Indian Ocean is often discussed in the literature in association with Wyrtki jets" (Fu, 2007). The Wyrtki jet, in turn, is primarily driven by wind (Han *et al.*, 1999). The wind along the equator is very clearly presented in Figure 3.7.1(b). The C-shape in SLA for the semi-annual signal (Fig. 3.7.1 a) was previously depicted by Sakova *et al.* (2006a,b) and Fu (2007). "This C-shaped pattern indicates the effects of the western boundary in reflecting Rossby waves" (Fu, 2007) with westward wave propagation along 4.5°S and 4.5°N that was described by Fu (2007) and can be seen from Movies movie_SLA_6m.avi, from Appendix and Sakova *et al.* (2006b). The spectral analysis of wind clearly shows the existence of semi-annual variability, not only along the equator, but also in the Arabian Sea (Fig. 3.7.1 b,d). Interestingly, there is one region in the Indian Ocean with much higher SST variability in semi-annual time scales than in other regions. It is the region along the Somali coast (Fig. 3.7.1 c). We suggest that this higher variability is a response to the strong alongshore semi-annual winds off Somalia (Fig. 3.7.1 d).

3.7.2 One year signal

The one-year signal has been extensively studied and described previously in the literature (see for example Schott *et al.*, 2001). The annual signal in SLA (Fig. 3.7.2 a) is generated off the coast of Somalia by the open ocean upwelling/downwelling associated with the annual cycle of the Indian monsoon (Fig. 3.7.2 a,b,c). Interestingly, because despite of a very strong annual signal in SLA in the south-eastern Indian Ocean (Fig. 3.7.2 a) that represents the Rossby waves first described by Masumoto and Meyers (1998) as a resonant response to the wind, the winds in this region are much weaker than the winds in the northern part of the Indian Ocean (Fig. 3.7.2 b,d).

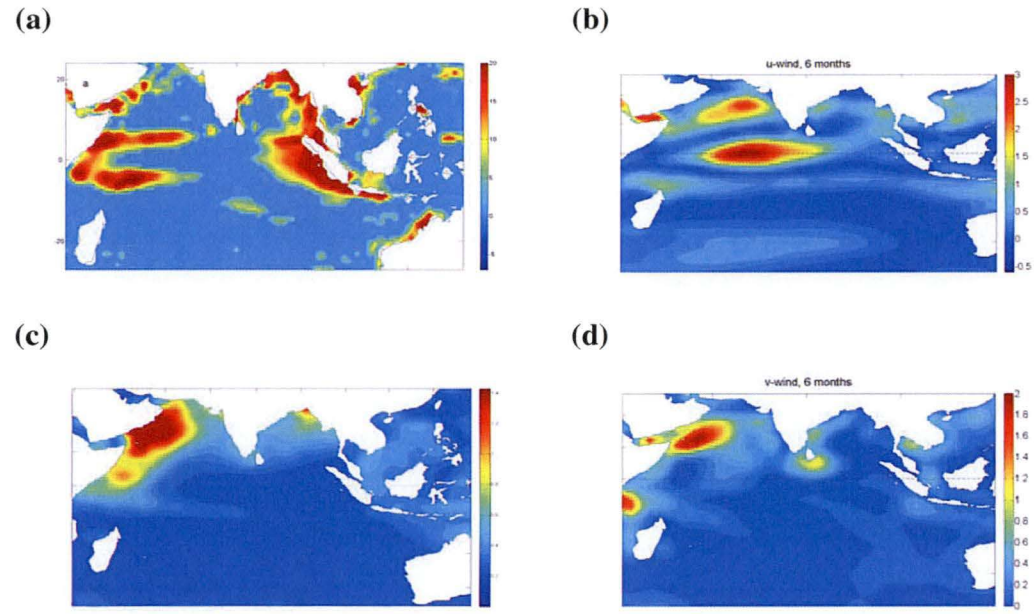

Figure 3.7.1. Maps of PSD for the 6-month signal: (a) altimetry SLA; (b) u-wind; (c) SST; and (d) v-wind.

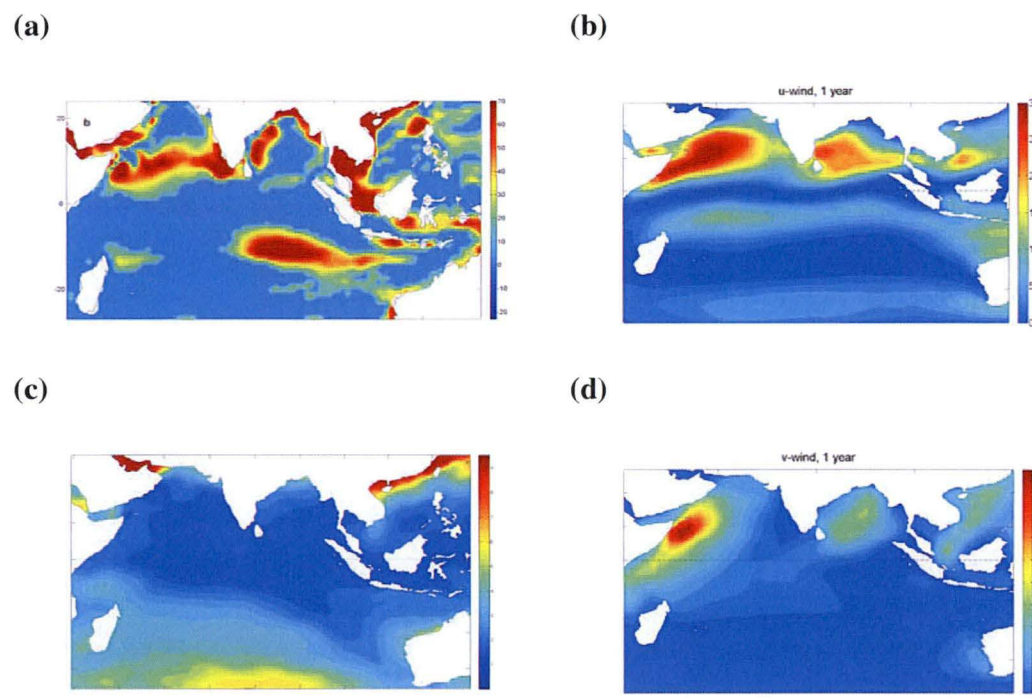

Figure 3.7.2. Maps of PSD for the 1-year signal: (a) altimetry SLA; (b) u-wind; (c) SST, and (d) v-wind.

3.7.3 18-20-month and 3-year signals

Analysis of all data sets included in the current study shows the existence of signals on the interannual scale in 3-year and 18-month bands. These two signals are analysed throughout Chapter 3 for each variable. While the spatial distributions have some similar features for all variables such as SLA (Fig. 3.3.7), SST (Fig. 3.5.1), v-wind (Fig.3.4.1), and subsurface temperature (Fig. 3.2.12), especially near the Sumatra-Java coast, we can identify differences in the spatial and temporal structure of these signals.

A significantly different spatial distribution is found for the meridional component of the wind (Fig. 3.4.1). Figure 3.4.4 shows that the 3-year wind vectors form a curl-like shape, while the 18-month wind vectors are directed mostly along the equator. The analysis of the temporal variability, or phase propagation, of SLA and wind for both these signals (3-year and 18-month) reveals that the winds in each band affect the sea surface in different ways. For the 3-year signal the winds along the Java coast - the southeast trade winds - provoke upwelling along the coast, rise the thermocline, and lower SST (Fig. 3.4.4, a). On the western side of the wind, the wind stress-induced downwelling gives rise to a deep, bowl-like mixed layer in the interior of the Indian Ocean at about (10°S, 90°E). After that the SLA perturbations start to propagate as free waves to the west and reach the western boundary of the Indian Ocean. A year and a half after that a similar process but of opposite sign happens again (Fig. 3.4.4, c). This signal exists during IOD events in 1994-1999, and its propagation can be seen from Movie movie_SLA_Wind_3y.avi, Appendix. The18-month wind component along the equator generates an anomaly in sea level height simultaneously almost along all the length of the Indian Ocean and can be seen from Movie movie_SLA_Wind_18m.avi, Appendix.

Figure 3.7.3 shows SLA over the western part of the Indian Ocean between 45°E - 85°E and 6°S – 10°S for the 3-year signal (left panel) and 18-month signal (right panel). These signals represent the response of the ocean to the wind during IOD years (Fig. 3.4.4). Figure 3.7.3 depicts the 3-year signal for the period starting from 1 March 1995 for every 8 weeks (total of 29 plots), and for the 18-month signal - starting from 11 October 1995 for every 4 weeks (also 29 plots).

The 3-year SLA signal clearly shows wave propagation to the west and looks to be the result of wind stress curl with a 3-year period (Fig. 3.4.4.a,c) centred at about 10°S and 90°E (see Chapter 3.4.5 for wind description). The 18-month SLA signal changes its sign quite sharply over the whole length of the spatial domain and possibly is a response of an 18-month wind directed along the equator (Fig. 3.4.4.b,d).

The significance of differences in spatial-temporal structure are discussed in the next section.

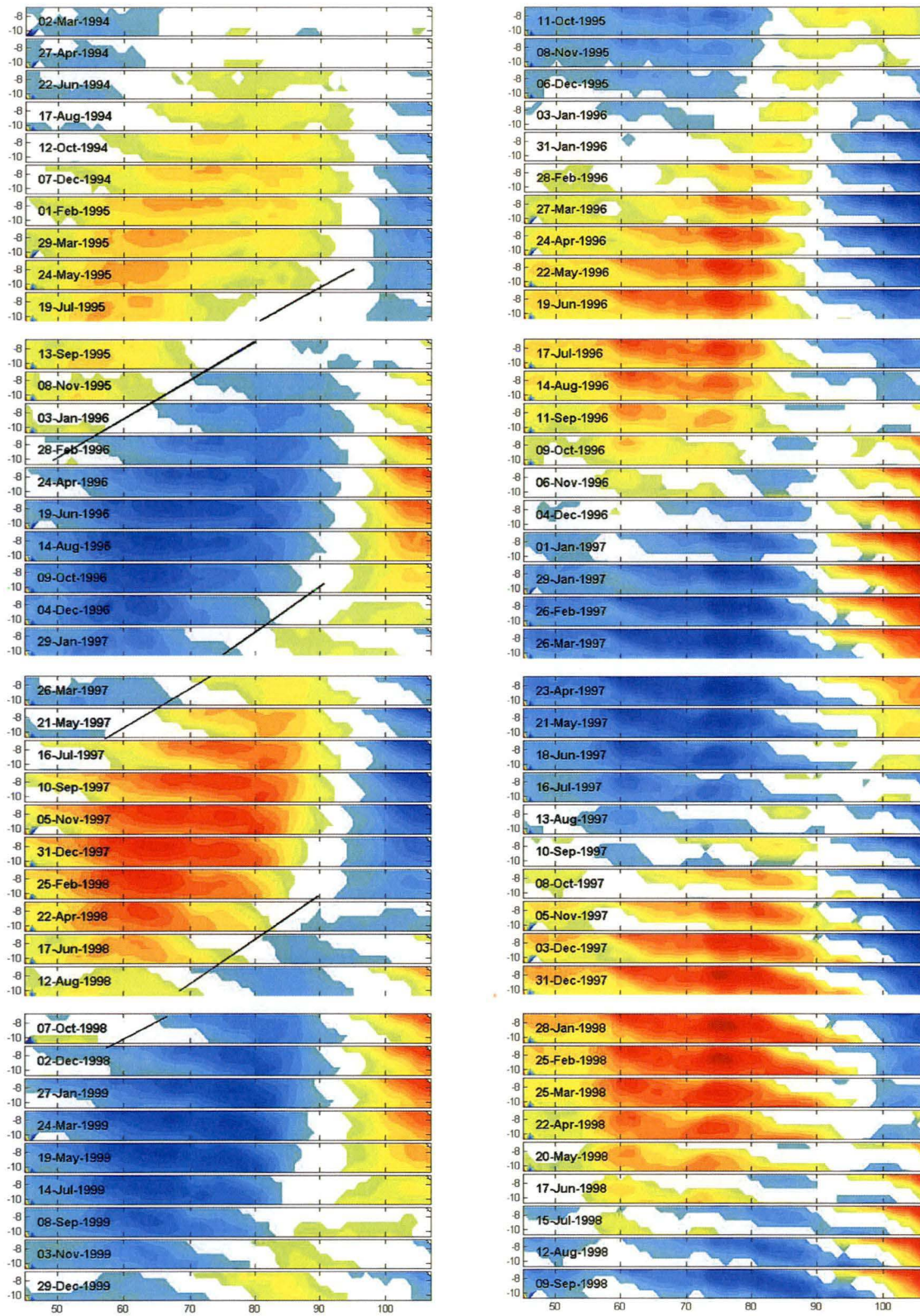

Figure 3.7.3. SLA over the Indian Ocean between 45°E - 106°E and 6°S – 10°S for the 3-year signal (left panel) and 18-month signal (right panel).

3.8 Conclusions

In parts 2-5 of this Chapter we conducted an analysis of the low-frequency variability of the Indian Ocean. In this analysis we used different data sets: XBT subsurface temperature, altimetry SLA, Reynolds NOAA Optimum Interpolation (Reynolds) SST and Kaplan SST anomalies data, as well as NCEP/DOE AMIP-II Reanalysis 2 wind data. The analysis was conducted using spectral analysis techniques. Five well separated spectral bands were identified that carry most of the low-frequency variability of the Indian Ocean: semi-annual (6 months), annual (12 months), 18-20-month, 3-year, and 5-8-years. The existence of semi-annual, annual, 2-3-year and 5-8-year quasi-periodical signals is well known; however, the 18-20-month signal has not previously been described. The discovery of a strong 18-20-month signal and its connection with an IOD mode (see the following Chapters) is the main result of this study. We underline that the above spectral bands arise in analyses of every data set used in the study.

Interestingly, despite the conclusions of previous studies pointing at the existence of the QB mode, no substantial signal with the bi-annual (~ 24-month) period was found. Because most of the previous analyses considered the interannual variability of the Indian Ocean as the variability with time scales of two years and longer (the signals of higher frequencies were often filtered out), we suggest that the QB signal corresponds to the signal with a period of 3 years of this study.

The 18-month signal and its relation with the 3-year signal is the subject of particular interest to us. Both these signals were particularly strong in the period 1991–2000, when several IOD events happened in a row. Both of them have maxima of variability in the Java upwelling region and in the western tropical Indian Ocean.

The suggested division of the low-frequency variability into five spectral bands is made mostly on the grounds of analysis of time series from about 1989 to 2004. A different time interval for the analysis can possibly possible yield somewhat different quasi-periodical signals. For example, analysis of wind for longer time periods, from 1979 to 2008, shows that the interannual variability of the Indian Ocean changed during these years (Sec. 3.5). The wavelet analysis of the wind (Fig. 3.5.2) shows that the 18-month signal in the Java upwelling region did not exist before 1990 and the 3-year signal changed its periodicity to 4-years before 1990 and after 2000. The spectral density maps (Fig. 3.5.3) of wind also point toward the existence of signals with periods of about 4-years in longer time series (1979-2008). Therefore, all conclusions about the interannual variability of the Indian Ocean are applicable to the limited time interval from about 1990 to 2008 only corresponding to the time spam of the altimetry and XBT data collection, and show different periodicity at other times, which can be seen from the reanalysis data. We will conduct analysis of a longer time series in Chapter 6 Then, we will apply spectral methods to the reanalysis data and proxy climate records (e.g. coral data)

During the writing of this thesis we have constantly heard an opinion that the 18-month signal simply represents a second harmonic of the three IOD events during 1991 to 1997, and that this signal is a manifestation of the spectral analysis technique applied to the oceanographic data. This opinion has some grounds. Both the 18-month and 3-year signals show maximum amplitude in the Java upwelling region, and their spatial distribution is similar in some respects. Despite this possibility, we believe that the 18-month signal exists in the Indian Ocean along with the 3-year signal as an independent mode, possibly as a result of a different response of the ocean to the same forcing.

Subsurface temperature (XBT temperature profiles)

The 18-month and 3-year signals were observed in this data set only near the Indonesian coast, up to 9°S (Fig. 3.2.12, Boxes 1-3) along XBT 1X-1 line (see Fig. 2.1.4 for Boxes along line description). Subsurface temperature at different depths near the Indonesian coast (7.0°S, 104.0°E) show (Fig. 3.2.5) that near the surface at about 5m-30m depth (Fig. 3.2.5 a,b), a clear 3-year signal is evident during 1991, 1994, 1997. But at the depth of about 70-100m (Fig. 3.2.5 c,d) one can see a clear drop in temperature not only during these years, but also between them, that represents the 18-months signal. The amplitude of the 18-month signal becomes even bigger at 100m (Fig. 3.2.6 d). A 6-months running mean of the subsurface data shows that at the depth of 120m (Fig. 3.2.8 c), the signal has an oscillating character with 5 cycles during 8 years; this corresponds to a period of about 19 months.

The two signals exhibit a different subsurface behaviour (Fig. 3.2.12). The 18-months signal is stronger and deeper than the 3-year signal near the coast (Box1, 6°S-7°S). With increasing distance from the coast, the 18-month signal decays quicker than the 3-year signal, and at 8°S-9°S it almost disappears while the 3-year signal is still quite strong. The faster decay of the 18-month signal compared to the 3-year signal can also be seen from the wavelet analysis (Fig. 3.2.14).

Altimetry SLA

Spectral analysis of altimetry SLA shows that along with areas where both signals (18-months and 3-years) exist there are also areas where only the 18-month signal is found (Fig. 3.3.3 c). For example, this is the case in the southern Indian Ocean at (24°S, 75°E). Generally, during 1992-2006, the 18-month signal appears to be stronger and distributed wider in the Java upwelling region (Fig. 3.3.7 c,d), while the 3-year signal is stronger in the middle of the Indian Ocean at about 5°S-15°S, 55°E-85°E. It is also noticeable that the 3-year signal has strong variability in the Indonesian Throughflow region (Fig. 3.3.7 d), while the 18-month signal does not (Fig. 3.3.7 c).

During the IOD years (Fig. 3.7.3) these two signals have different behaviour over the western part of the Indian Ocean between 45°E - 85°E and 6°S – 10°S. The 3-year SLA signal clearly shows wave

propagation to the west (Fig. 3.7.3, left panel), the 18-month SLA signal changes its sign quite sharply over the whole length of the spatial domain (Fig. 3.7.3, right panel).

These two signals evolve in a very different way in the eastern Indian Ocean (see Movies movie_SLA_18m.avi and movie_SLA_3y.avi and Figures 3.3.11 and 3.3.12). The 3-year signal near Indonesia develops simultaneously with a signal in the Indonesian Throughflow and western Pacific regions, whereas the 18-20-month signal develops near the Sumatra coast, and only then propagates east into the Indonesian Throughflow area and north to the Bay of Bengal.

Wind data

Analysis of the wind data shows that the distributions of PSD of the v-component (Fig. 3.5.1) is significantly different for the 18-month and 3-year signals. For the 18-month signal it is represented by one spot near the Java coast while for the 3-year signal it is spread between two spots. This difference can be observed not only in spatial distributions of the two signals, but also in their temporal variability (see Movies movie_SLA_Wind_18m.avi and movie_SLA_Wind_3y.avi). During IOD events, when the 3-year and 18-month wind signals exist, the 3-year wind looks like a curl with a centre at about 10°S, 90°E (Fig. 3.5.4 a,c), while the 18-month signal exists along the equatorial Indian Ocean in west/east direction (Fig. 3.5.4 b,d). These different winds produce different responses of the ocean. At a 3-year period, the SLA response generated by wind-stress curl in the eastern ocean starts to propagate westwards, likely as a packet of Rossby waves (Fig. 3.7.3 left panels), while the 18-month wind generates SLA along about 5°S-10°S simultaneously along the whole domain of the ocean (Fig. 3.7.3 right panels).

SST data

In this study we use two SST data sets: the reconstructed NOAA SST and Kaplan SST anomaly. Interestingly, that these two data sets produce quite different results for the18-month and 3-year signals. For example, visual analysis of NOAA SST data in the Java upwelling region suggests the existence of only a 3-year signal (Fig. 3.5.3, upper panel), and the presence of the 18-month signal in the spectrum (Fig. 3.5.3, bottom panel) can be considered as a second harmonic of the 3-year signal. Analysis of Kaplan SST anomaly shows the existence of 18-month signal not only in the spectrum (Fig. 3.5.4 e,f) but as an oscillation with a period of about 18 months and is present very clearly in the original time series (Fig. 3.5.4 b,c,d).

Conclusion

Generally, taking the above into consideration, we suggest that although both signals, 18-month and 3-year, are closely related, they exist as related, but separate modes of the Indian Ocean. We see features in the spatial-temporal behaviour of these modes that are unique for each of them. This points to these modes being independent, at least to some degree.

Chapter 4.
The 18-month signal and its connection with 3-year signal and IOD mode

In Chapter 3 we presented an analysis of the low-frequency variability of the Indian Ocean based on a number of independent observational and reanalysis data sets. It shows the existence of five strong, well separated spectral bands carrying most of the low-frequency signal. In this Chapter we investigate the connection of the 18-month and 3-year signals with the interannual variability of the Indian Ocean, known as the IOD mode, over the last two decades. We show that the interannual variability of a number of different variables exhibits characteristic periods of 18 months and 3 years, and that the positive and negative IOD events can be associated with the constructive interference of these signals.

4.1 Introduction

The IOD is a mode of interannual climate variability that involves the coupled ocean – atmosphere system. According to existing classifications of IOD (Webster *et al*, 1999; Yamagata *et al*, 2004; Meyers *et al*, 2006), the IOD events in two decades from 1980 to 2000 form the following sequence: 1980-81, **1982**, 1984-85, 1989, **1991**, 1992, **1994**, 1996, **1997**; where the years of the positive events are shown in bold. In recent years this sequence has continued as follows: a weak positive event, classified as IOD by Ummenhofer *et al.* (2009) in **2004**; a weak negative event classified as IOD by Luo *et al.* (2007) in 2005; a strong positive IOD in **2006**; another (weaker, but commonly recognized) positive IOD in **2007** (Behera *et al.*, 2008; Luo *et al.*, 2008).

There is little doubt today that strong SST anomalies in the eastern Indian Ocean are caused by abnormal easterlies, that the associated abnormal upwelling off the Indonesian coast represents a persistent property of IOD events, and that SST anomalies in the western part of the Indian Ocean vary significantly from event to event (Le Blanc and Boulanger, 2001; Huang and Kinter, 2002). Today there exists several different views on the origin of the SST anomaly at the western pole of the IOD: one view is that it is caused by abnormal easterlies and westward Rossby wave propagation, (e.g. Webster *et al.*, 1999); another is that it is caused by internal oceanic processes and collapse of the monsoonal wind system within the Arabian Sea rather than by the forcing from the eastern Indian Ocean (Prasad and McClean, 2004); or a third view is that it is an integral part of the TBO (Loschnigg *et al.*, 2003). Additionally it is known that the interannual SST anomaly in the west

is more influenced by ENSO (Luo *et al.* 2007) and surface heat fluxes (Prasad and McClean, 2004), and that it has a weaker variability than the anomaly in the east (Fischer *et al.*, 2005). These analyses agree with the earlier studies in the 1980's that describe the existence of the anomalous of wind and rainfall in fall in certain years in the eastern and central equatorial Indian Ocean (Reverdin *et al.*, 1986).

In the context of the above we assume that the variability in the eastern and central Indian Ocean is more closely related to the phenomena of IOD than that of the western pole of the dipole. The eastern pole mainly represents internal properties of the Indian Ocean in response to Kelvin waves generated by winds over the equatorial Indian Ocean and locally by winds along the Sumatra-Java coast (Murtugudde et al., 1999), while the western pole is more influenced by ENSO. It will be shown below that the 18-month signal is particularly strong in the eastern and central part of the Indian Ocean. Therefore, our investigation of the connection between the IOD and 18-month signal will be mainly focused on the central and eastern parts of the Indian Ocean.

4.2 Analysis of D20 from XBT data

We start our investigation of the 18-month signal with an analysis of the variability of subsurface temperature in the Java upwelling region using XBT data. The depth of D20 is a useful characteristic of the thermocline depth in this region.

Figure 4.2.1 represents an analysis of the IX-1 XBT temperature data in the Java upwelling region for the period 1989-2002, averaged in a rectangle with the corners at 7.0°S, 104.0°E and 8.0°S, 106.0°E. The panel (a) shows a typical temperature profile, where the black line corresponds to the depth of the 20°C isotherm. It contains a number of strong upward displacements of the thermocline corresponding to upwelling events, with cold water coming to the surface. The strongest upwelling can be observed during the 1994 and 1997 IOD events. The power spectrum of the depth of the 20°C isotherm, shown in Figure 4.2.1(b), contains three strong low-frequency maxima corresponding to periods of 6, 18.7, and 34 months. The 6-month maximum represents a semi-annual cycle connected with the development of the Wyrtki jet in the equatorial Indian Ocean.

The black line in Figure 4.2.1(c) represents the low-pass filtered D20 with the cut-off frequency set at approximately ~1/14 months to eliminate the one-year and shorter signals. The filtered signal is quite strong, reaching a range of more than 110 meters during 1997-1998. This reflects the fact that most of the variance of the D20 signal is concentrated in the low-frequency part of the spectrum (Fig. 4.2.1 b). In 1994 and 1997 cold water comes to the surface. This time difference roughly corresponds to the 3-year signal; however, between 1994 and 1997 there is also a clear peak at the beginning of 1996 that is not strong enough to bring the cold water to the surface. This lesser

oscillation of the low-pass filtered D20 between 1994 and 1999 roughly corresponds to a signal with a period close to 18 months: it has maxima during recognised IOD events (1994, 1997) and minima during recognised negative IOD events (1996, 1998); however, it also exhibits strong upward movement (for example, in early 1996) and downward movement (for example, in 1995) occurring at other times not associated with IOD events.

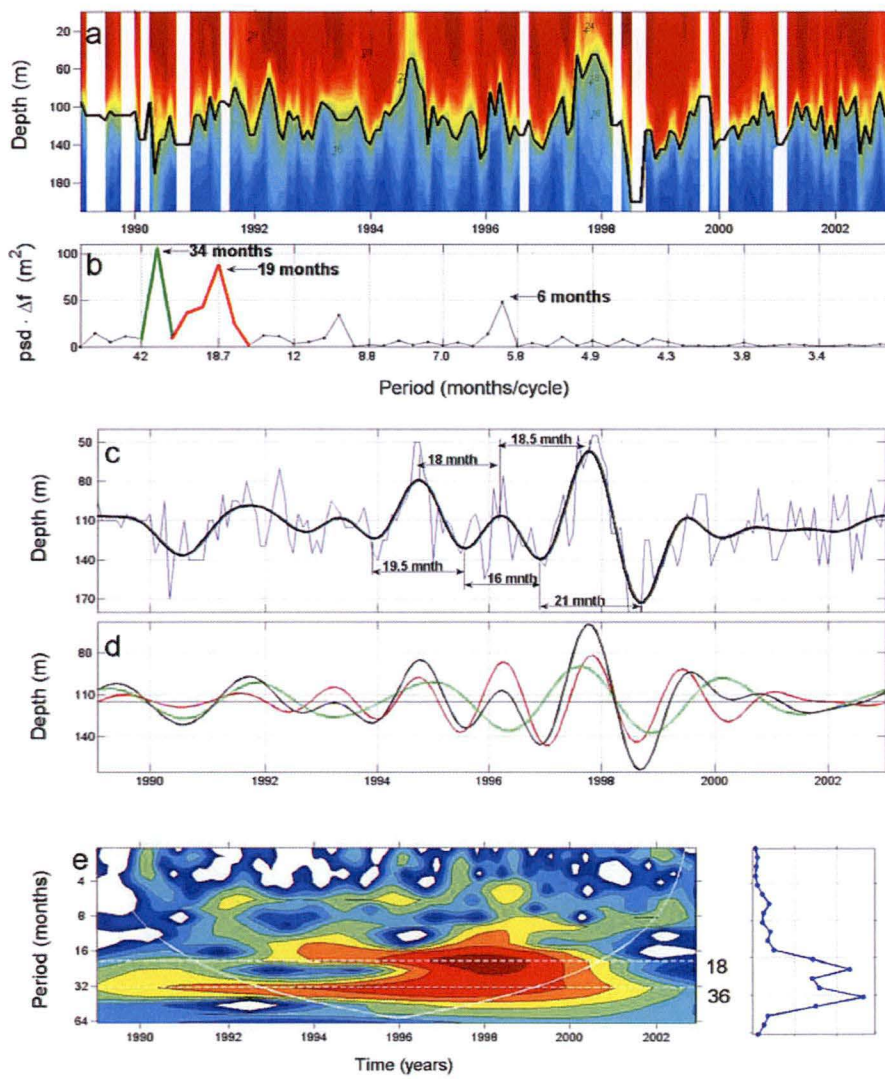

Figure 4.2.1. Analysis of the D20 in a rectangle with corners at 7.0°S, 104.0°E and 8.0°S, 106.0°E. (a) Temperature data; the depth of the D20 shown by the black line. (b) PSD of the depth of D20, where psd is the power spectral density, and Δf - frequency resolution in cycles per month; so that psd·Δf is equal to the time averaged variance, with the units of m². (c) Low-pass filtered depth of D20 using the cut-off frequency at ~1/14 months (black line) and the original signal (blue thin line). (d) Green line - 34-month signal, red line - 18-month signal, and black line - sum of two these two signals. (e) Wavelet spectrum.

Figure 4.2.1(d) shows separately the 3-year signal (green line) and the 18-month signal (red line), as well as the sum of these two signals (black line). Both of these signals are very strong between 1993 and 2000. They interfere constructively in 1990-1991, 1994 and 1997-1998, with the 1994 and 1997 maxima coinciding with the recognized IOD events. We suggest that the extremely shallow thermocline during IOD events of 1994 and 1997 can be caused by constructive interference of these two signals, as well as the negative IOD event in 1998. Because the Java upwelling has such a big role in IOD formation, a question arises whether this interpretation can also be applied to IOD understanding in broader terms. We return to this question later in the thesis.

Another related question is whether or how strongly are the 18-month and 3-year signals interconnected. Because their periods differ by a factor of two, it is possible that the 18-month signal arises as a second harmonic of the 3-year signal due to nonlinearity, such as the events when the cold sub-thermocline water lifts to the surface. In this case the 18-month signal may correspond merely to a change in the shape of the 3-year signal.

From Figure 4.2.1 it seems that the periods of maximum and minimum amplitude coincide; however, the time span of this analysis is very limited at only 13 years. The duration of the XBT data collection and satellite altimetry age does not yet allow us to extend this analysis further in time; however, we will return to this interesting problem later, during analysis of historic and reconstructed data.

The wavelet spectrum of D20 in Figure 4.2.1(e) confirms the observation that the 18-month signal was particularly strong from 1993 to 2000, and the 3-year signal was strong from 1989 to 2001. It is interesting that although the amplitude of the 3-year signal in the wavelet spectrum has a longer maximum, the amplitude of the 18-month signal is much higher during 1996-1998, in the period of high IOD activity.

4.3 Analysis of altimetry SSH

We showed above that the D20 signal in the Java upwelling region can be decomposed into several quasi-periodic components. We will now turn our attention to the altimetry sea surface height data for almost the same time period – from October 1992 to December 2003 – and for the same location – Java upwelling region, at 7.7°S, 105.0°E.

Because the SSH signal reflects integral properties of the ocean over depth, one can expect to find a similarity in the spectral decomposition of the SSH signal in this region. This is confirmed by the analysis shown in Fig. 4.3.1.

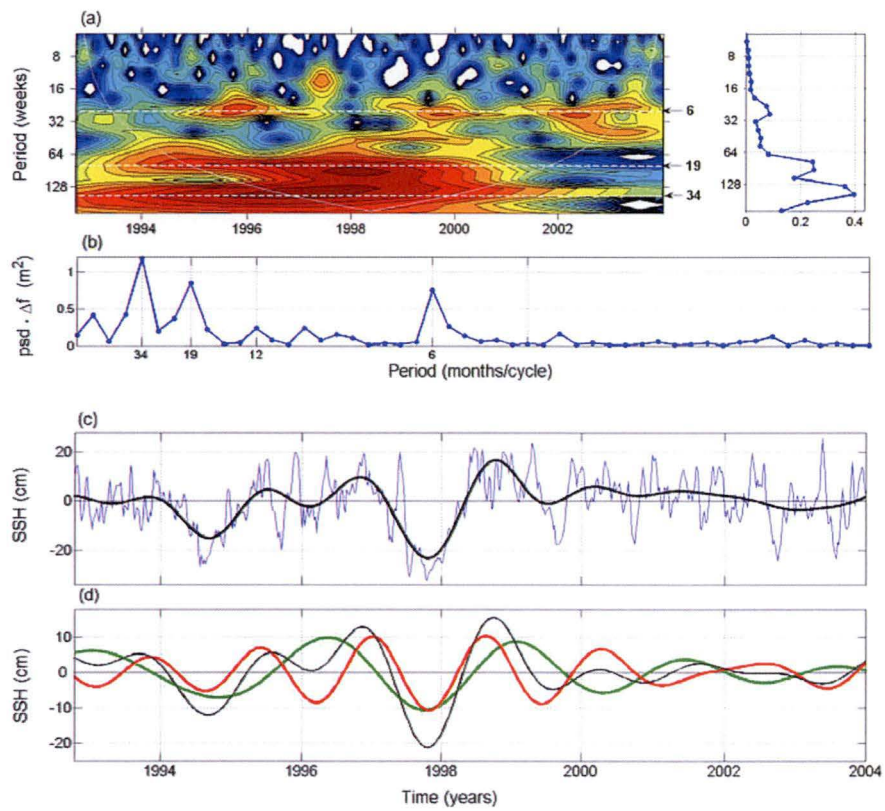

Figure 4.3.1. Analysis of altimetry SSH at 7.7°S, 105.0°E. (a) Wavelet spectrum; the white dashed lines correspond to 6-, 19-, and 34-month signals. (b) PSD of SSH, where psd is power spectral density, and Δf is frequency resolution in cycles per month; psd·Δf is equal to the time averaged variance, with units of m². (c) Low-pass filtered SSH with cut-off frequency at ~1/14 months (black line) and original SSH (thin blue line). (d) Band passed signals: 34-month (green line); 19-month (red line), and the sum of the two signals (black line).

As expected, the spectra of two variables - subsurface temperature and SSH are very similar (Fig. 4.2.1 b and Fig. 4.3.1 b) as well as their wavelet decompositions (Fig. 4.2.1 a and Fig.4.3.1 a). The wavelet decomposition of SSH shows the existence of the 6-month signal for the whole duration of the data set, while the 19- and 34-month signals clearly manifest themselves from the beginning of data set, in October 1992, until the end of 2000 (Fig. 4.3.1 a). These three components are also present in the frequency spectrum in Figure 4.3.1(b). The low-pass filtered sea level with cut-off at about 14 months (Fig. 4.3.1 c, black line) is low in 1994 and 1997 due to the extremely shallow thermocline during IOD events of 1994 and 1997. Figure 4.3.1(d) contains the band pass filtered signals for the main spectral bands. The 3-year band (green line) includes harmonics with periods from 26 months to 46 months; the 18-month band (red line) – with periods from 16.7 months to 23

months; and the overall low-pass filtered signal (black line) – with periods of 14 months and longer. Similarly to D20, the 3-year and 18-month signals interfere constructively in 1994, 1997, and partly in 1998, so that the depression of SSH during the positive IOD events of 1994 and 1997 may be seen as caused by constructive interference of these two signals, as well as the lift of SSH in 1998.

If the 18-month and 3-year signals are related to the IOD, one would expect to find these signals not only in the eastern Indian Ocean but also in the western tropical Indian Ocean. This can be confirmed from the altimetry data because it covers the whole Indian Ocean. We now conduct a similar analysis for the location in the western tropical Indian Ocean that has high overall variability of SSH in the 18-month band and 3-year band – 7.7°S, 76°E (see Fig. 3.3.7 for the spatial distributions of PSD for all spectral components). The location in the south-west tropical Indian Ocean where the PSD is highest is close to that used for the calculation of the DMI (Fig. 1.3.1).

As one can expect for that part of the Indian Ocean, the spectral analysis of SSH in the western Indian Ocean shows the existence of the one-year signal and absence of the 6-month signal (Fig. 4.3.2 a,b). Here the 19-month signal has almost the same amplitude as the one-year signal. The low-pass filtered SSH here has a positive anomaly at the end of 1994 and at the end of 1997 associated with propagation of downwelling Rossby wave associated with positive IOD events. Both signals of interest – the 18-month and 3-year – interfere constructively at that time, as well as at the beginning of 1999 (Fig. 4.3.2 d). Note that this analysis was made outside the region used for the DMI calculation (Fig. 1.3.1, western tropical Indian Ocean region, WTIO, at 50°E-70°E, and 10°S-10°N), close to the central Indian Ocean. The reason for using a different location is that we did not find a similarly clear 18-month signal in the WTIO region (not shown). If we consider that the 18-month signal is connected with the IOD mode, then the lack of this signal in the western Indian Ocean agrees with the conclusion that SST anomalies along the Sumatra-Java coast are a persistent property of IOD events, while the SST anomalies in the western part of the Indian Ocean vary significantly from event to event (Le Blanc and Boulanger, 2001; Huang and Kinter, 2002).

Figure 4.3.3 compares the temporal behaviour of the total low-frequency signal (with the cut-off frequency at approximately 14 months), the 3-year signal, and the 19-month signal of SSH at both locations above. The solid line represents the eastern Indian Ocean, the dashed line – the central Indian Ocean (76°E). All three signals have very similar patterns (Fig.4.3.3 a), but opposite signs. This is evidence of anti-correlation of the 18-month and 3-year signals between the eastern and central Indian Ocean.

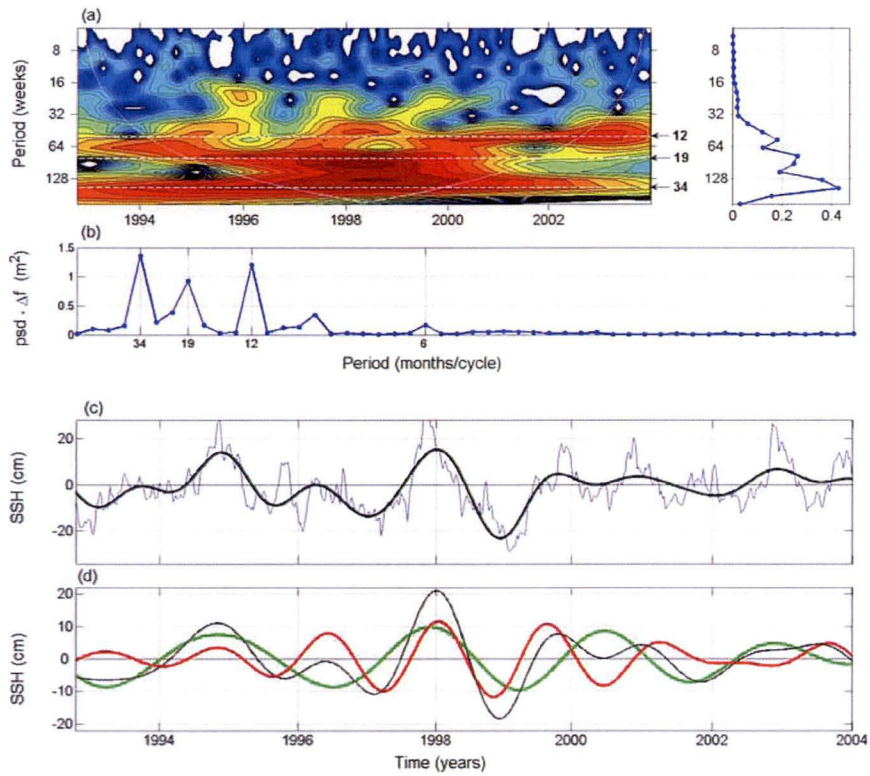

Figure 4.3.2. Same as Figure 4.3.1, except location at 7.7°S, 76°E.

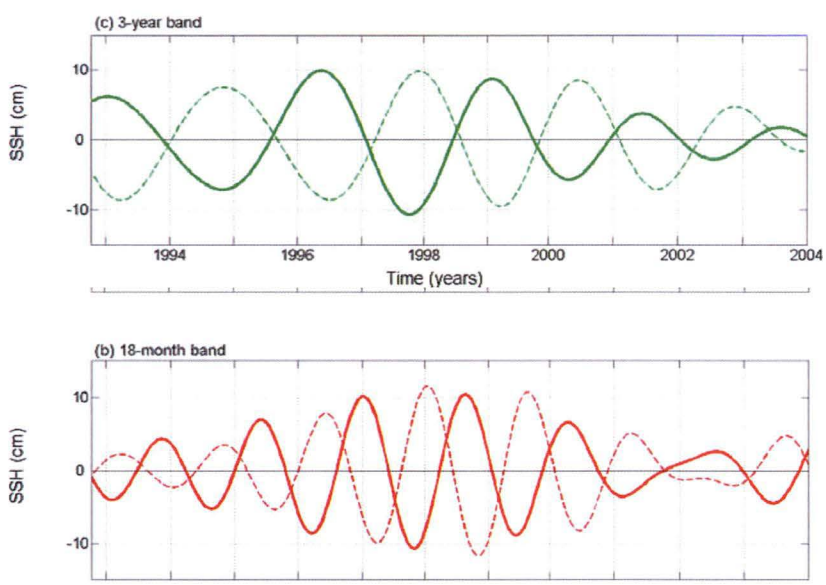

Figure 4.3.3. Low-frequency SSH at different locations in the Indian Ocean. The solid line represents the eastern location (7.7°S, 105.0°E), the dashed line – western location (7.7°S, 76.0°E): (a) low-pass filtered SSH with cut-off frequency at ~1/14 months; (b) 19-month signal; and (c) 3-year signal.

4.4 Analysis of SST

Analysis of SST data shows the existence of strong SST variability at 18-month and 3-year components in the Java upwelling region. This can be seen from SST spectral density maps (Fig. 3.5.1). Below we will analyse the temporal variability of these signals.

Results of this analysis for SST data (conducted similarly to that for SSH) are shown on Figure 4.4.1. We use Kaplan reanalysis data set for the same time period as XBT data (D20) – from 1989 to 2002 – and at the same location – 7.5°S, 107.5°N. Once again, the power spectrum contains clear 18-month and 3-year signals (Fig. 4.4.1 b). The spectrum has three standalone maxima with periods of about 18 months, 3 years and 4-7 years. The same maxima can be found in wavelet decomposition of the same data (Fig. 4.4.1 a). The 3-year signal is rather weak before 1996 (Fig. 4.4.1 d – green line) so that the low-pass filtered signal (with the cut-off at 14 months) shows oscillations with periods close to 18 months (Fig. 4.4.1 c, d – black line). In 1997 and 1998 the 18-month signal interferes with the 3-year signal constructively, and in the beginning of 1996 – destructively (Fig. 4.4.1 d).

The existence of low-frequency components (with periods longer than 3 years) in the surface temperature signal can possibly be explained by the influence of the Pacific Ocean. Figure 4.4.2 shows decompositions of the low-frequency signals for both D20 (a) and SST (b) at the same location in the Java upwelling region. The signal with period of 4 years and longer is represented by blue lines. It shows that for the surface signal (SST) the amplitude of low-frequency signal longer than 4 years is comparable with amplitudes of the 18-month and 3-year signals, while it is negligible for the subsurface (D20) signal. The 4-year and longer signal makes a strong contribution to the surface cooling during positive IOD in 1994 and surface warming in 1998. This indicates that there is an atmospheric teleconnection with the Pacific Ocean that generates the SST anomaly, but the teleconnection does not appear in the depth range of the thermocline.

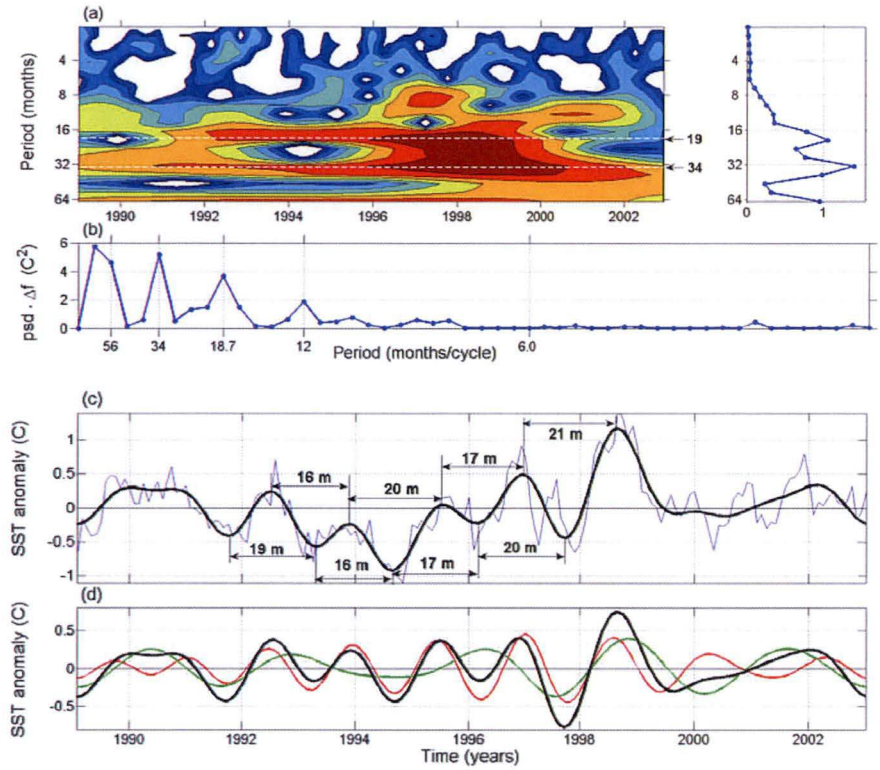

Figure 4.4.1. Analysis of the SST anomaly using Kaplan reanalysis data at 7.5°S, 107.5°E. (a) Wavelet spectrum, with the 19-, and 34-month signals shown by white dashed lines. (b) PSD of SST anomaly, where Δf is frequency resolution in cycles per month; psd·Δf is equal to the time averaged variance, with units of deg. C². (c) Low-pass filtered SST anomaly with cut-off frequency at ~1/14 months (black line) and the original SST anomaly (thin blue line). (d) 34-month signal (green line), 19-month signal (red line), and their sum (black line).

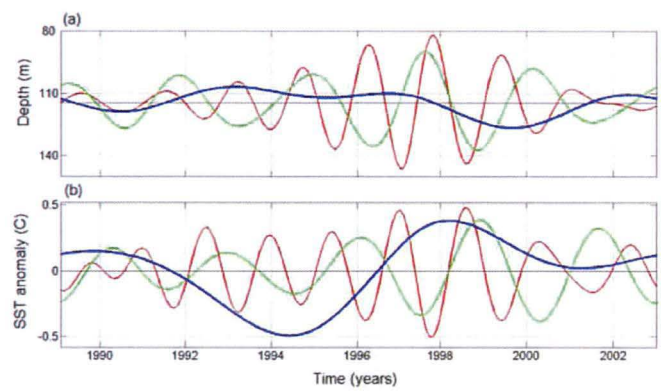

Figure 4.4.2. Spectral decomposition of D20 (a) and SST anomaly (b) in Java upwelling region into signal longer than 4 years (blue signal), 34-month signal (green line), and 18-month signal (red line).

4.5 Analysis of DMI

If the 18-month signal is connected with IOD mode, as we argue, we can expect to find it in the DMI, because this index is a quantitative description of IOD. To verify this, we will apply the same analysis as for D20, SSH and SST data to DMI. Wavelet analysis of DMI was previously conducted by Behera and Yamagata (2003) using time series from 1880 to 1990 (Fig. 4.5.1). They found that DMI "shows significant amound of power at the quasi-biennial period" (Fig. 4.5.1). They specifically noted variability "at about 2 years" during 1890-1910, 1955-1975, and 1990-2000 (Behera and Yamagata, 2003). We note in their figure that during 1990-2000 and 1890 the variability of DMI has two clear maxima: one shorter and another longer than two years, but not two years. This calls for a more rigorous spectral analysis.

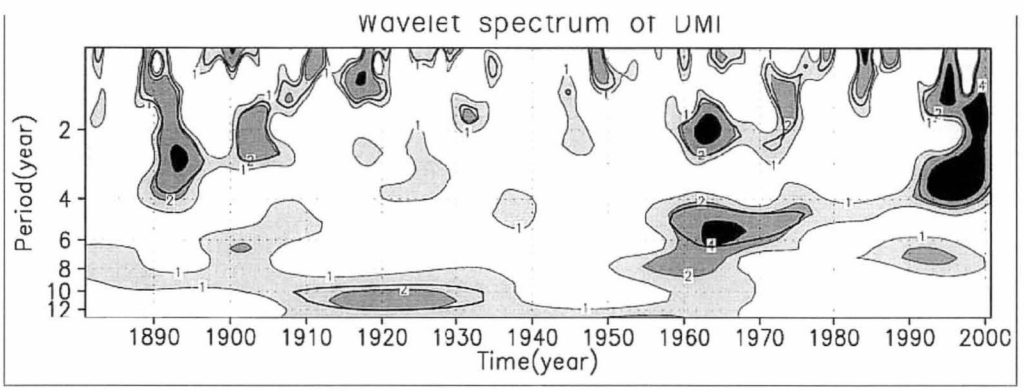

Figure 4.5.1 Wavelet power spectrum (using the Morlet wavelet) of the DMI. Shaded is the wavelet power at each period being normalized by the global wavelet spectrum, and the thick black contour is the 5% significance level (after Behera and Yamagata, 2003).

As discussed in Chapter 2, the common view today is that ENSO is an oscillatory phenomenon, while IOD represents a sequence of separate triggered events, seasonally locked to the boreal autumn. In contrast, in this work we show in a consistent way that it also can be considered as a result of interference of small number low-frequency signals. Because DMI is considered as an important indicator of the state of IOD, its frequency analysis can be more indicative than the analysis of time series of other variables. Below we analyse DMI calculated based on a number of different SST data sets (see Chapter 2.1.6 for DMI data description).

The results of analysis of different DMI time series are shown in Figures 4.5.2 and 4.5.3. Figure 4.5.2 represents the analysis of DMI index calculated by Saji in his initial paper (Saji *et al.*, 1999) using the GISST data set (1958 – 1998). Figure 4.5.3 presents the analysis of DMI derived from NOAA Optimum Interpolation Sea Surface Temperature Analysis data set (Reynolds *et al.*, 2002). It has been calculated by applying first a high pass filter with the cut-off period of 7 years, and then a 5-month running mean.

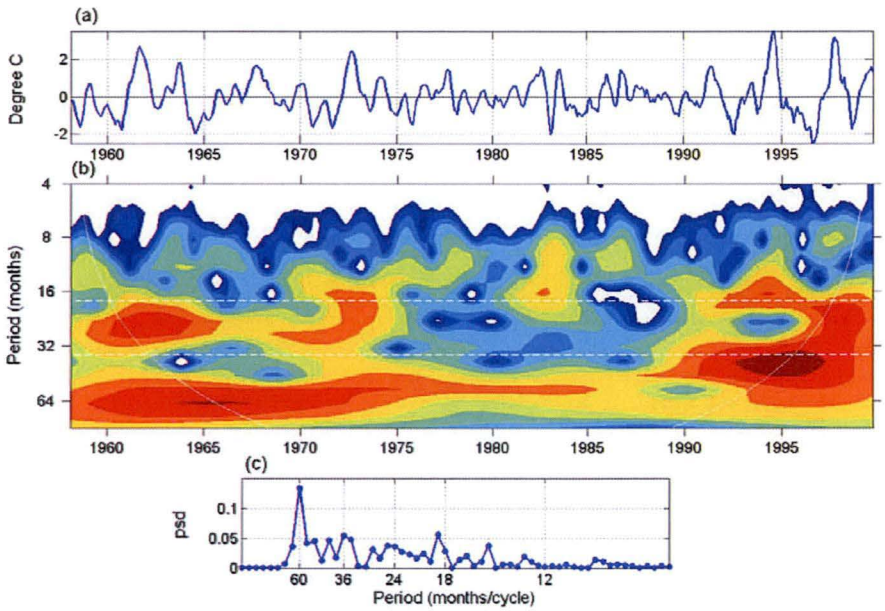

Figure 4.5.2. Spectral analysis of DMI used by Saji *et al.* (1999) for the period Mar.1958 – Oct.1999. (a) - time series; (b) – wavelet analysis; (c) – spectral analysis. White dashed lines in (b) correspond to periods of 18 and 36 month; solid white line – to the cone-of-influence.

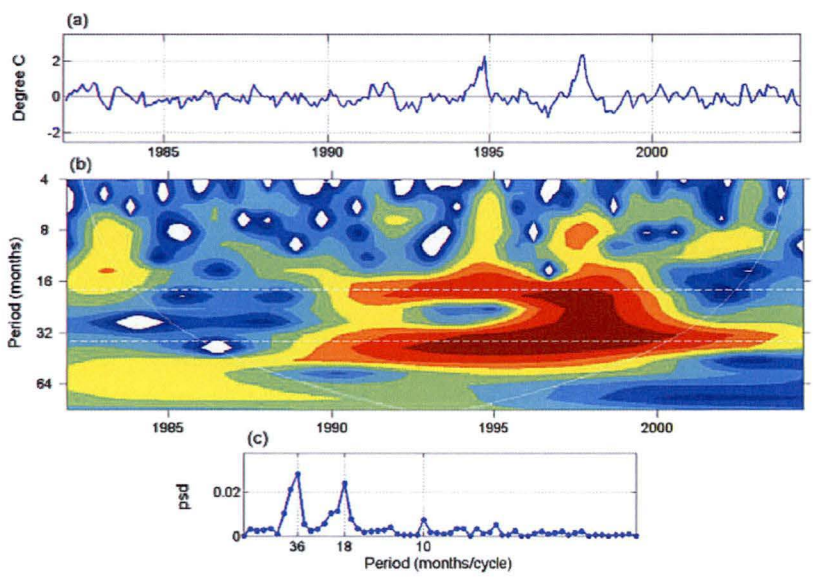

Figure 4.5.3. Spectral analysis of DMI calculated from NOAA reanalysis (Reynolds *et al.*, 2002). The panels (a), (b), (c) – as in Figure 4.2.8.

Both these time series show variability with period of 18-months and 3-years during 1990-2000 (Fig. 4.5.2 b and Fig. 4.5.3 b). In particular, the analysis of NOAA DMI time series in Figure 4.5.3 contains strong 18- month and 3-year signals, similar to the analysis of other data types in this paper.

Both these components start to develop simultaneously just before 1990, and continue to develop for several years. The wavelet decomposition in Figure 4.5.3 (b) shows that the 18-month signal decays just before 2000, while the 3-year signal exists until the end of the dataset.

The NOAA time series has a shorter time interval. This interval contains the 90s, which are the years of high activity of IOD, with several IOD events in a row: 1992, 1994, 1996, and 1997. For this reason its frequency spectrum in Figure 4.5.3 (c) reveals stronger and better separated maxima for signals with periods of 18 months and 3 years than that from DMI by Saji.

Figure 4.5.4 shows spectral decomposition of the NOAA DMI. It contains the signals corresponding to the 18-month (red line) and 3-year (green line) bands as well as the sum of these signals (black line). Both of these signals are very strong between 1993 and 2000. They interfere constructively in 1991, 1994, 1997, and 1998. The sum produces very clear positive IOD maxima in 1991, 1994 and 1997, and negative IOD maxima in 1992, 1996 and 1998.

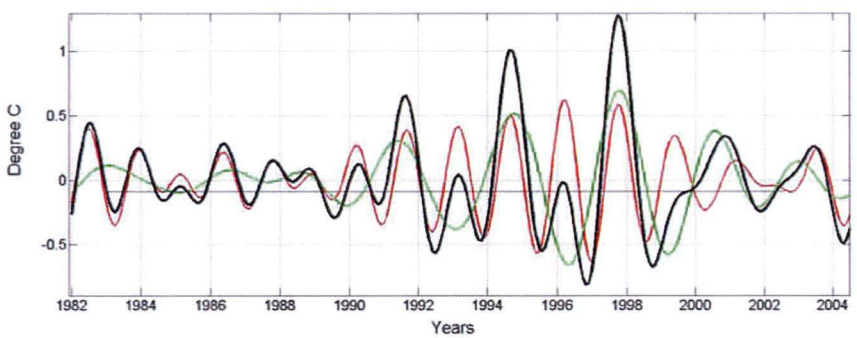

Figure 4.5.4. Decomposition of the DMI from NOAA reanalysis. Red line represents the 18-month signal, green line – the 3-year signal, and black is sum of these two signals.

4.6 Comparison of the 18-month signal in eastern and western Indian Ocean

Chapter 3 shows that the 18-month signal appears mainly in the eastern part of the Indian Ocean and seems non existent or very weak in the western Indian Ocean. In the eastern Indian Ocean this signal can be seen very clearly in subsurface temperature data (Fig. 3.2.4, Fig. 3.2.9), in spectral density maps of SSH (Fig. 3.3.7, Fig. 3.3.8), wind (Fig. 3.4.1), and SST (Fig. 3.5.1) along or close to the Sumatra-Java coast. Spectral density maps of SSH (Fig. 3.3.7), wind (Fig. 3.4.1), and SST (Fig. 3.5.1) do not show strong variability at this frequency in the western Indian Ocean, but it can be seen in regions close to central Indian Ocean. It was found in the previous section find that DMI

contains a strong 18-month signal. However, DMI represents a difference in SST between western and eastern part of the Indian Ocean (Fig. 1.3.1), and it is interesting to analyse its behaviour in each of these regions separately.

We now conduct a spectral analysis of SST separately for the two DMI regions, IODE and IODW. These two regions correspond to SETIO and WTIO regions on Figure 1.3.1. Figure 4.6.1 shows wavelet and spectral analysis of DMI (Fig. 4.6.1 a), IODE (Fig. 4.6.1 b), and IODW (Fig. 4.6.1 c).

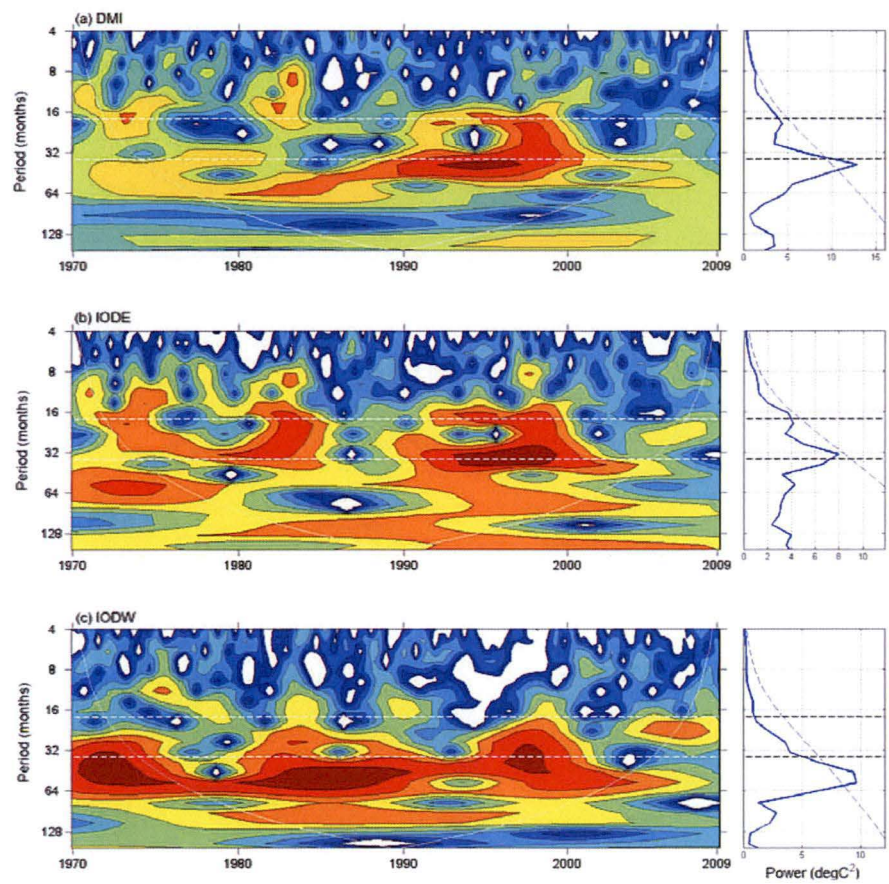

Figure 4.6.1. Wavelet analysis of dipole indices (left panels) and global wavelet spectrum (right panels). (a) – DMI; (b) – IODE; and (c) - IODW (see Fig.1.3.1 for region description). Dashed lines correspond to periods of 18 months and 3 years.

The 18-month signal clearly appears in DMI plot (Fig. 4.6.1 a) during 1991-1999 years and exists only in the eastern part of the Indian Ocean (Fig. 4.6.1 b, IODE). It is not present in the western part of the Indian Ocean. This conclusion agrees with the previous analysis of other variables (SSH, SST, and wind). The 3-year signal exists in both parts of the Indian Ocean – in the eastern part during 1990-2002 and, possibly, 1978-1995, and in the western part of the Indian Ocean during 1995-2000

(Fig. 4.6.1 c, IODW). It appears that the 3-year signal is present throughout the entire period, but its period has reduced from longer values before 1990 to shorter.

Because SST in the western part of the Indian Ocean does not exhibit 18-month variability, either the 18-month signal is not strongly related with IOD mode, or the region in the western part of the Indian Ocean used for DMI calculation (50°E-70°E, 10°S-10°N) has interannual variability different from that of IOD.

To answer this question, we first look at the SST variability in both regions. We will calculate SST over the regions used for DMI calculation, plotting SST time series for every second grid point on a 1-degree grid. Panels a and b of Figure 4.6.2 represent the low-frequency variability of SST for these two regions - south-eastern tropical Indian Ocean (90°E-110°E, 10°S-0°, upper panel), and the western tropical Indian Ocean (50°E-70°E, 10°S-10°N, lower panel). We used low-pass filtered NOAA Optimum Interpolation SST with cut-of frequency at about 14 months. In the east (Fig. 4.6.2 a) SST has clear oscillatory pattern with about 5 periods during a little less than 8 years from fall 1990 to fall 1998. That is, it represents the 18-month signal (8 years / 5 = 19.2 months). One can clearly see the SST cooling in fall 1994 and 1997 related to the upwelling along the Java coast during IOD events. In the west SST does not have a rise during the 1994 IOD event. There is a massive increase of temperature in 1997-1998, during the pacific El Niño. Overall, it seems that SST in these two regions does not show a clear dipole pattern. This conclusion agrees with observations by other authors that SST in these two areas of the Indian Ocean are not correlated, so "there is no seesaw = dipole" pattern (Hastenrath, 2003), and while the cold SST anomalies off Java and Sumatra represent a robust feature of all the IOD events, the behaviour of SST anomalies in the western Indian Ocean vary significantly from event to event (Huang and Kinter, 2002), which makes some authors to conclude even that "the dominant mode of interannual variability at the surface is characterized by a monopole (i.e. a basin-wide pattern) and related to the ENSO" (Rao *et al.*, 2002).

Some authors suggest that along with the surface dipole there also exists a subsurface dipole, and this dipole is closely connected with the IOD modes. Because altimetry SSH represents properties of subsurface stage of the ocean in an integral way, we now investigate the low-frequency variability of SSH in regions used for DMI calculation.

Figure 4.6.3 contains plots of SSH time series for every second grid point inside regions used for DMI calculation (see Fig. 1.3.1). For the south-eastern Indian Ocean (Fig. 4.6.3 a) we exclude from analysis the area north-east from Sumatra-Java, as well as small part of south-west area. The north-east from Sumatra-Java was excluded because the inner seas have different physics; the south-west area was excluded because of the winds persistent along the Sumatra coast that cause SSH there to be of opposite phase to that along the coast (see Fig. 3.4.4). For these reasons, SSH was plotted for two rectangles with corners at (90°E-102°E, 6.7°S-0.75°S) and (104°E-110°E, 9.7°S-7.7°N). In the

western Indian Ocean (Fig. 4.6.3 b) the area close to equator (1.7°S – 1.2°N) was also excluded because it has very diverse variability due to the equatorial wave guide.

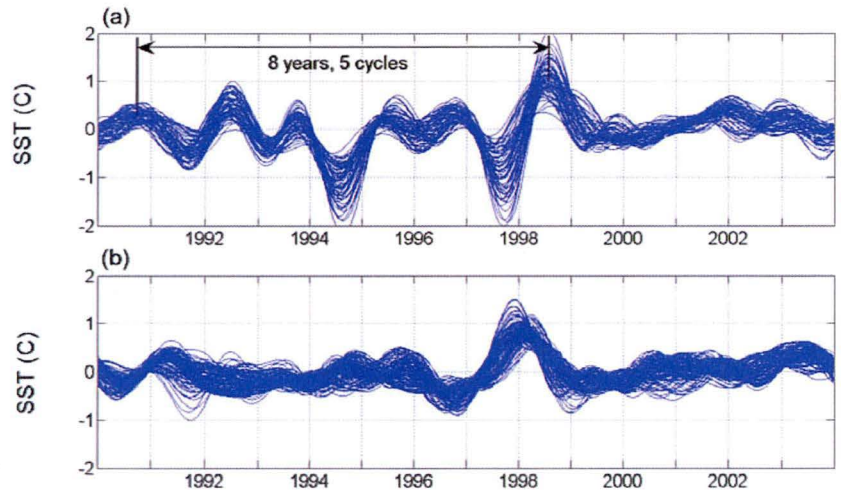

Figure 4.6.2. Low-frequency SST for two regions used for DMI calculation - south-eastern tropical Indian Ocean (90°E-110°E, 10°S-0°), and the western tropical Indian Ocean (50°E-70°E, 10°S-10°N).

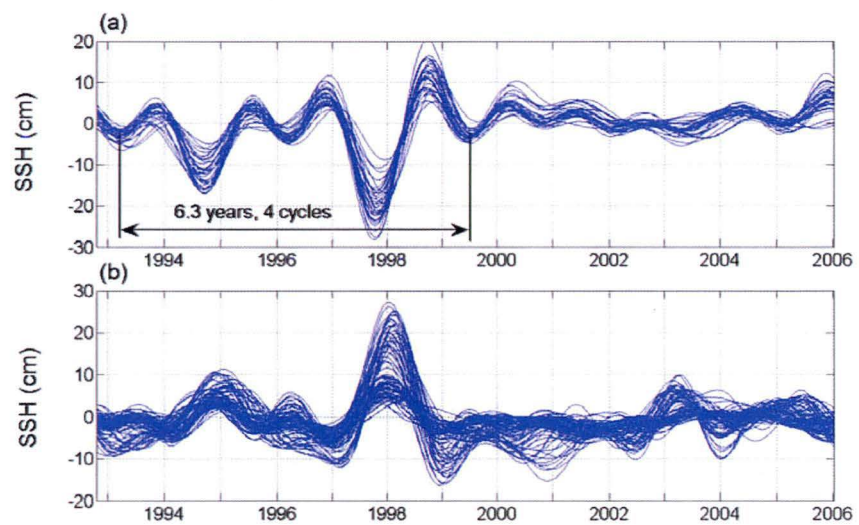

Figure 4.6.3. Low-frequency SSH for two regions used for DMI calculation - south-eastern tropical Indian Ocean and the western tropical Indian Ocean (see text for details).

One can see from the resulting plots (Fig. 4.6.3) that SSH for 1994-2000 in the south-eastern part of the Indian Ocean (Fig. 4.6.3 a) has clear opposite phase with that in the western Indian Ocean (Fig. 4.6.3 b), not only during 1997 but also during 1994. Because SSH is an accumulative property of the ocean over the depth, it represents the subsurface variability. Earlier the existence of subsurface dipole in the Indian Ocean was noticed by several authors (Rao *et al.*, 2002, Feng and

Meyers, 2004). Interestingly, SSH in the south-eastern part of the Indian Ocean as well as SSH in the western Indian Ocean have a clear minima/ maxima not only in the fall 1994 and 1997, but also between them in the beginning of 1996. The variability has 4 cycles during 6.3 years that can illustrate an existence of 18-monts signal (6.3 years / 4 = 18.9 months).

4.7 The 18-month signal as a coupled atmosphere-ocean mode

In the previous sections we investigated 18-month variability in the Indian Ocean using a number of different data sets. We found that in all investigated data sets the 18-month signal is, along with the 3-year signal and a signal with a period of more than 4 years, one of the major low-frequency components of variability in the Indian Ocean. One can expect that a signal of this magnitude and time scale should exist not only in the ocean but also in atmosphere and represent therefore a coupled atmosphere-ocean mode.

To verify this assumption, we first analyse surface wind data. Figure 4.7.1 shows the sea surface wind overlying SSH for two frequency bands: 3-year and 18-month, as well as the low-pass filtered signal with the cut-off frequency at approximately 14 months. We plot maps for different conditions of the Indian Ocean Dipole: neutral (no IOD, two plots), positive, and negative. In particular, we chose: November 2002 and May 1996 for neutral condition, November 2004 for positive IOD (with no ENSO at that time), and November 1996 for negative IOD. The map for May 1996 represents the neutral IOD at a time when there also are no significant interannual anomalies of SST; however, our analysis shows existence of a strong 18-month and 3-year signals at this time (see Fig. 4.2.1 d,e for subsurface temperature; Fig. 4.3.1 a,d , Fig. 4.3.2 a,d, and Fig. 4.3.3 b,e for altimetry SSH; Fig. 4.4.1 a,d for SST; and Fig. 4.5.2 – Fig. 4.5.4 for DMI).

It can be seen from Figure 4.7.1 that there is no significant low-frequency signal in November 2002, as well as no 18-months or 3-years signals, both in SSH and in wind. During the positive IOD of 1996 there is a very clear pattern of negative IOD, with a depression of thermocline in the east and rise in the west, and with strong west-north wind anomaly in central and east parts of the Indian Ocean. The pattern is similar for the 18-month and 3-year bands, as well as for the whole low-frequency signal. The same pattern but of opposite sign can be seen during the negative IOD in November 1996 (third row), with wind direction to south-east in the central and eastern parts of the tropical Indian Ocean. In two these cases we have a constructive interaction of the 3-year and 18-month signals that largely contributes to the strong anomaly in the eastern and western parts if the ocean. The winds have the same constructive interaction. These maps agree with our conclusion made earlier in this chapter that these two signals interact constructively during IOD events (Fig. 4.3.1 and Fig. 4.3.2).

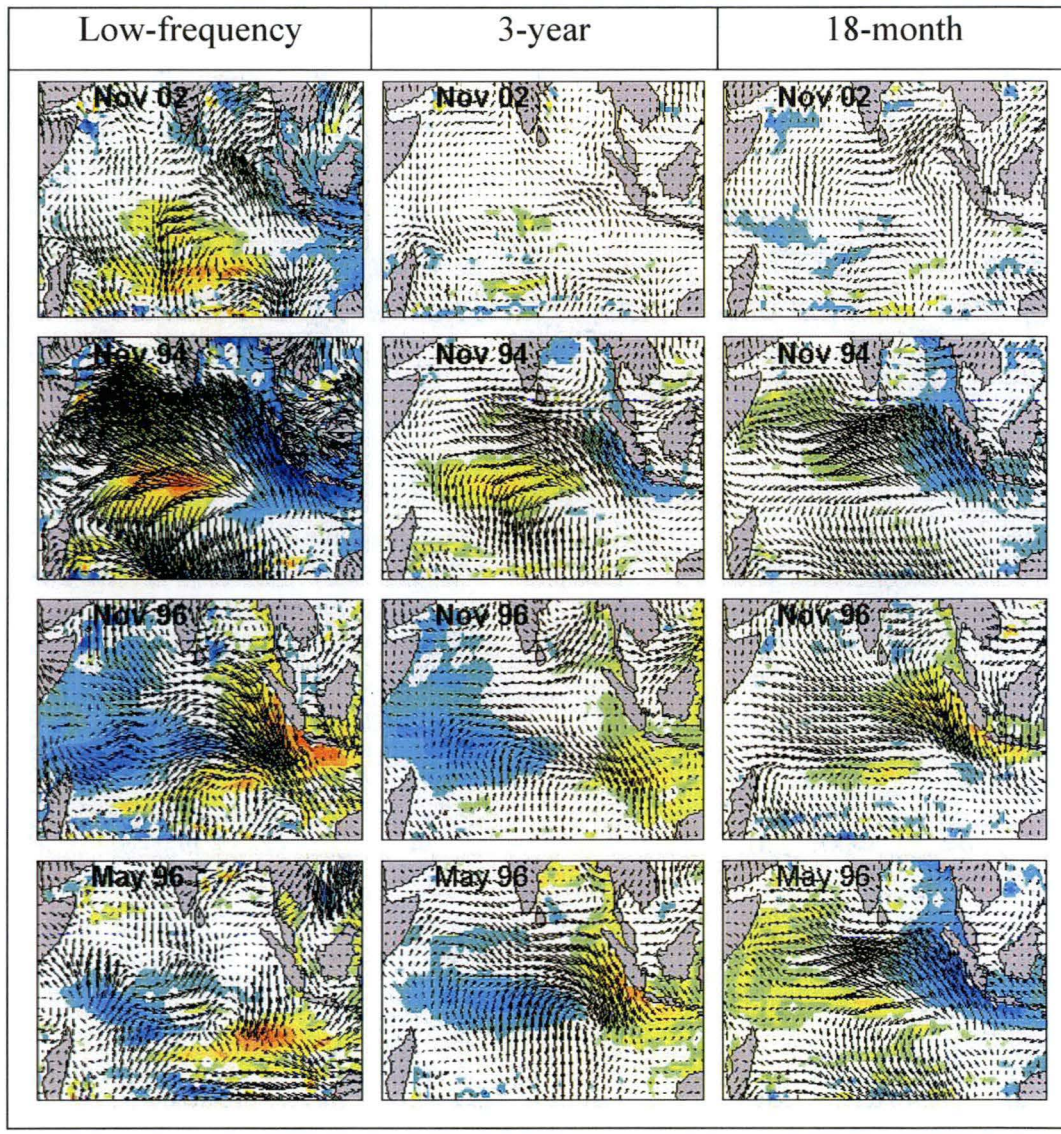

Figure 4.7.1. Wind over the SSH for low-pass filtered signal and for two frequency band: 3-year and 18-months. For different condition of IOD: neutral (no IOD) – upper row (November 2002); positive IOD – second row (November 1994); negative IOD - third row (November 1996); and neutral condition of IOD but when 18-month and 3-year signals exist in the Indian Ocean.

During May 1996 there is no significant interannual variability in SST and wind (Fig. 4.7.1, first column, fourth row). Interestingly, there are at the same time quite strong anomalies of the 3-year and 18-month signals for SSH and wind. For the 18-month signal we can see a depression of thermocline along the Sumatra-Java coast, a lift of thermocline in the west, and an anomaly in wind that is directed to north-west. The 3-year signal has opposite patterns both in SSH and wind. These two signals interfere destructively and mainly cancel each other, so that as a result there is no significant low-frequency variability at that time.

The next three figures show Hovmoeller diagrams of the Indian Ocean SSH anomalies, u-wind and v-wind for the period January 1993 to January 2008. The SSH anomaly is averaged over 11.7°S-4.8°S, while u-wind and v-wind are averaged over 4.8°S -2.9°N. Figure 4.7.2 shows the diagram for the low-frequency signal, Figure 4.7.3 – for the 3-year band, and Figure 4.7.4 – for the 18-month band. For u-wind blue colour represents the westward direction, red colour – eastward direction; for v-wind blue colour represents the southward direction, and red colour – northward.

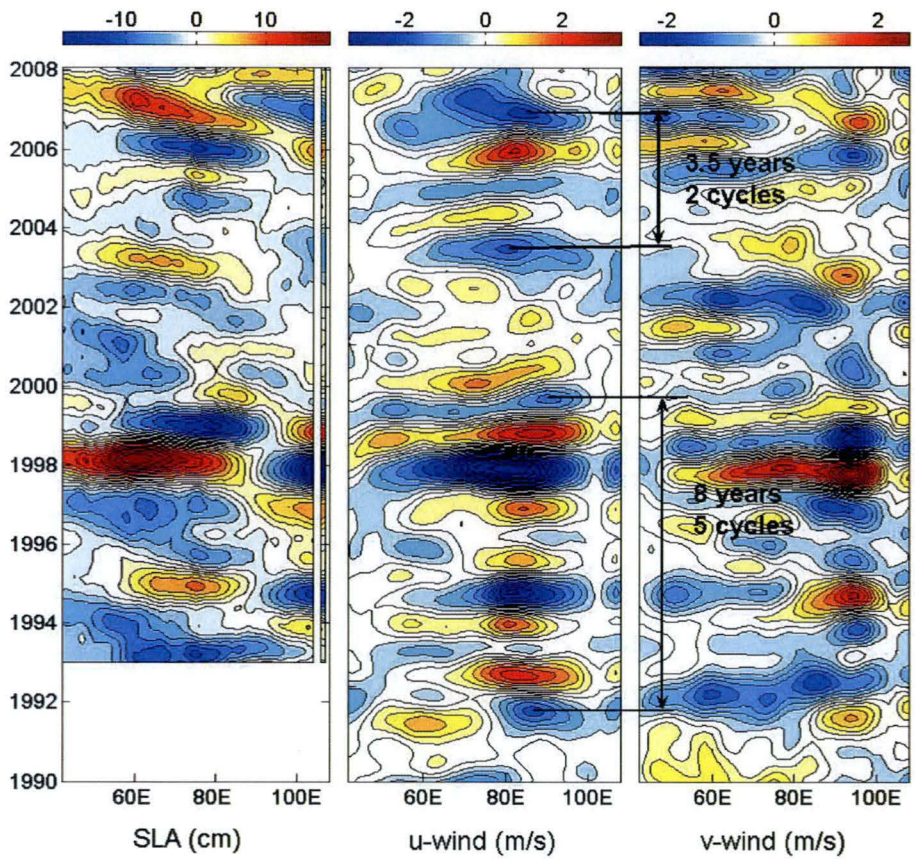

Figure 4.7.2. Hovmoeller diagrams of the Indian Ocean low-frequency signal with cut-off at 14 months for: (left) altimetry SLA; (middle) u-wind; and (right) v-wind. The SLA is averaged over 11.7°S-4.8°S (blue – negative, red – positive), u-wind (blue – westward, red – eastward) and v-wind (blue – southward, red – northward) are averaged over 4.8°S -2.9°N.

On the SSH anomaly diagram (left panel) one can see the IOD pattern in 1994, 1996, and 1997. There is also a quite clear positive IOD pattern during 2006. As it was stated before, today the recognized years for positive IOD are 1994, 1997, and 2006, and for negative IOD – 1996. However, before the positive IOD of 2006 there is a very noticeable pattern of negative IOD during fall 2005 – spring 2006. We can see the same for the positive IOD in 1994: one year prior to it, in 1993, there is a negative IOD pattern. The negative IOD that comes after a positive IOD has been described in the

literature, but a negative IOD coming before a positive IOD has not been noticed before. These positive-negative-positive patterns confirm the oscillatory character of IOD. These oscillations can be seen even more clearly from the wind diagrams (in the middle and right panels).

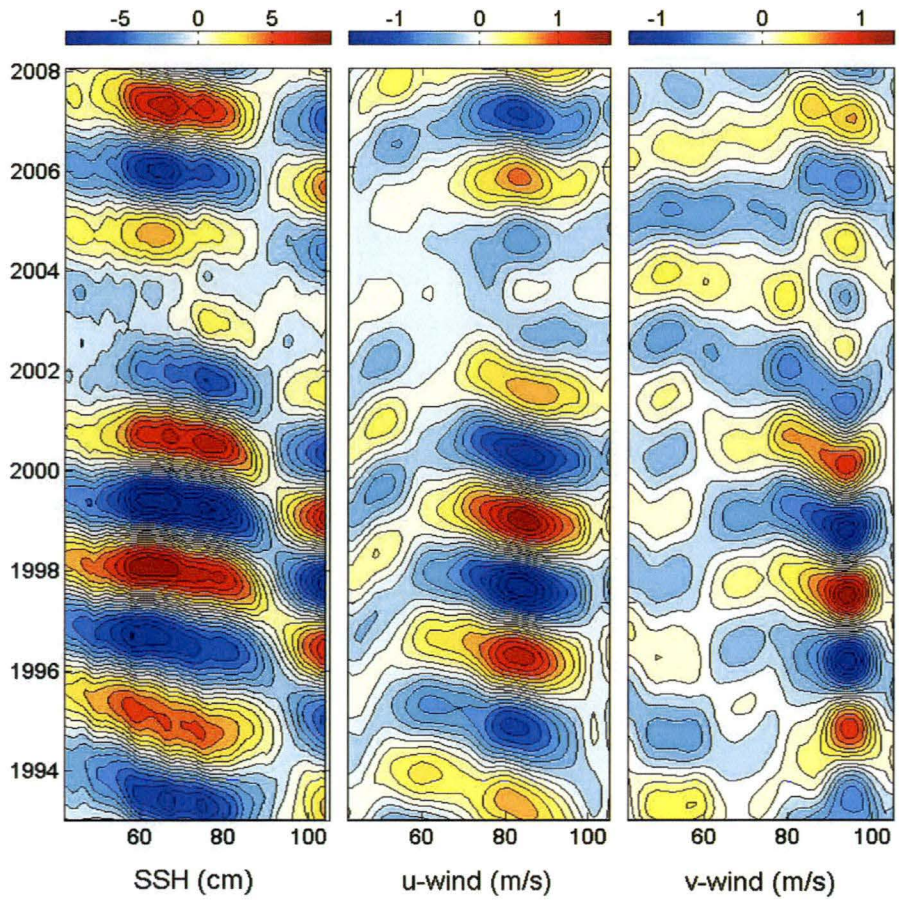

Figure 4.7.3. The same as Figure 4.7.2, but for the 3-year signal.

The u-wind anomaly has strongest oscillations in the southern-eastern tropical Indian Ocean at about 70°E-95°E. From 1991 to 1999, there are 10 changes of sign in the interannual u-wind anomaly. This corresponds to a cycle with the period of approximately 8 years / 5 cycles = 19.2 months. The same pattern can be seen for the v-wind anomaly in the region close to the Sumatra-Java coast (85°E-100°E). Interestingly, in the middle of the Indian Ocean basin, the u-wind starts oscillating well before the 2006 IOD, and passed about 2 full cycles from 2003 to 2006 (corresponding to the period of approximately 21 months).

The next two diagrams depict the variability of SSH and wind in the 3-year (Fig. 4.7.3) and 18-month (Fig. 4.7.4) spectral bands. In both bands the signals show clear and persistent oscillations during 1993-2001. SSH anomaly in the 3-year band propagates from 90°E to the west boundary of the Indian Ocean. The wind anomaly has maxima at about 80°E -90°E for u-wind and 90°E -100°E

for v-wind (also see Movie from Appendix movie_SLA_Wind_3y.avi). This confirms our previous suggestion that for the 3-year signal "wind stress-induced downwelling gives rise to a deep, bowl-like mixed layer in the interior of the Indian Ocean at about (10°S, 90°E). After that the SLA perturbations start to propagate as free Rossby waves to the west and reach the western boundary of the Indian Ocean. One year and a half after that, a similar process but of opposite sign happens again (Fig. 3.4.4, c)" (Chapter 3.7.3, Fig. 3.4.4; also Fig. 3.7.3). The 18-month wind along the equator generates anomaly in sea level height almost simultaneously along the whole extent of the Indian Ocean (Chapter 3.7.3 and Fig. 3.4.4, Fig. 3.7.3). This anomaly is particularly strong during 1997-2001 and can be seen from Movie movie_SLA_Wind_18m.avi from Appendix. In 2005-2008 the behaviour of the 18-month SSH anomaly changes and has a pattern that may be attributed to propagation of Rossby waves from east to west. This change in behaviour of the 18-month SSH anomaly from forced in 1997-2001 and 2005-2008 can perhaps be attributed to the change in the wind in these periods of time and if so, may point at a change from a wind-forced regime to a free-propagating regime.

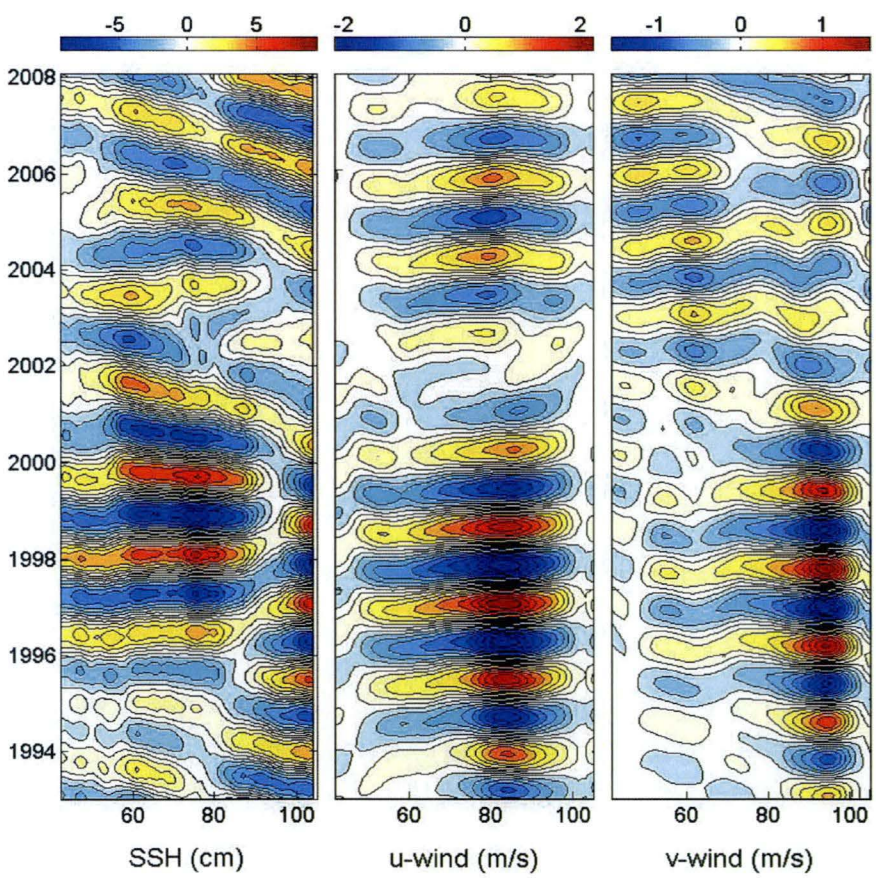

Figure 4.7.4. The same as Figure 4.7.2, but for the18-months signal.

Figure 4.7.3 shows that both signals exist before, during and after IOD. The relationship between wind and SSH is not simple. The 3-year wind in the south-eastern Indian Ocean creates propagating

Rossby waves, while the 18-month wind along the equator creates an almost uniform SSH anomaly. A strong 18-month wind anomaly during 1993-1996 does not create a strong SSH anomaly in the centre of the Indian Ocean. The 18-month SSH anomaly has a propagating pattern during 2004-2008, but there no strong signal in v-wind near Sumatra-Java coast in these years. We do not have explanations for these observations today, so that they require further investigation.

4.8 Conclusions

In this chapter we investigated the connection between the 18-month and 3-year signals and the IOD mode. Below we summarize our findings.

The analyses of different data sets show that these two signals exist in the Indian Ocean in all data sets analysed: subsurface temperature, altimetry SSH, meridional and zonal winds, SST, as well as in DMI. This persistence indicates that the 18-month and 3-year signals possibly represent own coupled atmosphere-ocean modes of the Indian Ocean. Both signals have oscillatory character; they exist in the ocean before, during and after recognized IOD events. Their existence before IOD event can be seen particularly clearly from surface wind data. The interannual variability phenomenon of the Indian Ocean known as IOD can largely be considered as interaction of these two quasi-periodical signals. Huge climate anomalies in the region during recognized IOD events in 1994, 1996 and 1997 can be explained as caused by a constructive interference of these signals. This interpretation of the IOD as an oscillatory process is somewhat contrary to a common view at it as a triggered phenomenon.

A separate analysis of SST and DMI for the east and west regions of the Indian Ocean shows that the 18-month signal is mainly presented in the eastern part of the Indian Ocean. This confirms the connection of this signal with the IOD mode because it was found previously that while "anomalies off Java and Sumatra are a robust feature of all the IOZM events, the centre of the warm SST anomalies in the western Indian Ocean varies significant from event to event" (Huang and Kinter, 2002).

In contrast to SST, the SSH signal in the western part of the Indian Ocean has a strong component with the 18-month period. We conclude that the 18-month signal is more connected with the so-called subsurface dipole (Rao *et al.*, 2002; Shinoda *et al.*, 2004a,b) than with surface SST anomaly.

Chapter 5

The IOD as an interannual oscillatory mode of the Indian Ocean and predictability of the IOD

In the previous Chapter we described the relationship between the IOD and the 18- and 36-month signals that exist in the Indian Ocean. In this Chapter we further describe the oscillatory nature of the IOD. We then test the use this oscillatory property for a medium term prediction of recent positive IOD events. Section 5.1 briefly reviews properties of the IOD that are important in the context of this chapter, although some of them have already been described in Chapter 1.

5.1 Introduction

The IOD is a major climate phenomenon that affects climate in many countries in the Indo-Pacific region and indeed the global oceans (Saji *et al.*, 1999; Yamagata *et al.*, 2004). Prediction or forecasting of the IOD sufficiently prior to its onset is important for reduction of its adverse economic impact. Yet, while the IOD was first described as an independent coupled ocean-atmosphere mode in 1999 (Saji *et al.*, 1999; Webster *et al.*, 1999), its predictability is substantially less than the predictability of ENSO (Luo *et al.*, 2007). This may be due in part to deficiencies in climate models. Cai *at al.* (2009) show that no model from 19 submitted for the Intergovernmental panel on Climate Change correctly simulated the observed mechanism of IOD for 2006-2008. Model improvement is limited by insufficient understanding of the dynamics and underlying physical mechanisms of the IOD. Lower predictability in the Indian Ocean might also be due to insufficient observations and methods for data assimilation to initialise coupled dynamical models, or it may be that the Indian Ocean is inherently more chaotic than the Pacific.

At present the common view on the process of IOD development and decay is that SST and associated south-easterly wind anomalies develop in boreal summer and intensify in the following months, e.g. (Saji *et al.*, 1999). A positive IOD peaks in October-November and then rapidly decays in early winter (Vinayachandran, *et al.*, 1999) leading to a negative IOD that fully develops by the next year (Webster *et al.*, 1999; Behera and Yamagata, 2003), creating a two-year time-scale (Feng and Meyers, 2003). The development of a positive IOD event is commonly viewed today as an isolated event that is triggered by a particular ocean-atmosphere state, (e.g. Annamalai *et al.*, 2003; Fischer *et al.*, 2005), in contrast to ENSO that has an oscillatory character, e.g. (Philander and Fedorov, 2003; Wang and Fiedler, 2006).

Today, there are a number of views on the nature of the IOD: that it is an inherent structure of the Indian Ocean (Saji *et al.*, 1999; Webster *et al.*, 1999; Iizuka *et al.*, 2000); driven remotely from the Pacific Ocean region by ENSO (Baquero-Bernal *et al.*, 2002; Shinoda *et al.*, 2004b); or that there exist two triggering mechanisms of the IOD, one of them independent of and the other dependent on ENSO (Fisher *et al.*, 2005).

In previous Chapters we showed the existence of strong 36- and 18-month quasi-periodic signals that are particularly strong during the years of high IOD activity. We suggest that individual IOD events may (at times) be interpreted as the constructive interference of these two signals. In this context, the IOD can be viewed as a continuous oscillatory process, rather than a triggered event.

The suggestion of the continuous character of the IOD is supported by observations by other authors. Webster *et al.* (1999) pointed at the possibility of the existence of a long-period oscillation in SST gradient along the equator. Murtugudde *et al.* (2000), on the basis of model output, noted that "weaker IOD events occur quite regularly that evolve similarly to the 1997 event". They suggested that "these events represent a natural mode of oscillation in the Indian Ocean". The existence of sequences when a negative IOD is followed by a positive IOD, or a biennial tendency of IOD, is also well documented (Saji *et al.*, 1999; Rao *et al.*, 2002; Behera. and Yamagata, 2003; Feng and Meyers, 2003). Recently Luo *et al.* (2007) noted that before the strong, commonly recognized positive IOD of 2006, there was a weak negative IOD in 2005.

There is also growing evidence of the development of anomalies in wind and subsurface temperature prior to the time when the IOD signature in SST can be seen. Vinayachandran *et al.* (1999) observed an anomalous equatorial westward wind event in April/May before the positive IOD of 1994. It is recognized that the subsurface dynamics plays an important role in the development and maintenance of the IOD (Webster *et al.*, 1999; Murtugudde *et al.*, 2000) and correlation between the thermocline depth and SST near the Sumatra-Java coast is well documented (e.g. Meyers, 1996; Annamalai *et al.*, 2005). Annamalai *et al.* (2005) pointed at the existence of preconditioning for the IOD when the thermocline in the eastern equatorial Indian Ocean can be shallower-than-normal due to the Pacific Decadal variability (with time scales longer than 8 years). Using recently deployed mooring buoys in the eastern Indian Ocean (1.5°S, 90°E), Horii *et al.* (2008) detected a negative temperature anomaly in the depth-range of the thermocline in May 2006; that is, three months before the 2006 positive IOD signature developed at the surface.

A recent, very strong IOD event that developed in boreal fall 2006 was followed by a weaker positive event in boreal fall 2007. They provided an opportunity to check the predictive skill of existing models. The evolution of both events was described in Behera *et al.* (2008) and Luo *et al.* (2008). The 2006 IOD event suddenly started in August, continued until November, and then rapidly disappeared. Luo *et al.* (2007, 2008) reported the first successful attempt of IOD prediction

(JAMSTEC, Japan). The authors stated that the coupled ocean-atmosphere general circulation model was able to predict "both the 2006 and 2007 positive IOD events up to 3 or 4 seasons ahead". They suggested that the subsurface dynamics can play an important role in the predictability of IOD. "The evolution of the 2006 positive IOD is consistent with the large-scale IOD dynamics, and therefore, it has long-lead predictability owing to the oceanic subsurface memory".

However, there seems to be no correct predictions of the positive IOD in 2008 and the following negative IOD in 2009. This can be seen from comments on the official IOD web page hosted by the Frontier Research Center for Global Change (JAMSTEC, Japan) http://www.jamstec.go.jp/frcgc/research/d1/iod/. On June 13, 2008, J. Luo wrote that according to "FRCGC/JAMSTEC seasonal forecasts initiated from 1 June 2008 ... a strong positive IOD would occur again this summer and fall, following the two positive IODs in 2006 and 2007. This IOD event might again cause extreme climate anomalies in broad areas". The Victorian (Australia) Department of Primary Industries newsletter "The Break" in May 2008 (vol.3, N 4) wrote "The Japanese, Australian, European and an American model (CFS) are each suggesting IOD+ like temperatures, which would make three of these in a row". But in July 2008, that is 1-2 months after forecasting, "The Break" stated that the "index used to measure the IOD has weakened considerably since its peak in early June" and on October 8, 2008, the Bulletin of the Australian Bureau of Meteorology wrote: "IOD is following its normal cycle...and is currently close to zero". In May 2009, the Australian Bureau of Meteorology predicted a negative IOD in 2009, but it has not come to a reality. This shows that despite some reported successful model-based IOD forecasts, the predictability of IOD even one season ahead needs improvement before it will be useful.

5.2 IOD as an oscillatory mode

Below we will try to substantiate the view that the low-frequency variability of the Indian Ocean associated with the IOD has an oscillatory character and consider implications of this hypothesis for the prediction of IOD.

We start our argument by considering the sequence of positive and negative IOD years in the period 1980-2006, because some basic features of these series can be seen without complicated analysis. Firstly, we observe that the years of IOD come in groups: there are 3 events from 1980 to 1985 (1980-81, **1982,** 1984-85); 6 events from 1989 to 1997 (1989, **1991,** 1992, **1994,** 1996, **1997**); and 3 or 4 events from 2004 to 2007 (**2004,** 2005, **2006-2007**) with a several years gap between these groups (The years of the positive events are shown in bold). For description of IOD year classifications see Chapter 4.1). Secondly, events within each of the groups are separated by either one or two years, and the adjacent events are almost always of alternating sign. These features may point to the existence of a background state of the Indian Ocean with a characteristic time scale of

about 5-10 years, as noted by Annamalai *et al.* (2005), that manifests itself in a stronger interannual variability at shorter time scales of 1-3 years. If so, then a detection of this state of higher interannual activity in the Indian Ocean can be considered as a precondition of IOD events.

Figure 5.2.1 presents Hovmoeller diagrams, similar to those in Figure 4.7.2, but extended in time (from 1980 to 2008) and space (Indian and Pacific Oceans). It shows the low-pass filtered (14 months and longer) altimetry SLA (left panel), the east-west component of the wind (u-wind, middle panel) and the north-south component of the wind (v-wind, right panel). The SLA is averaged over the Indian Ocean between 11.7°S and 4.8°S, the u-wind and v-wind between 4.8°S and 2.9°N. These choices are based on the variances of SLA and surface wind components during IOD years. A careful inspection of each year (see Movie movie_SLA_Wind_18m.avi, movie_SLA_Wind_3y.avi from Appendix) shows that locations of the maximum variability of the low-frequency wind anomaly in the Indian Ocean has a tendency to change over time (see Movie movie_SLA_Wind_18m.avi, movie_SLA_Wind_3y.avi from Appendix), and therefore the averaging area covers a larger zonal domain to include these maxima regions.

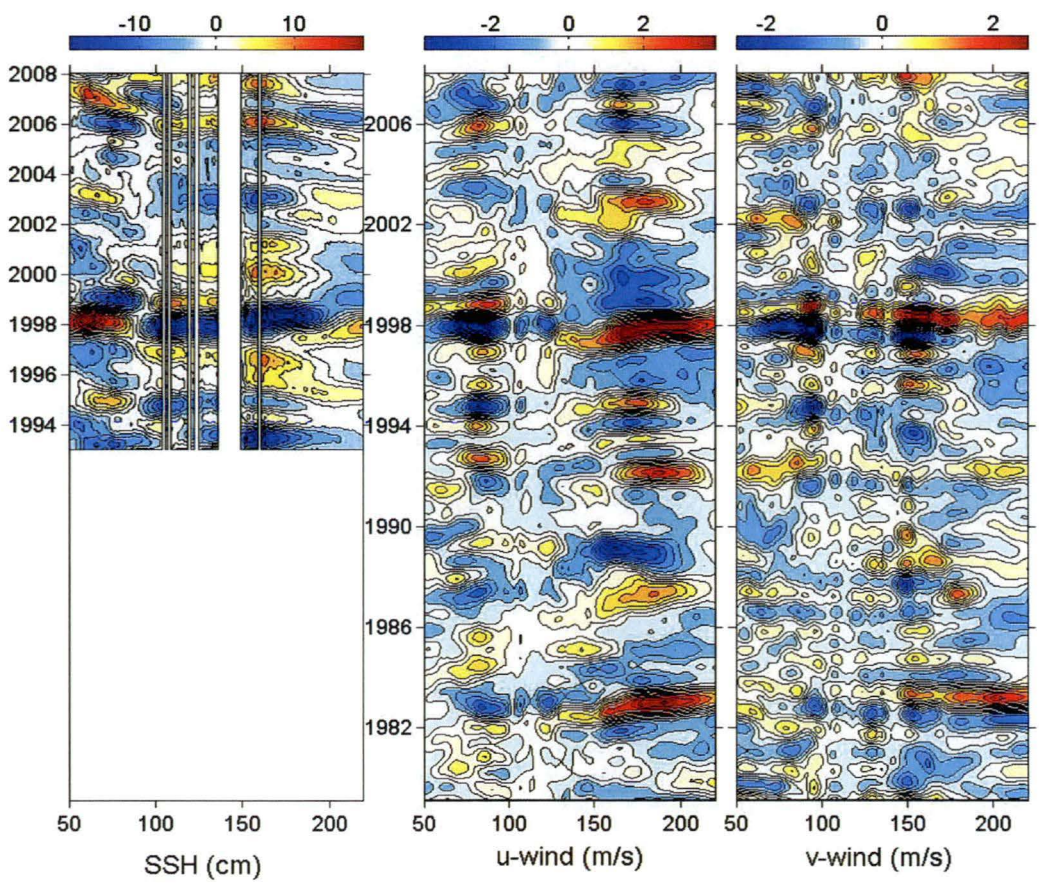

Figure 5.2.1. Hovmoeller diagrams of the low-frequency signal with cut-off at 14 months over Indian and Pacific Oceans for: (left) altimetry SLA; (middle) u-wind; and (right) v-wind. The SLA is averaged over 11.7°S-4.8°S (blue – negative, red – positive), u-wind (blue – westward, red – eastward) and v-wind (blue – southward, red – northward) are averaged over 4.8°S -2.9°N.

All three diagrams show a persistent variability throughout the whole period of time. From the SLA diagram, one can see near the Indonesian coast (at about 95°E-105°E) a pattern of positive IOD (low SSH) in 1994, 1997, and 2006. However, prior to the positive IODs, there is a noticeable pattern of negative IOD in 1993, 1996, and 2005. These oscillations can be seen even more clearly from the wind diagrams (in the middle and right panels). The u-wind anomaly has stronger oscillations in the south-eastern tropical Indian Ocean at about 70°E-95°E. From 1991 to 1999 there are 10 changes of sign of the interannual u-wind anomaly. This corresponds to a cycle with a period of approximately 8 years / 5 cycles = 19.2 months. The same pattern can be seen for the v-wind anomaly in the region close to the Sumatra-Java coast (85°E-100°E). We denoted this periodic pattern by arrows in Figure 5.2.2. Figure 5.2.3a shows the u-wind variability for five longitudes between 78.7E and 86.2E and their spectra (Fig. 5.2.3b). We can see big wind anomalies in 1994 and 1997. But there are periodical anomalies starting in 1992 and between these years. These anomalies create oscillations of the u-wind field with a period at about 18 months. This period is clearly seen in the computed spectra. Interestingly, in the middle of the Indian Ocean basin, the u-wind starts oscillating well before the 2006 IOD, and passes about 2 full cycles from 2003 to 2006 (corresponding to the period of approximately 21 months). There is also a strong correlation (or anti-correlation, depending on the chosen positive wind directions) between SLA and both wind components (Fig.5.2.2).

The wind components in the Pacific Ocean also have some periodic pattern, but the periodicity is not as clear as in the Indian Ocean, and seems to have a different time scale. We note that, because our main focus is at the Indian Ocean, we chose the averaging domains accordingly, to exhibit periodicity in the Indian Ocean. We suggest that for further study of signals in the Pacific, we would need to make averaging at different zonal locations.

Below we will primarily consider the interannual variability in the eastern part of the Indian Ocean, offshore of Indonesia, which is recognized to be a key region for the onset and manifestation of the IOD. The SST in this region is one of the two components used in the calculation of the DMI; however, the subsurface temperature anomaly may be a more indicative variable.

Figure 5.2.4 shows the temporal evolution of the subsurface temperature anomaly in the Java upwelling region. It is obtained by monthly averaging XBT data in a rectangle with corners 7.0°S, 104.0°E and 8.0°S, 106.0°E. One can see the cold water from below the thermocline reaching the surface due to upwelling in fall 1991, 1994, and 1997 (marked by thick arrows), which are the years of positive IOD. The cold water reaches the surface for a rather short period of time and persists for a much longer time in the depth-range of the thermocline – for up to one year. In addition, there are noticeable cold anomalies at the depth of about 50-150m in boreal springs of 1993 and 1996 and in boreal fall 1999 (marked by thin arrows). The period between all described six cold subsurface anomalies is about 1.6 years, or 19 months. Between these cold anomaly events, there are warm subsurface anomalies. Together with the cold anomalies they create consistent oscillations of

temperature at about the thermocline depth (around 100 m), when a cold anomaly is followed by a warm anomaly (and vice versa), that do not manifest themselves as clearly at the surface.

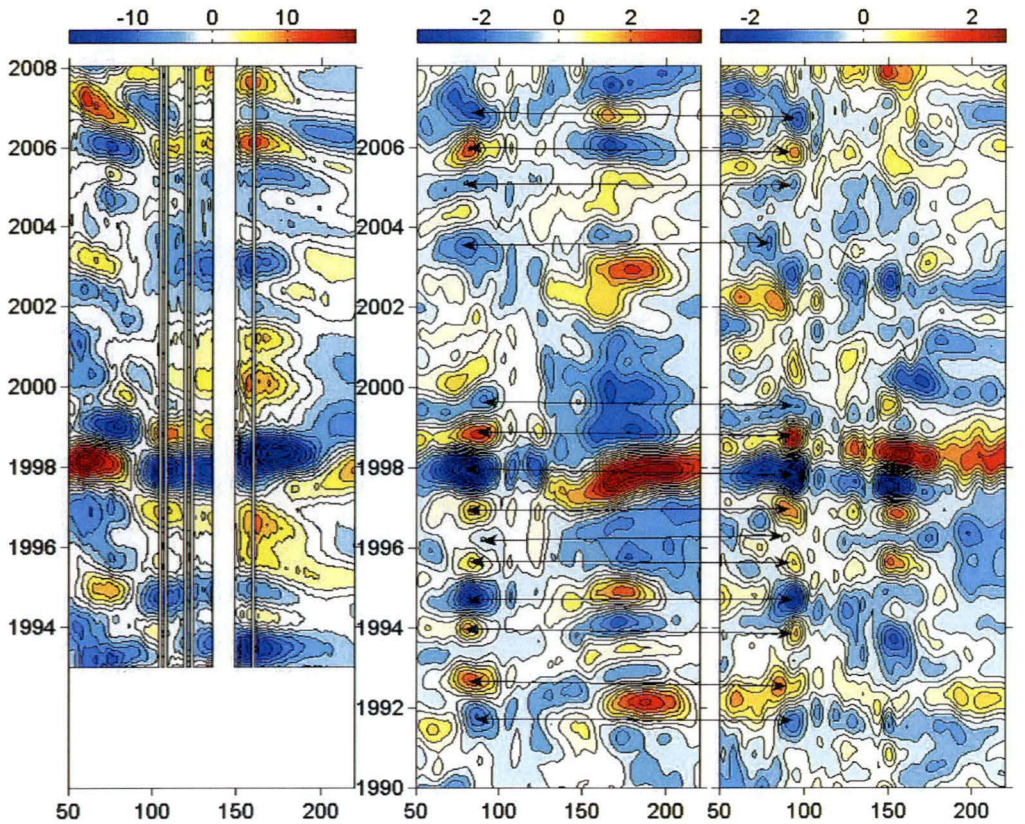

Figure 5.2.2. The same as Figure 5.2.1 but for the period from 1990 to 2008. Oscillations of the u- and v-wind components in the Indian Ocean are denoted by arrows.

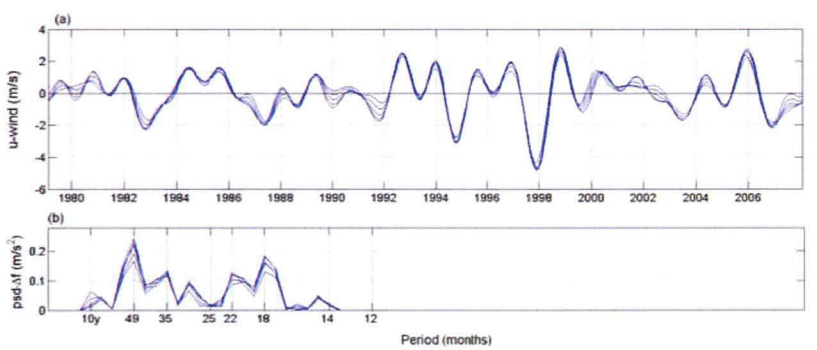

Figure 5.2.3 . (a) Low-frequency u-wind with cut-off at 14 months over the Indian Ocean for five longitudes from 78.7°E to 86.2°E (a) and their spectra (b). The wind is averaged over 4.8°S -2.9°N, as in Fig.5.2.1 and Fig.5.2.2.

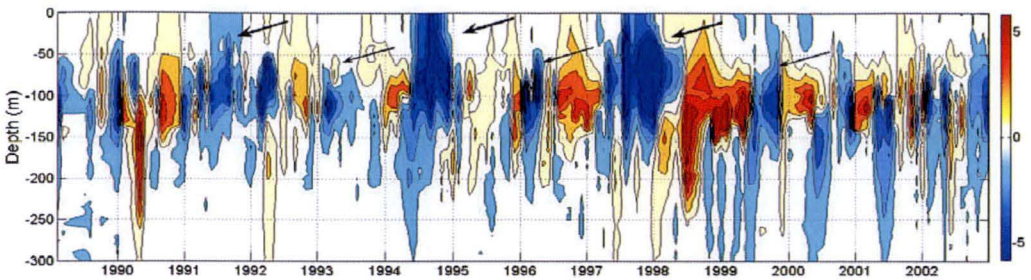

Figure 5.2.4. Subsurface temperature anomaly (°C) in the Java upwelling region, averaged in rectangle with corners at 7.0°S, 104.0°E and 8.0°S, 106.0°E.

The subsurface temperature at the same location at a number of different depths is presented in Figure 3.2.8. It shows that the subsurface temperature at 120m (close to the depth of the thermocline) has a clear oscillatory character, and passes 5 periods in 8 years from 1992 to 2000, with the mean period of about 19 months. Spectral analysis of the subsurface temperature (Fig. 3.2.6) exhibits two strong separated components with approximately 18- and 36-month periods at the depths of 30-120m. The same spectral components can be seen in the movement of 20°C isothermal surface (Fig. 4.2.1). Interestingly, these two spectral components decay very quickly with distance from the coast and almost disappear at 10°S (see Fig. 2.1.4 for description of the boxes). In 1999-2002, when no IOD events occurred, the behaviour of subsurface anomalies has changed (Fig. 5.2.4), with the cold anomalies appearing at 100m and below rather regularly but oscillating more rapidly and not connected to the surface.

In the previous chapters we showed that the variability in the Indian Ocean at time scales between 1 year and 4 years is mainly concentrated in spectral bands corresponding to the periods of 18- and 36-months. These signals have been found in SLA (Fig. 3.3.7), subsurface temperature data particularly close to the Sumatra-Java coast (Fig. 3.2.4, Fig. 3.2.6 – Fig. 3.2.12), wind data (Fig. 3.4.1), SST in the eastern pole of the dipole (IODE) (Fig. 4.6.1b): NOAA SST (Fig. 3.5.1 – Fig. 3.5.3) and Kaplan SST (Fig. 3.5.4). These signals are particularly strong during the years of high IOD activity, at least during last two decades, so that individual IOD events can be interpreted as their constructive interference. In this context, the IOD can be viewed as a continuous oscillatory process, rather than a triggered event. This opens up a possibility of using the current state of the 18- and 36-month signals for a medium term forecast of the IOD. Below we attempt to determine the current state of these signals by varying the end time of the SSH time series at a location in the Indonesia upwelling region and make a hind-cast of the IOD for April 2006, and April 2007.

5.3 Predictability of the IOD

Below we consider the possibility of using the current estimates of the state of the 18-and 36-month signals for the prediction of the IOD. We start with the analysis of SSH, as it has a contribution from the depth-integrated water density. Figure 5.3.1 shows analysis of the temporal variability of SSH in the Java upwelling region, at 7.7°S, 105.0°E for the period from October 1992 to September 2006. This analysis is similar to the one presented in Figure 4.3.1, but the time period extends to the onset of the positive IOD event of 2006 (the total of 728 weekly entries).

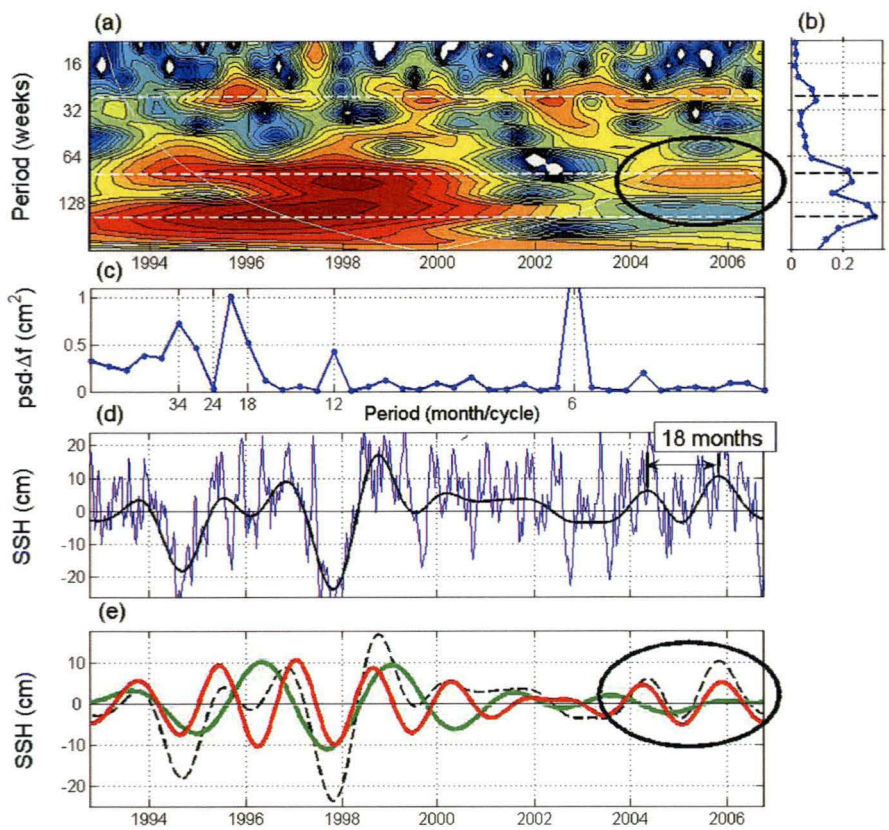

Figure 5.3.1. Analysis of the altimetry SSH at 7.7°S, 105.0°E for the period from October 1992 to September 2006. (a) Wavelet spectrum; the white dashed lines correspond to 6-, 19-, and 34-month signals. (b) Global wavelet spectrum; the black dashed lines correspond to 6-, 19-, and 34-month signals. (c) PSD of SSH, where psd is power spectral density, and Δf is frequency resolution in cycles per month; psd·Δf is equal to the time averaged variance, with units of cm². (d) Low-pass filtered SSH with cut-off frequency at ~1/14 months (black line) and original SSH (thin blue line). (e) Band passed signals: 36-month (green line); 19-month (red line), and low-pass filtered SSH (black dashed line).

The wavelet decomposition (Fig.5.3.1a) and the band pass filtered signals (Fig.5.3.1e) show that both 18-and 36-month signals were strongly presented throughout the period of high IOD activity in the 1990s. There are no signals between 2000 and 2004. Later on, before the onset of IOD in October 2006, the 18-month signal (marked by black ovals) was already developed. This signal (Fig. 5.3.1e, red line) started to develop in 2003, and as well as the total low-pass filtered signal (dashed black line) had a minimum in December 2004 and a maximum in November 2005. Its pattern agrees with the classification of 2004 as a year of positive IOD by Ummenhofer *et al.* (2009) and 2005 as a year of weak negative IOD by Luo *et al.* (2007).

Therefore, before the onset of the strong IOD of 2006 there were already two periods of the 18-month SSH signal in the Java upwelling region. The analysis shows no substantial presence of the 36 months signal, but this may be partly due to the insufficient resolution of the data near the end of the time series to detect its development in the wavelet decomposition.

The general problem we face for the prediction based on the amplitude of components with particular time scales is that the decomposition of the signal near the end of the time series becomes unreliable. It seems that one needs at least 1 period, and better 2 or more periods of the developed signal to achieve a reasonable estimate.

Figure 5.3.2 shows SSH analysis for longer than given in Figure 5.3.1 time series - up to December 2008. The thin blue line (Fig. 5.3.2a) represents the original signal, the black line – the low-pass filtered SLA with cut-off at 14 months. Figure 5.3.2b shows the 18-month (red line) and 3-year (green line) signals, and signal with the period longer than 4 years (blue line). This time series (up to December 2008) shows the existence of 36 month signal, that we did not see in the time series up to October 2006. (This example clearly shows the complication of using spectral analysis for detecting signals at the end of a time series). The low-pass filtered signal (Fig. 5.3.2 a,b black lines) has moderate oscillation during 2003-2007, that seems to decay in 2008. During the fall of 2005, the 18- and 36-month signals add constructively, which results in a weak negative IOD of 2005. During the boreal fall of 2006 they add constructively again, and that results in a stronger positive IOD of 2006.

Figures 5.3.3 a-d show the 18-month (blue thin line) and low-pass filtered (black thin line) signals of time series up to December 2008. Also they show the 18-month signal (magenta thick line) calculated from the SSH time series for the periods starting in October 1992 and ending in April 2005, April 2006, April 2007 and April 2008, respectively.

In April 2005, no signature of the 18-month signal can yet be seen (Fig. 5.3.3 a), although in the time series ending in December 2008 the signal clearly exists at this time with an amplitude of about 6 cm. But in the time series finishing in April 2006 (Fig. 5.3.3.b, magenta line), the signal is well developed, has a very similar shape to the low-pass filtered signal (black line) and almost coincides

with the "real" 18-month signal (blue line) obtained from the time series ending in December 2008. The red dashed line represents the forecast for the 18-month signal for the next 7 months (up to November 2006) on the assumptions that the signal will not change its periodicity and amplitude. This assumption of constant phase and amplitude is certainly not likely to be the situation as we can see from the previous plots but we are using this approach to see how robust this technique is for prediction of IOD events.

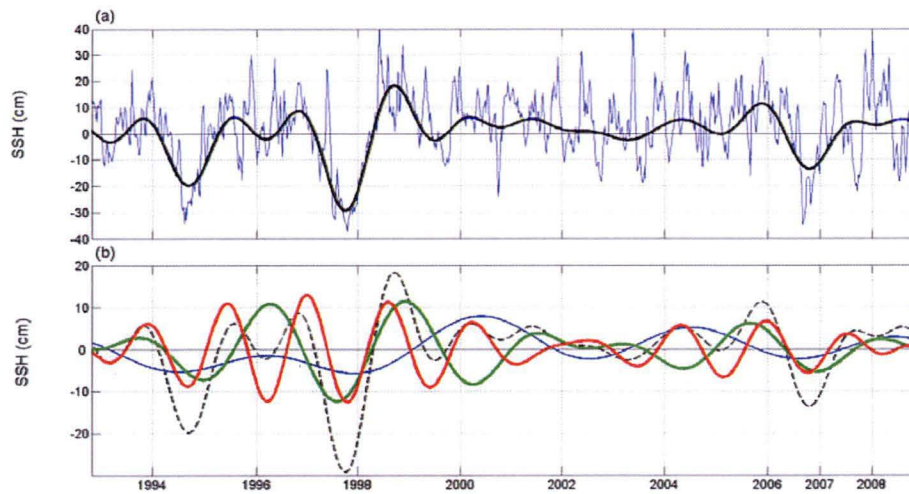

Figure 5.3.2. Analysis of the altimetry SSH at 7.7°S, 105.0°E for the period from October 1992 to December 2008. (a) Low-pass filtered SSH with cut-off at 14 months (black line) and original SSH (thin blue line). (b) Band passed signals: 18-month (red line); 3-years (green line); with periods longer than 4 years (blue line); and low-pass filtered SSH (black dashed line).

Prediction of the signal development matches the actual behaviour obtained from the longer time series (blue line) quite well. The red line predicts the lift of the thermocline in the fall of 2006 that contributes to the possibility of the cold water reaching the surface. Hence we could claim that in April 2006 there existed a precondition for the development of a positive IOD in fall 2006. To the best of our knowledge, no such prediction of positive IOD in fall 2006 was made at that time.

Unfortunately, the temporal resolution of the series seems to be not sufficient to determine the amplitude of the 36 month signal at the end of time series (green line in Fig.5.3.2 b). Therefore, the forecast made in April 2006 should be based only on the 18-month signal, which is better developed and requires less time for determination of its amplitude than the 36 month signal.

In April 2007 the estimated 18-month signal (Fig. 5.3.3 c, thick magenta line) had a positive value of about 5 cm. Taking into consideration the periodicity of this signal, its expected value at the time of fall 2007 (Fig. 5.3.3, red dashed line) is close to zero. In addition, the 18-month signal also had a tendency to decay. Therefore, one could expect no major IOD events during fall 2007.

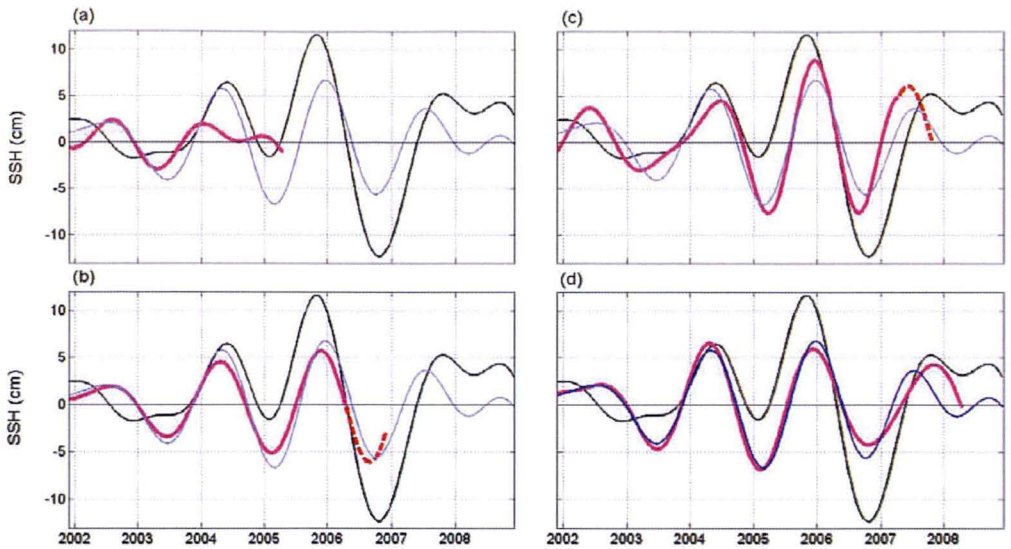

Figure 5.3.3. Analysis of the altimetry SSH at 7.7°S, 105.0°E and forecast of the 18-month signal. On all subplots the black lines represent low-pass filtered SSH with cut-off at 14 months, and thin blue lines represent the 18-month signal calculated from the time series for the whole period from October 1992 to December 2008. The thick magenta lines represent 18-month signal calculated from the time series ending in April 2005 (a); in April 2006 (b); in April 2007 (c); and in April 2008(d). The red dashed lines represent the forecasts of the 18-month signal from April to November 2006 (b) and from April to November 2007 (c).

Fall 2007 is considered as a year of weak positive IOD. From Figure 5.3.2a, one can see that the drop in the depth of the thermocline in Fall 2007 happened due to the SSH variation on timescales shorter than 14 month (black line), so that the cold SST anomaly in the fall of 2007 has occurred due to the high-frequency peak in fall 2007. The annual signal was much stronger in falls 2006, 2007, and 2008 than in 1994-1998, when interannual variability was mostly responsible for the SSH anomaly (Fig.5.3.2a).

The prediction of a positive IOD in 2008 based on the model output ("The Break", May 2008, vol.3, N 4) has not been realized. This can be explained by the decay of the low-frequency signal by this time (Fig. 5.3.2 a, black line). This also can explain the absence of a negative IOD in 2009 that has been predicted by Australian forecasting models in May 2009. This raises a question about how well the current models represent the interannual variability of the Indian Ocean, and particularly the variability with time scales of about 18 months.

5.4 Conclusions

In this Chapter we argued that the IOD has an oscillatory nature. This can be seen from analyses of different data sets as well as from a simple consideration of the sequence of positive and negative IOD years in 1980-2006. The years of IOD come in groups when positive IOD events are followed by a negative IOD and vice versa. The spectral analysis of the variability of the Indian Ocean shows the existence of oscillatory modes with periods of about 18 months and 36 month that are particularly strong during the years of high IOD activity.

We suggest that gaining an understanding of the oscillatory nature of interannual processes in the Indian Ocean and their relatively inertial character may lead to an improvement in the medium term forecasts of the IOD. We showed that the development of quasi-periodic signals in wind, subsurface temperature and altimetry SLA occurs up to two years before the similar signal manifests as SST anomaly. Development of the 18- and 36-month signals in the Java upwelling region can be considered as a precondition for the development of IOD, because these signals lift (depress) the thermocline and increase (reduce) chances of the cold water being lifted to the surface. To use this understanding for the IOD prediction, we face a problem of detecting a quasi-periodic signal at the end of a data set.

The other question that arises is the importance of constant monitoring of the state of subsurface dynamics. Because subsurface anomalies manifest mainly in the eastern Indian Ocean in the Sumatra-Java upwelling region, we suggest that continuously in-situ measurements of temperature close to the western coast of Sumatra at the depth of thermocline could be beneficial for the IOD prediction.

What we don't have here is any statistics or uncertainty in the predictive skill. This is something for the future but could be done with Monte Carlo simulations and/or models. However it is one of the requirements that would be needed for a proper forecasting system.

Chapter 6
Periods of IOD activity and historical data analysis

In Chapter 5 we proposed the idea that the interannual variability of the Indian Ocean, known as IOD, has an oscillatory character. This appearance of the IOD manifests itself in such a way that there typically are several IOD events in a row with one year or two year intervals between them; and these sequences are separated by much longer intervals. It was shown that during the periods of IOD activity two quasi-periodical signals with periods of about 3 years and 18 months exist in the ocean state variables, and their interference is largely responsible for the cold SST anomaly in the Java upwelling region and, possibly, for the IOD itself.

In the last two decades there were two periods of IOD activity: 1989-1999 and 2004-2007; however, it is not clear whether the observed character of the variability is specific to this period or if it persisted over a larger period of time. Below we investigate whether the same pattern of IOD activity can be found in the past (prior to 1989), and if can we also then find the two quasi-periodic signals associated with the IOD events. The relationship between 18-month and 3-year signals will be also under investigation.

6.1 Periods of IOD activity

6.1.1 Introduction

The idea that certain periods of time are characterized by IOD activity is not new. Based on the SST observations in the eastern equatorial Indian Ocean, Annamalai *et al.* (2005) noted that during the period 1950-2003 the IOD "events are strong in two decades, namely, 1960s and 1990s". Using model and singular value decomposition analysis, the authors found that the appearance of IOD depends on the phase of Pacific decadal variability. The Pacific decadal variability influences the IOD by changing the winds over the Indian Ocean ("atmospheric teleconnection") and by modulating the depth of the thermocline off south Java ("oceanic teleconnection"). The anomalously cool SST in the equatorial eastern Indian Ocean develops only "during decades when the thermocline is anomalously shallow, allowing entrainment of colder waters into the mixed layer". The authors suggested using the depth of the thermocline in the eastern equatorial Indian Ocean as a precondition for stronger or weaker IOD activity.

Ashok *et al.* (2004) also noted the possible existence of the "decadal IOD" "for the first time" (although we note that their paper was submitted half a year later than the paper of Annamalai *et al.* 2005). The authors found the strong decadal IOD occurrence from the late 1950s to 1960s and again from the late 1980s to 1990s. They write that the IOD mode index contains a quasi-decadal peak in the frequency spectrum at 125 months significant at the 90% confidence level (although they do not provide any evidence to support this statement, either in this or other referred papers).

Tozuka *et al.* (2007) extended both of these studies using a 200 year long output from a coupled ocean-atmosphere model (SINTEX_F1). They pointed to the existence of a clear east-west SST anomaly dipole pattern, similar to IOD, in both observation data and model output on decadal timescales. They argued that this pattern can be considered as a "decadal modulation of interannual IOD events", but not as a "decadal IOD".

6.1.2 The IOD activity index

Because all our analysis and conclusions are strongly based on identified years of IOD events, we start with the analysis of existing classifications of IOD years provided by different authors. These classifications are collected from four papers: Rao *et al.*, 2002; Yamagata *et al.*, 2004; Meyers *et al.*, 2006; and Ummenhofer *et al.*, 2009, and represented in Figures 1.3.3 to Fig. 1.3.6. All of the figures are included in Figure 6.1.1 below. We can see that in many cases the years that are considered as IOD years by one author are not consider as such by others. For example, during 1950-2000, Rao *et al* (2002) consider 18 years as IOD years, Ummenhofer *et al.* (2009) – 15 years, and only 8 of them are classified by both authors as years of IOD, that is less than 50%. This shows that the classification of IOD years is a quite complicated and not straightforward task.

For a clearer picture we introduce the IOD activity index as explained below. From the available four classifications we use only two. We do not use the classification by Yamagata *et al.* (2004) because they selected years of IOD and ENSO for purposes of composite analysis only and we do not use the classification by Meyers *et al.* (2006) because the classification by Ummenhofer *et al.* (2009) is an extended and corrected version of classification by Meyers *et al.* (2006) (G. Meyers, 2009 – personal communication).

The activity index is derived as follows. In Figure 6.1.1 red and blue indicate years of positive and negative IOD events according to the classifications of Rao *et al.* (2002); Yamagata *et al.* (2004); Meyers *et al.* (2006), and Ummenhofer *et al.* (2009). For calculation of IOD activity index we used only classifications by Rao *et al.* (2002) and Ummenhofer *et al.* (2009). The column labelled R+U contains a 1 if an event is identified in one of the classifications and a 2 if an event is identified in both. The right hand column in Figure 6.1.1 is the three-year running sum that we consider as the IOD activity index. This index is plotted in Figure 6.1.2.

	Yamagata	Rao	Meyers	Ummenh.	R + U	3 years sum
1950						0
1951						0
1952						1
1953					1	2
1954					1	3
1955					1	2
1956						2
1957					1	3
1958					2	4
1959					1	4
1960					1	4
1961					2	3
1962						4
1963					2	3
1964					1	3
1965						1
1966						0
1967						1
1968					1	1
1969						1
1970						0
1971						1
1972					1	1
1973						2
1974					1	2
1975					1	2
1976						1
1977						0
1978						0
1979						1
1980					1	1
1981						3
1982					2	2
1983						3
1984					1	2
1985					1	2
1986						1
1987						0
1988						2
1989					2	2
1990						3
1991					1	3
1992					2	3
1993						4
1994					2	2
1995						3
1996					1	3
1997					2	3
1998						3
1999					1	1
2000						0

Figure 6.1.1. Classifications of IOD years by Rao *et al.* (2002); Yamagata *et al.* (2004); Meyers *et al.* (2007), and Ummenhofer *et al.* (2009). Here the red colour shows positive IOD events, blue color – negative. The R+U column is a sum of IOD events from classifications by Rao *et al.* (2002) and Ummenhofer *et al.* (2009); and the last column contains a three years running sum of the R+U column.

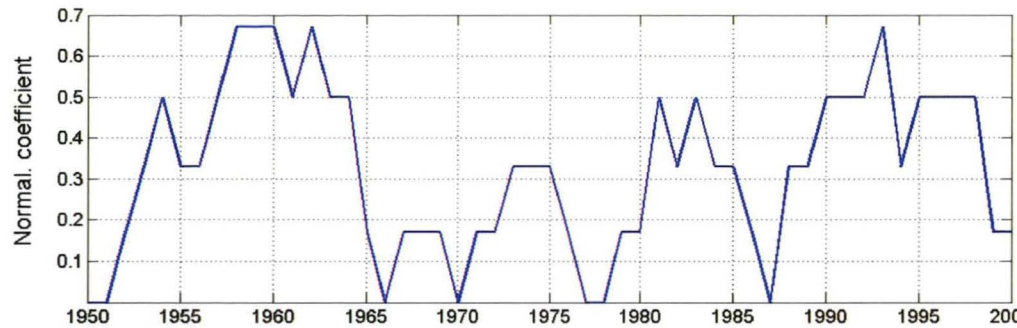

Figure 6.1.2. IOD activity index, calculated as a three-year running mean of the IOD occurrence (see Fig. 6.1.1) based on two classifications by Rao *et al.* (2002) and Ummenhofer *et al.* (2009).

This figure shows two long periods of high consistent activity of IOD: from 1952 to 1964 and from 1989 to 1998, and shorter period from 1980 to 1985. These periods of IOD activity agree with the previous findings by Annamalai *et al.* (2005); Ashok *et al.* (2004); and Tozuka *et al.* (2007).

6.1.3 Reconstructed sea level data

In previous chapters, based on several different data sets, we found that during IOD years 1989-1998 and 2005-2007 two clear and dominant signals developed in the Indian Ocean with periods of 18 and 36 months. To investigate the existence of these signals on a longer time scale and their relationship with the introduced above IOD activity index, we now analyse the available longer time series.

We use the reconstructed sea level data for 1950-2000 hosted by CSIRO Division of Marine and Atmospheric Research, Hobart (Church *et al.*, 2004). To investigate variability during different time periods, we subdivide this 51 year data set into four different time intervals, of 15 years each, and analyse them separately. The periods are:

- 1987 to 2001 as a recognized period of high IOD activity that largely coincides with the period of availability of altimetry SLA data;
- 1951 to 1965 as the second recognized period of high IOD activity (Fig.6.1.2);
- 1966 to 1980 with has lower activity in Figure 6.1.2;
- 1972 to 1988 which has an intermediate level of activity, with gap (Fig. 6.1.2).

Figure 6.1.3 presents the wavelet (a) and spectral (b) analysis of the SSH in a centre of action for IOD (7°S, 105°E) for the above four time intervals: 1951-1965, 1966-1980, 1972-1988, and 1987-2001.

The spectral analysis shows that the 18-month signal is noticeable, as expected, in 1987-2001 (Fig. 6.1.3 (4b) and in 1951-1965 (1b), but there is no such signal in 1966-1980 (2b) and 1972-1988 (3b). The wavelet analysis shows that the 18-month signal exists during 1992-1999 (4a) and during 1952-

1959 (1a), although according to 1b and 4b its amplitude in the 1990s is two times bigger than in the 1950s. During both these periods, along with the 18-month signals, we can clearly see the 3-year signal (Fig. 6.1.3 1a and 4a). From 1959 to 1964, the 18-month and 3-year signals merged into one signal with a period a little bit longer than two years - of about 26 months (from the wavelet analysis, Fig. 6.1.3 1a); it also can be seen in the frequency spectrum (Fig 6.1.3 1b).

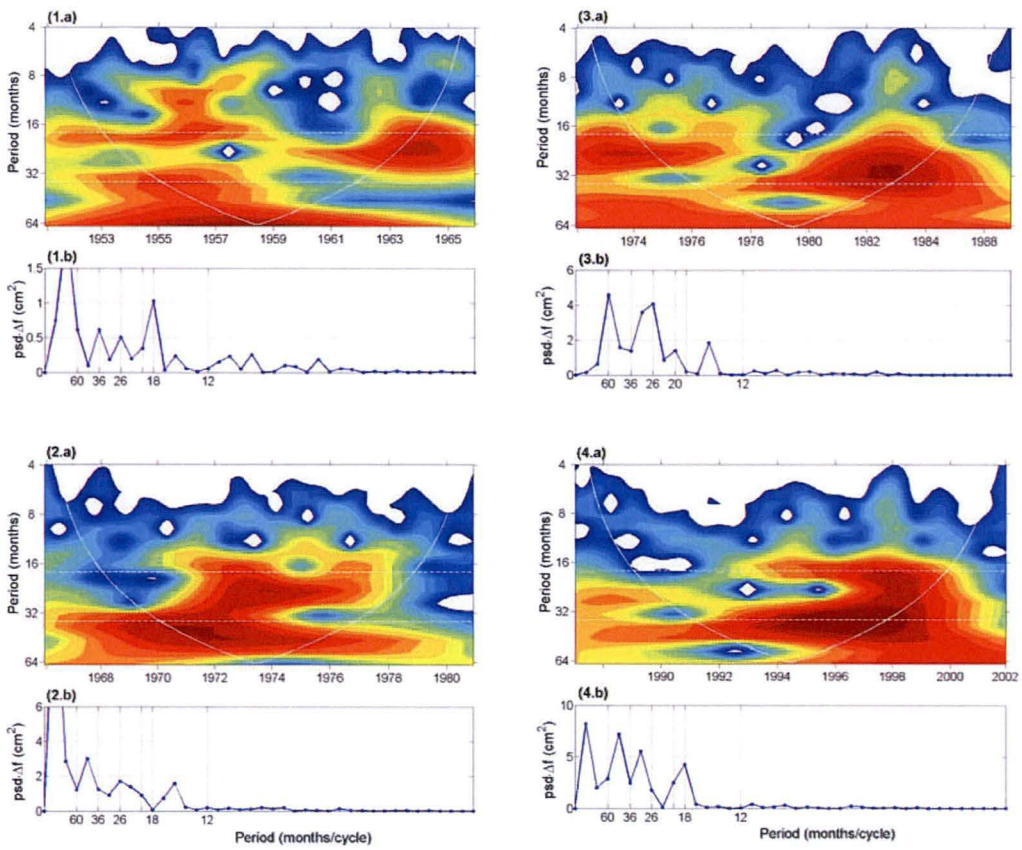

Figure 6.1.3. Wavelet (a) and spectral (b) analysis of reconstructed sea level data for the location 7°S, 105°E for four time intervals: (1) 1951-1965, (2) 1966-1980, (3) 1972-1988, and (4) 1987-2001. White dashed lines correspond to periods of 18- and 36- months.

Below we present the spectral density maps for each frequency for three 15-year periods: 1951-1965, 1966-1980, and 1987-2001 (Fig. 6.1.4 – Fig. 6.1.6). The maps are calculated using the algorithm described in Section 3.3.3.

Analysing these maps, we can note that generally the variance of SSH was higher in 1987-2001 than during the two other periods and that their amplitude in 1987-2001 is at least two times bigger than in 1952-1965. As expected, Figure 6.1.6 shows a clear 18-month and 3-year signal that developed in the eastern Indian Ocean close to Indonesia during 1987-2001. This map is very similar to the one obtained from altimetry SLA data (see Fig. 3.3.7). Further on, the 18-month signal, is clearly presented in this SSH reanalysis data during 1951-1965 (Figure 6.1.4). This 18-month signal exhibits

high variability south-west of the Sumatra-Java coast, with another area of weaker variability in the western part of the Indian Ocean south from the equator. There is also a weak 26-month signal with the spatial distribution similar to that of the 18-month and 3-year signals. The 18-month signal is almost completely absent during 1966-1980, but instead there appears a signal with a longer time scale of about 26 months.

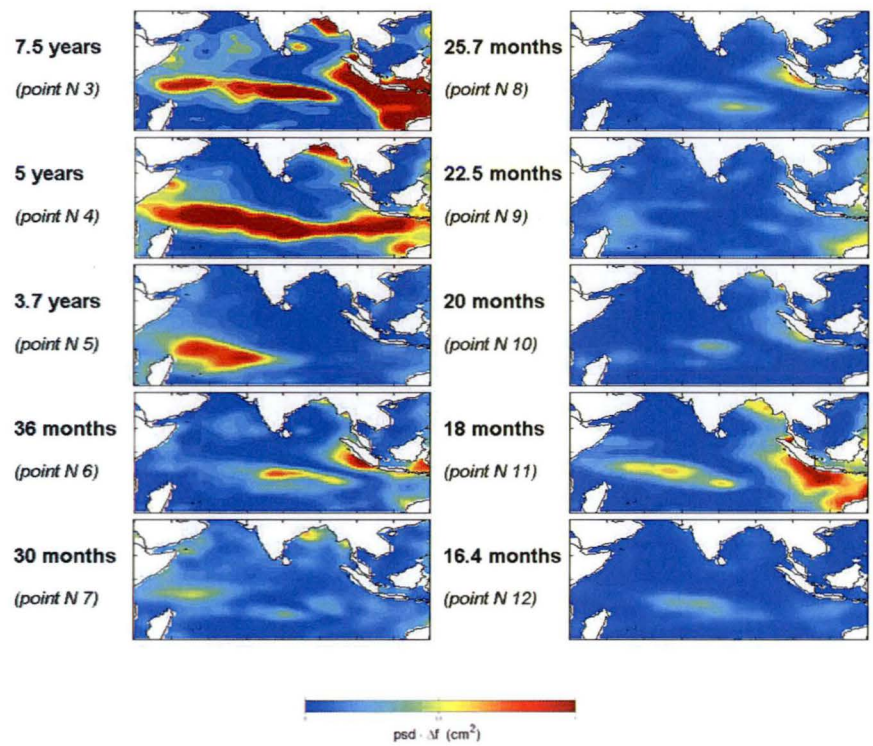

Figure 6.1.4. Maps of PSD of reconstructed sea level for individual spectral components in 1951-1965.

Therefore, during the periods of high IOD activity (Fig. 6.1.2) the SSH reanalysis data shows the presence of the 18-month and 3-year signals in the Indian Ocean, while outside these periods it shows signals with a different time scale. The spatial distribution of the 18-month signal during 1952-1965 is very similar to that during 1987-2001.

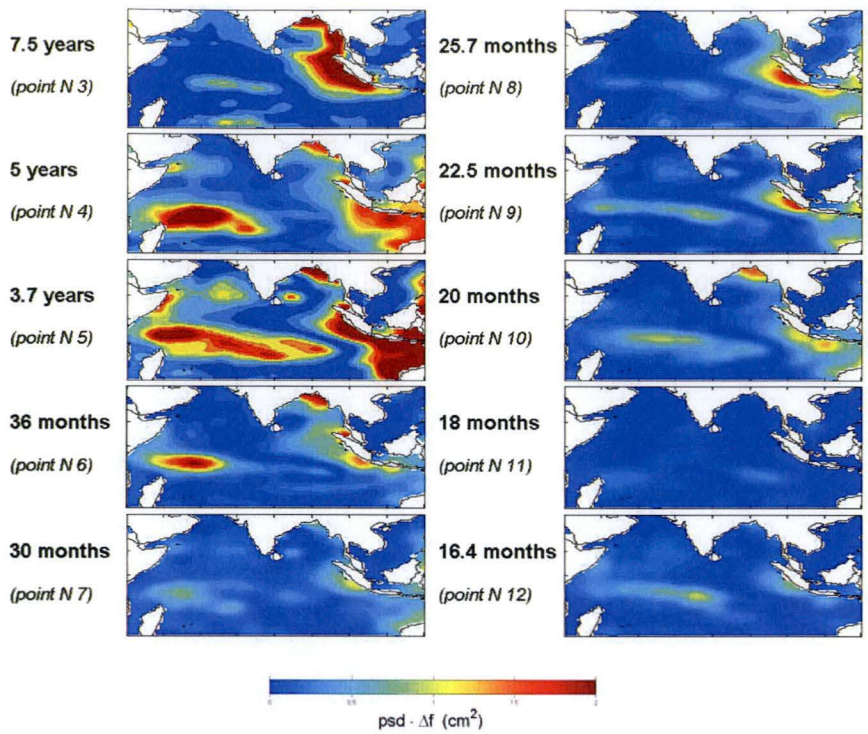

Figure 6.1.5. As in Figure 6.1.4 but for 1966-1980.

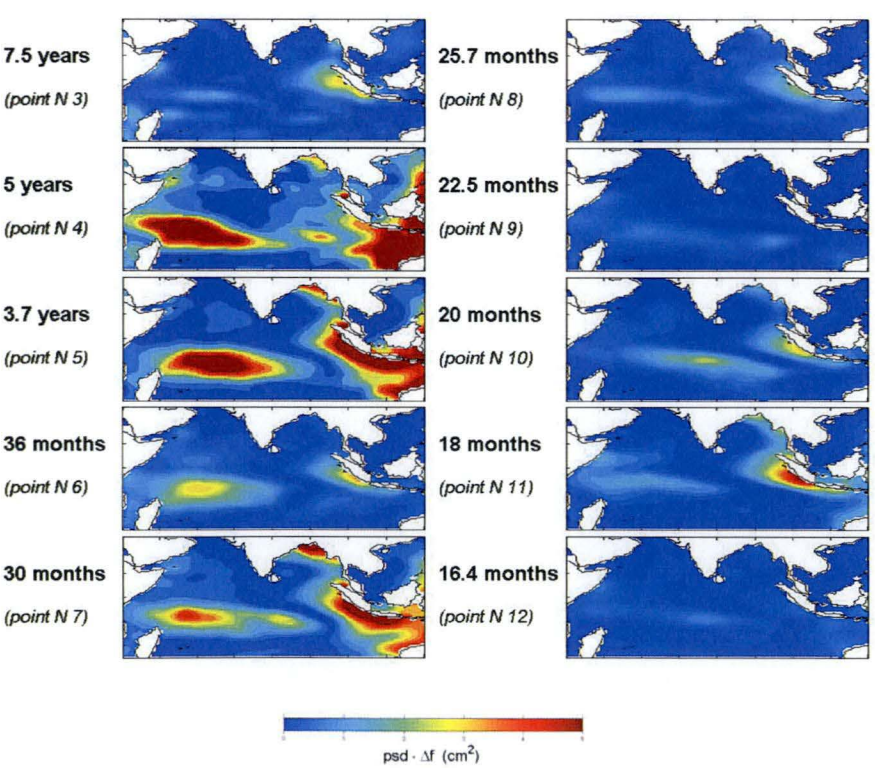

Figure 6.1.6. As in Figure 6.1.4 but for 1987-2001.

6.1.4 Preconditions for development of the 18-month signal

As we outlined in introduction to this Chapter, Annamalai *et al.* (2005) demonstrated that the depth of the thermocline (h) in the eastern equatorial India Ocean can be considered as a precondition for the IOD because "the IOD events are favoured only when h is shallow enough in the eastern equatorial Indian Ocean for SST to cool water below 27.5°C, the threshold required for deep convention in the Tropics". They introduced the IOD preconditioning index (Fig. 6.1.7) that represents a decadal time scale of difference in h. We can see from this figure that shallower-than-normal h was observed in 1958-1969 and 1990-1996. In the previous section based on the reconstructed sea level data, we found that during these years the 18-month signal has developed in the eastern tropical Indian Ocean. Based on this and previous analyses, we suggest that during periods when the thermocline in the eastern equatorial Indian Ocean is shallow enough, the 18-month and, possible, 3-year signals start to develop and, most importantly, are supported by the response of the Indian Ocean system during several successive years.

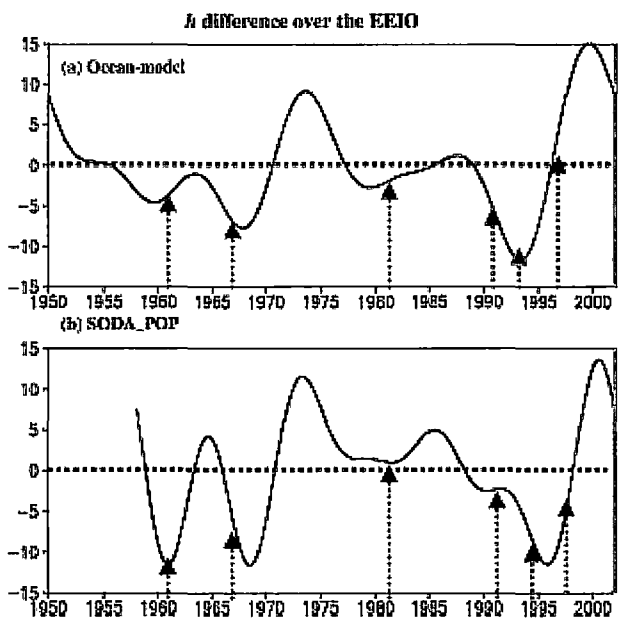

Figure 6.1.7. Time evolution of the preconditioning index representing the decadal time scale difference in h (depth of thermocline) over the eastern equatorial Indian Ocean, from (a) the ocean model and (b) SODA-POP (the Simple Ocean Data Assimilation Parallel Ocean Program). The dotted vertical lines indicate years of strong IOD events (after Annamalai *et al.*, 2005).

6.2 Historical data analysis

6.2.1 Introduction

In the previous section we documented the 18- and 36-month signals in the Indian Ocean since 1950 (Fig. 6.1.3). It is now interesting to see whether this variability is mainly a feature of that particular period, or if it also existed before 1950. The answer can provide important clues to our understanding of the origin of these signals, their behaviour, and their role in the IOD.

In this section we analyse a number of available historical data sets for the presence of the 18- and 36-month signals. The availability and quality of the historical data impose rather big limitations and restrictions for this investigation, for the following reasons:

(a) Spectral analysis is very sensitive to the accuracy of each point in the time series. A single wrong value in the time series can produce unpredictable (aliased) results. This particularly applies to using the coral data as proxy climate records.

(b) Reconstructed data sets often use the data for the last two decades to obtain the basis vectors for the subspace of the system. This may implicitly propagate the characteristic features of the system for the last decades over a much longer time period, regardless of whether these features existed in reality. We are not sure if this applies to the temporal variability, but comparisons between some available reconstructed products with reanalysis products points towards such a possibility.

(c) The 18-month signal has biggest variability in most data sets (SSH, SST, depth of thermocline) in a very limited area over the Indian Ocean – the narrow strip along the Sumatra-Java coast (Fig. 3.3.7, Fig. 6.1.4, and Fig. 6.1.6). This substantially restricts the suitability of the existing historical and reanalysis data sets for searching for the presence of this signal in the past.

(d) Uncertainty in the existing classifications of the past IOD events, particularly before 1950. For example, for the period from 1874 to 1940, there are a total of 33 IOD events in three different classifications (by Rao *et al.*, 2002; Meyers *et al.*, 2007; Ummenhofer *et al.*, 2009), and only 7 of them are classified as IOD years by all three studies.

6.2.2 Classifications of IOD before 1950

We start with presenting existing historical classifications of IOD. The table with these classifications for the period after 1950 has been shown in Figure 6.1.1. Figure 6.2.1 presents the classifications of IOD years before 1950. It can be seen that the classification of IOD years differs significantly, particularly when comparing classifications by Rao *et al.* (2002) with those by Meyers *et al.* (2007) and Ummenhoffer *et al.* (2009). The differences occur because Rao *et al.* (2002) focused the classification on the SST difference across the Indian Ocean, while Meyers *et al.* (2007) and Ummenhoffer *et al.* (2009) focused on the upwelling region off Sumatra and Java. Taking account of the times when Rao agrees with Meyers and Ummenhoffer (noted in the column labeled

all), there are several periods when IOD events happened in a sequence: in 1885-1896, 1901-1910, 1917-1926, and, possibly, 1942-1946. These time intervals can be assumed to be the periods of high IOD activity.

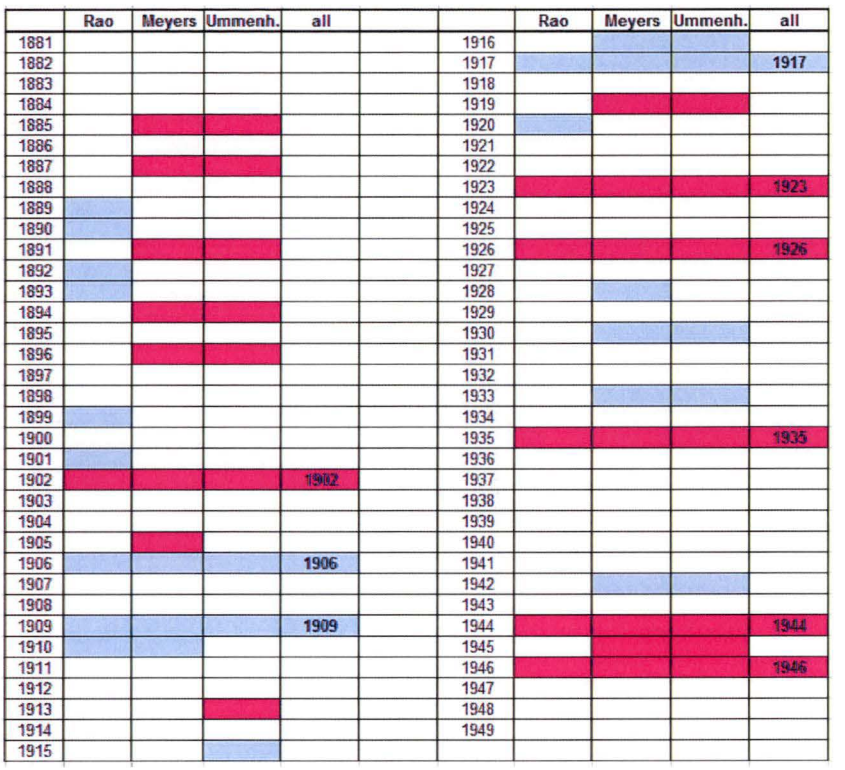

Figure 6.2.1. Classifications of IOD events prior to 1950 by Rao *et al.* (2002); Meyers *et al.* (2006); and Ummenhofer *et al.* (2009). Red colour denotes a positive IOD event, blue – a negative event. The last column marks years considered as IOD years by all three authors.

6.2.3 Tide gauge data

The records of tide gauge data are dated back to 1700 (see Chapter 2.1.1 for data description). This is the longest existing observation record of any type. Unfortunately, due to the location of tide gauge stations they do not reveal much about the open ocean signals. Never-the-less, we searched for the 18-month and 3-year signals in the available data. Results are discussed below.

First, we select the tide gauge stations that are located in regions associated by the previous analyses with high levels of the 18-month signal. There are very few tide gauge stations with historic records over the Indian Ocean (see Fig. 2.1.1 for station positions and Fig. 2.1.2 for data descriptions). Unfortunately, in most locations, the data were collected irregularly, with big gaps between measurements, which make these data unsuitable for reliable use of spectral analysis. Below we describe several tide gauge data sets and results of their analysis.

Christmas Island station (10.25°S, 105.40°E) N 563/001. This station is near the Java upwelling region, which represents the best possible location for our purposes. But, unfortunately, the records were made only from 1962 to 1991, and the measurements are very sparse, with the longest period of continuous measurements of 18 months, and with only 45 monthly measurements during 30 years of observations altogether.

Cocos Island (12.07°S, 96.53°E) station N 680/520, (West Island) has good data for 3 years of observation 1968-1970, and station N 680/521 (Home Island) has good data starting from 1986 (up to 2007). Spectral analysis of this later data set (not shown) shows the absence of an 18-month signal. This agrees with the distribution of SSH anomaly in this frequency band (Fig. 3.5.2), with no significant variability of the 18-month band in this area.

Diamond Harbour (22.12°N, 88.10°E) station N 500/131 has a very good and long data set (from Jan. 1948 to Dec. 2006), but its position does not allow us to observe any interesting variability.

Ko Taphao Noi (07.50°N, 98.26°E) station N 545/001. Spectral and wavelet analyses of data from this station are presented on Figure 6.2.2 a,b,c. The wavelet decomposition (Fig. 6.2.2 a) is very similar to that of altimetry (Fig. 3.3.4 d) and subsurface temperature (Fig. 3.2.9) during 1992-2000. Similar to other locations, this station clearly shows the existence of signals with periods of 18 months and 3-4 years. We find that the wavelet decomposition exhibits a similar shape also in the 1940s, with a maximum at 20 months (Fig. 6.2.2 c). This is one of the suggested periods of high activity of the IOD (Fig. 6.2.1).

Colombo-A (06.56°N, 79.51°E) station N 520/002 has data from January 1953 to December 1965, a total time span of 13 years. The spectrum has maxima at 4 years and at 22 months (Fig. 6.2.2 d).

Cochin (09.58°N, 76.16°E) station N 500/081 (Fig. 6.2.2 e,f) as well as the *Colombo-A station* are interesting only because they show some variability around 18-months during periods of high IOD activity in 1990-1999 (Fig. 6.2.2 e) and more clearly during 1945-1951.

Overall, our analysis of the historic tide gauge data does not yield particularly convincing results, except, possibly, the fact that *Ko Taphao Noi* station can register a signal very similar to that from the Sumatra-Java upwelling region in 1992-1999. This happens due to the propagation of the signal to the north that can be seen from Movie movie_SLA_18m.avi from Appendix. It is interesting that in 1944-1952, the signal from this station has a similar spectrum to that in 1992-2002, although much weaker in amplitude.

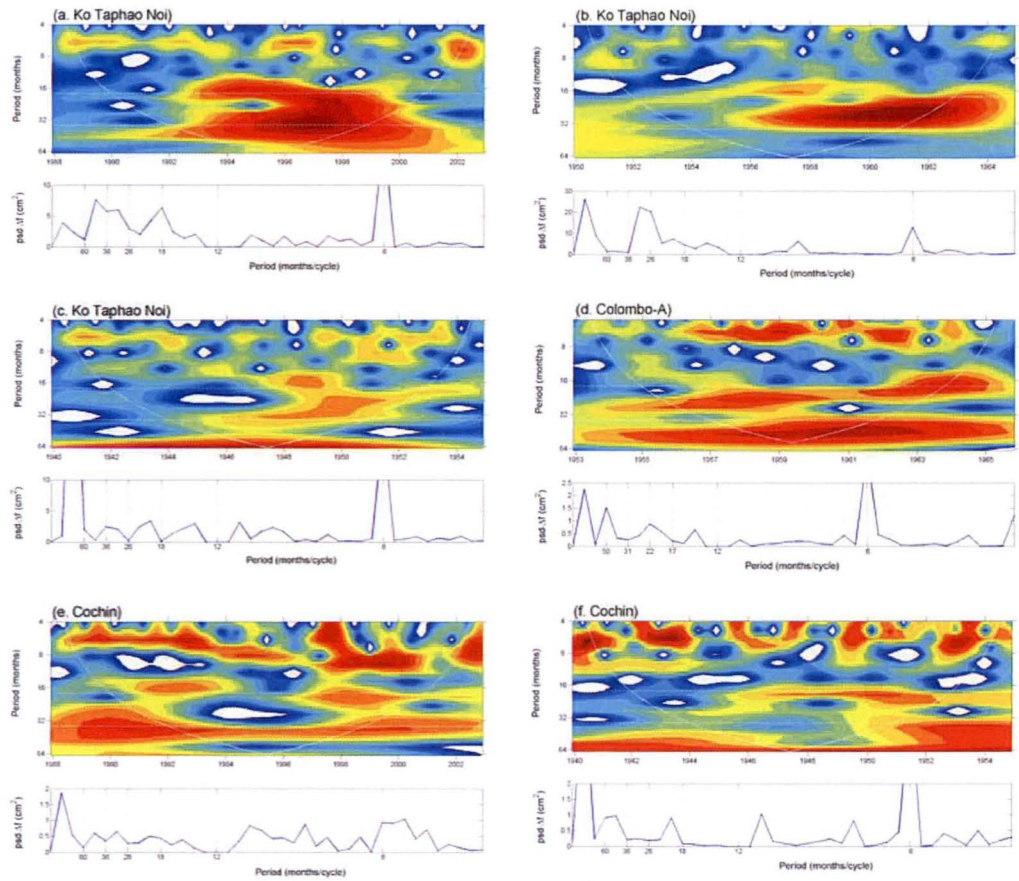

Figure 6.2.2. Wavelet and spectral analyses of tide gauge data for different stations: (a)-(c) *Ko Taphao Noi* (07.50°N, 98.26°E); (d) *Colombo-A* (06.56°N, 79.51°E) ; (e)-(f) *Cochin* (09.58°N, 76.16°E). White dashed lines denote 18-and 36-month signals.

6.2.4 Coral data as proxy climate records

Below we analyse a different data sets: coral Oxygen Isotope data from Bali (8.15°S, 115.30°E) (1782 – 1989) and Mentawai Islands (2.5°S, 99°E) (1858 – 1997).

Figure 6.2.3 shows a wavelet decomposition of coral records from Bali for the period from 1782 to 1989. Most of the signal variance is in the low frequency part of the spectra. The variability with period between 1 and 3 years does exist, but is rather patchy, so it is difficult to make any conclusions. Let us examine two periods that according to the IOD classifications may be the periods of high IOD activity: 1901-1910 (Fig. 6.2.1) and 1953-1964 (Fig. 6.1.1 & Fig. 6.2.1). The wavelet and spectral analyses of these periods are shown in Figures 6.2.4 and 6.2.5.

In ten years from 1901-1910 there were possibly six IOD events; three of them are recognized by all three authors (Fig. 6.2.1). The variability during these years in the coral records is not very strong (Fig. 6.2.3), but (and this is very interesting) it has a clear signal with the 18-month period

(Fig. 6.2.4 b, low panel). This signal started in 1900 and decayed in 1910 (Fig. 6.2.4 a, upper panel), showing a good match with the period of high IOD activity (Fig. 6.2.4 a,b). There is no significant signal with a 3-year period during this time in the spectrum of coral data.

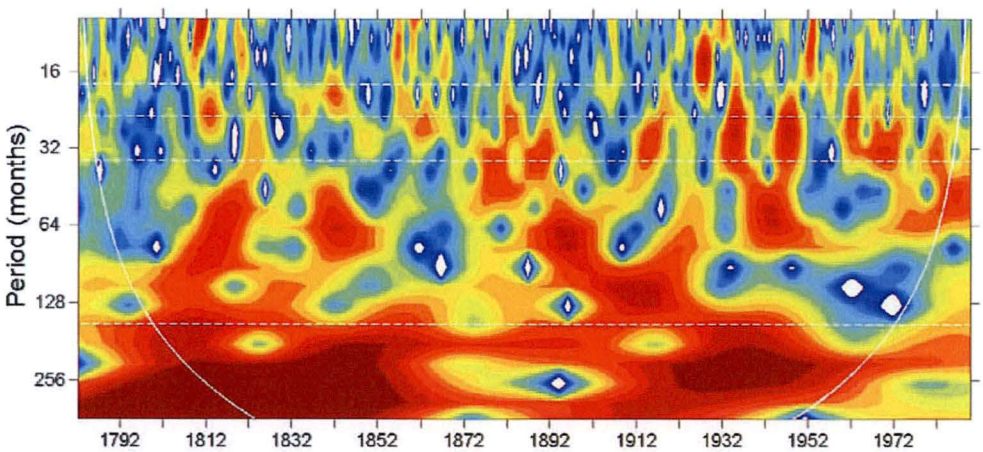

Figure 6.2.3. Wavelet and spectral analyses of coral data set from Bali (8.15°S, 115.30°E). White dashed lines correspond to periods of 18-, 24- and 36-months.

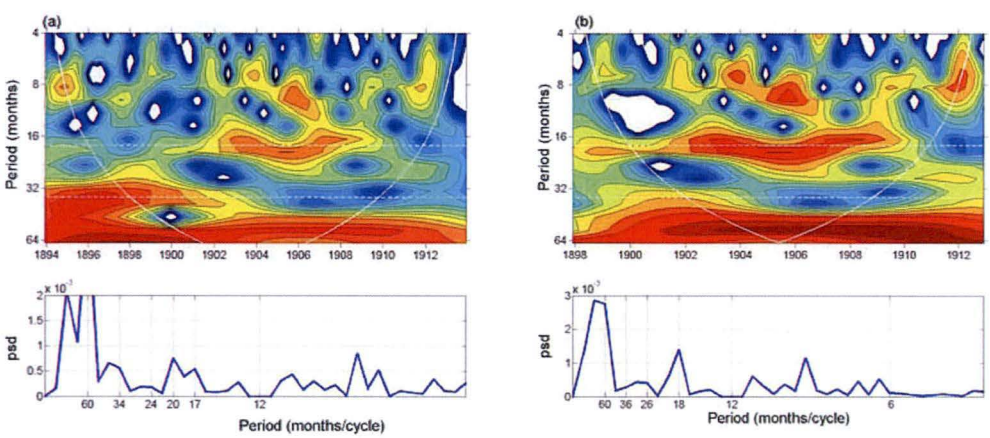

Figure 6.2.4. The same as Figure 6.2.3 but for: (a) 1894-1913 and (b) 1898-1912 years.

During 1950-1964 there is a clear peak in the spectrum at 18 months (Fig. 6.2.5 b, lower panel). The wavelet decomposition shows that this 18-month signal started in 1949 and decayed in 1959 (Fig. 6.2.5 a). It seems that the period of this signal gradually changed from 18 to 28 months. During this period of 12 years from 1953 to 1964, there are 11 years considered as IOD years by at least one of the classifications in Fig. 6.1.1. Similarly in the period 1898-1912, no significant 3-year signal is found. We stress that for both of these examples, the 18-month signal exists only during the periods of IOD activity and is absent both before and after this period (Fig. 6.2.4.a & Fig. 6.2.5 a, upper panels).

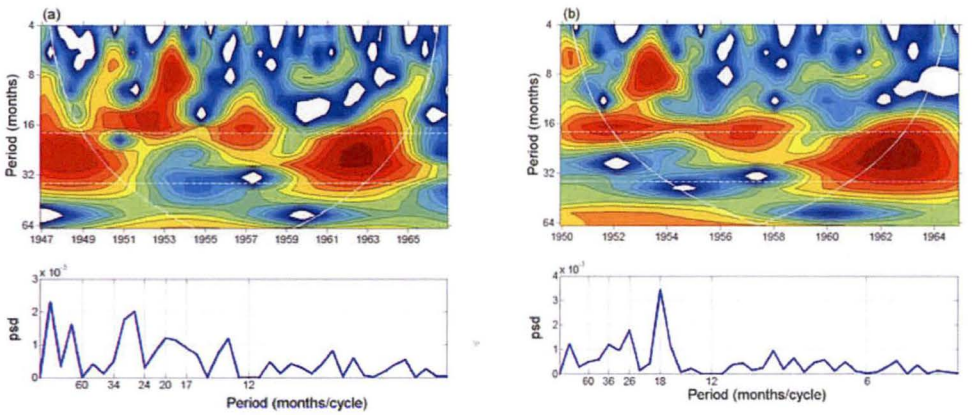

Figure 6.2.5. The same as Figure 6.2.3, but for: (a) 1947-1966 and (b) 1950-1964 years.

Analysis of the coral data set from the Mentawai location shows the same (as for the Bali data set) high variability of signals with different time scales (not shown). Figure 6.2.6 shows the wavelet and spectral analyses for the same periods of high IOD activity as above. The 18-month signal (16-month for 1949-1963) is present during both periods in the wavelet decompositions (upper panels) and also can be clearly seen in spectra (lower panels).

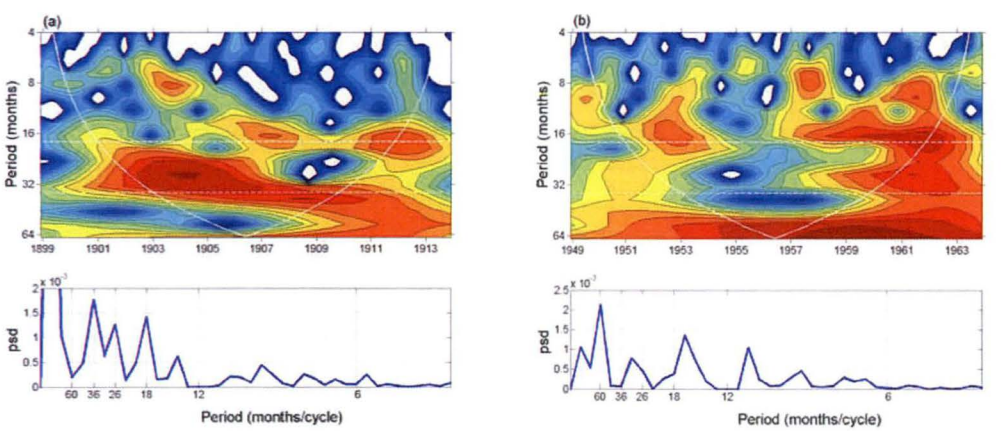

Figure 6.2.6. The same as Figure 6.2.3 but for the Mentawai data set: (a) 1899-1913 and (b) 1949-1963 years.

Regarding the other periods characterised by high IOD activity, such as 1917-1926, one still can find some signature of the 18-month signal, but the spectra are usually very wide with the maximum at a period longer than 18 months.

6.2.5 Reconstructed SST

In the previous section, we found evidence of the existence of the 18-month signal during 1900-1910 in coral data sets. Because the coral data were collected 10 metres below the sea surface, we can expect to find this signal in the SST reanalysis data. As an example, we use the HadISST reanalysis data. Figure 6.2.7 represents the wavelet and spectral analysis of SST, these data have been averaged along quite a big area of the equatorial easterly Indian Ocean used for calculation of DMI – IODE for the same time period as for coral data analysis in Figure 6.2.4. The existence of the 18-month and 3-year signals is still quite clearly evident (lower panels). The wavelet decomposition shows the presence of the 18-month signal during 1902-1910. The 3-year signal, that was absent in the coral data, is quite strongly presented in the HadISST data. A possible explanation for this discrepancy is that for calculation of the IODE, a very large area in the equatorial eastern Indian Ocean was used that is strongly influenced by the Pacific and therefore contains the 3-year component, while the coral data were collected in a particular local location where the ratio of these two signals favours the 18-month signal.

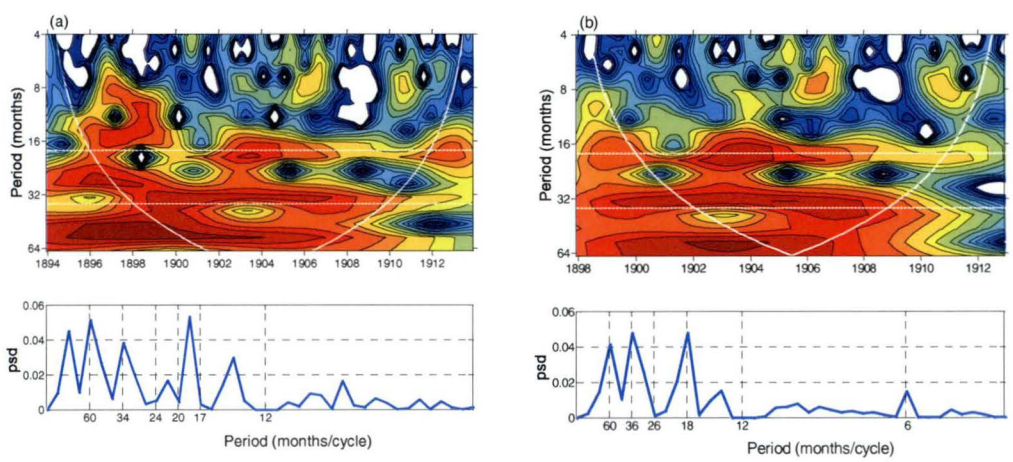

Figure 6.2.7. Wavelet and spectral analyses of IODE from the HadISST data set. White dashed lines correspond to periods of 18-, 24- and 36-months.

Analysis of HadISST data during 1947-1966 shows strongest variability at periods of approximately 24-26 months (not shown).

6.3 Conclusions

In this Chapter we have tried to extend the previous analysis of the IOD and associated it with ocean variability to time prior to the epoch of satellite observations. We considered the existing classifications of the IOD; reanalyses of SST; reconstructed sea level data; DMI index derived from the SST reanalysis; and finally, historic tide gauge and coral data.

To confirm the findings of a number of previous studies suggesting that IOD events occur mostly during some continuous periods of time that we refer to as the periods of IOD activity, we introduced the IOD activity index. It is based on the existing classifications of IOD and represents the certainty of occurrence of IOD in particular years. In the following analysis of various data for the last six decades we confirmed that during each period of IOD activity, a strong 18-month signal has always developed in the Indian Ocean.

We also attempted to confirm the main findings of previous chapters by analyzing the available historic data sets (tide gauge data and coral data); however, due to the limitations of these datasets, it is difficult to draw any definite conclusions in regard to quantitative characteristics of the interannual variability of the Indian Ocean. At this stage it seems that the available data do not contradict the findings of the previous chapters of this thesis, and in some cases corroborate nicely with those findings. For example, the wavelet analysis of the coral data shows the presence of a strong 18-month signal during the period of IOD activity in 1898-1912, and to a lesser degree, in 1947-1966 (Fig. 6.2.4 and 6.2.5). Hence we believe that the 18-month signal seen in the Indian Ocean is a permanent feature and is not restricted to events of the last century (since the 1950s).

Chapter 7.
Conclusions

This thesis has investigated the low-frequency variability of the Indian Ocean, by which we understand processes with characteristic periods from 6 months to several years. The analysis is based on a number of observational and reanalysis data sets including altimetry SLA, SST, subsurface temperature from the XBT lines, surface winds, DMI, historic tide gauge records and coral core records. To a large degree the analysis that was undertaken became possible because of the availability of sufficiently long time series of satellite SLA observations.

The main analysis methods used in the thesis are spectral analysis, wavelet analysis and a variety of other methods including EOF analysis. Our principal approach was to decompose a complex signal into a number of simpler signals and try to understand the variability of the Indian Ocean based on studying the properties and behaviour of these more basic signals. Despite the extensive literature on the variability of the Indian Ocean, to the best of our knowledge no systematic analysis of this kind has been conducted so far.

The commonly accepted, present-day division of the variability of the Indian Ocean distinguishes the following characteristic time scales: semi-annual (6 months), annual (1 year), quasi-biennial (2-3 years), ENSO (3-7 years), decadal and bi-decadal. In this thesis, based on the results of analysis of a number of independent data sets, we argue in favour of a different division for the signals with periods from 1 year to 3 years. In particular, we discover a strong 18-month signal. We demonstrate that this signal, overlooked or misunderstood in previous studies, plays a major role in the variability of the tropical Indian Ocean in general, and specifically in the life cycle of the IOD. We consider implications of this finding for understanding of the physical nature of IOD and its prediction.

The main results of our analysis are as follows.

1. It is found that in most regions of the Indian Ocean, the low-frequency variability is concentrated in five spectral bands: semi-annual, annual, 18-20 months, 3 years, and 4 years and longer; at least during the last two decades.

2. Using several data sets as: altimetry SLA, reconstructed sea level, wind and SST, the spatial distributions of the power spectral density of signals in each major band have been investigated, as well as their spatio-temporal variability by means of movies.

3. The presence of a strong and well defined 18-month signal is one of the main findings of this study. The 18-month signal presents only during years when the IOD is active or begins to develop. That points on a close connection of this signal with the IOD mode.

4. Despite the conclusions of previous studies pointing at the existence of the quasi-biannual mode, no substantial signal with the bi-annual (24 month) period was found; at least during the last 20 years.

5. Contrary to the common view, we argue that the IOD represents a continuous oscillatory process rather than every event is triggered by a particular ocean-atmosphere state. This is confirmed by finding that the IOD events come in groups, when positive IOD are followed by a negative IOD and vice versa. This phenomenon can be largely described as the interference of two quasi-periodic 18-month and 3-year signals.

6. Consistent with some prior studies (Annamalai *et al.*, 2005; Ashok *et al.*, 2004), it is found that there are periods of high and low activity of the IOD, so that the IOD events do mostly occur in a sequence during the periods of high IOD activity.

7. The analysis of long-term reconstruction and reanalysis data shows that during the last 60 years periods of developed 18-month signal strongly correlate with periods of high IOD activity.

8. We hope that knowledge of continuous character of IOD events can help for the IOD prediction, which have a major economic impact on the countries in the Indian Ocean region including Australia. Our pilot attempts of forecasting the known behaviour of the IOD mode in the past indicate that the development of the 18-month signal can considered as a precondition of the IOD and may provide now the best opportunity for the medium-term (about 2 seasons in advance) forecast.

The above findings pose a number of questions for future research. What is the relation between the 18-month and 3-year signals? What is the degree of their independence or interconnection? What physical mechanisms are behind the 18-month and three-year time scales?

The existence of strong 18-month and 3-year signals in SST and surface wind points at the importance of considering the whole ocean-atmosphere system for understanding of the variability of the Indian Ocean at these time scales. Further analysis and comparison of features of the 18-month and 3-year signals in both the ocean and atmosphere can yield important findings for understanding of the functioning of this coupled system.

A signal with a period of about 18-months was recently discovered in the Pacific Ocean (Keenlyside *et al.*, 2007). The authors call it a sub-ENSO mode. Our research indicates that the 18-month signal is a mode of the Indian Ocean and likely to be connected in some way to the Pacific signal. It is interesting to investigate the connection between the 18-month signals in the Indian and Pacific oceans in more detail.

Overall, it seems to us that this study has posed more questions than it has provided answers. However we hope that the findings and analyses of this thesis, and in particular the concepts of the 18-month and 3-year signals and their connection with the IOD, will be gradually accepted by the scientific community and prove to be productive in future research, both observational and theoretical.

List of Figures

Figure 3.1.5 (a) Time series of normalized Monsoon rainfall index (CI1) and westerly shear index anomalies (WSI1). Black dots signify strong and weak TBO years, where both the CI1 and WSI1 are relatively greater or less than in preceding and following years. (b) Power spectrum of the monthly values of CI1, with the 95% significance level shown as the dotted line. (c) Power spectrum of the monthly values of WSI1 (after Loschnigg, 2003).

Figure 3.1.6. Variance preserving spectra (cm^2) of dynamic height anomaly from (a,c) XBT data and (b,d) the POP model at the southern (a, b) and northern (c, d) ends of the IX 1 line (after McClean *et al.*, 2005; the mark at 16.4 months estimated and added by Sakova).

Figure 3.1.7. Spectra of SSH (upper curve; cm^2 $cycles^{-1}$ day^{-1}) and zonal wind stress [lower curve; 0.1 × (dyne cm^{-2})^2 $cycles^{-1}$ day^{-1}]. The spectra are averaged over 10°S–10°N, 40°–100°E. The periods for the major spectral peaks are indicated. The 95% error bar for the spectra is shown (after Fu, 2007).

Figure 3.1.8. (a) Time series of interannual anomalies of along path wind averaged along the equatorial and coastal waveguides in the Indian and Pacific Oceans (see text). (b) Variance-preserving spectra of the wind series in (a). The line frequencies plotted are, from left to right, for 10, 5, 2, 1, and 0.5 yr (after Wijffels and Meyers, 2004).

Figure 3.2.1. Standard deviation of the sea surface height anomaly in the tropical Indian Ocean (in cm). The shaded areas correspond to standard deviation larger than 5 cm. The straight lines show XBT sections IX-1 and IX-12 (after Feng and Meyers, 2003).

Figure 3.2.2. Time series of temperature profile (upper panel) and interannual temperature anomaly profile (lower panel) at the northern end of IX-1 section of XBT line, 6.78°S, 105.17°E. The station position is marked as a red dot in the inset of the upper panel (after Feng and Meyers, 2003).

Figure 3.2.3. Annual mean temperature structure (upper panel) and interannual temperature standard deviation (lower panel) in the upper 440m along the XBT IX-1 section. The shaded areas in the lower panel denote standard deviation larger than 0.5°C. The inset shows the location of the XBT IX-1 section (after Feng and Meyers, 2003).

Figure 3.2.4. (a) IOTA temperature data in Box 2 (Fig. 2.1.4) with corners at 7.0°S, 104.0°E and 8.0°S, 106.0°E. The yellow line represents the depth of the 20°C isotherm. (b) PSD of the depth of the 20°C isotherm. Here psd is power spectral density, and Δf is frequency resolution in cycles per month; psd·Δf is equal to the time averaged variance, with units of m^2.

Figure 3.2.5. Subsurface temperature from IOTA data set averaged in Box 2 (Fig. 2.1.4) with corners at 7.0°S, 104.0°E and 8.0°S, 106.0°E at different depths: 5m, 30m, 70m, 100m, 120m, and 140m.

signals. (b) Global wavelet spectrum; the black dashed lines correspond to 6-, 19-, and 34-month signals. (c) PSD of SSH, where psd is power spectral density, and Δf is frequency resolution in cycles per month; psd·Δf is equal to the time averaged variance, with units of cm^2. (d) Low-pass filtered SSH with cut-off frequency at ~1/14 months (black line) and original SSH (thin blue line). (e) Band passed signals: 36-month (green line); 19-month (red line), and low-pass filtered SSH (black dashed line).

Figure 5.3.2. Analysis of the altimetry SSH at 7.7°S, 105.0°E for the period from October 1992 to December 2008. (a) Low-pass filtered SSH with cut-off at 14 months (black line) and original SSH (thin blue line). (b) Band passed signals: 18-month (red line); 3-years (green line); with periods longer than 4 years (blue line); and low-pass filtered SSH (black dashed line).

Figure 5.3.3. Analysis of the altimetry SSH at 7.7°S, 105.0°E and forecast of the 18-month signal. On all subplots the black lines represent low-pass filtered SSH with cut-off at 14 months, and thin blue lines represent the 18-month signal calculated from the time series for the whole period from October 1992 to December 2008. The thick magenta lines represent 18-month signal calculated from the time series ending in April 2005 (a); in April 2006 (b); in April 2007 (c); and in April 2008(d). The red dashed lines represent the forecasts of the 18-month signal from April to November 2006 (b) and from April to November 2007 (c).

Figure 6.1.1. Classifications of IOD years by Rao *et al.* (2002); Yamagata *et al.* (2004); Meyers *et al.* (2006), and Ummenhofer *et al.* (2009). Here the red colour shows positive IOD events, blue color – negative. The R+U column is a sum of IOD events from classifications by Rao *et al.* (2002) and Ummenhofer *et al.* (2009); and the last column contains a three years running sum of the R+U column.

Figure 6.1.2. IOD activity index, calculated as a three-year running mean of the IOD occurrence (see Fig. 6.1.1) based on two classifications by Rao *et al.* (2002) and Ummenhofer *et al.* (2009).

Figure 6.1.3. Wavelet (a) and spectral (b) analysis of reconstructed sea level data for the location 7°S, 105°E for four time intervals: (1) 1951-1965, (2) 1966-1980, (3) 1972-1988, and (4) 1987-2001. White dashed lines correspond to periods of 18- and 36- months.

Figure 6.1.4. Maps of power spectral density of reconstructed sea level for individual spectral components in 1951-1965.

Figure 6.1.5. As in Fig. 6.1.4 but for 1966-1980.

Figure 6.1.6. As in Fig. 6.1.4 but for 1987-2001.

Figure 6.1.7. Time evolution of the preconditioning index representing the decadal time scale difference in h (depth of thermocline) over the eastern equatorial Indian Ocean, from (a) the ocean

References

Abram, N. J., M. K. Gagan, Z. Y. Liu, W. S. Hantoro, M. T. McCulloch, and B. W. Suwargadi, 2007: Seasonal characteristics of the Indian Ocean Dipole during the Holocene epoch. *Nature*, **445,** 299-302.

Allan, R. J., 2000: ENSO and climatic variability in the last 150 years. *El Niño and the Southern Oscillation: Multiscale Variability and its Impacts on Natural Ecosystems and Society.*, M. V. Diaz HF Ed., Cambridge University Press, 3-56.

Allan, R., D. Chambers, W. Drosdowsky, H. Hendon, M. Latif, N. Nicholls, I. Smith, R. Stone, and Y. Tourre, 2001: Is there an Indian Ocean dipole, and is it independent of the El Niño - Southern Oscillation? *Published in Exchanges*, **21.**

Allan, R. J., C. J. C. Reason, J. A. Lindesay, and T. J. Ansell, 2003: Protracted ENSO episodes and their impacts in the Indian Ocean region. *Deep-Sea Research, Part II- Topical Studies in Oceanography*, **50,** 2331-2347.

Annamalai, H., R. Murtugudde, J. Potemra, S. P. Xie, P. Liu, and B. Wang, 2003: Coupled dynamics over the Indian Ocean: spring initiation of the Zonal Mode. *Deep-Sea Research Part II-Topical Studies in Oceanography*, **50,** 2305-2330.

Annamalai, H., J. Potemra, R. Murtugudde, and J. P. McCreary, 2005: Effect of preconditioning on the extreme climate events in the tropical Indian Ocean. *Journal of Climate*, **18,** 3450-3469.

Ashok, K., W. L. Chan, T. Motoi, and T. Yamagata, 2004: Decadal variability of the Indian Ocean dipole - art. no. L24207. *Geophysical Research Letters*, **31,** 24207-24207.

Baquero-Bernal, A., M. Latif, and S. Legutke, 2002: On dipolelike variability of sea surface temperature in the tropical Indian Ocean. *Journal of Climate*, **15,** 1358-1368.

Behera, S. K., R. Krishnan, and T. Yamagata, 1999: Unusual ocean-atmosphere conditions in the tropical Indian Ocean during 1994. *Geophysical Research Letters*, **26,** 3001-3004.

Behera, S. K., P. S. Salvekar, and T. Yamagata, 2000: Simulation of interannual SST variability in the tropical Indian Ocean. *Journal of Climate*, **vol.13, no.19,** 3487-3499.

Behera, S. K. and T. Yamagata, 2003: Influence of the Indian Ocean Dipole on the southern oscillation. *Journal of the Meteorological Society of Japan*, **81,** 169-177.

Behera, S. K., J.Luo and T. Yamagata, 2008: Unusual IOD event of 2007. *Geophysical Research Letters*, **35,** 14.

Black, E., J. Slingo, and K. R. Sperber, 2003: An observational study of the relationship between excessively strong short rains in coastal East Africa and Indian Ocean SST. *Monthly Weather Review*, **131,** 74-94.

Birol, F. and R. Morrow, 2001: Source of the baroclinic waves in the southeast Indian Ocean. *Journal of Geophysical Research*, **106,** 9145-9160.

Brandt, P., L. Stramma, F. Schott, J. Fischer, M. Dengler, and D. Quadfasel, 2002: Annual Rossby waves in the Arabian Sea from TOPEX/POSEIDON altimeter and in situ data. *Deep-Sea Research Part II-Topical Studies in Oceanography*, **49,** 1197-1210

Cai, W., A. Sullivan, and T. Cowan, 2009: How rare are the 2006-2008 positive Indian Ocean Dipole events? An IPCC AR4 climate model perspective. *Geophysical Research Letters*, **36**.

Challenor, P. G., P. Cipollini, D. Cromwell, K. L. Hill, G. D. Quartly, and I. S. Robinson, 2004: Characteristics of mid-latitude Rossby wave propagation from multiple satellite datasets. *International Journal of Remote Sensing*, **25,** 1297-1302.

Chambers, D. P., B. D. Tapley, and R. H. Stewart, 1999: Anomalous warming in the Indian Ocean coincident with El Nino. *Journal of Geophysical Research*, **vol.104, no.C2,** 3035-3047.

Charles, C. D., K. Cobb, M. D. Moore, and R. G. Fairbanks, 2003: Monsoon-tropical ocean interaction in a network of coral records spanning the 20th century. *Marine Geology*, **201,** 207-222.

Chelton, D. B. and M. G. Schlax, 1996: Global observations of oceanic Rossby waves. *Science*, **272,** 234-238.

Church, J. A., N. J. White, R. Coleman, K. Lambeck, and J. X. Mitrovica, 2004: Estimates of the regional distribution of sea level rise over the 1950-2000 period. *Journal of Climate*, **17,** 2609-2625.

Church, J. A. and N. J. White, 2006: A 20th century acceleration in global sea-level rise - art. no. L01602. *Geophysical Research Letters*, **33,** 1602-1602.

Clark, C. O., P. J. Webster, and J. E. Cole, 2003: Interdecadal variability of the relationship between the Indian Ocean zonal mode and East African coastal rainfall anomalies. *Journal of Climate*, **16,** 548-554.

Clarke, A. J. and X. Liu, 1993: Observations and dynamics of semiannual and annual sea levels near the eastern equatorial Indian Ocean boundary. *Journal of Physical Oceanography*, **23,** 386-399.

Claerbout, J., 1976: Fundamentals of geophysical data processes.

Danielson, G. C. and C. Lanczos, 1942: Some Improvements in Practical Fourier Analysis and Their Application to X-ray Scattering From Liquids. *J. Franklin Inst*, **233**.

Daubechies, I., 1992: *Ten lectures on wavelets. CBMS-NSF Lecture Notes nr. 61*, Society for Industrial & Applied.

Dommenget, D. and M. Latif, 2002: A cautionary note on the interpretation of EOFs. *Journal of Climate*, **vol.15, no.2,** 216-225.

Du, Y., T. D. Qu, and G. Meyers, 2008: Interannual variability of sea surface temperature off Java and Sumatra in a global GCM. *Journal of Climate*, **21,** 2451-2465.

Emery, W. J. and R. E. Thomson, 2001: Data analysis methods in physical oceanography. Second edition ed. Elsevier Science B.V., 638 pp.

Feng, M. and G. Meyers, 2003: Interannual variability in the tropical Indian Ocean: a two-year time-scale of Indian Ocean dipole. *Deep-Sea Research Part II-Topical Studies in Oceanography*, 2009, **50,** 2263-2284.

Fischer, A. S., P. Terray, E. Guilyardi, S. Gualdi, and P. Delecluse, 2005: Two independent triggers for the Indian ocean dipole/zonal mode in a coupled GCM. *Journal of Climate*, **18,** 3428-3449.

Fu, L., 2001: Ocean circulation and variability from satellite altimetry. *Ocean Circulation and Climate: Observing and Modelling the Global Ocean*, G. Siedler, J. C. J., and J. Gould, Eds., Academic Press, 715.

Fu, L. L., 2007: Intraseasonal variability of the equatorial Indian Ocean observed from sea surface height, wind, and temperature data. *Journal of Physical Oceanography*, **37,** 188-202.

Gagan, M. K., L. K. Ayliffe, D. Hopley, J. A. Cali, G. E. Mortimer, J. Chappell, M. T. McCulloch, and M. J. Head, 1998: Temperature and surface-ocean water balance of the mid-Holocene tropical Western Pacific. *Science*, **279,** 1014-1018.

Gronell, A. and S. E. Wijffels, 2008: A semiautomated approach for quality controlling large historical ocean temperature archives. *Journal of Atmospheric and Oceanic Technology*, **25,** 990-1003.

Han, W. Q., J. P. McCreary, D. L. T. Anderson, and A. J. Mariano, 1999: Dynamics of the eastern surface jets in the equatorial Indian Ocean. *Journal of Physical Oceanography*, **29,** 2191-2209.

Hastenrath, S., A. Nicklis, and L. Greischar, 1993: Atmospheric-Hydrospheric Mechanisms of Climate Anomalies in the Western Equatorial Indian-Ocean. *Journal of Geophysical Research-Oceans*, **98,** 20219-20235.

Hastenrath, S., 2002: Dipoles, temperature gradients, and tropical climate anomalies. *Bulletin of the American Meteorological Society*, **83,** 735-738.

Hastenrath, S., 2003: Of dipoles and spherical cows - How empirical analyses, provide but a limited perspective - Reply. *Bulletin of the American Meteorological Society*, **84,** 1424-1425.

Horii, T., H. Hase, I. Ueki, and Y. Masumoto, 2008: Oceanic precondition and evolution of the 2006 Indian Ocean dipole - art. no. L03607. *Geophysical Research Letters*, **35,** 3607-3607.

Huang, B. H., and Kinter, J. L., 2002: Interannual variability in the tropical Indian Ocean. *Journal of Geophysical Research-Oceans*, **107,** C11.

Iizuka, S., T. Matsuura, and T. Yamagata, 2000: The Indian Ocean SST dipole simulated in a coupled general circulation model. *Geophysical Research Letters*, **27,** 3369-3372.

Jensen, A. and A. la Cour-Harbo, 2001: Ripples in Mathematics. The Discrete Wavelet Transform. *Springer Verlag*.

Jin, F. F., J. S. Kug, S. I. An, and I. S. Kang, 2003: A near-annual coupled ocean-atmosphere mode in the equatorial Pacific ocean - art. no. 1080. *Geophysical Research Letters*, **30,** 1080-1080.

Kanamitsu, M., W. Ebisuzaki, J. Woollen, S-K Yang, J.J. Hnilo, M. Fiorino, and G. L. Potter, 2002: NCEP-DEO AMIP-II Reanalysis (R-2)

Kang, I. S., J. S. Kug, S. I. An, and F. F. Jin, 2004: A near-annual Pacific Ocean basin mode. *Journal of Climate*, **17,** 2478-2488.

Kaplan, A., M. A. Cane, Y. Kushnir, A. C. Clement, M. B. Blumenthal, and B. Rajagopalan, 1998: Analyses of global sea surface temperature 1856-1991. *Journal of Geophysical Research-Oceans*, **103,** 18567-18589.

Keenlyside, N. S., M. Latif, and A. Durkop, 2007: On sub-ENSO variability. *Journal of Climate*, **20,** 3452-3469.

Killworth, P. D. and J. R. Blundell, 2003a: Comments on "The effect of bottom topography on the speed of long extratropical planetary waves" - Reply. *Journal of Physical Oceanography*, **33,** 1542-1547.

Killworth, P. D. and J. R. Blundell, 2003b: Long extratropical planetary wave propagation in the presence of slowly varying mean flow and bottom topography. Part I: The local problem. *Journal of Physical Oceanography*, **33,** 784-801.

Killworth, P. D. and J. R. Blundell, 2003c: Long extratropical planetary wave propagation in the presence of slowly varying mean flow and bottom topography. Part II. Ray propagation and comparison with observations. *Journal of Physical Oceanography*, **33,** 802-821.

Latif, M. and T. P. Barnett, 1995: Interactions of the Tropical Oceans. *Journal of Climate*, **8,** 952-964.

Latif, M., A. Groetzner, M. Munnich, E. Maier-Reimer, S. Venzke, and T. P. Barnett, 1996: Mechanism for decadal climate variability. *Mechanism for decadal climate variability*, 48.

Le Blanc, J. L. and J. P. Boulanger, 2001: Propagation and reflection of long equatorial waves in the Indian Ocean from TOPEX/POSEIDON data during the 1993-1998 period. *Climate Dynamics*, **17,** 547-557.

Li, T., Y. S. Zhang, C. P. Chang, and B. Wang, 2001: On the relationship between Indian Ocean sea surface temperature and Asian summer monsoon. *Geophysical Research Letters*, **28,** 2843-2846.

Li, T. and Y. S. Zhang, 2002: Processes that determine the quasi-biennial and lower-frequency variability of the South Asian monsoon. *Journal of the Meteorological Society of Japan*, **80,** 1149-1163.

Loschnigg, J., G. A. Meehl, P. J. Webster, J. M. Arblaster, and G. P. Compo, 2003: The Asian monsoon, the tropospheric biennial oscillation, and the Indian Ocean zonal mode in the NCAR CSM. *Journal of Climate*, **16,** 1617-1642.

Luo, J. J., S. Masson, S. Behera, and T. Yamagata, 2007: Experimental forecasts of the Indian Ocean Dipole using a coupled OAGCM. *Journal of Climate*, **20,** 2178-2190.

Luo, J. J., S. Behera, Y. Masumoto, H. Sakuma, and T. Yamagata, 2008: Successful prediction of the consecutive IOD in 2006 and 2007 - art. no. L14S02. *Geophysical Research Letters*, **35,** S1402-S1402.

Mallat, S. G., 1989: A Theory for Multiresolution Signal Decomposition - the Wavelet Representation. *Ieee Transactions on Pattern Analysis and Machine Intelligence*, **11,** 674-693.

Masumoto, Y. and G. Meyers, 1998: Forced Rossby waves in the southern tropical Indian Ocean. *Journal of Geophysical Research-Oceans*, **103,** 27589-27602.

Matano, R. P., 1995: Numerical experiments on the effects of a meridional ridge on the transmission of energy by barotropic Rossby waves. *Journal of Geophysical Research*, **100,** 18271-18280.

Matei, D., N. Keenlyside, M. Latif, and J. Jungclaus, 2008: Subtropical forcing of tropical Pacific climate and decadal ENSO modulation. *Journal of Climate*, **21,** 4691-4709.

McClean, J. L., D. P. Ivanova, and J. Sprintall, 2005: Remote origins of interannual variability in the Indonesian Throughflow region from data and a global Parallel Ocean Program simulation. *Journal of Geophysical Research-Oceans*, **110,** 10013-10013.

Meehl, G. A., 1993: A coupled air-sea biennial mechanism in the tropical Indian and Pacific regions: role of the ocean. *Journal of Climate*, **vol.6, no.1,** 31-41.

Meehl, G. A. and J. M. Arblaster, 2002: The Tropospheric Biennial Oscillation and Asian-Australian Monsoon Rainfall. *Journal of Climate*, **15,** 722-744.

Meehl, G. A., J. M. Arblaster, and J. Loschnigg, 2003: Coupled Ocean-Atmosphere Dynamical Processes in the Tropical Indian and Pacific Oceans and the TBO. *Journal of Climate*, **16,** 2138-2158.

Meyers, G., 1996: Variation of Indonesian throughflow and the El Nino Southern Oscillation. *Journal of Geophysical Research-Oceans*, **101,** 12255-12263.

Meyers, G. and L. Pigot, 1999: Analysis of frequently repeated XBT lines in the Indian Ocean. *CSIRO Marine Laboratories Report,* Hobart, Australia, 43pp.

Meyers, G., P. McIntosh, L. Pigot, and M. Pook, 2007: The years of El Nino, La Nina, and interactions with the tropical Indian ocean. *Journal of Climate*, **20,** 2872-2880.

Morrow, R. and F. Birol, 1998: Variability in the southeast Indian Ocean from altimetry: Forcing mechanisms for the Leeuwin Current. *Journal of Geophysical Research-Oceans*, **103,** 18529-18544.

Morrow, R., F. Birol, D. Griffin, and J. Sudre, 2004: Divergent pathways of cyclonic and anti-cyclonic ocean eddies - art. no. L24311. *Geophysical Research Letters*, **31,** 24311-24311.

Murtugudde, R. and A. J. Busalacchi, 1999: Interannual variability of the dynamics and thermodynamics of the tropical Indian Ocean. *Journal of Climate*, **12,** 2300-2326.

Murtugudde, R., J. P. McCreary, and A. J. Busalacchi, 2000: Oceanic processes associated with anomalous events in the Indian Ocean with relevance to 1997-1998. *Journal of Geophysical Research-Oceans*, **105,** 3295-3306.

Nicholls, N., 1989: Sea Surface Temperatures and Australian Winter Rainfall. *Journal of Climate*, **2,** 965-973.

Nicholson, S. E., 1997: An analysis of the ENSO signal in the tropical Atlantic and western Indian Oceans. *International Journal of Climatology*, **17,** 345-375.

Perigaud, C. and P. Delecluse, 1992: Annual sea level variations in the southern Indian Ocean from Geosat and shallow-water simulation. *Journal of Geophysical Research*, **97,** 20,169-20,178.

Perigaud, C. and P. Delecluse, 1993: Interannual sea level variations in the tropical Indian Ocean from Geosat and shallow water simulations. *Journal of Physical Oceanography*, **vol.23, no.9,** 1916-1934.

Philander, S. G. and A. Fedorov, 2003: Is El Nino sporadic or cyclic? *Annual Review of Earth and Planetary Sciences*, **31,** 579-594.

Prasad, T. G. and J. L. McClean, 2004: Mechanisms for anomalous warming in the western Indian Ocean during dipole mode events. *Journal of Geophysical Research-Oceans*, **10**

Rao, S. A., S. K. Behera, Y. Masumoto, and T. Yamagata, 2002: Interannual subsurface variability in the tropical Indian Ocean with a special emphasis on the Indian Ocean Dipole. *Deep-Sea Research Part II-Topical Studies in Oceanography*, **49,** 1549-1572.

Rayner, N. A., D. E. Parker, E. B. Horton, C. K. Folland, L. V. Alexander, D. P. Rowell, E. C. Kent, and A. Kaplan, 2003: Global analyses of sea surface temperature, sea ice, and night marine air temperature since the late nineteenth century. *Journal of Geophysical Research,* **108** (D14), 4407.

Reason, C. J. C., R. J. Allan, J. A. Lindesay, and T. J. Ansell, 2000: ENSO and climatic signals across the Indian Ocean basin in the global context. I. Interannual composite patterns. *International Journal of Climatology*, **20,** 1285-1327.

Reddy, P. R. C., P. S. Salvekar, and D. W. Ganer, 2004: Westward propagating twin gyres in the equatorial Indian Ocean. *Geophysical Research Letters*, **31**.

Reverdin, G., D. L. Cadet, and D. Gutzler, 1986: Interannual displacements of convection and surface circulation over the equatorial Indian Ocean. *Quarterly Journal of the Royal Meteorological Society*, **112**, 43-67.

Reynolds, R. W. and T. M. Smith, 1994: Improved Global Sea-Surface Temperature Analyses Using Optimum Interpolation. *Journal of Climate*, **7**, 929-948.

Reynolds, R. W., N. A. Rayner, T. M. Smith, D. C. Stokes, and W. Q. Wang, 2002: An improved in situ and satellite SST analysis for climate. *Journal of Climate*, **15**, 1609-1625.

Saji, N. H., B. N. Goswami, P. N. Vinayachandran, and T. Yamagata, 1999: A dipole mode in the tropical Indian Ocean. *Nature*, **401**, 360-363.

Sakova, I., G. Meyers, and R. Coleman, 2006a: On the low frequency variability in the Indian Ocean. *(In) Dynamic Planet - Monitoring and Understanding a Dynamic Planet with Geodetic and Oceanographic Tools*, Springer-Verlag, P. Tregoning and C. Rizos (Eds), 47-50.

Sakova, I. V., G. Meyers, and R. Coleman, 2006b: Interannual variability in the Indian Ocean using altimeter and IX1-expendable bathy-thermograph (XBT) data: Does the 18-month signal exist? - art. no. L20603. *Geophysical Research Letters*, **33**, 20603-20603.

Schott, F. A. and J. P. McCreary, 2001: The monsoon circulation of the Indian Ocean. *Progress in Oceanography*, **51**, 1-123.

Schott, F. A., S.-P. Xie, and J. P. McCreary, 2009: Indian Ocean circulation and climate variability. *Reviews of Geophysics*, **47**.

Shankar, D., V. V. Gopalakrishna, S. S. C. Shenoi, F. Durand, S. R. Shetye, C. K. Rajan, Z. Johnson, N. Araligidad, and G. S. Michael, 2004: Observational evidence for westward propagation of temperature inversions in the southeastern Arabian Sea. *Geophysical Research Letters*, **31**.

Sheng, Y., 1996: Wavelet transform. The transforms and applications handbook, D. Poularikas, Ed., CRC Press.

Shinoda, T., H. H. Hendon, and M. A. Alexander, 2004a: Surface and subsurface dipole variability in the Indian Ocean and its relation with ENSO. *Deep-Sea Research Part I-Oceanographic Research Papers*, **51**, 619-635.

Shinoda, T., M. A. Alexander, and H. H. Hendon, 2004b: Remote response of the Indian Ocean to interannual SST variations in the tropical Pacific. *Journal of Climate*, **17**, 362-372.

Song, Q., G. A. Vecchi, and A. J. Rosati, 2007: Indian Ocean variability in the GFDL coupled climate model. *Journal of Climate*, **20**, 2895-2916.

Tailleux, R., 2003: Comments on "The effect of bottom topography on the speed of long extratropical planetary waves". *Journal of Physical Oceanography*, **33**, 1536-1541.

Tomczak, M. and J. S. Godfrey, 1994: *Regional Oceanography: An introduction*. Elsevier Sci.

Tomczak, M. and J. S. Godfrey, 2002: *Regional Oceanography: an introduction*. Elsevier Sci.

Torrence, C. and G. P. Compo, 1998: A practical guide to wavelet analysis. *Bulletin of the American Meteorological Society*, **79**, 61-78.

Tourre, Y. M. and W. B. White, 1995: ENSO signals in global upper-ocean temperature. *Journal of Physical Oceanography*, **vol.25, no.6,** 1317-1332.

Tourre, Y. M. and W. B. White, 1997: Evolution of the ENSO signal over the Indo-Pacific domain. *Journal of Physical Oceanography*, **27,** 683-696.

Tourre, Y. M., B. Rajagopalan, Y. Kushnir, M. Barlow, and W. B. White, 2001: Patterns of coherent decadal and interdecadal climate signals in the Pacific Basin during the 20th century. *Geophysical Research Letters*, **28,** 2069-2072.

Tourre, Y. M. and W. B. White, 2003: Patterns of coherent climate signals in the Indian Ocean during the 20th century - art. no. 2224. *Geophysical Research Letters*, **30,** 2224-2224.

Tozuka, T., J. J. Luo, S. Masson, and T. Yamagata, 2007: Decadal modulations of the Indian Ocean dipole in the SINTEX-F1 coupled GCM. *Journal of Climate*, **20,** 2881-2894.

Venzke, S., M. Latif, and A. Villwock, 2000: The coupled GCM ECHO-2. Part II: Indian ocean response to ENSO. *Journal of Climate*, **13,** 1371-1383.

Ummenhofer, C. C., M. H. England, P. C. McIntosh, G. A. Meyers, M. J. Pook, J. S. Risbey, A. S. Gupta, and A. S. Taschetto, 2009: What causes southeast Australia's worst droughts? *Geophysical Research Letters*, **36**

Vaid, B. H., C. Gnanaseelan, and P. S. Salvekar, 2008: Observed twin gyres and their interannual variability in the equatorial Indian Ocean using Topex/Poseidon altimetry. *Current Science*, **95,** 30-35.

Venzke, S., M. Latif, and A. Villwock, 2000: The coupled GCM ECHO-2. Part II: Indian ocean response to ENSO. *Journal of Climate*, **13,** 1371-1383.

Vialard, J., G. R. Foltz, M. J. McPhaden, J. P. Duvel, and C. D. Montegut, 2008: Strong Indian Ocean sea surface temperature signals associated with the Madden-Julian Oscillation in late 2007 and early 2008. *Geophysical Research Letters*, **35.**

Vinayachandran, P. N., N. H. Saji, and T. Yamagata, 1999: Response of the Equatorial Indian Ocean to an unusual wind event during 1994. *Geophysical Research Letters*, **26,** 1613-1616.

Vinayachandran, P. N., S. Iizuka, and T. Yamagata, 2002: Indian Ocean Dipole mode events in an ocean general circulation model. *Deep-Sea Research Part II-Topical Studies in Oceanography*, **49,** 1573-1596.

Wang, B., R. G. Wu, and R. Lukas, 2000: Annual adjustment of the thermocline in the tropical Pacific Ocean. *Journal of Climate*, **13,** 596-616.

Wang, L. P., C. J. Koblinsky, and S. Howden, 2001: Annual Rossby wave in the southern Indian Ocean: Why does it "appear" to break down in the middle ocean? *Journal of Physical Oceanography*, **31,** 54-74.

Wang, C. Z. and P. C. Fiedler, 2006: ENSO variability and the eastern tropical Pacific: A review. *Progress in Oceanography*, **69,** 239-266.

Webster, P. J., A. M. Moore, J. P. Loschnigg, and R. R. Leben, 1999: Coupled ocean-atmosphere dynamics in the Indian Ocean during 1997-98. *Nature*, **vol.401, no.6751,** 356-360.

White, W. B. and D. R. Cayan, 2000: A global El Nino-Southern Oscillation wave in surface temperature and pressure and its interdecadal modulation from 1900 to 1997. *Journal of Geophysical Research-Oceans*, **105,** 11223-11242.

White, W. B., 2001: Evidence for coupled Rossby waves in the annual cycle of the Indo-Pacific ocean. *Journal of Physical Oceanography*, **31,** 2944-2957.

White, W. B. and R. J. Allan, 2001: A global quasi-biennial wave in surface temperature and pressure and its decadal modulation from 1900 to 1994. *Journal of Geophysical Research-Oceans*, **106,** 26789-26803.

White, W. B. and Y. M. Tourre, 2003: Global SST/SLP waves during the 20th century. *Geophysical Research Letters*, **30,** 12.

White, W. B., Y. M. Tourre, M. Barlow, and M. Dettinger, 2003: A delayed action oscillator shared by biennial, interannual, and decadal signals in the Pacific Basin - art. no. 3070. *Journal of Geophysical Research-Oceans*, **108,** 3070-3070.

White, W. B. and Y. M. Tourre, 2007: A delayed action oscillator shared by the ENSO and ODO in the Indian Ocean. *Journal of Oceanography*, **63,** 223-241.

Wijffels, S. and G. Meyers, 2004: An intersection of oceanic waveguides: Variability in the Indonesian throughflow region. *Journal of Physical Oceanography*, **34,** 1232-1253.

Woodworth, P. L. and R. Player, 2003: The permanent service for mean sea level: An update to the 21st century. *Journal of Coastal Research*, **19,** 287-295.

Wu, R. G. and B. P. Kirtman, 2005: Near-annual SST variability in the Equatorial Pacific in a coupled general circulation model. *Journal of Climate*, **18,** 4454-4473.

Wu, S. and Q. Liu, 2005: Some problems on the global wavelet spectrum *Journal of Ocean University of China* **4,** 398-402

Wyrtki, K., 1973: An equatorial jet in the Indian Ocean. *Science*, **181,** 262-264.

Yamagata, T., K. Mizuno, and Y. Masumoto, 1996: Seasonal variations in the equatorial Indian Ocean and their impact on the Lombok throughflow. *Journal of Geophysical Research-Oceans*, **101,** 12465-12473.

Yamagata, T., S. Behera, J. Luo, S. Masson, M. Jury, and S. Rao, 2004: Coupled Ocean-Atmosphere variability in the Tropical Indian Ocean. *Ocean-Atmosphere Iteraction and Climate Variability*, A. book, Ed.

Yeh, S. W. and B. P. Kirtman, 2005: Pacific decadal variability and decadal ENSO amplitude modulation - art. no. L05703. *Geophysical Research Letters*, **32,** 5703-5703.

Yuan, D. L., 2005: Role of the Kelvin and Rossby waves in the seasonal cycle of the equatorial Pacific Ocean circulation - art. no. C04004. *Journal of Geophysical Research-Oceans*, **110,** 4004-4004.

Yuan, D. and W. Han, 2006: Roles of Equatorial Waves and Western Boundary Reflection in the Seasonal Circulation of the Equatorial Indian Ocean. *Journal of Physical Oceanography*, **36,** 930.

Xie, S.-P., H. Annamalai, F. A. Schott, and J. P. J. McCreary, 2002: Structure and Mechanisms of South Indian Ocean Climate Variability. *Journal of Climate*, **15,** 864-878.

List of Acronyms

D20 - Depth of the 20°C Isothermal Surface

DFT - Discrete Fourier Transform

DMI - Dipole Mode Index

ENSO - El Niño - Southern Oscillation

EOF - Empirical Orthogonal Functions

FFT - Fast Fourier Transform

GISST - Global Sea-Ice and Sea Surface Temperature Data Set

IFFT - Inverse Fast Fourier Transform

IOD - Indian Ocean Dipole

IODE - South-Eastern Tropical Indian Ocean Dipole Mode (see Fig.1.3.1)

IODW - Western Tropical Indian Ocean Dipole Mode (see Fig.1.3.1)

IOTA - Indian Ocean Thermal Archive

IOZM - Indian Ocean Zonal Mode

JAMSTEC - Japan Agency for Marine-Earth Science and Technology

NCAR - National Center for Atmospheric Research

NCEP - National Center for Environmental Prediction

NOAA - National Oceanic and Atmospheric Administration

PSD, psd - Power Spectra Density

QB - Quasi-biennial

SLA - Sea Level Anomaly

SSH - Sea Surface Heights

SST - Sea Surface Temperature

TBO - Tropospheric Biennial Oscillation

XBT - Expendable Bathythermograph